An investigation on the effect of structural and microstructural attributes on magnetostriction of Tb-Dy-Fe and Fe-Ga alloys

A Thesis

Submitted for the Degree of

Doctor of Philosophy

in the Faculty of Engineering

By

Mithun Palit

Department of Materials Engineering

Indian Institute of Science

Bangalore-560012, India

July 2012

To

My Parents and Teachers

Synopsis

Magnetostrictive materials form an important class of magnetic materials keeping in view of their potential applications as sensors and/ or actuators. Amongst several materials in this class, RFe_2 type (R represents rare earths) intermetallics display maximum promise owing to giant magnetostriction exhibited by them. In this thesis, one such mixed rare earth compound $(Tb,Dy)Fe_2$ has been chosen for investigations. Several aspects such as phase equilibria, evolution of texture and microstructure of directionally solidified alloys have been studied in this thesis, where existing literature cannot provide a clear insight. Finally, a correlation between texture and microstructure with magnetostriction has been brought out to understand the process-structure-property relationship of such practically important intermetallic compound. Apart from the investigation on the well known magnetostrictive material $(Tb,Dy)Fe_2$, attempts have been made to understand the role of microstructure, especially the ordered phases on the magnetostriction of an emerging magnetostrictive material Fe-Ga. The description of the experimental work carried out and the analysis of data have been presented in the subsequent chapters of this thesis with a brief review of existing literature at the beginning.

The thesis is divided into eight chapters. The first chapter presents a brief introduction on the material systems considered for the present study, with a view to present the scopes available for further investigations. Subsequently, in the second chapter of this thesis, a summary of existing literature has been narrated to highlight the perspective of the work presented in the subsequent chapters. An introduction about magnetostriction and magnetostrictive material has been presented with a review of studies carried out on different materials is also included in this chapter. The search for magnetostriction at ambient temperature resulted in discovery of giant magnetostriction in RFe_2 type compounds at room temperature. Therefore, a brief discussion has been presented in this chapter on several aspects of these intermetallic compounds such as origin of large magnetostriction, crystal structure, anisotropy compensation and different methods attempted to process these compounds. In addition, several potential applications of this magnetostrictive material have been presented. A brief description of binary Tb-Fe and Dy-Fe diagrams has been compiled and presented in the chapter, with a short description on the limited understanding available

till date on the ternary phase equilibria of Tb-Dy-Fe. Since directional solidification is most widely used method for producing $(Tb,Dy)Fe_2$ for numerous practical applications, a brief review on directionally solidified $(Tb,Dy)Fe_2$ has also been covered. The second chapter also contains a summary of several emerging magneto-elastic materials currently being considered for practical applications. However, importance has been given to Fe-Ga alloys as it displays the maximum potential amongst the emerging material systems. Subsequently, a brief review on structure-property relationship on Fe-Ga alloys has been presented. The chapter ends with brief statements on grey areas in terms of understanding that exists in the literature and which also forms basis of the work presented in subsequent chapters.

In the third chapter of the thesis an investigation to understand the ternary phase equilibria of Tb-Dy-Fe has been presented. The study aims at understanding the effect of Tb/Dy ratio on phase equilibria and magnetic properties of $Tb_xDy_{1-x}Fe_{1.95}$ (x=0-1) alloys. An attempt has been made to understand the nature of the phase field of $(Tb,Dy)Fe_2$ with various Tb/Dy ratio. Microstructural and micro-chemical analysis along with study of lattice parameter has been used to predict the nature of phase equilibria and the deviation from the pseudo-binary behaviour assumed so far. A series of magnetic properties such as Curie temperature, magnetostriction, hyperfine field, ac susceptibility, spontaneous magnetostriction and coercivity have been measured and corroborated with the observed microstructural features. The study indicates several deviations from binary Tb-Fe and Dy-Fe. The microstructural investigations indicate that volume fraction of pro-peritectic phase varies in non-linear fashion when plotted as a function of Tb concentration. Further, from the microstructural investigations and study of lattice parameter and Curie temperature, a schematic sketch of a section of the ternary diagram, where (Tb,Dy) / Fe =1.95, has been formulated and presented in this chapter.

As discussed earlier, directional solidification technique is most widely adopted method for processing the $(Tb,Dy)Fe_2$ for practical applications. Therefore, the fourth chapter presents a study on directional solidification of $Tb_{0.3}Dy_{0.7}Fe_{1.95}$ alloy by modified Bridgman technique. Although several studies reported in the available literature on Bridgman solidification of Tb-Dy-Fe alloy, very less attention has been paid on issues such as solidification microstructure and evolution of texture. Therefore, in this chapter more attention has been paid on those issues. The alloy in a shape of cylindrical rods of 15 mm Φ and 80 mm long, were directionally solidified with a series of growth rate ranging from 5 to

100 cm/h, at a constant temperature gradient of 150^{o}C/ cm. Systematic investigation on evolution of microstructure from bottom to top has been carried out and different microstructural features such as island banding or peritectic coupled growth have been reported. The same chapter also presents evolution of texture with growth rate. A mechanism based on atomic attachment kinetics is proposed in this chapter to explain the orientation selection with growth rate. At the end of this chapter, a correlation between magnetostriction and static strain co-efficient ($d\lambda/dH$) with texture and microstructure has been brought out.

The microstructural feature observed in Bridgman solidified samples presented in chapter 4 indicates mostly plane front solidification. Therefore, in order to understand the microstructure and texture evolution in cellular/ dendritic regime, directional solidification of $Tb_{0.3}Dy_{0.7}Fe_{1.95}$ by zone melting technique has been adopted, which is presented in chapter 5. The zone melting process offered a lesser temperature gradient of 100^{o}C/cm and therefore offered opportunity to study the texture and microstructure evolution in cellular/ dendritic regime. A detailed texture study has been reported in this chapter, adopting texture goniometer as well as calculation of texture co-efficient from slow scanned x-ray diffraction data. Since, the solidification is cellular/ dendritic in the case of zone melted alloys, the orientation selection mechanism proposed in the previous chapter is not applicable. Accordingly, several possible configurations of non-planar interfaces have been worked out with the aid of stereograms. The concept of such theoretical model is explained in detail in chapter 5. Finally, a mechanism based on atomic attachment kinetics has been proposed and the morphology of the modelled interface has been correlated to the shape of cell/ dendrite cross-section. The study on orientation selection mechanism described in chapter 4 and 5 together explains completely the evolution of different texture components under different directional solidification conditions.

The sixth chapter of the thesis enumerates the study on the effect of ordered and disordered phases on magnetostriction of emerging magnetostrictive alloy Fe-Ga. A series of alloy compositions of Fe-x at % Ga (x=17, 20, 23 and 25) were subjected to different thermal treatments and characterized for microstructural features and magnetostriction. Transmission electron microscopy has been adopted for identifying the different ordered phases. Microstructure investigation of slow cooled, quenched and quenched+ aged alloys reveals type of the solid state transformation from disordered to ordered phases. A detailed discussion on this aspect has been made in this chapter. The investigations indicate formation

of ordered DO_3 phase from disordered A2 phase by first order transformation in 17 and 20 at% Ga alloys. The correlation of microstructure and magnetostriction indicates disordered A2 phase or ordered DO_3 phase alone, exhibiting good magnetostriction. The magnetostriction however decreases substantially when these two phases are present together.

An overall summary of experimental results and the interpretation has been presented in chapter 7 and some scopes for further studies are highlighted in chapter 8.

Acknowledgements

It is my pleasure to express my deep appreciation and gratitude to my research supervisors Prof. K. Chattopadhyay and Dr. S. Pandian (Scientist 'G', DMRL, Hyderabad) for their guidance, advice, encouragement and support. They provided a friendly atmosphere that helped me to learn lot of things. Their cheerful disposition, openness to new ideas and warm support will be remembered at all times.

I express my thanks to Prof. Vikram Jayaram, Chairman, Dept. of Materials Engineering, Prof. T Abhinandanan, Dr. Satyam Suwas and Dr. S Karthikeyan, faculties at Dept. of Materials Engineering at IISc, Bangalore, for their teaching during course semester. The knowledge on crystallography, thermodynamics and texture that I gathered from their teaching helped me to understand several critical issues of my thesis.

I am also thankful to Dr. G Malakondaiah, Director, DMRL, Hyderabad, for the encouragement and support he rendered throughout the execution of my thesis work. I would also like to acknowledge the continued encouragement from Prof. D. Banerjee (former CCR&D(AMS) at DRDO and currently with IISc, Bangalore) and express my thanks for introducing me to the potential research opportunities in the area of magnetostrictive materials. I am thankful to Dr S V Kamat, Head Advanced Magnetics Group and Functional Materials Division of DMRL for his continued support, encouragement and valuable suggestions. I am also thankful to Dr V Chandrasekaran former Head Advanced Magnetics Group of DMRL for his support

I thank Dr. A.M. Sriramamurthy, (Former Director, DMRL and currently with ARC-I), Shri Niranjan Das and Shri Satyapal Singh of DMRL, for the numerous thought provoking discussions which helped me tremendously during design of directional solidification furnace based on Bridgman technique. I also thank Prof. G Markandeyulu, IIT, Madras for providing the zone melting facility for the experiments.

I would like to thank Dr. A K Singh and Dr S Banumathy, of DMRL, for helping me in carrying out the texture experiments and analyzing the data. I acknowledge the support of Dr K Satya Prasad for helping me in investigating the samples under transmission electron microscope and analyzing the data. I am also thankful to Dr K Muraleedharan, Dr R Balamuralikrishnan, Dr P Ghosal and Mr Rajdeep Sarkar of Electron Microscopy Group of DMRL for helping me in several aspects of transmission and scanning electron microscopy. I express my gratitude to Structural Failure Analysis Group of DMRL for rendering support in preparing specimens for microstructural observations. I am also thankful to Analytical Chemistry Group of DMRL for their support in analyzing chemical compositions of the alloy.

Working in Advanced Magnetics Group of DMRL has been very enjoyable. I thank all my fellow Scientists and Technical staff for their support. Special thanks to Dr J Arout Chelvane and Mr Himalay Basumatary for their help in executing some critical experiments and analysis of results. The thought provoking debates we used to have provided me several understandings on certain aspects of my thesis work. Apart from their technical help, I cherish the memory of their support as friends in several pale moments. I sincerely

acknowledge the support of Mr M Suresh, Mr Jagbir and Md Rabbani for their continuous support in operation and maintenance of all facilities used for my thesis work.

I would like to thank Defence R&D Organization (DRDO) for providing financial support for the work carried out for my thesis.

My lab mates in nanomaterials lab and other friends at IISc have been supportive and provided a lively time during interaction through various discussion. I thank all of them for their company, co-operation and providing me a homely atmosphere whenever I visited IISc and had opportunity to spend time with them. Especially, I cherish the memorable time I spent with, Shyam, Chandra Sekhar, Chandan, Sanjay, Siddarada, Kaka, Kirtiman, Hindol, Shibayan, Surender, Basha and many others, probably the list is too long to be put here.

I thank Rama for all her help and support in many counts especially for making my stay comfortable whenever I visited the department and I also thank Bharathi and Narayan for the same.

I sincerely acknowledge the support and encouragement from my parents, which helped me to stay firm even through the tough time. The emotional support and encouragement rendered by Asish, my dearest friend at Hyderabad is highly acknowledged. He made my thesis writing period comfortable by sharing many sundry works, which helped me to remain completely unperturbed.

I greatly appreciate the support and encouragement of my wife during the entire thesis period. She herself undertook the sole responsibility of running day to day family life and thereby making me more focused on thesis writing. I value her patience, sacrifice and her enthusing words in odd days.

Mithun Palit

Contents

List of Tables

List of Figures

Chapter 1

Introduction

The discovery of giant magnetostriction in RFe_2 [R—rare earth] compounds triggered intensive research interest on the metallurgical aspects and underlying physics of binary and pseudo-binary ($RR'Fe_2$) systems [1-4]. As a potential candidate for sensors and actuators applications, research on this material were mostly focused on optimization of composition and grain orientation in order to achieve high magnetomechanical energy density and magnetomechanical coupling co-efficient [5-9]. The magnetomechanical coupling co-efficient is related to the efficiency of the material to convert input electrical energy to mechanical vibrations. Therefore, essentially for a device, large magnetostriction should be obtained at lower applied field. This particular characteristics of magnetostrictive alloy requires low coercivity and low magnetocrystalline anisotropy. The coercivity of the material is related to microstructural features present in the material. On the other hand, magnetocrystalline anisotropy is related to composition and grain orientation of the material. Several attempts are noticed in literature that attempts alloy modification to address these issues. The other approach for achieving large magnetostriction at a small applied magnetic field is development of grains orientated closer to easy magnetization direction (EMD) <111>, by adopting directional solidification techniques. In order to develop grain orientation in the cylindrical rods of this material; methods such as zone melting (for dia ≤ 8 mm) and modified Bridgman (for dia. ≥10 mm) are generally adopted [7-12].

The previous studies on Tb-Dy-Fe alloys indicate substantial influence of microstructure and texture on magnetostrictive properties. The relationship between microstructure and property can be better understood in the light of understanding of ternary phase equilibria. Unfortunately, the available literature till date ignores the ternary interactions and considers Tb-Dy-Fe as pseudo-binary system owing to chemical similarity of Tb and Dy. However, such assumption restricts a complete understanding of evolution of microstructure with change of composition. Further, in recent time a need is also felt of finding alternate and more abundant rare earth combinations due to fluctuations in supply of rare earth elements.

In case of the studies reported on directional solidification, different types of texture formation have been observed but a complete understanding of evolution of texture components of such diverse nature is still not available. However, understanding of texture evolution mechanism is extremely important as it helps to design the parameters of directional solidification process for obtaining materials with large magnetostriction. The other issue associated with directional solidification process is formation of microstructural features and their distribution, which plays a crucial role in magnetostrictive property of the alloy. Further, since the giant magnetostrictive phase (Tb,Dy)Fe_2 forms by peritectic reaction, a rich diversity of microstructure can be obtained depending on growth condition. Therefore, it is also required to address the microstructural evolution in order to complete the understanding of process-structure-property relationship.

The (Tb,Dy)Fe_2 alloy although exhibit large magnetostriction, it poses several challenges such as inherent brittleness and reactivity of rare earth elements. As a result, a need is felt to identify an alternative material for magnetostrictive applications. Amongst several materials with good magneto-mechanical properties, Fe-Ga is considered to be the best candidate as potential alternative to (Tb,Dy)Fe_2. The Fe-Ga alloy undergoes a number of complex ordering transformations. Therefore, understanding of formation of several ordered phases and their effect on resultant magnetostriction is quite important. The research in this material is in nascent stage and therefore the understanding on phase transformation and their role in magnetostriction is not well understood. Further, most of the reports on the study of structure-property relationship were carried out on a single crystalline alloy. But, ordered phase formation and their role on magnetostriction is supposed to be different in case of a polycrystalline bulk alloys. Such structure-property relationship in bulk polycrystalline alloy will be useful for development of this material for several practical applications.

In view of the above, a study has been taken up to understand the role of structural and microstructural parameters on magnetostriction of Tb-Dy-Fe and Fe-Ga alloys. In case of Tb-Dy-Fe alloy, a study has been taken up to understand the nature of ternary phase equilibria. Accordingly, the effect of Tb/Dy ratio on phase relationship and magnetic properties in a section where (Tb,Dy)/Fe is 1.95 has been studied. Regarding directional solidification of (Tb,Dy)Fe_2 two techniques were adopted *viz.* Modified Bridgman and zone melting, so that the orientation and microstructure evolution can be studied for the entire range from planar to dendritic solidification conditions. Detailed texture studies have been

carried out for the samples grown at wide range of growth rates and mechanism of orientation selection has been proposed based on atomic attachment kinetics at solid-liquid interface. In case of Fe-Ga alloy, polycrystalline samples of varying Ga concentrations prepared with different thermal history and characterized for presence/ absence of ordered phases. The nature of phase transformation has been studied and related with magnetostrictive properties of polycrystalline alloys.

References:

[1] A E Clark, S H Belson and N Tamagawa, "*Magnetocrystalline Anisotropy in Cubic Rare Earth-Fe_2 Compounds",* AIP Conf. Proc.,10 (1973) 749.

[2] K H J Buschow, in: E.P. Wohlfarth (Ed.), "*Ferromagnetic Materials"*, vol. 1, North Holland, Amsterdam, (1980).

[3] A E Clark, R Abbundi, O McMasters and H Savage, "*Magnetostriction of rare earth-Fe_2 laves phase compounds",* Physica B, 86-88 (1977) 73.

[4] A E Clark, S H Belson and N Tamagawa, *"Huge magnetocrystalline anisotropy in cubic rare earth-Fe_2 compounds"*, Phys. Lett. A, 42 (1972) 160.

[5] J S Abell, D Butler, R D Greenough, V Joyce and K C Pitman, *"Magnetomechanical coupling in $Dy_{0.73}Tb_{0.27}Fe_2$",* J. Mag. Mag. Mater., 62 (1986) 6.

[6] N C koon, A I Schindler and F L Carter, *"Giant magnetostriction in cubic rare earth-iron compounds of the type RFe_2",* Phys. Lett. A, 37 (1971) 413.

[7] O.D. McMasters, J.D. Verhoeven, E.D. Gibson, *"Preparation of Terfenol-D by float zone solidification",* J. Mag. Mag. Mat. 54-57 (1986) 849.

[8] J.D. Verhoeven, E.D. Gibson, O.D. McMasters, H.H. Baker, "*The growth of single crystal Terfenol-D crystals*", Metall. Trans. 18A (1987) 223.

[9] Chengchang Ji, Jianguo Li, Weizeng Ma, Yaohe Zhou, *"Preparation of Terfenol-D with precise <110> orientation and observation of the oriented growth crystal morphology",* J. Alloys Compd. 333 (2002) 291.

[10] Y. Zhao, C. Jiang, H. Zhang, and H. Xu, *"M agnetostriction of <110> oriented crystals in the TbDyFe alloy",* J. Alloys Compd. 354 (2003) 263.

[11] W Mei, T Okane, T Umeda and S Zhou, *"Directional solidification of Tb-Dy-Fe"*, J. Alloys Compd., 248 (1997) 151.

[12] J D Verhoeven, E D Gibson, O D McMasters and J E Ostenson, *"Directional solidification and heat treatment of TerfenoI-D magnetostrictive materials"*, Metall. Trans. A, 21 (1990) 2249.

Chapter 2

Literature Review

2.1. Magnetostriction

A magnetostrictive material is one which changes its dimension under the influence of applied magnetic field [1]. The phenomenon of magnetostriction was first observed by Joule [2] in a steel bar when external magnetic field was applied. Thereafter this phenomenon is termed as 'Joule Effect', in order to describe strain produced in a material when it is subjected to magnetic field. With the course of time many such related and similar phenomenon was discovered such as Villari effect (inverse Joule effect), Wiedmann effects, Mattuci effects and ΔE effect [3,4]. The magnetostrictive properties are consequence of change in state of magnetization under the application of external field and therefore are common in all magnetic materials. However, ferromagnetic and ferrimagnetic materials exhibit larger magnetostriction as compared to paramagnetic materials.

2.2. Magnetostrictive Materials:

The magnetostriction in a material is related to spin-orbit coupling which results in magneto-crystalline anisotropy of the material. The role of anisotropy in magnetostriction was first realized upon discovery of large magnetostriction at low temperature in rare earth elements such as Tb and Dy, which are having large anisotropy. In these materials large basal plane strain (~1%) was reported [5-7] which is incomparably higher than the ferromagnetic transition metals such as Fe, Co and Ni [3]. However due to low magnetic ordering temperature of the rare earth, the magnetostrictive properties could not be utilized for any application. Subsequently studies have been carried out by Carr *et.al.* [8] on magnetostriction of alloys of transition metals and ferrites. However the magnetostriction was found to be extremely less. Rhyne et.al. [9] explained the less magnetostriction in these transition metals and their alloys with the help of itinerant electron theory. Therefore, ferromagnetic transition metals and alloys could not show much promise for large magnetostriction, whereas rare earth elements exhibited large magnetostriction at extremely low temperature. As a result researchers started exploring magneto-elastic properties of cubic intermetallic compounds involving rare earth elements in order to discover a magnetostrictive material capable of

producing large strain at ambient temperature. Amongst several such compounds, most extensively studied are RZn (R implies rare earth) type compounds, having CsCl type structure. Morin and Schmidt [10] studied the low temperature magnetostriction and easy magnetization direction of these compounds. Amongst RZn type compounds, GdZn exhibits highest Curie temperature of 270 K and large magnetostriction of ~ 10^4 microstrains at 4K. The same authors also discussed about the magnetostriction of NaCl type compounds such as RSb, RP, RAs and RBi and found interesting low temperature magnetostrictive properties but the Curie temperature could not be improved.

The other type of rare earth based intermetallic compound that drew greater attention of research community are of RM_2 (M stands for metals) and RT_2 (T stands for transition metals) types. Most of these compounds form in the C15 type Laves phase crystal structure. In this class of alloys, RAl_2 type compounds were most thoroughly studied owing to their exciting low temperature magnetic properties. Purwins and Leson [11] described these compounds in the light of crystal field theory and proposed non-collinear spin structure in such compounds, which is arising from non-magnetic Al. Since, the Curie temperature of RAl_2 type compounds was found to be less, RNi_2 type compound was thought to be of interest in order to enhance the Curie temperature. Although the magnetostrictive properties of RNi_2 type compounds are not extensively studied, from available reports it can be observed that most of such compounds exhibit Curie temperature even lesser than RAl_2 type compounds [12]. Levitin and Markosyan [12] proposed that the Ni- sublattice is non-magnetic in these compounds. As a result, the Curie temperature is much lower. The Curie temperature however, is found to improve largely in RCo_2 type compounds. Taylor [13] studied magnetostriction of RCo_2 type compounds and observed that the volume magnetostriction in these compounds depends on Co sublattice moment, which in turn depends on the type of rare earth element forming the RCo_2 compound. For example Co has no moment in paramagnetic YCo_2 whereas the Co sublattice moment is 1 Bohr Magnetron in $GdCo_2$. Nakamura [14] and Hathway et. al. [15] showed the variation of volume magnetostriction in RCo_2 (R= Gd, Tb, Dy, Ho, Er and Tm) and correlated the observed magnetostriction with Co sublattice moments. Although the Curie temperature could be largely improved, the highest Curie temperature is observed only 256K in $TbCo_2$, which is still below the ambient temperature. Therefore, RFe_2 type compounds were explored [16-20], in order to improve Curie temperature further without much compromise on the anisotropy

exhibited by rare earth elements. The Curie temperature was found to improve much above ambient temperature and large magnetostriction was observed for RFe_2 type compounds owing to strong Fe-Fe interactions [6,7,19-21].

The summary of magnetostriction and Curie temperature of several RM_2 and RT_2 type compounds are presented in Table 2.1 based on several reports [8-28] pertaining to studies on such compounds. It can be clearly observed that the RFe_2 type compounds exhibit large magnetostriction with higher Curie temperature and therefore shows a promise for practical applications.

2.3. Giant magnetostrictive RFe_2 intermetallics:

The RFe_2 compounds exhibit large room temperature magnetostriction as observed first by Koon *et. al.* [29] and Clark *et.al.* [16]. Amongst RFe_2 compounds, $TbFe_2$ displayed highest positive magnetostriction [30] and $SmFe_2$ displays highest negative magnetostriction at room temperature [16]. The large magneto-crystalline anisotropy plays a key role for large magnetostriction exhibited by this class of material. Further, in RFe_2 compounds, the R-Fe interaction is large. As a result the R sublattice magnetization is nearly kept intact at room temperature, leading to high Curie temperature of these compounds. The large anisotropy in these compounds is derived from considerable amount of spin-orbit interaction displayed by rare earth atoms with unfilled 4f shell configurations. For example, Tb in $TbFe_2$ is having oblate 4f shell configuration, whereas Sm in $SmFe_2$ is having prolate 4f shell configuration. Owing to such anisotropic shape, the electron cloud does not change its shape when rare earth ion is transferred into a crystal lattice. Since, the spin-orbit interaction of the 4f electrons is much greater than the crystal field energy, the rotation of the magnetic moment of rare earth atom in an external field reorients the electron cloud with respect to crystalline environment. This causes lattice deformation and is responsible for large anisotropic single-ion magnetostriction [31].

The RFe_2 compounds are having topologically close packed Laves phase (C15) structure (Fig. 2.1) having space group $Fd\bar{3}m$. The rare earth atoms (marked A) occupies the corner and face centre positions and also the alternate tetrahedral sites (marked B) in the lattice. Thus, rare earth atoms form a diamond like structure, which consists of two interpenetrating face centred lattice (formed by A and B type Rare earth atoms) displaced by (¼, ¼, ¼) along [111] (Fig. 2.1). Based on the non-spherical 4f shell configuration and

position of atoms, Clark et.al. [32] developed a model for large rhomobohedral distortion of the RFe_2 type intermetallic. In case of $TbFe_2$, the oblate shape of the 4f shell lies perpendicular to the <111> direction. As a result a contraction occurs along the direction perpendicular to <111>. This leads to increase in length along <111>, called spontaneous magnetostriction. The reverse phenomenon occurs in $SmFe_2$, where the shape of the 4f orbital is oblate and therefore contraction occurs along <111> and expansion along the direction perpendicular to <111>. Thus, $TbFe_2$ exhibits positive magnetostriction and $SmFe_2$ negative magnetostriction. In the case of $EuFe_2$ and $GdFe_2$, the 4f electron cloud is spherical and therefore significant rhombohedral distortion of lattice is not observed. In case of $DyFe_2$, the magnetization being along <100>, no lattice distortion is observed although the 4f shell is non-spherical. This is attributed to no overlap of electron cloud of neighbouring rare earth atoms along <100> or a direction perpendicular to it. Therefore λ_{111} is much higher than $\lambda_{100.}$ Accordingly, in $SmFe_2$ and $TbFe_2$ higher magnetostriction is observed [17,30,33]. In these cases, magnetization lies along <111> compared to $DyFe_2$ and $HoFe_{2,}$ where magnetization lies along <100>.

2.4. Anisotropy Compensation:

As discussed earlier, the magnetocrystalline anisotropy of RFe_2 compounds plays a crucial role for its magnetostriction. This class of compounds exhibit very high magnetocrystalline anisotropy; for example, the magnetocrystalline anisotropy constant (K_1) of $TbFe_2$ is -7600 kJm^{-3}, which is three orders of magnitude larger than that of cubic metal Fe or Ni [17]. However, large anisotropy also restricts the achievable magnetostriction at lower applied field, which is important for applications [34]. Clark et.al. [17] has reported that the signs of anisotropy constant varies in different binary compounds (Table 2.2). Therefore, it is possible to judicially select a pair of rare earth elements to form an anisotropy compensated pseudo binary compounds. For example, $Tb_{0.27}Dy_{0.73}Fe_2$ and $Ho_{0.85}Tb_{0.15}Fe_2$ exhibit low anisotropy and large magnetostriction and are suggested as potential application in magnetostrictive transducer [35-37]. These compounds also exhibit a complex set of spin re-orientations as a function of composition and temperature. Therefore, extensive studies on these materials were carried out through magnetization [38,39], Mossbauer [40,41] and single crystal torque magnetometry measurements [42-44].

2.5. Applications and processing of $Tb_{0.3}Dy_{0.7}Fe_2$:

The realization of large magnetostriction at low applied field in anisotropy compensated RFe_2 intermetallics, in particular $Tb_{0.3}Dy_{0.7}Fe_2$, drew considerable attention from research community because of their wide applications as ultrasonic transducers, delay lines, linear motors, vibration dampers, interconnects and micro-positioners *etc* [17,45-52]. It is viable to process the material through different routes such as conventional powder metallurgical (P/M) route [53-55], directional solidification [56-65] and single crystal growth [66-69]. However, the material processed through P/M route suffers from oxygen pick up during processing and Kim et.al. [70] observed the detrimental role of rare-earth oxide inclusions on magnetostrictive property of $(Tb,Dy)Fe_2$. Mei. et.al. [55], prepared the magnetically aligned green compact of $(Tb,Dy)Fe_2$ and found strong <111> texture formation. After sintering of the aligned compacts, the texture was found to be retained, although the magnetostriction was found to be little more than that displayed by the polycrystalline bulk alloy. However, the magnetostriction realized was much less compared to the directionally solidified alloy. The lower magnetostriction in sintered compact is attributed to the high coercivity resulting from very fine grain size. On the contrary, the directionally solidified alloy is having larger grains leading to low coercivity. Wu *et. al.* and Wang *et. al.* [67,68] attempted to grow single crystal of $Tb_{0.3}Dy_{0.7}Fe_2$ by Czochralski technique. However, the single crystal of this material is found to be extremely brittle and the method restricts the growth of larger size components required for applications. Therefore, directional solidification technique became the most viable option for commercial application of $Tb_{0.3}Dy_{0.7}Fe_2$ intermetallic, also popularly known as TERFENOL D^{TM} [63]. The directional solidification also helps to achieve better magnetomechanical coupling co-efficient (efficiency to convert input electrical signal to mechanical vibration) as the material displays anisotropic magnetostriction along <111>. Therefore, it is important to understand the phase relationship in this material and the effect of directional solidification parameters on microstructure, texture and magnetostriction.

2.6. Phase equilibria of Tb-Dy-Fe:

2.6.1. Binary Dy-Fe system:

The Fe-Dy system, investigated by Van Der Goot and Buschow [71] and its phase diagram is shown in Figure 2.2. The phase diagram was generated using systematic

metallography, x-ray diffraction, thermal analysis and microprobe analysis. It indicates presence of four intermetallic phases *viz.* $DyFe_2$, $DyFe_3$, Dy_6Fe_{23} and Dy_2Fe_{17}. Amongst the intermetallic compounds $DyFe_3$ (melting point 1305^oC) and Dy_2Fe_{17} (melting point 1375^oC) formed congruently, whereas the other two intermetallic compounds $DyFe_2$ and Dy_6Fe_{23} formed by peritectic reaction. Landin *et. al.* [72] carried out studies on theoretical prediction of phase diagram and observed that the liquidus slope in the vicinity of $DyFe_3$ shows a very asymmetric shape in the diagram proposed by Vandergoot *et. al.* [71]. Accordingly, they have proposed [72] a more symmetric shape of the liquidus around RFe_3 intermetallic phase. However, in their assessment Dy_6Fe_{23} phase does not form through a peritectic reaction. Rather, it forms by a peritectoid transformation at a few degrees below the peritectic temperature proposed by Vandergoot *et. al.* [71].

The phase with giant magnetostrictive property *i.e.* $DyFe_2$ forms by a peritectic reaction of $L+DyFe_3 \rightarrow DyFe_2$ at 1270^oC and at composition of 33.5 at% of Dy. The peritectic product phase $DyFe_2$ does not exhibit any solubility till the peritectic reaction temperature. This behaviour is reported in both the phase diagrams reported by Vandergoot et.al [71] and Landin et.al. [72]. Both phase diagrams also indicate very limited terminal solid solubility of both the elements and the presence of an eutectic reaction $L \rightarrow DyFe_2 + Dy$ at a temperature of 890^oC and 71.5 at% Dy composition.

2.6.2. Binary Tb-Fe system:

The binary Tb-Fe system investigated by Dariel *et. al.* [73] is shown in Figure 2.3. The phase diagram was developed using standard metallography, DTA, X-ray diffraction and electron microprobe analysis. The phase diagram also exhibits presence of four intermetallic phases *viz.* $TbFe_2$, $TbFe_3$, Tb_2Fe_{17} and Tb_6Fe_{23}. The Tb_6Fe_{23} phase was found to form only after long annealing treatment and this observation is in agreement with the reports of Kripyakevich *et. al.* [74] and Ray [75]. However, Oesterrecher [76] did not observe the presence of Tb_6Fe_{23} phase in cast as well as heat treated alloys. All the intermetallic compounds in this binary alloy forms by peritectic reaction, which is in contrast to Dy-Fe binary, where two intermetallic phases *viz.* $DyFe_3$ and Dy_2Fe_{17} forms congruently.

The $TbFe_2$ forms by peritectic reaction $L+TbFe_3 \rightarrow TbFe_2$ at 1187^oC and $TbFe_3$ also forms by a peritectic reaction $L+Tb_6Fe_{23} \rightarrow TbFe_3$ at 1212^oC. The phase diagram reported by Dariel *et. al.* [73] indicates no solubility range for $TbFe_3$ and $TbFe_2$ although Gilmore and

Wang [77] reported a solubility range for $TbFe_3$. The peritectic reaction temperature for formation of $TbFe_2$ is less compared to that of $DyFe_2$. Further, Dariel *et. al.* [73] reported that the $TbFe_2$ phase is rhombohedrally distorted and accordingly they have indexed the XRD pattern in terms of rhombohedral lattice. This rhombohedral distortion is probably the result of large spontaneous magnetostriction along [111] arising from large magneto-crystalline anisotropy. The eutectic reaction in this binary system occurs at a temperature of 847^{o}C and 72 at% Fe composition. The eutectic reaction temperature in Tb-Fe binary [73] system is less compared to that of Dy-Fe binary system [71].

2.6.3. Ternary Tb-Dy-Fe system:

It has been established that the anisotropy compensated ternary Laves phase compound $(Tb,Dy)Fe_2$ [35-37] is more suitable for application rather than binary compounds $TbFe_2$ or $DyFe_2$. In spite of interesting properties, ternary phase diagram information on Tb-Dy-Fe is almost completely missing. In the existing literature, very few reports [72,78-80] are available that attempt to explain the nature of ternary phase diagram. Since, Tb and Dy are chemically similar and exhibit complete miscibility in solid as well as in liquid state, most of the researchers have assumed a pseudo binary behaviour of ternary Tb-Dy-Fe alloys and explained the obtained experimental results on this basis.

The theoretical prediction of ternary Tb-Dy-Fe phase diagram by Landin *et. al*. [72] exhibits no significant deviation from the binary phase equilibria [71,73] and therefore indicating a pseudo-binary behaviour of the Tb-Dy-Fe system. These authors [72] did not use any ternary interaction parameters and they assumed very limited possibility of ternary interactions due to chemical similarity of Tb and Dy. The ternary section reported by them also corroborates well with the experimental measurements by Westood *et. al.* [79] on $Tb_{0.27}Dy_{0.73}Fe_x$ (x = 0.8-3.0) alloys except for the liquidus curve in the composition range 0.3-0.5 mole fraction Fe. The ternary diagram reported by Landin *et. al.* indicates appearance of the same intermediate phases as observed in individual binary phase diagrams of Tb-Fe and Dy-Fe and does not indicate any solubility range for the intermediate phases. However, Westwood *et. al.* [79] observed a Widmanstätten precipitate in $Tb_{0.3}Dy_{0.7}Fe_{1.95}$ alloy and attributed it to the existence of solid solubility in $(Tb,Dy)Fe_2$. The existence of solid solubility in $Tb_{0.3}Dy_{0.7}Fe_{1.95}$ is strikingly different from perfect stoichiometric nature of RFe_2 (R= Rare Earth) phase reported in Tb-Fe and Dy-Fe binary diagrams [71,73]. In the same

report, Westwood *et. al*. also described the microstructural change in $Tb_{0.3}Dy_{0.7}Fe_x$ alloys as a function of Fe-concentration. The formation of Widmanstätten precipitate is also observed during the single crystal growth of $Tb_{0.3}Dy_{0.7}Fe_{1.95}$ as observed by Wu *et. al* [67]., Wang *et. al.*[68] and Bi *et. al* [80]. Therefore the existence of solid solubility at least for the composition $Tb_{0.3}Dy_{0.7}Fe_{1.95}$ can be testified with substantial experimental evidences reported in the available literature.

Following the work of Westwood *et .al.* [79], Mei. *et. al.* [78] studied the segregation pattern of rare earth elements in the same alloy and interpreted the results with an assumption that the $Tb_xDy_{1-x}Fe_2$ alloys have same nature of solubility range of Laves phase prevailing from Tb-rich side to Dy-rich side. The schematic ternary phase diagram of Tb-Dy-Fe as proposed by Mei *et al.* [78] is shown in Figure 2.4. The proposed diagram indicates both $TbFe_2$ and $DyFe_2$ binary Laves phases have solubility range extending towards rare earth rich side and Laves phase of all intermediate compositions, with different Tb/Dy ratio, exhibit identical solid solubility. However, experimental reports are not available to validate this proposition as most of the available reports concentrated on commercially used TERFENOL-D^{TM} composition *i.e.* $Tb_{0.27}Dy_{0.73}Fe_{1.95}$. Therefore, there exists a scope for understanding the change of phase equilibria imparted upon by mixing of two rare earth elements Tb and Dy at different proportions.

2.7. Studies on directional solidification of Tb-Dy-Fe:

As discussed in the previous section, the directional solidification of Tb-Dy-Fe alloys showed the highest promise for preparing components for transducer and actuator applications. Therefore, several researchers attempted to grow the material in grain oriented condition. The survey of existing literature shows that primarily few methods were adopted *viz.* Conventional Zone melting (container less or with container) [56,58,61,63,66,81-87], Electron beam zone melting [60,88], Bridgman technique [59,62-66,89-92] and directional solidification under microgravity [57,93].

McMasters *et. al*. [58] first reported the preparation of directionally grown Terfenol-D^{TM} of 9 mm dia. by float zone melting technique. They have reported congruent solidification of magnetostrictive phase $(Tb,Dy)Fe_2$ above a growth rate of 35 μm/ s. They also reported formation of a skeleton network of pure rare earth metal along the inter-dendritic region. The cellular-dendritic growth morphology of $(Tb,Dy)Fe_2$ was also reported

by several other researchers [56,61,63,66,81-84] and in each case the pure rare earth element was found to be distributed in between cells/ dendrites. Ji *et. al.* [84] carried out directional solidification with a super high temperature gradient (500-900 K/ cm) zone melting facility and reported two distinct solidification morphologies *viz.* ordered plate like and cylindrical rod shape. After a series of experiments they concluded that for a given temperature gradient a platelet like structure appears at lower growth rates and the morphology gradually changes to cylindrical or rod shape as the growth velocity is increased. However, the authors could not explain the reason for such morphological transition, which is more likely to be due to the instability with increase in growth rate. Similar morphological transition has also been observed [82] during optical zone melting of Tb-Dy-Fe alloy. In another report by Ji *et. al.* [56], the relationship of solidification morphology with obtained grain orientation has been investigated. In this report, the different crystal morphology is attributed to grains of different orientations; however the supportive angular relationship has not been indicated in their report. The growth conditions presented in this study [56] correspond to the ordered plate morphology regime indicated in their other report [84]. Therefore, according to Ji *et.al*. [56,84], the ordered platelet type morphology in the transverse section corresponds to <110> growth orientation. But the formation of irregular shape grains at higher growth rate is not clear. Apart from the microstructural morphology, several reports [56,61,81-84] also addressed the formation of growth texture during solidification. Most of the reports indicate formation of <110> texture during solidification. However, Ji *et.al.* [56] reported a mixed <311> and <110> texture at the beginning of solidification, when the sample was grown at 9.2 μm/s. In another report, Ji *et .al.* [82] obtained <111> growth texture, when the sample was directionally grown by optical zone melting at the rate of 5 mm/h. Mei *et. al.*[89] and Verhoeven *et. al.* [66] observed growth of <112> texture at higher growth rate and explained a growth by a twin based mechanism leading to the above texture formation. However, no clear evidence has been presented for formation of such {111} twins. Bi *et. al*. [80] has carried out investigation on several defects formed in directionally grown Tb-Dy-Fe and reported twin formation in zone melted alloy but it does not appear clearly how such growth twins were indexed as {111} type twins. The electron beam zone melting of Tb-Dy-Fe alloys [60,88] also indicate microstructure similar to the conventionally zone melted alloy but in this case strong <112> orientation was observed.

Compared to reports on zone melted Tb-Dy-Fe, fewer reports [59,62-66,89-92] are available on Tb-Dy-Fe directionally solidified by Bridgman technique. Since, the Bridgman technique is used for preparation of large scale components, practical issues such as macro-segregation [59], suitable post-solidified heat treatment [63,90], microstructural evolution [63-65] and texture [90,92] were of prime interest. While, Verhoeven *et. al.* [90] and Palit *et. al.* [63-65,92] reported a plane front solidification morphology, Park *et .al* [59] reported dendritic solidification even adopting comparatively lower growth rate. Although, the gradient obtained during the process adopted by Park *et. al.* [59] is not indicated in their report, the instability in the growth front observed is possibly owing to lower temperature gradient achieved in their process. Amongst very few reports on texture study of Tb-Dy-Fe directionally grown by Bridgman technique, Verhoeven *et. al.* [90] and Palit *et. al.* [92] reported the formation of <112> grain orientation. Minagawa *et.al.* [57,93] studied directional solidification of Tb-Dy-Fe under microgravity and magnetic field. They could produce grain oriented poly-crystals with <111> growth texture. This results in very large magnetostriction.

In several studies on directional solidification, the role of microstructure [56,59,63-66,84,92] and texture [66,67,81-83,89-92] on magnetostrictive property is quite evident. The theoretical study of De Simone *et. al.* [94] and the measurement on single crystal by Teter *et. al.* [95] also reveals the effect of grain orientation on magnetostrictive properties. This is supported by the studies on magnetic domain by magnetic force microscopy [86-87]. In most of the studies by zone melting [56,66,81-84,89] the effect of different grain orientations on magnetostrictive property has been explained in the light of different twin configurations and their angular relationship with easy direction. However, a more analytical approach can be seen in the report by De Simone *et.al.* [94], where minimization of energy is used to interpret the effect of different crystallographic orientation on magnetostriction.

2.8. Current trend in exploration of new magneto-elastic materials:

Although (Tb,Dy)Fe_2 exhibits excellent magnetostrictive properties, it posses certain challenges to the research community. The material is extremely reactive to the environment and also expensive, as it contains nearly 60 wt% of rare earth element. The material is also extremely brittle and therefore is difficult for handling and machining. Peterson *et. al.* [96] studied the strength of Terfenol-D and reported extreme brittleness. Further, due to inherent

anisotropy, the field required to obtain desired magnetostriction for a device is high (~500-1000 Oe). Therefore, exploration for new magneto-elastic materials is being carried out to get rid of all the problems encountered in (Tb,Dy)Fe_2.

Several new magneto-elastic materials are being proposed for transducer and actuator applications. FePd, FePt and CoPt intermetallics [97-100] formed in $L1_0$ crystal structure have shown promise for magnetostrictive applications owing to their large magnetocrystalline anisotropy. Apart from these, ferromagnetic shape memory alloys based on Heusler alloys have also being considered for magneto-elastic actuator applications. Amongst several Heusler alloys, Ni-Mn-Ga [101-104] and Co-Ni-Al [105-107] have shown maximum promise. Ni-Mn-Ga is brittle compared to Co-Ni-Al and both of the alloys exhibit linear magnetostrictive response to the applied field only at extremely high field (> 1Tesla). Similar problems also encountered in case of FePd, FePt and CoPt intermetallics and therefore fabrication of a portable actuator is difficult with these materials. On the contrary, Fe-Al [108-111] and Fe-Ga [111-116] alloys exhibit large magnetostriction and linear magnetostrictive response at lower applied field and therefore can become a promising candidate for actuator applications. The Fe-Ga alloys, however exhibit larger magnetostriction than Fe-Al.

The large magnetostriction in Fe-Ga alloy was first reported by Clark *et. al.* [112] and subsequently named as Galfenol^{TM} by Naval Ordnance Laboratory, USA. A comparison of the field dependent magnetostriction between (Tb,Dy)Fe_2 and Fe-Ga is presented in Figure 2.5. The comparison indicates, sharper slope of magnetostriction of Fe-Ga than (Tb,Dy)Fe_2. However, saturation magnetostriction of Fe-Ga is much less compared to (Tb,Dy)Fe_2. Further, the cost of Fe-Ga based actuator is less compared to (Tb,Dy)Fe_2 and hence it is more economical. Therefore, Fe-Ga shows better promise as a material for an actuator rather than a transducer.

2.9. Brief review on the studies on magnetostrictive Fe-Ga alloy:

Among the possible low-cost Fe based magnetostrictive alloys, Fe-Al and Fe-Be alloys have long been known to have appreciable low field magnetostriction and good mechanical properties. Fe–19.2 at.% Al alloy has a λ_{100} of about 142 microstrains, whereas, Fe-6.8 at.% Be alloy exhibits λ_{100} of 101 microstrains [117]. The magnetostriction monotonically increases with Al and Be addition, although the enhancement is restricted by

limited solid solubility of these elements in Fe. The common feature of both the Al and Be elements is the absence of *d*-shell electrons. The ground-state electronic configurations of Al and Be are [Ne] $3s^2 3p^1$ and [He] $2s^2$, respectively. Although the mechanism of improvement in magnetostriction by addition of nonmagnetic Al and Be is unclear, it appears that the addition of elements devoid of *d*-shell electrons or having completely filled *d* shell, can induce large magnetostriction in Fe. Gallium appears to be one such element, having requisite electronic structure ([Ar] $3d^{10}4s^2 4p^1$) and large solid solubility in Fe (~ 10 at% at room temperature and 35 at% at 1000^{o}C) [118]. Therefore, researchers [111-116] started exploring the magnetostrictive property of Fe-Ga and discovered [112] large magnetostriction at low applied magnetic field.

Ruqian Wu [119] proposed that the large magnetostriction originates from degeneracy in d-orbital of Fe due to addition of Ga whereas Clark *et. al.* [116] proposed the large magnetostriction in bulk single crystal bcc Fe–Ga is owing to lattice softening. The theory of lattice softening by Ga addition is also supported by elastic modulus measurement by Wuttig *et.al.* [120]. Several studies [121-126] indicate that the magnetostriction coefficient λ_{100} of single crystal Fe-Ga exhibits maxima at 19 at % and 27 at% Ga concentrations. The concentrations correspond to the two maxima changes with nature of thermal history of the material [121-126]. The variation of the magnetostriction as a function of Ga content was interpreted in terms of the variation of magnetoelastic coupling co-efficient due to short range ordering between the Ga atoms [127-129]. However, several other reports [121-126,130-133] indicate the variation of λ_{100} is intimately related to presence of several ordered phases such as B2, DO_3 and $L1_2$ in the microstructure. Conflicting interpretations can be observed in the existing literature about the role of ordered phases on magnetostriction of Fe-Ga alloys.

Clark et. al. [134] has also investigated the effect of minor alloying additions such as Co, Mn, Cr, V, C etc. on the magnetostrictive properties of Fe-Ga alloy. The elements like Co, Mn, Cr and V were found to stabilize the ordered DO_3 phase and no significant improvement in magnetostriction was observed [134]. However, minor addition of C was found to improve the magnetostriction. Srisukhumbowornchai *et. al.* [135] and Summers *et.al.* [136] investigated effect of partial substitution of Ga by Al and observed increase in magnetostriction.

Cheng *et. al.* [137] investigated the structure-property relationship in melt spun Fe-17at% Ga and Fe-21at% Ga alloys, with an objective to stabilize the high temperature disordered phase A2. A substantial increase in the value of magnetostriction observed, when the melt spinning was carried out at higher wheel speed. The large magnetostriction of 130 microstrains observed in 17 at% alloy was attributed by them to the presence of single phase A2. In the same Fe-17 at% Ga alloy, Zhang *et. al.* [138] carried out melt spinning at different wheel speed and studied the magnetostrictive properties. In contrast to the observation of Cheng *et. al.* [137], they observed a large negative magnetostriction of -2100 microstrains and attributed it to formation of DO_3 phase during melt spinning.

Since, the magnetostriction in Fe-Ga alloy is anisotropic with λ_{100} much higher than λ_{111}, research efforts are made to impart texture in this material. Kellogg *et. al.* [139,140] studied the dependence of saturation magnetostriction on texture and grain morphology in polycrystalline $Fe_{83}Ga_{17}$ alloy and observed magnetostrictive strains of 300 microstrains in an alloy textured along <100>. It was proposed that the control of crystallographic texture can be achieved through rolling deformation in order to maximize the resulting magnetostrictive strain. Several other researchers [141-143] also carried out investigation on rolling and recrystallization texture of Fe-Ga and their effect on magnetostriction. Na *et. al.* [143] investigated the secondary recrystallization behaviour of Fe-Ga and observed the role of B and S in modifying grain boundary characteristics that influences the secondary recrystallization process.

Srisukhumbowornchai and Guruswamy [135,144] studied the directional solidifications of Fe-Ga alloys using chill casting and float zoning techniques and reported large improvement is magnetostriction. Magnetostriction as high as 271 microstrains at applied magnetic field of 65 Oe could be obtained in the grain oriented Fe-27.5 at.% Ga rod using float zoning technique with pulling rate of 22.5 mm/h. The float zoning technique resulted in formation of a growth texture which was within 14^o away from [001]. The chill cast alloy on the other hand shows formation of weak texture.

2.10. Scope of the present work:

The survey of available literature on magnetostrictive $(Tb,Dy)Fe_2$ and Fe-Ga alloy indicates there exist some grey area, that can be taken up for further study and understanding.

Such unresolved issues have been taken up for the current study and are summarized as follows:

(i) As a potential material for transducer and actuator applications, most of the research has been directed towards optimization of composition and grain orientation in order to achieve better magnetostrictive performance. However less attention has been paid to understand the nature of ternary phase equilibria of Tb-Dy-Fe. It is important to understand the effect of variable Tb/Dy ratio on phase equilibria and microstructure of Tb-Dy-Fe alloys and the resultant effect on magnetostrictive performance. Unfortunately, it can be noted that the existing literatures ignore the ternary interactions and consider Tb-Dy-Fe as pseudo-binary system owing to chemical similarity of Tb and Dy. In recent time a need is also felt of finding alternate and more abundant rare earth combinations due to fluctuations in supply of rare earth elements. From this point of view it is important to investigate the effect of Tb/Dy ratio on microstructure and magnetic properties of magnetostrictive $(Tb,Dy)Fe_2$ compound.

(ii) Grain orientation plays a crucial role in magnetostrictive property of directionally grown $(Tb,Dy)Fe_2$ alloys. In the available literature formation of different texture such as <110>, <112>, <111> and <311> have been reported by several researchers. However, a complete understanding of evolution of texture components of such diverse nature is still evasive. Therefore, it is important to investigate texture evolution and understand the mechanism of their evolution as a function of growth conditions.

(iii) Most of the reports related to directionally grown $(Tb,Dy)Fe_2$ have adopted zone melting technique. However, for growing large components for practical application Bridgman technique needs to be adopted as zone melting technique has restriction on size of the samples can be grown. The understanding on effect of process variables of Bridgman technique and the microstructure and texture that evolve is rather incomplete. Therefore, a scope exists to understand the complex interplay of process variables on evolved microstructural features and texture of $(Tb,Dy)Fe_2$, directionally grown by Bridgman technique.

(iv) The magnetostriction in Fe-Ga alloys is sensitive to the presence of different ordered phases that form as a result of different thermal treatments. Conflicting interpretations can be

noticed in the existing literature about the role of these ordered phases. Further, most of the reports on such study of structure-property relationship were carried out on single crystalline alloy. The understanding on the ordered phase formation and their role on magnetostriction can be different in case of a polycrystalline bulk alloy. Since, the Fe-Ga alloy demonstrates it's potential as future material for actuator applications, it is important to study the ordered phase formation and their effect on the magnetostrictive performance of a polycrystalline bulk Fe-Ga alloy.

Table 2.1: Magnetostriction and Curie temperatures of RM_2 and RT_2 type Laves phase compounds [8-28].

Compound	λ_{111} (microstrains)	λ_{100} (microstrains)	T_C (K)
$NdAl_2$		-700	61
$TbAl_2$	-3000		114
$DyAl_2$		-1700	68
$TbMn_2$	-3000		40
$TbFe_2$	4000 [24], 4500 [23]		711
$DyFe_2$		433	635
$HoFe_2$		85	612
$TmFe_2$	-3500 [26], -2600 [23]		610
$TbCo_2$	4400		256
$DyCo_2$		-2000	159
$HoCo_2$		-2200	85
$ErCo_2$	-2500		36
$TbNi_2$	1500		45
$DyNi_2$		-1300	30
$HoNi_2$		-1000	22

Table 2.2: Magnetostriction and first order anisotropy constant (K_1) of binary RFe_2 Laves phase compounds [17].

Binary RFe_2 Compounds	λ (microstrains)	K_1 (kJm^{-3})
$SmFe_2$	-1560	-970
$TbFe_2$	+1753	-7600
$DyFe_2$	+433	+2100
$HoFe_2$	+85	+560
$ErFe_2$	-200	-330
$TmFe_2$	-210	-53

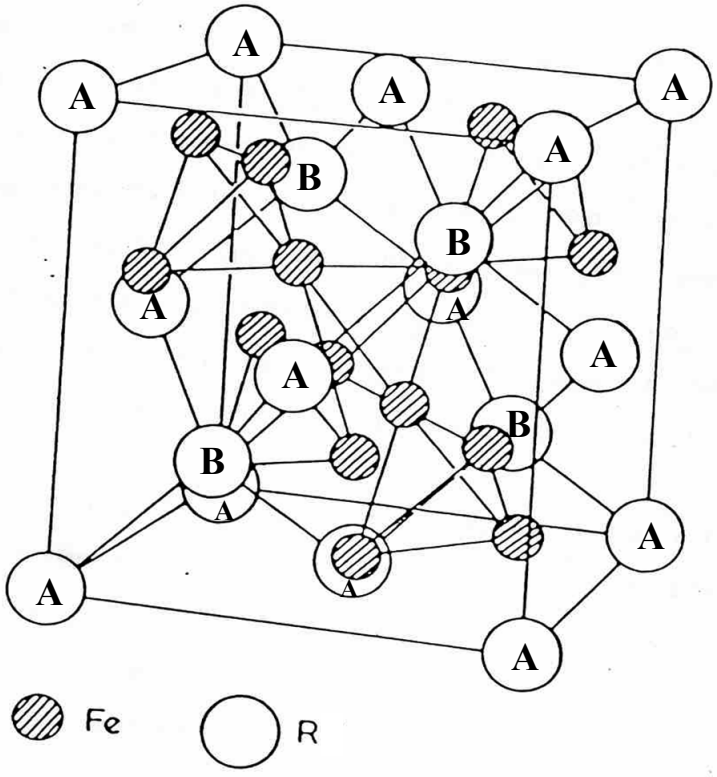

Figure 2.1: Crystal structure of binary RFe_2 compound (C15 type Laves phase); R atoms distributed into A and B type sites

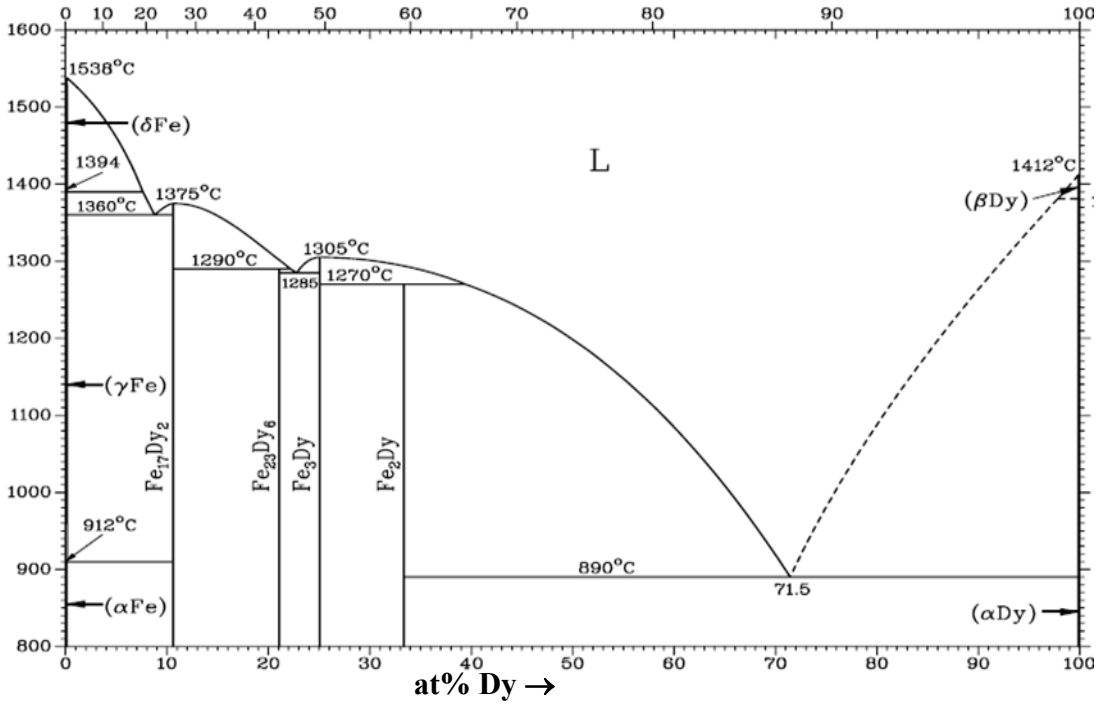

Figure 2.2: Binary phase diagram of Dy-Fe [71]

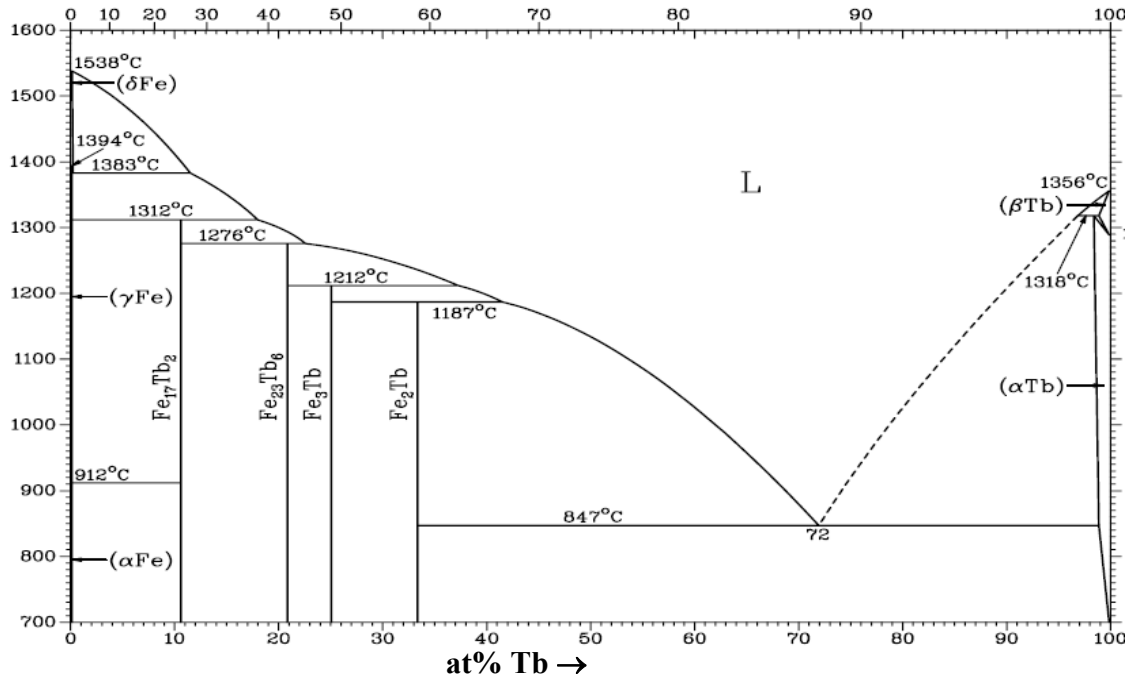

Figure 2.3: Binary phase diagram of Tb-Fe [73]

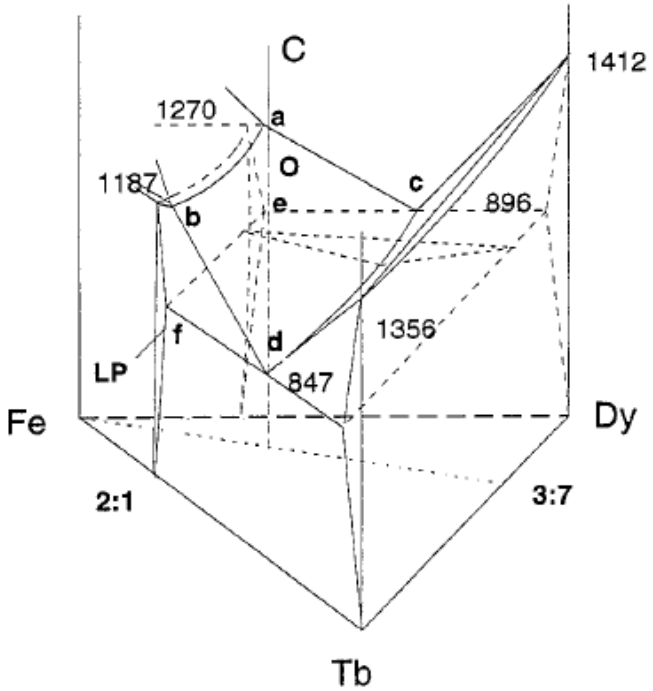

Figure 2.4: Ternary phase diagram of Tb-Dy-Fe proposed by Mei *et. al.* [78]

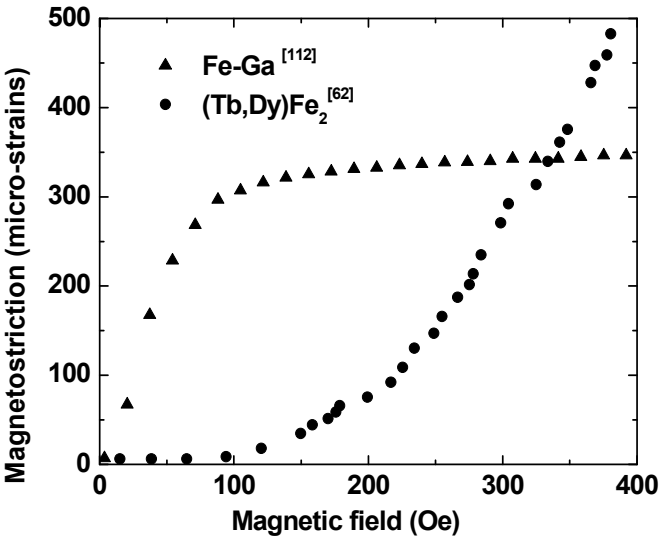

Figure 2.5: A comparison between magnetostriction of $(Tb,Dy)Fe_2$ and Fe-Ga alloys [62,112]

References:

[1] B D Culity *"Introduction to Magnetic Materials"*, Addison-Wesley Publishing Company Inc., Phillipines, (1972).

[2] Joule, J.P. *"On the Effects of Magnetism upon the Dimensions of Iron and Steel Bars"*, Phil. Mag. 30 (1847) 225.

[3] R. Bozorth, "*Ferromagnetism"*, Van Nostrand. (1951)

[4] K H J Buschow, in: E.P. Wohlfarth (Ed.), "*Ferromagnetic Materials"*, vol. 1, North Holland, Amsterdam, (1980).

[5] A E Clark, B F De Savage and R. Bozoroth, *"Anomalous Thermal Expansion and Magnetostriction of Single-Crystal Dysprosium"*, Phys. Rev., 138 (1965) A216.

[6] S legvold, J Alstad and J Rhyne, *"Giant Magnetostriction in Dysprosium and Holmium Single Crystals",* Phys. Rev. Lett., 10 (1963) 509.

[7] J Rhyne and S Legvold, Phys. Rev., *"Magnetostriction of Tb Single Crystals"*, 138 (1965) A507.

[8] W J Carr, *Magnetostriction, Chap 10 in: "Magnetic properties of metals and alloys"*, Cleveland OH, American Society of metals (1965).

[9] J J Rhyne, R J Elliot (Ed), *Chap. 4 in: "Magnetic properties of rare earth metals"*: London, Plenum Press, (1972).

[10] P Morin and D Schmidt, in: E P Wohlfarth and K H J Buschow (Eds), *"Ferromagnetic materials"*, Vol. 5, Amsterdam, North Holland, (1990).

[11] H G purwins and A Leson, "*Magnetic properties of (rare earth)Al_2 intermetallic compounds"*, Adv. Phys., 39 (1990) 309.

[12] R Z Levitin and A S Makosyan, *"Magnetoelastic properties of RE-3d intermetallics"*, J. Mag. Mag. Mat., 84 (1990) 247.

[13] K N R Taylor, *"Intermetallic rare-earth compounds"*, Adv. Phys., 20 (1971) 551.

[14] Y Nakamura, J. Mag. Mag. Mat., *"Magnetovolume effects in Laves phase intermetallic compounds"*, 31-34 (1983) 829.

[15] K Hathway and J Cullen, J. Phys.: Condens. Matter., *"Magnetic and magnetovolume properties of RCo_2 compounds and alloys from energy band structure",* 3 (1991) 8911.

[16] A E Clark and S H Belson, Phys. Rev. B, "*Giant Room-Temperature Magnetostrictions in $TbFe_2$ and $DyFe_2$"*, 5 (1972) 3642.

[17] A E Clark, *"Introduction to Highly Magnetostrictive Rare-Earth-Materials"*, U S Navy J Underwater Acoustics, 27 (1977) 109.

[18] A E Clark, S H Belson and N Tamagawa, *"Huge magnetocrystalline anisotropy in cubic rare earth-Fe_2 compounds"*, Phys. Lett. A, 42 (1972) 160.

[19] A E Clark, S H Belson and N Tamagawa, "*Magnetocrystalline Anisotropy in Cubic Rare Earth-Fe_2 Compounds",* AIP Conf. Proc.,10 (1973) 749.

[20] U Atzmony, M P Dariel, E. R. Bauminger, D. Lebenbaum, I. Nowik, and S. Ofer, Phys. Rev. B, "*Spin-Orientation Diagrams and Magnetic Anisotropy of Rare-Earth-Iron Ternary Cubic Laves Compounds"*, 7 (1973) 4220.

[21] J B A A Elemans and K H J Buschow, *"The Magnetic Structure of Tm_2Fe_{17}* ",Phys. Stat. Sol., 24 (1974) K125.

[22] B Barbara, M F Rossignol and M Uehara, "*Spontaneous cell distortion due to the crystal field in some rare earth-Al_2 Laves phases",* Physica B, 86-88 (1977) 183.

[23] B Barbara, J Giraud, J La Forest, R Lemaire, E Siaud and J Schweizer, "*Spontaneous magnetoelastic distortion in some rare earth-iron Laves phases",* Physica B, 86-88 (1977) 155.

[24] A E Clark, R Abbundi, O McMasters and H Savage, "*Magnetostriction of rare earth-Fe_2 laves phase compounds",* Physica B, 86-88 (1977) 73.

[25] R Abbundi, A E Clark and N C Koon, *"Temperature dependence of the magnetostriction and magnetization in single crystal $HoFe_2$"*, J. Appl. Phys., 50 (1979) 1671.

[26] R Abbundi and A E Clark, *"Low temperature magnetization and magnetostriction of single crystal $TmFe_2$"*, J. Appl. Phys., 49 (1978) 1969.

[27] D Gignoux, R Givord, R Perrier de la Bathie and F Sayetat, **"** *Magnetic properties and spontaneous distortion in $TbCo_2$"*, J. Phys. F : Met. Phys., 9 (1979) 763.

[28] J R Cullen, *"Materials with large magnetostriction"*, Scripta Metall. et. Mater., 33 (1995) 1849.

[29] N C koon, A I Schindler and F L Carter, *"Giant magnetostriction in cubic rare earth-iron compounds of the type RFe_2"*, Phys. Lett. A, 37 (1971) 413.

[30] A E Clark, in: E.P. Wohlfarth (Ed.), *Ferromagnetic Materials*, vol. 1, North Holland, Amsterdam, (1980).

[31] K P Belov, G I Kataev, R Z Levitin, S A Nikitin and V I Sokolov, *"Giant Magnetostriction",* Sov. Phys. USP, 26 (1983) 518.

[32] A E Clark, J R Cullen, O D Mc Master and E R Callen, "*Rhombohedral distortion in highly magnetostrictive Laves phase compounds"* AIP Conf. Proc., 24 (1976) 192.

[33] A E Clark, *"Magnetic and magnetoelastic properties of highly magnetostrictive rare earth-iron Laves phase compounds",* AIP Conf. Proc. 18 (1974) 1015.

[34] C M Williams and N C Koon, *"Anisotropy of single crystal $Ho_2Dy_yTb_{1-x-y}Fe_2$ Laves phase compounds",* Physica B. 86 (1977) 147.

[35] R Abbundi, A E Clark and O D McMasters, "*Temperature dependence of the magnetostriction in $Sm_xDy_{1-}xFe_2$ compounds"*, J Appl. Phys., 535 (1982) 2664.

[36] N C Koon, A I Schindler, C M Williams and F L Carter, *"Magnetostrictive properties of $Ho_xTb_{1-x}Fe_2$",* J. Appl. Phys., 45 (1974) 5389.

[37] J S Abell, D Butler, R D Greenough, V Joyce and K C Pitman, *"Magnetomechanical coupling in $Dy_{0.73}Tb_{0.27}Fe_2$",* J. Mag. Mag. Mater., 62 (1986) 6.

[38] C M Williams and N C Koon, "*Anisotropy energy measurements on single-crystal $Tb_{0.15}Dy_{0.85}Fe_2$",* Phys. Rev. B, 11 (1975) 4360.

[39] A E Clark, AIP Conf. Proc., *"Highly Magnetostrictive Rare Earth Alloys"*,34 (1976) 13.

[40] D Sarkar, R Segnan and A E Clark, AIP Conf. Proc., "*Mössbauer Effect Studies in Amorphous $TbFe_2$, $DyFe_2$, $HoFe_2$ and $ErFe_2$"*, 18 (1974) 636.

[41] U Atzmony, M P Dariel, E R Bauminger, D Lebenbaum, I Nowik and S Offer, *"Magnetic anisotropy and spin rotations in $Ho_xTb_{1-x}Fe_2$ cubic Laves compounds",* Phys. Rev. Lett., 28 (1972) 244.

[42] C M Williams and N C Koon, *"Anisotropy measurements on single crystal $Tb_{0.15}Dy_{0.85}Fe_2$",* AIP Conf. Proc., 18 (1973) 1247.

[43] C M Williams, N C Koon and J B Milstein, *"Room temperature composition dependence of the anisotropy energy of $Ho_xTb_{1-x}Fe_2$ single crystals",* AIP Conf. Proc., 29 (1976) 191.

[44] C M Williams and N C Koon, "*Torque measurements on single crystal $Dy_xTb_{1-x}Fe_2$ compounds",* J Mag. Mag. Mater. 15-18 (1980) 553.

[45] J S Swell and P M Kuhln, *"Power sonics and ultrasonic transducer design"*, Eds: B Harmonic and J N Decarpigney, Springer-Verlag, Berlin, (1988).

[46] Tomohito Akuta, Proc. 10th International Workshop on *"Rare earth magnets and their applications*", Tokyo, Japan, (1989).

[47] Rune Adolfson, Proc. 2nd International Conf. On "*Giant magnetostrictive and amorphous alloys for sensors and actuators"*, Marbella, Spain, (1988).

[48] Robert S Reed, Proc. *"Conf. 59th shock and vibration symp."*, 6 (1988).

[49] A V Krishna Murty, M Anjanappa and Y F Wu, *"The use of magnetostrictive particle actuators for vibration attenuation of flexible beams"*, J. Sound and Vibrations, 206(2) (1997) 133.

[50] E Hristoforou, M Neagu and H Chiriac, *"New self excited accelerometer based on magnetostrictive delay lines"*, IEEE Trans. Magn.,35 (1999) 3622.

[51] H C Hardee and N L Hardee, *"Magnetostrictive-driven fretting machines for interconnection research"*, J. Alloys and Compd., 258 (1997) 83.

[52] J L Prieto, C Aroca, P Sanchez, E Lopez and M C Sanchez, *"Current essects in magnetostrictive piezoelectric sensors"*, J. Mag. Mag. Mat., 174 (1997) 289.

[53] S W Or, N Nersessian, G P McKnight and G P Carman, *"Dynamic magnetomechanical properties of [112]-oriented Terfenol-D/ epoxy 1-3 magnetostrictive particulate composites"*, J. Appl. Phys., 93 (2003) 8510.

[54] Pekka Ruuskanen, *"Microstructure and magnetostriction of $Fe_{1-x}Tb_x$ alloys prepared by solid state synthesis"*, J. Mag. Mag. Mat., 265 (2003) 257.

[55] Wu Mei, Takateru Umeda, Shouzeng Zhou and Run Wang, *"Preperation and magnetostriction of Tb-Dy-Fe sintered compacts"*, J. Mag Mag. Mat., 14 (1997) 100.

[56] Chengchang Ji, Jianguo Li, Weizeng Ma, Yaohe Zhou, *"Preparation of Terfenol-D with precise <110> orientation and observation of the oriented growth crystal morphology",* J. Alloys Compd. 333 (2002) 291.

[57] Hideki Minagawa, Keiji Kamada, Hideaki Nagai, Yoshinori Nakata, Takeshi Okutani, *"Synthesis of $Tb_{0.3}Dy_{0.7}Fe_{1.9}$ magnetostrictive alloy by unidirectional solidification in magnetic field and microgravity"*, J. Magn. Magn. Mater. 248 (2002) 230.

[58] O.D. McMasters, J.D. Verhoeven, E.D. Gibson, *"Preparation of Terfenol-D by float zone solidification",* J. Mag. Mag. Mat. 54-57 (1986) 849.

[59] W. J. Park, J. C. Kim, B. J. Ye, Z. H. Lee, *"Macrosegregation in Bridgman growth of Terfenol-D and effects of annealing"*, J. Cryst. Growth 212 (2000) 283.

[60] L. Wu, W. Zhan, X. Chen, *"Directional growth of single crystal Terfenol-D by the electron beam zoning method"*, J. Mag. Mag. Mat. 164 (1996) 367.

[61] Y. Zhao, C. Jiang, H. Zhang, and H. Xu, *"M agnetostriction of <110> oriented crystals in the TbDyFe alloy",* J. Alloys Compd. 354 (2003) 263.

[62] J. D. Snodgrass and O. D. McMaster, "*Optimized TERFENOL-D manufacturing processes"*, J. Alloys Compd. 258 (1997) 24.

[63] Mithun Palit, S. Pandian, R. Balamuralikrishnan, A.K. Singh, Niranjan Das, V. Chandrasekharan, G. Markandeyulu, "*Microstructure and magnetostriction of $Tb_{0.3}Dy_{0.7}Fe_{1.95}$ prepared under different solidification conditions by zoning and modified Bridgman techniques*", J. Appl. Phys. 100 (2006) 074913.

[64] Mithun Palit, J. Arout Chelvane, S. Pandian, Niranjan Das and V. Chandrasekaran, *"Effect of solidification rate on the microstructural features and magnetostriction of directionally solidified $Tb_{0.3}Dy_{0.7}Fe_{1.95}$"*, Scripta Mater. 58 (2008) 819.

[65] Mithun Palit, J. Arout Chelvane, S. Pandian, M. Manivel Raja and V. Chandrasekaran, "*Phase relationship, magnetic properties and Mössbauer studies in as cast and directionally solidified $Tb_{0.3}Dy_{0.7}Fe_{1.95}$",* Materials Char. 60 (2009) 40.

[66] J.D. Verhoeven, E.D. Gibson, O.D. McMasters, H.H. Baker, "*The growth of single crystal Terfenol-D crystals*", Metall. Trans. 18A (1987) 223.

[67] Guang-heng Wu, Xue-gen Zhao, Jing-hua Wang, Jing-yuan Li, Ke-chang Jia and Wen-shan Zhan, *"<111> oriented and twin free single crystal of Terfenol-D grown by Czochralski method with cold crucible"*, Appl. Phys. Lett. 67 (14) (1995) 2005.

[68] B W Wang, S C Busbridge, Z J Guo and Z D Zhang, "*Magnetization process and magnetostriction of $Tb_{0.27}Dy_{0.73}Fe_2$ single crystal along <110> direction"*, J. Appl. Phys., 93 (2003) 8489.

[69] Jing-lan Chen, Shu-xiaGao, Wen-hong Wwang, Ming Zhang, Guang-heng Wu, Yang-xian Li, Jiang-ping Qu and Gui-zhi Xu, "*Single crystals of $Tb_{0.3}Dy_{0.7}Fe_2$ grown by Czochralski method with cold crucible",* J. Cryst. Growth, 236 (2002) 305.

[70] Do Hyung Kim, Oh Yeoul Kwon, Jong Chul Kim and Zim Hyoung Lee, *"Effect of oxygen impurity on magnetostriction of directionally solidified $Tb_{0.3}Dy_{0.7}Fe_{1.8}$",* IEEE Trans. Magn., 40 (2004) 2781.

[71] A. S. Van der Goot and K. H. J. Buschow, *"The dysprosium-iron system: Structural and magnetic properties of dysprosium-iron compounds"*, J. Less-Common Met. 21 (1970) 151.

[72] Susanne Landin and John Ågren, "*Thermodynamic Assessment of the Fe-Dy and Fe-Tb Phase Diagrams and Prediction of the Fe-Tb-Dy Phase Diagram*", J. Alloys Compd., 207/208 (1994) 449.

[73] M P dariel, J T Holthus and M R Pickus, *"The terbium-iron phase diagram"*, J. Less Common Metals, 45 (1976) 91.

[74] P I Kripyakevich and D P Frankevich, Sov. Phys. Crystallogr., 10 (1966) 468.

[75] A E Ray, Proc. Rare Earth Res. Conf. 7th, Coronado, Calif., (1968) 473.

[76] H Oesterreicher, J. Less Common Metals, *"The strength of magnetic exchange in compounds $TbFe_2$, $TbFe_3$ and Tb_2Fe_{17} with aluminum substitution for iron"*, 46 (1976) 127.

[77] G M Gilmore and F E Wang, "*Note on the structure of $TbFe_2$ and $TbFe_3$",*Acta Crystallogr., 23 (1967) 177.

[78]W. Mei, T. Okane and T. Umeda, *"Phase diagram and inhomogeneity of (TbDy)- Fe(T) (T = Mn, Co, Al, Ti) systems",* J. Alloys and Compd., 248 (1997) 132.

[79] P Westwood, J. S. Abell, and K. C. Pitman, "*Phase relationships in the Tb-Dy-Fe ternary system",* J. Appl. Phys. 67 (1990) 4998.

[80] Y J Bi, J S Abell and A M H Hwang, *"Defects in Terfenol-D crystals"*, 99 (1991) 159.

[81] T Ma, C Jiang, X Xu and H Xu, *"Manetostriction of <110> oriented crystals in $Tb_{0.36}Dy_{0.64}(Fe_{1-x}Co_x)_2$ (x=0-0.3) alloys",* J. Alloys and Compd., 388 (2005) 34.

[82] C Ji, Y Yu, W Ma, J Li and Y Zhou, *"Effects of crystal growth velocity on the crystal orientations and microstructures in an optical image zone melting furnace"*, J Alloys Compd., 337 (2002) 309.

[83] M Xhang, X Gao, S Zeng Zhou and Z Shi, *"High performance giant magnetostrictive alloy with <110> crystal orientation"*, J. Alloys and Compd., 381 (2004) 226.

[84] C Ji, S Zhu, J Li and Y Zhou, *"Solidification characteristics of $Tb_{0.27}Dy_{0.73}Fe_x$ (x=1.8,1.95) alloys during the directional solidification"*, Mat. Sci. Engg. B, 122 (2005) 174.

[85] M Wun-Fogle, J B Restorff and A E Clark, *"Hysteresis and magnetostriction of $Tb_xDy_yHo_{1-x-y}Fe_{1.95}$ [112] dendritic rods",* J. Appl. Phys., 85 (1999) 6253.

[86] M Wun-Fogle, J B Restorff, A E Clark and J F Lindberg, "*Magnetization and magnetostriction of dendritic [112] $Tb_xDy_yHo_zFe_{1.95}$ (x+y+z=1) rods under compressive stress"*, J. Appl. Phys., 83 (1998) 7279.

[87] D G Lord, A P Holden and P J Grundy, *"Magnetic force microscopy of Terfenol D fracture surfaces"*, J Appl. Phys., 81 (1987) 5728.

[88] L. Wu, W. Zhan, X. Chen, *"Macrosegregation phenomenon in Terfenol-D rods"*, J. Alloys Compd., 255 (1997) 262.

[89] W Mei, T Okane, T Umeda and S Zhou, *"Directional solidification of Tb-Dy-Fe"*, J. Alloys Compd., 248 (1997) 151.

[90] J D Verhoeven, E D Gibson, O D McMasters and J E Ostenson, *"Directional solidification and heat treatment of TerfenoI-D magnetostrictive materials"*, Metall. Trans. A, 21 (1990) 2249.

[91] O D McMasters, *"Method of forming magnetostrictive rods from rare earth-iron alloys"*, US Patents No: 4,609,402 (1986).

[92] Mithun Palit, J. Arout Chelvane, Himalay Basumatary, S. Banumathy, A.K. Singh, S. Pandian, V. Chandrasekaran, "*Comparative effect of texture and microstructure on the magnetostriction of directionally solidified $Tb_{0.3}Dy_{0.7}Fe_{1.95}$ alloy",* Intermetallics 18 (2010) 1027.

[93] Hideki Minagawa, Keiji Kamada, Tomoya Konishi, Hideaki Nagai, Yoshinori Nakata, masataka Sasamori, Takeshi Okutani, *"Unidirectional solidification of $TbFe_2$ alloy using magnetic field and microgravity"*, J. Magn. Magn. Mater. 234 (2001) 437.

[94] Antonio DeSimone and Richard D James, *"A theory of magnetostriction oriented towards application",* J. Appl. Phys., 81 (1997) 5706.

[95] J P Teter, A E Clark and O D Mc Masters, *"Anisotropic magnetostriction in $Tb_{0.27}Dy_{0.73}Fe_{1.95}$"*, J. Appl. Phys., 61 (1987) 3787.

[96] D T Peterson, J D Verhoeven, O D McMasters and W A Spitzig, *"Strength of Terfenol-D"*, J. Appl. Phys., 65 (1989) 3712.

[97] V V Maykov, A Ye Yennakov, G V Yvanov, V I Khrabrov and L M Magnat, Phys. Met. Metall. 67 (1989) 76.

[98] K. Tanaka, T Ichitsubo and M Koiwa, *"Effect of external fields on ordering of FePd*", Mater. Sci. Eng. A, 312 (2001) 118.

[99] H Shima, K Oikawa, A Fujita, K Fukamichi, K Ishida, *" Magnetic anisotropy and mangnetostriction in $L1_0$ FePd alloy"*, J. Magn. Magn. Mater. 272-276 (2004) 2173.

[100] A K Kulovits, J P Leonard, J M K Wiezorek, *"Microstructure of pulsed laser deposited FePd thin films on amorphous and crystalline substrates"*, Intermetallics, 15 (2007) 1606

[101] K Ullakko, J K Huang, V V Kokorin, R C O'Handley, Scripta Mater., *"Magnetically controlled shape memory effect in Ni_2MnGa intermetallics",* 36 (1997) 1133.

[102] S J Murray, M Marioni, S M Allen, R C O'Handley, *"6% magnetic-field-induced strain by twin boundary motion in ferromagnetic Ni-Mn-Ga",* Appl. Phys. Lett., 77 (2000) 886.

[103] S J Murray, M Farinelli, J K Huang, S M Allen, and R C O'Handley, *"Field-induced strain under load in NiMnGa magnetic shape memory materials,"* J. Appl. Phys.,83 (1998) 7297.

[104] R.D. James, M. Wuttig, Philos. Mag. A , *"Magnetostriction of maretensite",* 77 (1998) 1273.

[105] R Kainuma, Y Imano, W Ito, Y Sutou, H Morito, S Okamoto, O Kitakami, K Oikawa, A Fujita, T Kanomata and K Ishida, *"Magnetic-field-induced shape recovery by reverse phase transformation",* Nature, 439 (2006) 957.

[106] Y Tanaka, K Oikawa, Y Sutou, T Omori, R Kainuma and K. Ishida, *"Martensitic transition and superelasticity of Co–Ni–Al ferromagnetic shape memory alloys with $\beta + \gamma$ two-phase structure",* Mater. Sci. Engg. A, 438-440 (2006) 1054.

[107] Yuuki Tanaka, Toshihiro Ohmori, Katsunari Oikawa, Ryosuke Kainuma and Kiyohito Ishida, *"Ferromagnetic Co-Ni-Al Shape Memory Alloys with $\beta+\gamma$ Two-Phase Structure"*, Mater. Trans. JIM, 45 (2004) 427.

[108] A Taylar, R M Jones, *"Constitution and magnetic properties of iron-rich iron-aluminum alloys",* J. Phys. Chem. Solids, 6 (1958) 16.

[109] R C Hall, J. Appl. Phys., *"Magnetostriction of Aluminum-Iron Single Crystals in the Region of 6 to 30 Atomic Percent Aluminum",* 28 (1957) 707.

[110] R C Hall, J. Appl. Phys, *"Single-Crystal Magnetic Anisotropy and Magnetostriction Studies in Iron-Base Alloys"***,** 31 (1960) 1037.

[111] J R Cullen, A E Clark, M Wun-Fogle, J B Restorff, T A Lograsso, *"Magnetoelasticity of Fe–Ga and Fe–Al alloys",* J. Mag. Mag. Mat., 226-230 (2001) 948.

[112] A E Clark, J B Restorff, M Wun-Fogle,T A Lograsso, D L Schlagel, *"Magnetostrictive properties of body-centered cubic Fe-Ga and Fe-Ga-Al alloys",* IEEE Trans. Magn., 36 (2000) 3238.

[113] A E Clark, M Wun-Fogle, J B Restorff, T A Lograsso, J R Cullen, *"Effect of quenching on the magnetostriction of $Fe_{1-x}Ga_x$ (0.13<x<0.21)",* IEEE Trans. Magn., 37 (2001) 2678.

[114] S Guruswamy, N Srisukhumbowornchai, A E Clark, J B Restorff, M Wun-Fogle, Scripta Mater., *"Strong ductile and low-field magnetostrictive alloys based on Fe-Ga",* 43 (2000) 239.

[115] Y Furuya, C Saito, T Okazaki, "*Large magnetostriction in Fe-Ga rapid-solidified alloy",* J. Japan Inst. Metals, 66 (2002) 901.

[116] A E Clark, K B Hathaway, M Wun-Fogle, J B Restorff, T A Lograsso,V M Keppens, G Petculescu and R A Taylor, *"Extraordinary magnetoelaticity and lattice softening in BCC Fe-Ga alloys",* J. Appl. Phys, 93 (2003) 8621.

[117] P Mungsantisukm, R P Corson and S Guruswamy, *"Influence of Be and Al on the magnetostrictive behavior of FeGa alloys",* J. Appl. Phys. 98 (2005)123907.

[118] H. Okamoto, *"Binary Alloy Phase Diagram"*, ASM International, Materials Park, OH, 1996.

[119] Ruqian Wu, *"Origin of large magnetostriction in FeGa alloys",* J. Appl. Phys. 91(2002) 7358.

[120] Manfred Wuttig, Liyang Dai and James Cullen, *"Elasticity and magnetoelasticity of Fe–Ga solid solutions"*, Appl. Phys. Lett. 80 (2002) 1135.

[121] J R Cullen, A E Clark, M Wun-Fogle, J B Restorff and T A Lagrasso, *"Magnetoelasticity of Fe–Ga and Fe–Al alloys",* J. Mag. Mag. Mater. 226–230 (2001) 948.

[122] A E Clark, K B Hathaway, M Wun-Fogle, J B Restorff, T A Lograsso, V M Keppens, *"Extraordinary magnetoelasticity and lattice softening in bcc Fe-Ga alloys"*, J Appl. Phys. 93 (2003) 8621.

[123] S. Datta, M Huang, J Raim, TA Lograsso, AB Flatau, *"Effect of thermal history and gallium content on magneto-mechanical properties of iron gallium alloys"*, Mat. Sci. Engg. A 435–436 (2006) 221.

[124] Q. Xing, Y. Du, R.J. McQueeney, T.A. Lograsso, "*Structural investigations of Fe–Ga alloys: Phase relations and magnetostrictive behavior"*, Acta Mater. 56 (2008) 4356.

[125] H Cao, P M Gehring, C P Devreugd, J A Rodriguez-Rivera, J Li, and D Viehland, *"Role of Nanoscale Precipitates on the Enhanced Magnetostriction of Heat-Treated Galfenol ($Fe_{1-x}Ga_x$) Alloys"*, Phys. Rev. lett. 102 (2009) 127201.

[126] A.E. Clark, M. Wun-Fogle, J.B. Restorff and T.A. Lagrasso, J R Cullen, *"Effect of quenching on the magnetostriction on $Fe_{1-x}Ga_x$ (0.13x<0.21)"*, IEEE Trans Magn. 37 (2001) 2678.

[127] R A Dunlap, J D McGraw, S P Farrell, *"A Mössbauer effect study of structural ordering in rapidly quenched Fe–Ga alloys"*, J. Magn. Magn. Mater 305 (2006) 315.

[128] J.M. Borrego, J.S. Blazquez, C.F. Conde, A. Conde and S. Roth, *"Structural ordering and magnetic properties of arc-melted FeGa alloys*", Intermetallics 15 (2007) 193.

[129] Y Du, M Huang, S. Chang, D L Schlagel, T A Lograsso, and R J McQueeney, *"Relation between Ga ordering and magnetostriction of Fe-Ga alloys studied by x-ray diffuse scattering",* Phys. Rev. B 81(2010) 054432.

[130] Himalay Basumatary, Mithun Palit, J. Arout Chelvane, S. Pandian, M. Manivel Raja and V. Chandrasekaran, *"Structural ordering and magnetic properties of $Fe_{100-x}Ga_x$ alloys"*, Scripta mater. 59 (2008) 878.

[131] O. Ikeda, R. Kainuma, I. Ohnuma, K. Fukamichi and K. Ishida, *"Phase equilibria and stability of ordered b.c.c. phases in the Fe-rich portion of the Fe–Ga system"*, J. Alloy Compd. 347 (2002) 198.

[132] N. Srisukhumbowornchai and S. Guruswamy, *"Influence of ordering on the magnetostriction of Fe–27.5 at.% Ga alloys"*, J. Appl. Phys. 92 (2002) 5371.

[133] Liu Libao, Fu Shiyou, Liu Guodong, Wu Guangheng, Sun Xiudong, Li Jianqi, *"Transmission electron microscopy study on the microstructure of $Fe_{85}Ga_{15}$ alloy"*, Physica B 365 (2005) 102.

[134] A.E. Clark, J.B. Restorff, M. Wun-Fogle, K.B. Hathaway, T.A. Lograsso, M. Huang and E. Summers, *"Magnetostriction of ternary Fe–Ga–*X *(*X *= C,V,Cr,Mn,Co,Rh) alloys*", J. Appl. Phys. 101 (2007) 09C507.

[135] N Srisukhumbowornchai and S Guruswamy, *"Large magnetostriction in directionally solidified FeGa aand FeGaAl allys"*, J. Appl. Phys., 90 (2001) 5680.

[136] E M Summers, T A Lograsso and M Wun-Fogle, "*Magnetostriction of binary and ternary Fe–Ga alloys"*, J. Mater. Sci., 42 (2007) 9582.

[137] S F Cheng, B N Das, M Wun-Fogle, P Lubitz, and A E Clark, *"Structure of melt-spun Fe-Ga-based magnetostrictive alloys"*, IEEE Trans. Mag., 38 (2002) 2838.

[138] M C Zhang, H L Jiang, X X Gao, J Zhu and Z Zhou, *"Magnetostriction and microstructure of the melt spun $Fe_{83}Ga_{17}$ alloy"*, J. Appl. Phys., 99 (2006) 023903.

[139] R A Kellogg, A B Flatau, A E Clark, M Wun-Fogle, and T A Lograsso, "*Texture and grain morphology dependencies of saturation magnetostriction in rolled polycrystalline $Fe_{83}Ga_{17}$"*, J. Appl. Phys. 93 (2003) 8495.

[140] R.A. Kellogg, A.B. Flatau, A.E. Clark, M. Wun-Fogle and T.A. Lograsso, *"Temperature and stress dependencies of the magnetic and magnetostrictive properties of $Fe_{0.81}Ga_{0.19}$",* J. Appl. Phys., 91 (2002) 7821.

[141] N Srisukhumbowornchai and S Guruswamy, *"Crystallographic textures in rolled and annealed Fe-Ga and Fe-Al alloys"*, Metall. Mater. Trans. A, 35 (2004) 2963.

[142] J H Li, X X Gao, J Zhu, X Q Bao, T. Xia, and M.C. Zhang, *"Ductility, texture and large magnetostriction of Fe-Ga based sheets"*, Scripta Mater., 63 (2010) 246.

[143] Suok-Min Na and Alison B Flatau, *"Secondary recrystallization, crystallographic texture and magnetostriction in rolled Fe–Ga based alloys",* J. Appl. Phys., 101 (2007) 09N518.

[144] S Guruswamy, N Srisukhumbowornchai, A E Clark, J B Restorff and M Wun-Fogle, *"Strong, ductile, and low-field-magnetostrictive alloys based on Fe-Ga",* Scripta Mater. 43 (2000) 239.

Chapter 3

Effect of mixing of rare earth on the phase relationship and magnetic properties of $Tb_xDy_{1-x}Fe_{1.95}$ alloys

3.1. Introduction:

The discovery of giant magnetostriction in RFe_2 [R—rare earth] compounds was followed by intensive study on unravelling the metallurgical aspects of both binary and pseudo-binary ($RR'Fe_2$) systems, in particular, to understand the complex interplay between the phase equilibria and the magnetic properties displayed by them [1-7]. As a potential material for sensors and actuators application, research on this material were mostly directed towards optimization of composition and grain orientation in order to achieve high magnetomechanical energy density and magnetomechanical coupling co-efficient [8-20]. Further, an efficient device that operates at low magnetic bias field but produces high value of magnetostriction requires minimization of the inherent magnetocrystalline anisotropy of the active material. This can be achieved by selection of suitable pseudo-binary $(R,R')Fe_2$ compositions with R = Tb, Sm, Er and R′ = Dy, Ho such that RFe_2 and $R' Fe_2$ have opposite signs of magnetocrystalline anisotropy but same signs of magnetostriction [1]. Available resources to date indicate that, $Tb_{0.3}Dy_{0.7}Fe_{1.95}$ exhibits optimum combination of high magnetostriction and low anisotropy.

In several studies conducted so far on $Tb_{0.3}Dy_{0.7}Fe_{1.95}$ alloy, clearly demonstrate that magnetostrictive properties are sensitive to the composition, microstructure and heat treatment [16-20]. Therefore, a complete understanding of ternary phase equilibria of Tb-Dy-Fe is essential to arrive at optimum composition and conditions for solidification and heat treatment of this material. Although a substantial information are available in the existing literature on the magnetic properties and effect of alloying additions to the $Tb_{0.3}Dy_{0.7}Fe_{1.95}$ [10,14,20], very limited attention has been paid on the understanding of the nature of ternary phase equilibria of Tb-Dy-Fe alloys [12,21,22]. The theoretical prediction of ternary Tb-Dy-Fe phase diagram by Landin *et.al.* [21] exhibits no significant deviation from the binary phase equilibria [23-24] and therefore indicating pseudo-binary behaveour of the Tb-Dy-Fe

system. However, Westwood *et.al.* [12] reported the existence of solid solubility in (Tb,Dy)Fe_2 in a $Tb_{0.3}Dy_{0.7}Fe_{1.95}$ alloy, which is strikingly different from perfect stoichiometric nature of RFe_2 (R= Rare Earth) phase reported in Tb-Fe and Dy-Fe binary diagrams [23-24]. In the same report, Westwood *et.al.* also described the microstructural change in $Tb_{0.3}Dy_{0.7}Fe_x$ alloys as a function of Fe-concentration. Following the work of Westwood *et.al.* [12], Mei. *et.al.* [22] described the segregation pattern of rare earth elements in the same alloy and interpreted the results with an assumption that the $Tb_xDy_{1-x}Fe_2$ alloys have same nature of solubility range of Laves phase prevailing from Tb-rich side to Dy-rich side. However, none of the reports resorted to any experimental studies to understand the nature of phase equilibria of Tb-Dy-Fe as a function of Tb/Dy ratio. Therefore, there exists a scope for understanding the change of phase equillibria imparted upon by mixing of two rare earth elements Tb and Dy at different proportions. This understanding is of utmost importance, as this complements the existing information and forms a complete understanding on ternary phase equilibria of Tb-Dy-Fe. Therefore, the current study has been taken up to explore the phase equilibria and magnetic properties of ternary Tb-Dy-Fe alloys as a function of Tb/Dy ratio. A series of alloys $Tb_xDy_{1-x}Fe_{1.95}$ were prepared and the microstructure and magnetic properties were investigated.

3.2. Experimental:

3.2.1. Alloy Preparation:

$Tb_xDy_{1-x}Fe_{1.95}$, x= 0, 0.2, 0.3, 0.4, 0.5, 0.6, 0.7, 0.8 and 1 alloys were prepared by vacuum induction melting of the high purity elemental ingredients (>99.5%) in recrystallized alumina crucibles. A vacuum induction melting furnace of the make of M/s Consarc, UK was used for this purpose (Fig. 3.1). All the alloy compositions were prepared in 500 g scale and at an induction power of 10 kW. The molten alloys were cast in the quartz tubes of 20 mm dia. and 100 mm length, kept inside the furnace chamber under high vacuum. To ensure close to equilibrium condition during solidification of the alloys, the quartz tube mould was insulated heavily all along by thermally insulating material. A schematic picture of the insulated mould is shown in Figure 3.2. The chemical compositions of all alloys were estimated by ICP-OES technique and the chemical compositions were found to be close to the nominal composition in most cases (Table 3.1). The alloy samples were subsequently

vacuum sealed in quartz tubes and heat treated separately at 850°C and 1000°C for 48 hours followed by oil quenching.

3.2.2. Microstructural Characterization:

Using standard metallographic technique the samples were prepared and etched with 4 % Nital (96 ml Methanol + 4 ml HNO_3) for microstructural observation using optical microscope & scanning electron microscope (SEM) [Leo 440 i]. The micro-chemical analysis was carried out to identify the composition of the phases using an (Oxford Instruments) Energy Dispersive Spectrometer (EDS) attached to SEM. The micro-chemical analysis of the fine precipitates was carried out using Wavelength Dispersive Spectrometry (WDS) of a field emission Electron Probe Micro Analyzer (EPMA) [JEOL]. To obtain x-ray powder diffraction patterns, alloy powders in as cast as well as heat-treated conditions were first stress relieved at 350°C for 30 hrs and step scanned (3 sec at each step of 0.02 degree) using x-ray diffractometer (Philips model PW3020). The x-ray diffraction patterns of all the samples were obtained using Cu k_α radiation.

3.2.3. Characterization of Magnetic Properties:

(i) Magnetostriction: The magnetostriction of cast and heat treated samples was measured as a function of applied magnetic field using a magnetic field and temperature compensated resistance strain gauge and a strain measurement system of the make of M/s Vishay Micro-measurement systems, USA. The surface of the cylindrical samples (20mm dia and 40 mm length) were polished and cleaned with surface conditioners. The gauge was affixed to the polished and cleaned surface using adhesive (ANABOND-M^{TM}). A typical setup used for magnetostriction measurement is shown in Figure 3.3.

(ii) Coercivity: The coercivity of the cast and heat treated alloys were measured using coercivemeter (M/s Laboratorio Elektrophysique). The cylindrical samples were placed horizontally inside a coil kept in a metallic chamber shielded from external magnetic field. A Hall probe was placed touching the tip of the cylindrical samples to measure the flux coming out of the samples. The coercivity was measured by plotting second and fourth quadrants of the hysteresis loop.

(iii) Magnetization and Curie temperature: Magnetization measurements were carried out upto an applied field of 20 kOe at room temperature using a vibrating sample

magnetometer (M/s ADE Technologies, USA). For the measurement of Curie temperature (T_C), magnetization was measured at a constant magnetic field of 50 Oe in the temperature range 300–700 K. All measurements were carried out by mounting a sample of 30-40 mg mass on a vertically placed glass rod vibrating at a frequency of 70 Hz.

(iv) Spin re-orientation transition, Hyperfine field and spontaneous magnetostriction: The spin re-orientation transition was characterized for all the alloys by (i) a susceptometer (Cryobind make) in the temperature range 80 – 300 K at an applied ac field of 1 Oe, (ii) Mössbauer spectroscopy (make M/s Fastcomtec, Germany) under transmission mode at room temperature using ^{57}Co as the source and (iii) Splitting of (440) peak in x-ray diffractogram. The Mössbauer data were analyzed using PCMOSS II software to obtain the fit of hyperfine field distributions. The splitting of (440) peak is also used for calculation of spontaneous magnetostriction, which is an indicative of the anisotropy of the alloy.

3.3. Results and Discussions:

3.3.1. Microstructure:

3.3.1.1. ***Pro-peritectic Phase:*** The microstructure of as cast $DyFe_{1.95}$ and $TbFe_{1.95}$ alloys solidified under identical conditions shows presence of major phase RFe_2 (R=Tb or Dy), pro-peritectic RFe_3 and a eutectic mixture of RFe_2 and rare earth (will be henceforth denoted as eutectic phase) (Fig. 3.4). The x-ray diffraction studies also confirm the presence of these phases in the samples (Fig. 3.5). The pro-peritectic RFe_3 phase in the post-solidified microstructure is the result of incomplete peritectic reaction due to the sluggish diffusion of rare earth atoms. Although the mold was designed to ensure very slow rate of solidification, the condition is still different from the ideal equilibrium solidification. Therefore, Scheil's equations [25] was used to estimate the volume fraction of pro-peritectic phase in the binary alloys, based on the data obtained from binary equilibrium diagrams of Tb-Fe and Dy-Fe [23-24]. It is found that at peritectic temperature (1270^{o}C for Dy-Fe and 1187^{o}C for Tb-Fe) for nominal composition *i.e.* 66.1 at%, the volume fraction of RFe_3 is 39% for binary Tb-Fe whereas it is 32 % for binary Dy-Fe. Therefore, the volume fraction of RFe_3 at peritectic temperature for mixed rare earth alloys ($Tb_xDy_{1-x}Fe_{1.95}$ with $0< x <1$) is expected to increase with Tb concentration. Assuming that the solidification conditions are same in case of all the alloys and diffusion of both Tb and Dy is of the same order, the extent of the incomplete peritectic reaction will be similar. Hence, with increase in Tb content, one can expect more

volume fraction of unreacted phase in post-solidified microstructure. This is consistent with our observation in Figure 3.6 which exhibits the increase in volume fraction of pro-peritectic RFe_3 phase with Tb concentration. However, the plot shows a minima and maxima in the volume fraction for the compositions x=0.4 and x=0.6 respectively. Apart from notable difference in volume fraction of pro-peritectic phase, the nature of phase equilibria remains unaltered for all the alloy compositions i.e. pro-peritectic $(Tb,Dy)Fe_3$ and eutectic phase [$(Tb,Dy)Fe_2$ + (Tb,Dy)-solid solution] present along with the major phase $(Tb,Dy)Fe_2$ (Fig. 3.4 and 3.5). The volume fraction of $(Tb,Dy)Fe_3$ phase was found to decrease upon heating at 850^{o}C for 48h and 1000^{o}C for 48 h and followed by oil quenching, (Figs. 3.6, 3.7 and 3.8). This decrease in volume fraction of pro-peritectic phase due to heat treatment is consistent with the metastable existence of this phase.

The eutectic phase is found in very small volume fraction for Dy-rich alloys, whereas the volume fraction of this phase is found nearly 2% in $TbFe_{1.95}$ alloy (Fig. 3.4). The eutectic phase is observed with a droplet like feature for Dy-rich composition whereas it is observed to be spread across interdendritic region for Tb-rich compositions (Fig. 3.4).

3.3.1.2. ***Widmanstätten Precipitate:*** A Widmanstätten type precipitate phase was found to be present in the microstructure of the Dy-rich alloys (x=0-0.5) (Figs. 3.9, 3.10), which was observed earlier by Westwood *et.al.* [12] in $Tb_{0.3}Dy_{0.7}Fe_{1.95}$ composition. The precipitate observed for x=0 composition is relatively coarser and with an increase in Tb concentration the precipitate becomes finer. The composition of the precipitate was analysed using EPMA and is given in Table 3.2. The EPMA analysis indicates that the precipitate is of $(Tb,Dy)Fe_3$ type. A typical micrograph depicting the precipitate observed in x=0.5 alloy and the elemental composition across the phase is shown in Figure 3.11. The precipitate phase however is not observed in Tb-rich alloys (x>0.5). The precipitate is found absent in the alloy heat treated at 1000^{o}C followed by oil quenching (Fig. 3.12).

Although the solid solubility of Laves phase RFe_2 (R= rare earth) has not been indicated in reported binary diagrams of Tb-Fe and Dy-Fe [23-24], the observation of Widmanstätten precipitate of $(Tb,Dy)Fe_3$ in this study clearly indicates the possibility of existence of a high temperature phase field for $(Tb,Dy)Fe_2$. Westwood *et.al.* [12] also reported the formation of similar precipitate in $Tb_{0.3}Dy_{0.7}Fe_{1.95}$ alloy and attributed it to the presence of a solid solubility range of $(Tb,Dy)Fe_2$ extending towards rare earth rich side.

Since, in this study, the precipitate phase is identified as $(Tb,Dy)Fe_3$, such precipitation is only possible if the alloy while cooling first encounters the phase field of $(Tb,Dy)Fe_2$ and thereafter enters into the mixed phase field of $(Tb,Dy)Fe_2 + (Tb,Dy)Fe_3$. This implies that at room temperature, the phase field of $(Tb,Dy)Fe_2$ is skewed and displaced from stoichiometric composition towards rare earth rich side in such a way that the composition range of stability is richer in rare earth than the nominal composition. This condition prevails for temperature range from room temperature to a temperature lying in between 850°C and 1000°C. Further, in the present study, the precipitate phase is found to dissolve completely after heating at 1000°C for 48 hours followed by oil quenching. This dissolution substantiates the existence of a high temperature single phase field that the alloy encounters first while cooling.

A micro-chemical study, using EPMA was carried out to identify the chemical composition of Laves phase [$(Tb,Dy)Fe_2$] at the vicinity of Widmanstätten precipitate. The composition is plotted in Fig. 3.13. It reveals that the compositions of Laves phase in x= 0 - 0.5 alloys are richer in rare earth compared to nominal composition and therefore condition for precipitation of $(Tb,Dy)Fe_3$ exists. With increase in Tb concentration (x>0.5), the composition of the $(Tb, Dy)Fe_2$ phase becomes richer in Fe than nominal composition (Fig. 3.13) and therefore condition for precipitation does not prevail. Therefore, for Dy-rich alloys ($x \leq 0.5$), $(Tb,Dy)Fe_2$ exhibits solid solubility towards rare earth rich side of stoichiometric composition, whereas the solubility range shifts towards Fe-rich side with Tb addition and accordingly Widmanstätten precipitates of $(Tb,Dy)Fe_3$ is present/ absent in the post-solidified microstructure.

This change of solubility range is also reflected in the variation of lattice parameter (Fig. 3.14), which is expected to be influenced by the composition of $(Tb,Dy)Fe_2$ phase. The lattice parameter is largely governed by two factors (i) it should decrease whenever Fe atoms substitute rare earth atoms (ii) it should increase due to substitution of Dy atoms by bigger Tb atoms. For, Dy-rich (x=0-0.5) compositions, the lattice parameter is governed mostly by the first factor, as the trend of lattice parameter corroborates to the variation of composition of $(Tb,Dy)Fe_2$ phase as a function of Tb concentration (Fig. 3.14). However, in Tb rich alloys ($x \geq 0.5$) the lattice parameter increases with Tb addition, although the composition of $(Tb,Dy)Fe_2$ phase shifts towards Fe-rich side. This anomaly is attributed to dominant effect of the second factor causing increase in lattice parameter with Tb addition. The decrease in lattice parameter of $(Tb,Dy)Fe_2$ in the samples quenched from 850°C and 1000°C indicates

that the composition of $(Tb,Dy)Fe_2$ is richer in Fe at high temperature. Therefore, the phase field of $(Tb,Dy)Fe_2$ should bend towards Fe-rich side with increase of temperature. The trend of lattice parameter therefore indicates that the nature of the defect in Laves phase $(Tb,Dy)Fe_2$ is anti-site type. The Dy-rich compositions (x=0-0.5) exhibit substitution of rare earth to Fe site, whereas, Tb-rich compositions (x>0.5) exhibits substitution of Fe to rare earth sites. This observation is in concurrence with the earlier reports by Thoma et. al. and Zhu et.al. [26-27] who proposed that the solubility range in AB_2 type Laves phase can exist owing to anti-site types of defects in A or B site.

Based on the observed microstructural features, micro-chemical analysis and lattice parameter values, a schematic of phase field of $(Tb,Dy)Fe_2$ is brought out in Figure 3.15 as a function of Tb concentration. The phase diagram (Fig. 3.15) indicates clearly that the high temperature solid solubility condition favourable for precipitation of Widmanstätten precipitate is prevalent for Dy-rich compositions (x=0-0.5) whereas it does not exist for Tb-rich alloys (x>0.5). The construction of proposed phase field is further validated from the increase in volume fraction of the eutectic phase with Tb addition (Fig 3.4). Owing to shift of phase field of $(Tb,Dy)Fe_2$ the gap between nominal composition and the phase field boundary of $(Tb,Dy)Fe_2$ increases and therefore volume fraction of eutectic increases with Tb addition.

3.3.2. Magnetic properties:

3.3.2.1. Magnetostriction:

The magnetostriction of the as cast $Tb_xDy_{1-x}Fe_{1.95}$, plotted as a function of applied magnetic field (H), is shown in Fig.3.16. It is observed that the magnetostriction (λ) corresponding to an applied field of 5 kOe, generally increases with increase of Tb concentration in the alloy (Fig.3.16 a). This appears to be an expected trend since $TbFe_2$ displays larger magneto-crystalline anisotropy and therefore larger magnetostriction than $DyFe_2$. With a view to observe the variation in the slope of λ-H curve as a function of Tb concentration in the alloy, the magnetostriction measured for each alloy composition was normalized to its magnetostriction value measured at H=5kOe (Fig.3.16 b). It is seen that the slope is higher for x=0.4 and lower for x=0 and 0.2. The variation in the slope between x=0.3 and 0.5 does not show any perceptible difference. However, for $x \geq 0.6$, the variation is

significant and is in accordance with the high anisotropy for the chosen composition and the microstructural features. The magnetostriction of the alloys and the slope of λ-H curve improve upon heat treatment (Fig. 3.17), owing to the dissolution of pro-peritectic phase and Widmanstätten precipitates. Although x= 0.4 alloy exhibit highest slope in as cast condition, the x=0.3 alloy exhibit highest slope after heat treatment at 1000^{o}C. In order to understand further about the wide variation in magnetostriction as a function of varying concentration of Tb and Dy in the alloys, we carried out further studies by measuring in the alloys (i) the Fe hyperfine field by taking the Mössbauer spectra of the samples, (ii) the split of the (440) diffraction line in the X-ray diffraction pattern, (iii) the magnetic susceptibility and (iv) coercivity.

3.3.2.2. Mössbauer Spectrometry, Magnetization:

The ^{57}Fe Mössbauer spectra at 300 K for $Tb_xDy_{1-x}Fe_{1.95}$ with x > 0 display a superposition of two sextets for the Laves phase $(Tb,Dy)Fe_2$ with the intensity ratio approximately 1:3 (Fig.3.18). However, the $DyFe_{1.95}$ (x=0) exhibits a single six line spectrum for the Laves phase. It has been reported that in RFe_2 type cubic Laves phase compounds, the nature of Mössbauer spectra depends on the angle that the easy magnetization direction (EMD) makes with the electric field gradient at the Fe nuclei [28]. A simple six line spectra would indicate that the EMD lies along [100] crystallographic direction and all the iron atoms in the crystal structure are magnetically equivalent. Whereas, the presence of two sextets with intensity ratio 1:1 or 1:3 would indicate that the EMD lies along <110> or <111>, respectively and the iron atoms are distributed between two magnetically inequivalent sites. Thus, for x=0 and 0.2 alloys the EMD lies along <100> and for x>0.2 the EMD changes from <100> to <111>. The alloy with <111> as EMD is expected to exhibit more magnetostriction owing to rhombohedral distortion than the alloy exhibiting EMD along <100>. Accordingly, the magnetostriction measured at higher field is more for Tb rich alloys as compared to Dy-rich alloys. The hyperfine field of Fe for the $(Tb,Dy)Fe_2$ Laves phase has been calculated from Mössbauer spectra, and is found to increase with Tb addition (Table 3.3). However, the saturation magnetization does not exhibit any significant variation with increase of Tb addition (Fig. 3.19).

3.3.2.3. Curie Temperature:

The shift in the phase field of major phase $(Tb,Dy)Fe_2$ as proposed earlier (Fig. 3.15) should also influence the Curie temperature (T_C) of this phase owing to change in the Fe-concentration in the $(Tb,Dy)Fe_2$ phase. Accordingly, T_C of $(Tb,Dy)Fe_2$ the all the alloys was measured from thermo-magnetic (Magnetization vs. Temperature) plots obtained from VSM. It is observed that the Curie temperature of major phase $(Tb,Dy)Fe_2$ varies significantly with Tb addition (Fig. 3.20). The T_C is determined by two factors (i) increase in rare earth iron exchange interaction (ii) increase in Fe-Fe exchange interaction. The first factor is influenced by hyperfine field of Fe. It is observed from Table 3.3, that the hyperfine field of Fe in $(Tb,Dy)Fe_2$ increases with Tb addition, as a result the (Tb,Dy)-Fe interaction becomes stringer. The second factor is however influenced by the composition of $(Tb,Dy)Fe_2$ phase. Hence, for the Dy-rich compositions ($x \leq 0.5$) the trend is similar to the trend of variation in composition of Laves phase $(Tb,Dy)Fe_2$ (Figs. 3.13 and 3.15). Therefore, for these alloys the T_C of the $(Tb,Dy)Fe_2$ is found to be more where it is richer in Fe promoting more Fe-Fe interaction. Further, a general increase in T_C with Tb addition also supports the proposed shift of Laves phase composition towards Fe-rich side with Tb addition (Fig. 3.15) that promotes stronger Fe-Fe interactions. Therefore the increase of T_C with Tb addition is due to a combined effect of stronger (Tb,Dy)-Fe and Fe-Fe interactions. The increase of hyperfine field of Fe with Tb addition (Table 3.3) favours enhanced (Tb,Dy)-Fe exchange interaction whereas shift of Laves phase composition towards Fe-rich side with Tb addition (Figs. 3.13 and 3.15) promotes stronger Fe-Fe interactions.

3.3.2.4. Splitting of (440) line in the diffraction pattern:

Rhombohedral distortion of RFe_2 due to spontaneous magnetostriction along <111> results in splitting of (440) diffraction line of the x-ray diffractogram into $(\bar{4}40)$ and $(4\bar{4}0)$ [6]. Hence, x-ray diffraction patterns of $Tb_xDy_{1-x}Fe_{1.95}$ were taken at close interval of Bragg angles as to clearly identify the splitting (Fig. 3.21 a). Further, the intensity contribution arising from $k\alpha_2$ has been removed before calculating the split width. It is observed that alloys with x>0.2 show clear splitting of the (440) line indicating rhombohedral distortion and existence of EMD along <111>, whereas such splitting is absent in x=0, 0.2 alloys indicating the EMD is along <100>. It follows from the above observation that the EMD

changes to <111> for compositions 0.2 < x ≤ 1, which is in agreement with the results of Mössbauer study.

The spontaneous magnetostriction occurring in alloys x>0.2 was calculated from the splitting of (440) peak using the formula [29]:

$\lambda_{111} = \frac{\Delta\theta}{\tan\theta}$; Where $\theta = (\theta_1 + \theta_2)/2$ and $\Delta\theta = |(\theta_1 - \theta_2)|$, θ, θ_1, and θ_2 are Bragg angles corresponding to (440), $(\bar{4}40)$ and $(4\bar{4}0)$ peaks. The spontaneous magnetostriction (Fig. 3.21b) increases with Tb addition and it is attributed to the relatively higher anisotropy derived from Tb as compared to Dy.

3.3.2.5. Ac susceptibility measurement:

The result of Mössbauer spectroscopy and x-ray peak splitting indicates that for realising larger magnetostriction, the material should exhibit <111> as EMD. However, Cubic Laves phase compounds show several spin reorientation transitions [SRT] when cooled below its Curie temperature [30-31]. Thus, it is important to know the temperature range, where the material exhibits <111> as EMD. In order to identify this temperature range, initial ac susceptibility (χ_{ac}) of the alloys was measured as a function of temperature (Fig. 3.22). An anomaly is observed for alloys with 0.2 < x ≤ 1, which corresponds to the change of EMD from <100> to <111>. However, no such spin re-orientation could be observed for the compositions x = 0 and 0.2 since these alloys show <100> as EMD even at room temperature. This observation made from the ac susceptibility measurement (χ_{ac}) is consistent with the results obtained from Mössbauer spectroscopy and X-ray diffraction studies (Fig. 3.18 and 3.21).

3.3.2.6. Coercivity of the alloys:

The slope of λ-H curve at low field (Fig. 3.16 b), indicates maximum slope at x=0.4. The slope of λ-H curve at low field depends on several factors such as the anisotropy, and presence of secondary phases contributing for domain wall pinning, etc. Coercivity is a measure for broadly understanding the ability of the magnetic domains to respond to reversal. Lower coercivity is preferred for achieving large magnetostriction at lower magnetic field. Hence, coercivity of the cast and heat treated $Tb_xDy_{1-x}Fe_{1.95}$ alloys, plotted as a function of

Tb concentration (Fig. 3.23), shows variation in coercivity with increasing Tb concentration in the alloy. Correlating with the microstructure of these alloys, it is evident that the coercivity increases owing to increase in the volume fraction of the pro-peritectic RFe_3 phase and the presence of Widmanstätten precipitate. However, upon heat-treatment, a fall in the coercivity is noticed which is presumably on account of dissolution of the pro-peritectic phase and Widmanstätten precipitate. The minimum coercivity occurring at x=0.4 is mainly attributed to the near zero anisotropy compensation and further to the presence of minimum volume fraction of the pro-peritectic phase in relatively low volume fraction. At x>0.4 however, the effect of large anisotropy offered by Tb contributes for increasing the coercivity.

3.4. Summary and Conclusions:

Alloys of $Tb_xDy_{1-x}Fe_{1.95}$ (x=0-1) were prepared by vacuum induction melting. The cast alloys were heat treated at 850^{o}C for 48h and 1000^{o}C for 48h followed by oil quenching. The cast and heat treated samples were characterized for microstructural features and magnetic properties.

The alloys exhibit microstructure consisting of three phases *viz.* $(Tb,Dy)Fe_2$ as major phase, pro-peritectic $(Tb,Dy)Fe_3$ and eutectic phase. The volume fraction of pro-peritectic phase in as-cast alloys exhibit minima at x=0.4 and maxima at x=0.6 composition, which is attributed to minimum and maximum volume fraction of pro-peritectic phase formation at peritectic temperature at those compositions. The volume fraction of pro-peritectic phase decreases with heat treatment at 850^{o}C/ 48 h and further reduces upon heat treatment at 1000^{o}C/48 h.

A Widmanstätten type precipitate of $(Tb,Dy)Fe_3$ is observed for Dy rich compositions ($0 \leq x \leq 0.5$) and not observed for the compositions richer in Tb. The precipitate however dissolves when samples were quenched after the heat treatment of 1000^{o}C/ 48h. This indicates there is an extension of the phase field of $(Tb,Dy)Fe_2$ phase towards rare earth-rich side for Dy-rich compositions. The study of lattice parameter, micro-chemical composition using EPMA, indicates that the phase field of Laves phase shifts towards Fe-rich side with Tb addition; as a result the condition for Widmanstätten precipitate formation does not remain prevalent. The proposed nature of the phase field also corroborates to volume fraction of remnant pro-peritectic phase and the eutectic phase in the microstructure.

The Curie temperature of the Laves phase [$(Tb,Dy)Fe_2$] in $Tb_xDy_{1-x}Fe_{1.95}$ also supports the proposed shift of phase field of $(Tb,Dy)Fe_2$ towards Fe-rich side. The Curie temperature also found to follow the trend of variation of composition of $(Tb,Dy)Fe_2$. Higher T_C is observed for Tb-rich alloys owing to stronger Fe-Fe interactions derived from higher Fe-concentration in Laves phase present in those alloy compositions. The increase in Curie temperature with Tb addition is also resulting from stronger (Tb,Dy)-Fe interaction, which is derived from increase in Fe-hyperfine field in Tb-rich alloys. A spin reorientation transition on Tb addition from [100] easy direction of magnetization to [111] easy direction of magnetization is observed from Mössbauer, ac susceptibility and x-ray studies.

Magnetostriction at high field (> 3kOe) increases with Tb addition however slope of the λ-H curve is maximum for x=0.4 alloy. The increase in magnetostriction with Tb addition is related to increase in magneto-crystalline anisotropy with Tb addition. The slope of the curve is however found to be related to coercivity and the anisotropy of the alloys. The minimum coercivity occurring at x=0.4 is mainly attributed to the near zero anisotropy compensation and further to the presence of minimum volume fraction of the pro-peritectic phase in relatively low volume fraction. At x>0.4 however, the effect of large anisotropy offered by Tb contributes for increasing the coercivity as a result the slope of λ-H curve decreases.

Table 3.1: The compositions of $Tb_xDy_{1-x}Fe_{1.95}$ (x=0-1) alloys as estimated by ICP-OES is compared with the nominal compositions.

Sample	Nominal Composition (wt %)			Estimated Composition (wt%) (± 1 %)		
	Tb	Dy	Fe	Tb	Dy	Fe
x=0	-	60	40	-	60.7	39.3
x=0.2	11.8	48.0	40.2	12.1	48.2	39.7
x=0.3	17.6	42.1	40.3	16.7	42.8	40.5
x=0.4	23.6	36.1	40.3	23.9	36.5	39.6
x=0.5	29.5	30.1	40.4	28.3	30.7	41.0
x=0.6	35.4	24.1	40.5	36.0	23.2	40.8
x=0.7	41.4	18.1	40.5	41.2	17.5	41.3
x=0.8	47.3	12.1	40.6	46.9	12.2	40.9
x=1	59	-	41	58.6	-	41.4

Table 3.2: Composition of Widmanstätten precipitate phase present in alloys $Tb_xDy_{1-x}Fe_{1.95}$ (x=0-0.4) analyzed using WDS detector of EPMA.

Alloy $Tb_xDy_{1-x}Fe_{1.95}$	Tb (at %)	Dy (at %)	Fe (at %)
x=0	--	26.4	73.6
x=0.2	3.3	22.5	74.2
x=0.3	7.3	18.9	73.8
x=0.4	9.4	16.1	74.5
x=0.5	13.1	13.8	73.1

Table 3.3: Hyperfine field and Fe-magnetic moment of $Tb_xDy_{1-x}Fe_{1.95}$ alloys obtained from Mössbauer spectrometry.

Conc. of Tb (x)	**H_f (±2 kOe)**	**Fe mag. moment (μB)**
$DyFe_{1.95}$	206	1.37
$Tb_{0.3}Dy_{0.7}Fe_{1.95}$	210	1.4
$Tb_{0.5}Dy_{0.5}Fe_{1.95}$	211	1.41
$Tb_{0.7}Dy_{0.3}Fe_{1.95}$	213	1.42
$TbFe_{1.95}$	215	1.43

Figure 3.1: Vacuum induction melting furnace of the make of M/s Consarc, UK, used to prepare the alloys

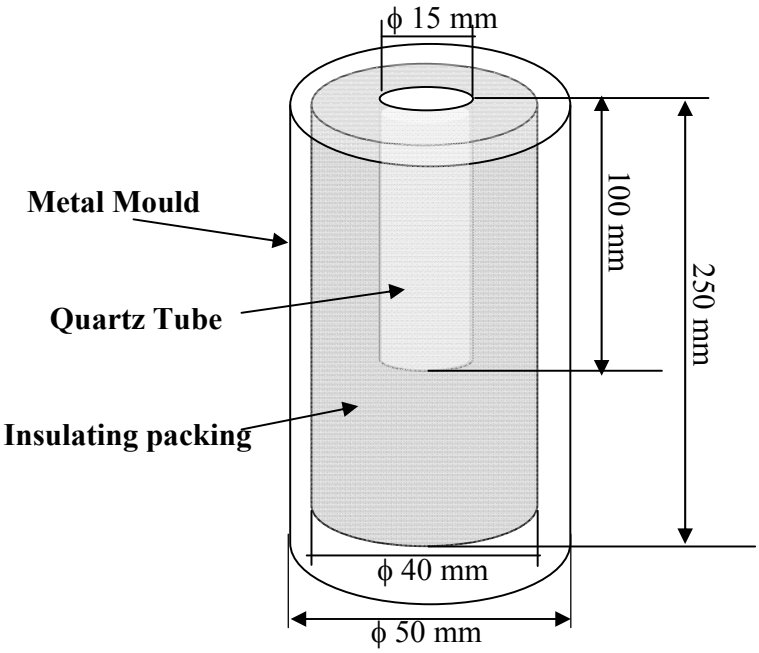

Figure 3.2: Schematic of mold used for preparation of the alloys to ensure the solidification to occurs at slow rate

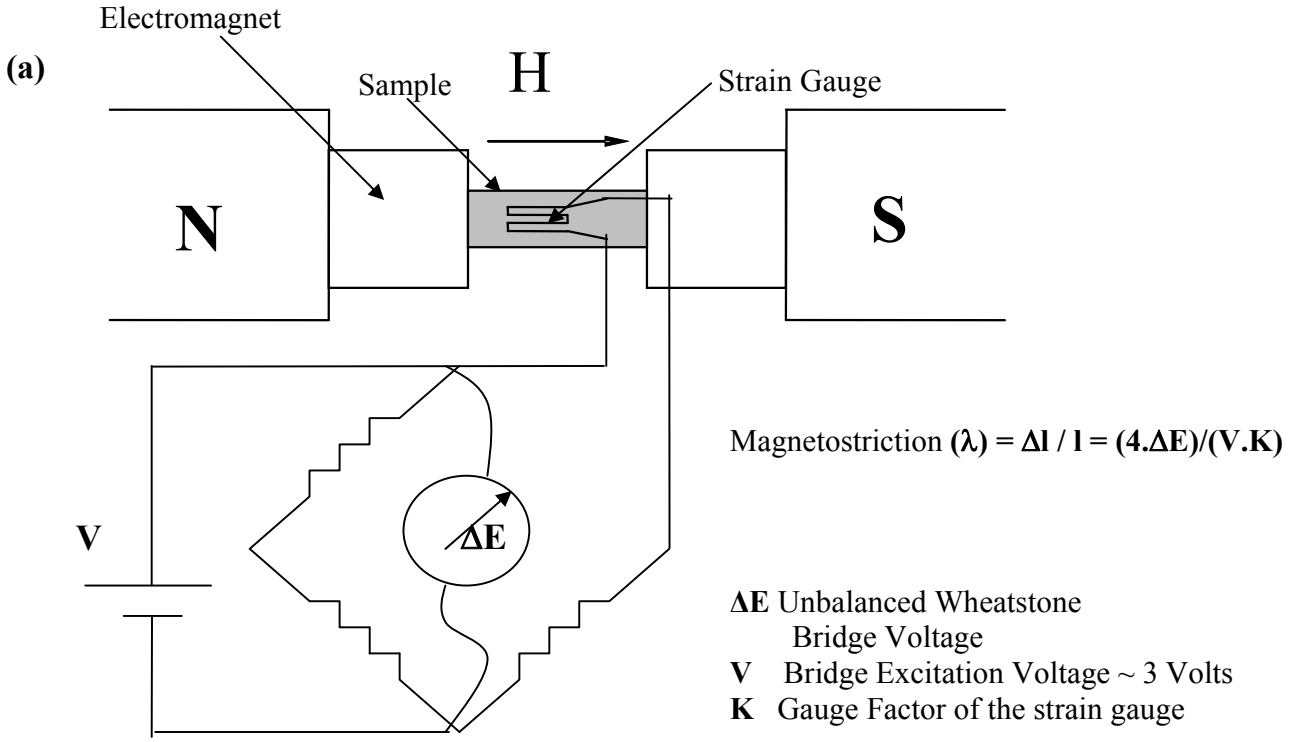

(b)

Figure 3.3: (a) Schematic of the setup used for magnetostriction measurement (b) The photo of a sample during measurement

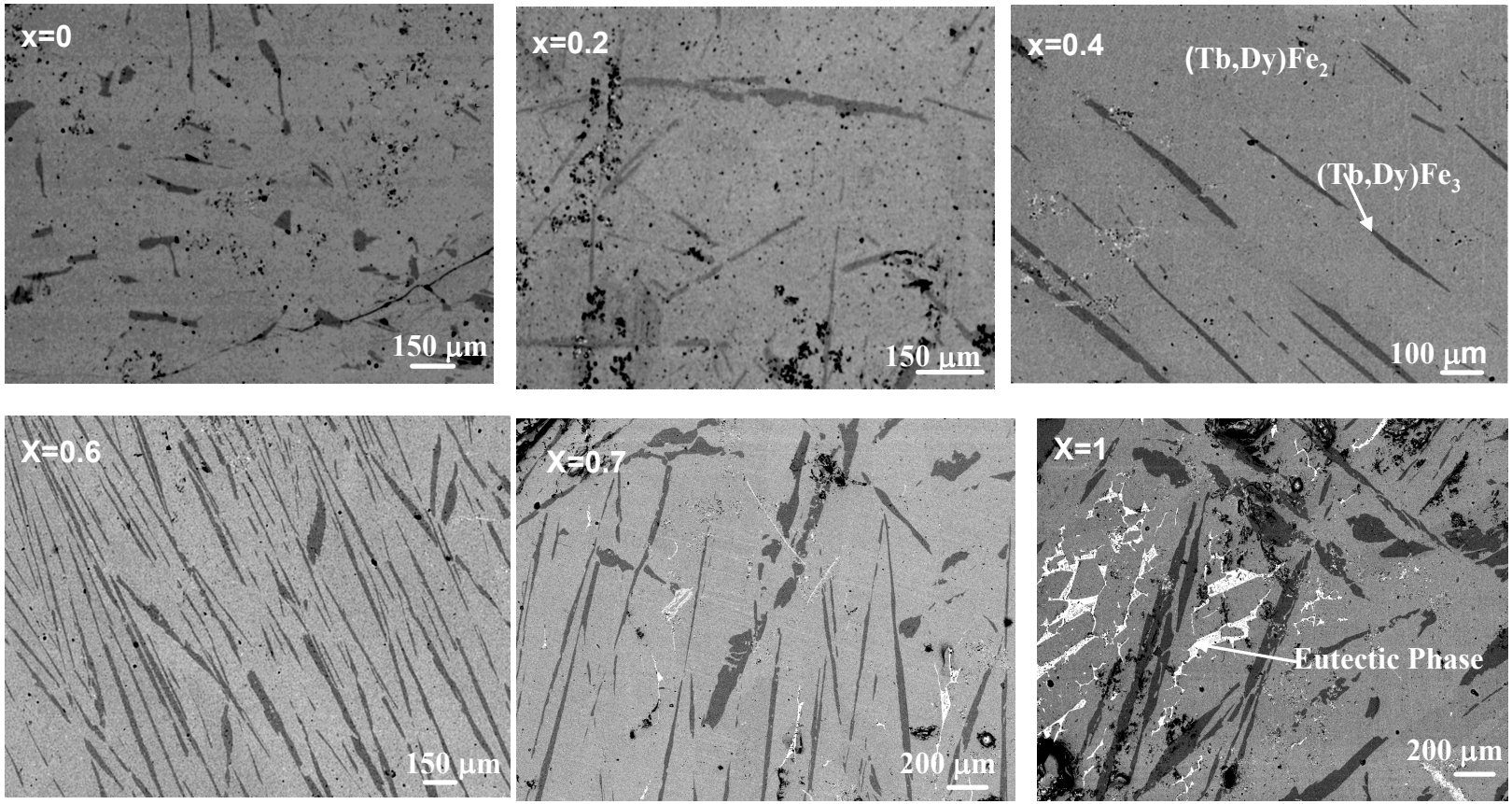

Figure 3.4: Back scattered electron (BSE) image of as-cast $Tb_xDy_{1-x}Fe_{1.95}$ alloys exhibiting variation in volume fraction of pro-peritectic $(Tb,Dy)Fe_3$ and eutectic phases.

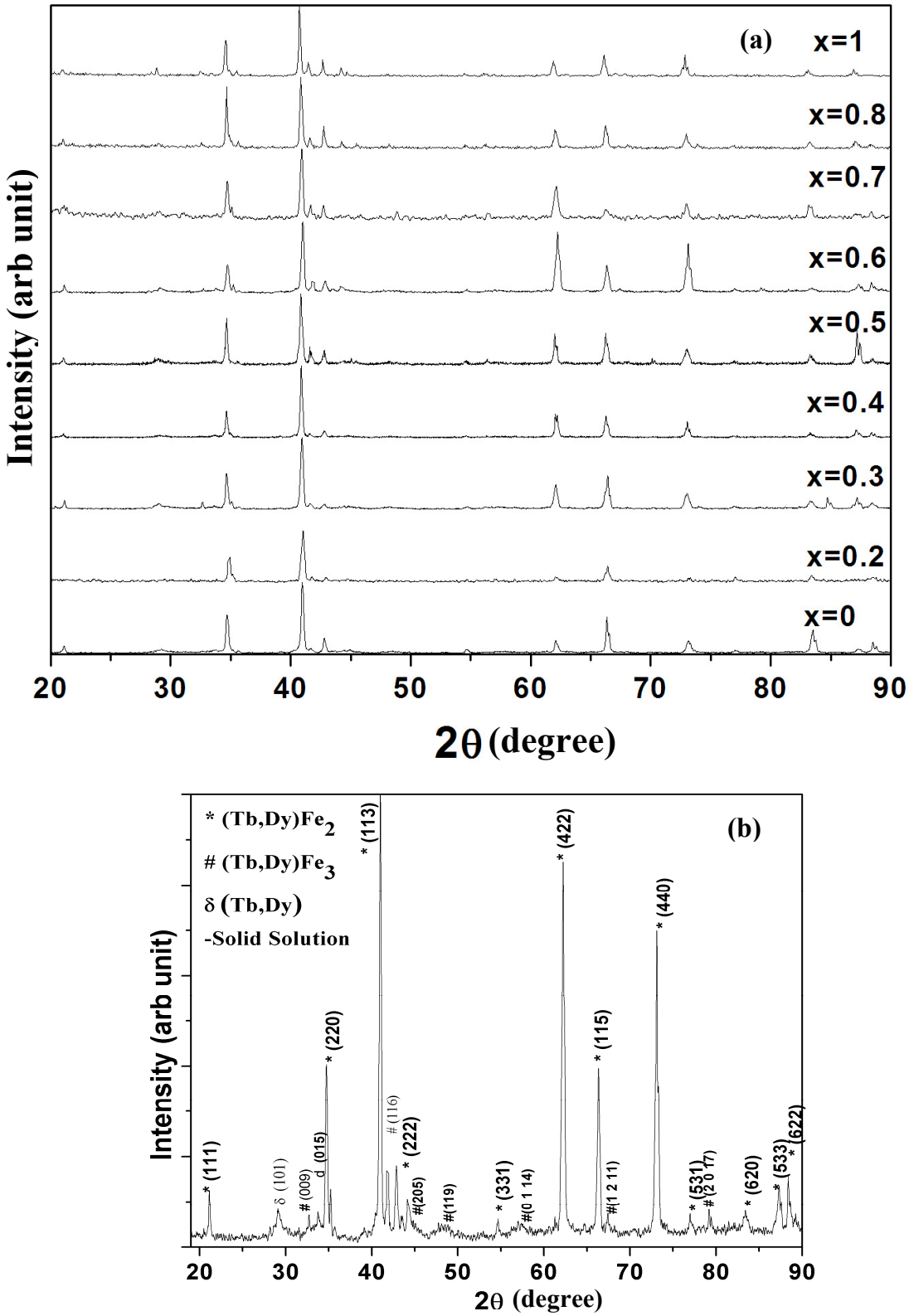

Figure 3.5: (a) X-ray difractograms of $Tb_xDy_{1-x}Fe_{1.95}$ alloys (b) Magnified view of diffractogram corresponding to x=0.6 alloy, exhibiting presence of different phases.

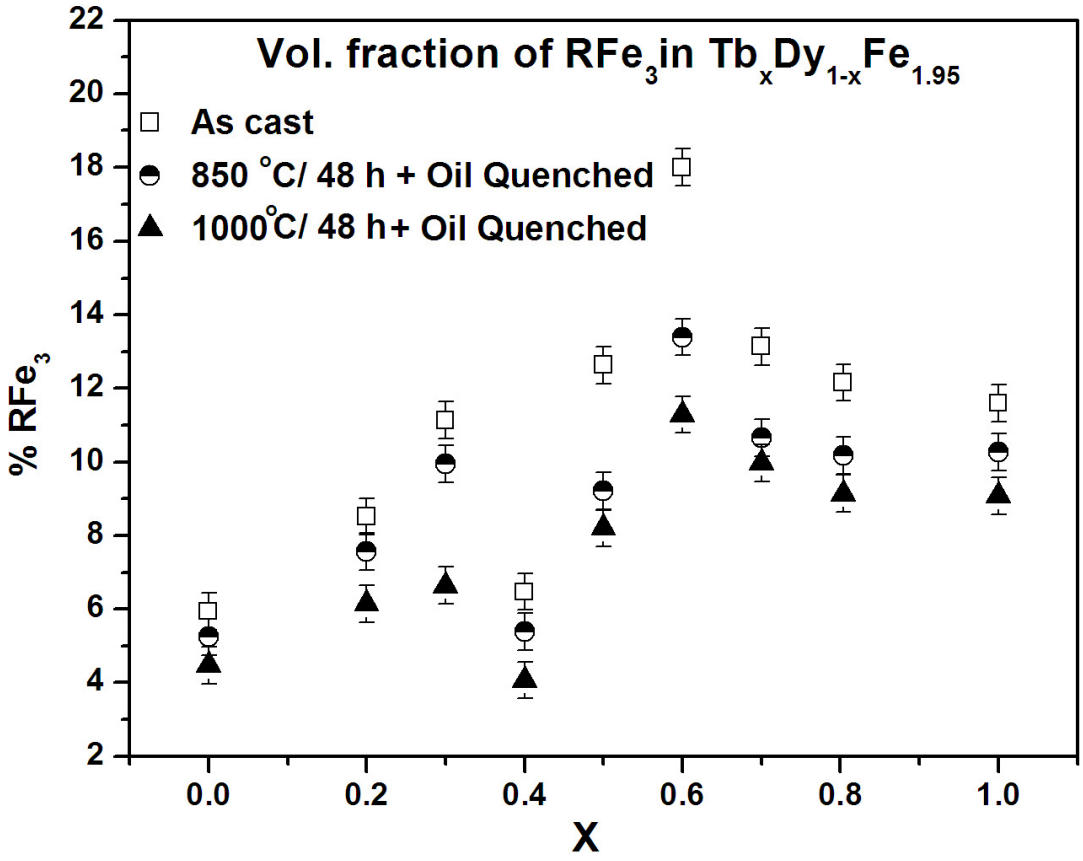

Figure 3.6: Volume fraction of pro-peritectic RFe_3 phase plotted as a function of concentration of Tb in as-cast and heat treated $Tb_xDy_{1-x}Fe_{1.95}$ alloys.

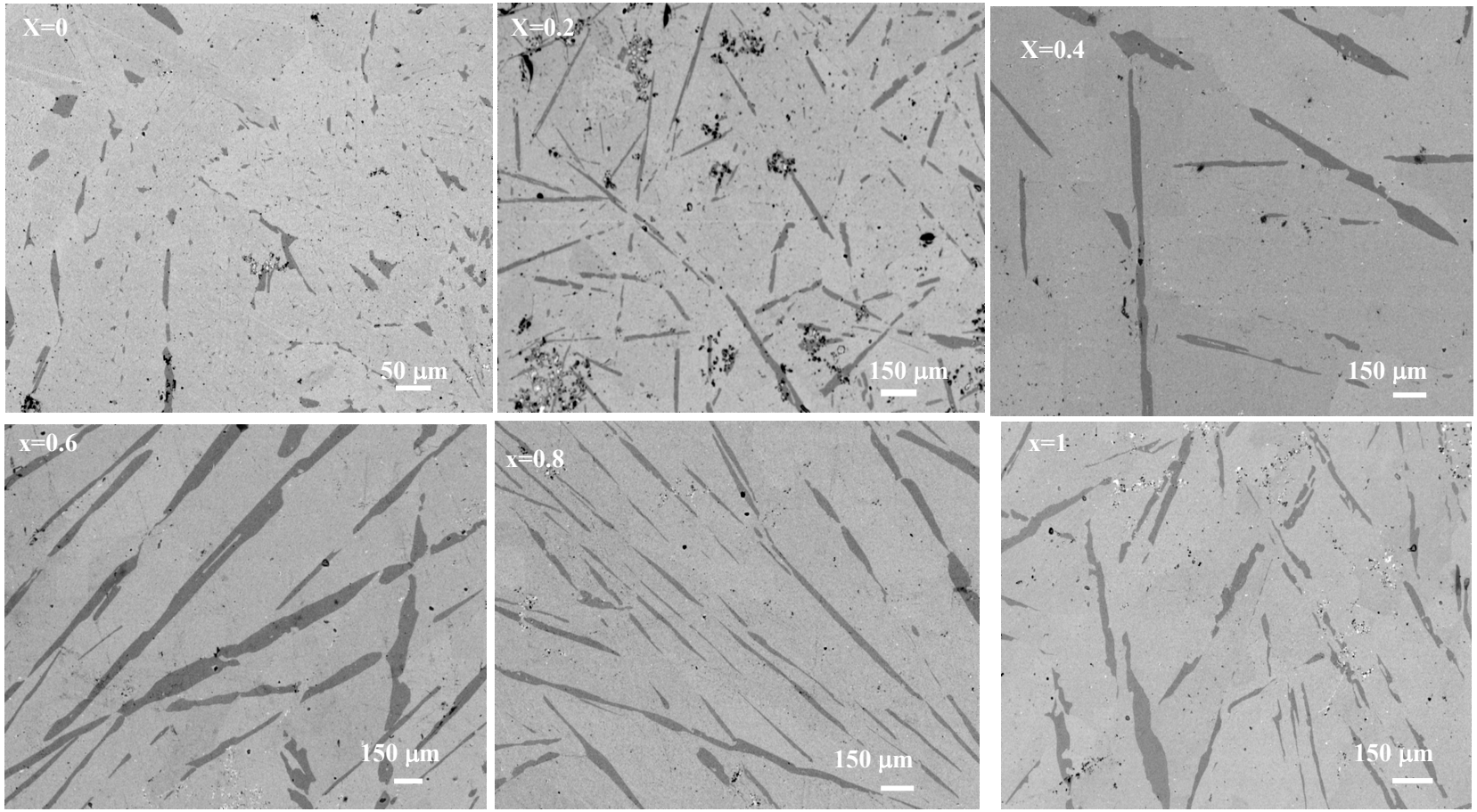

Figure 3.7: BSE image of $Tb_xDy_{1-x}Fe_{1.95}$ alloys heat treated at 850^{o}C/ 48 h followed by oil quenching.

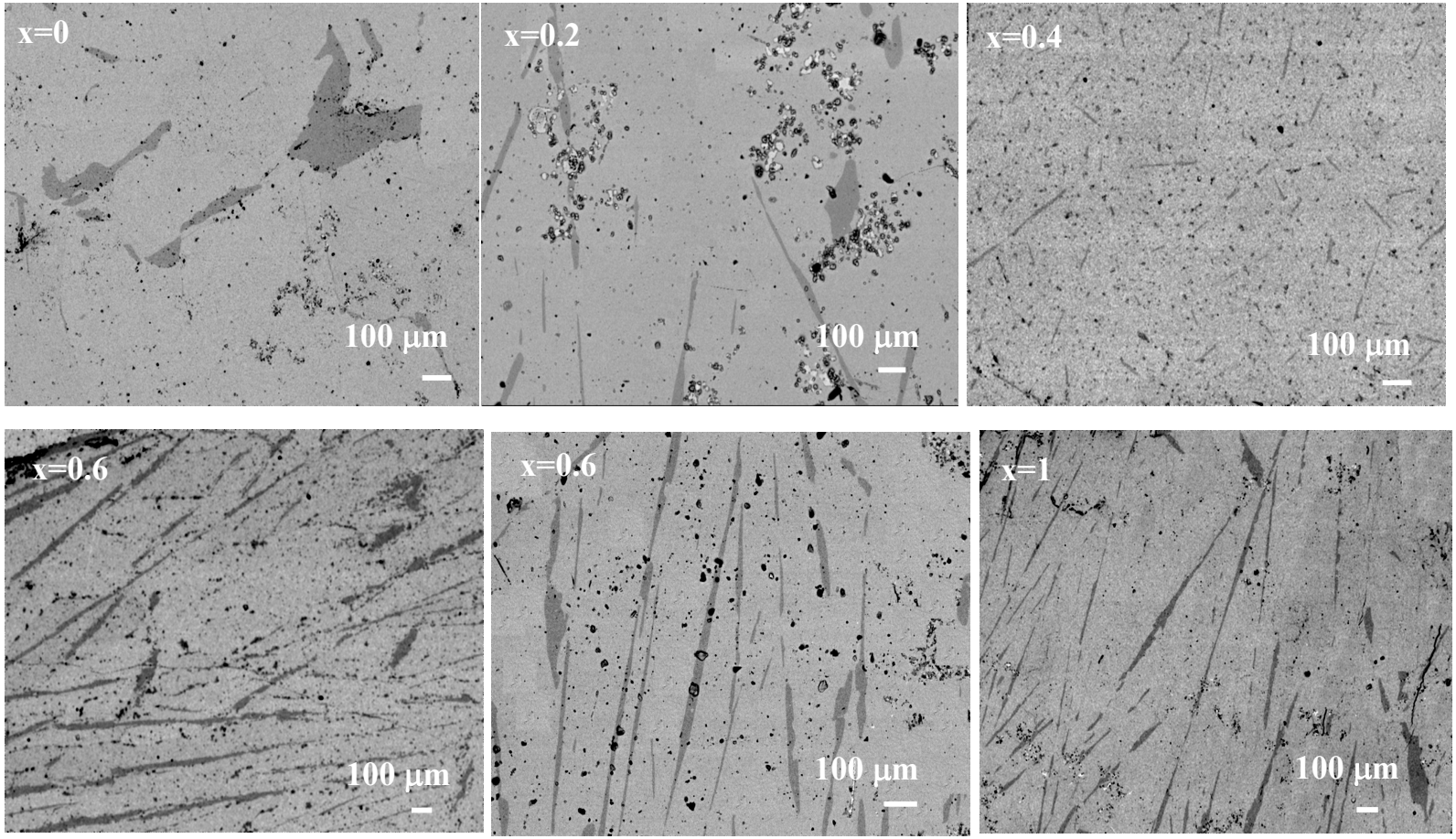

Figure 3.8: BSE image of $Tb_xDy_{1-x}Fe_{1.95}$ alloys heat treated at 1000°C/ 48 h followed by oil quenching, exhibiting reduction in volume fraction of pro-peritectic RFe_3 phase.

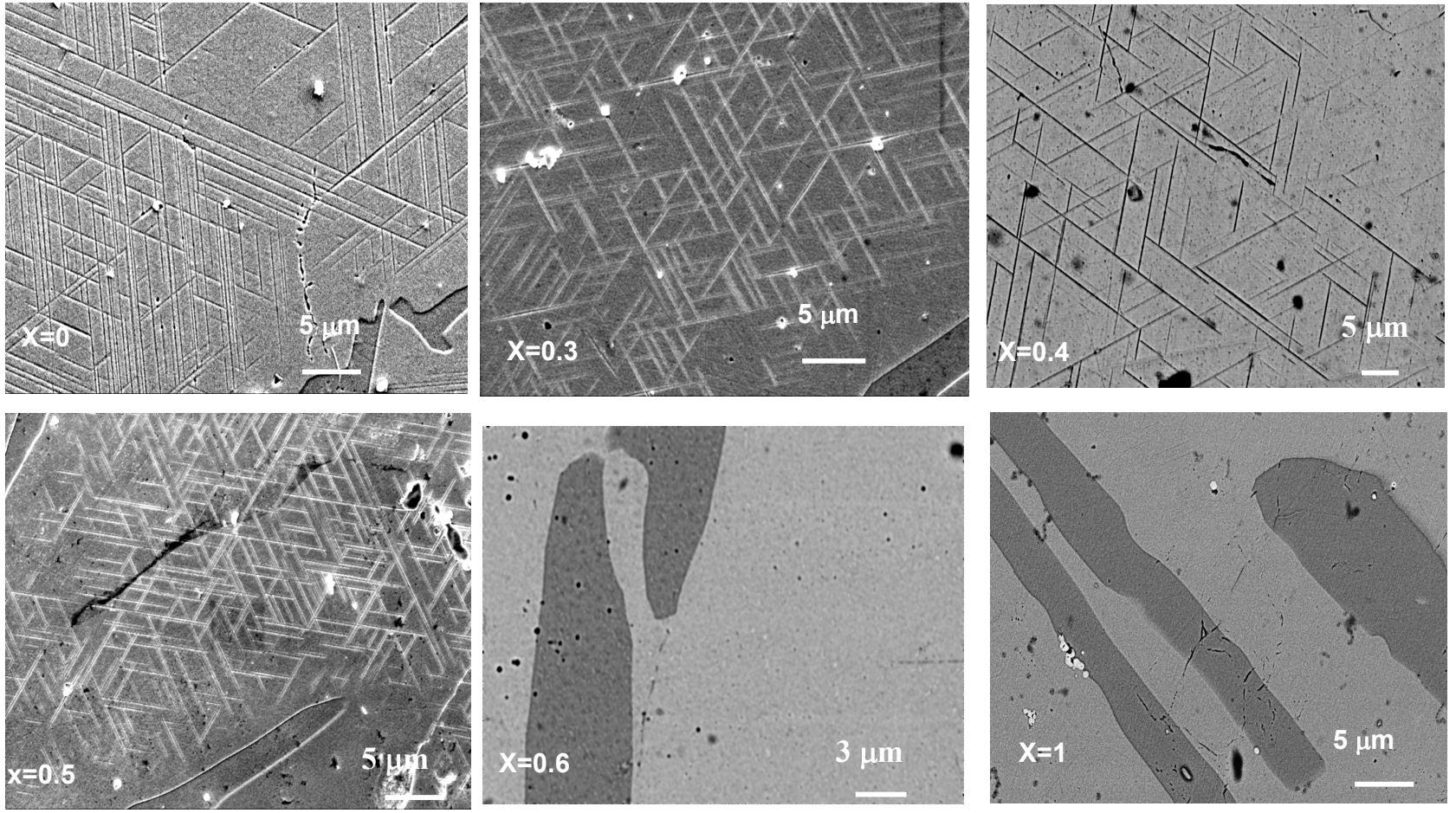

Figure 3.9: Microstructure exhibiting presence/ absence of Widmanstätten precipitate in as-cast $Tb_xDy_{1-x}Fe_{1.95}$ alloys.

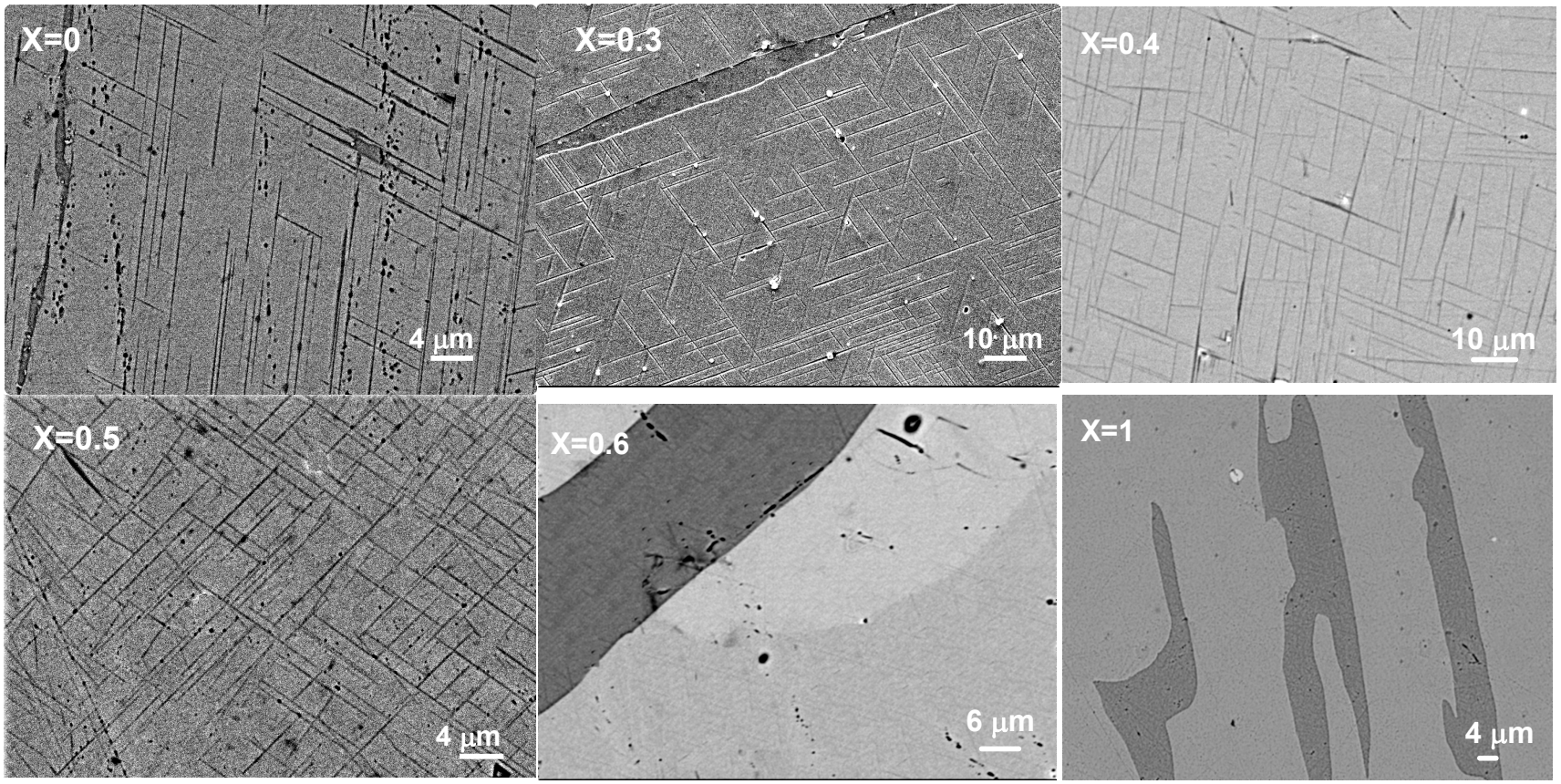

Figure 3.10: Microstructure exhibiting presence/ absence of Widmanstätten precipitate in $Tb_xDy_{1-x}Fe_{1.95}$ alloys heat treated at 850^{o}C/ 48 h followed by oil quenching.

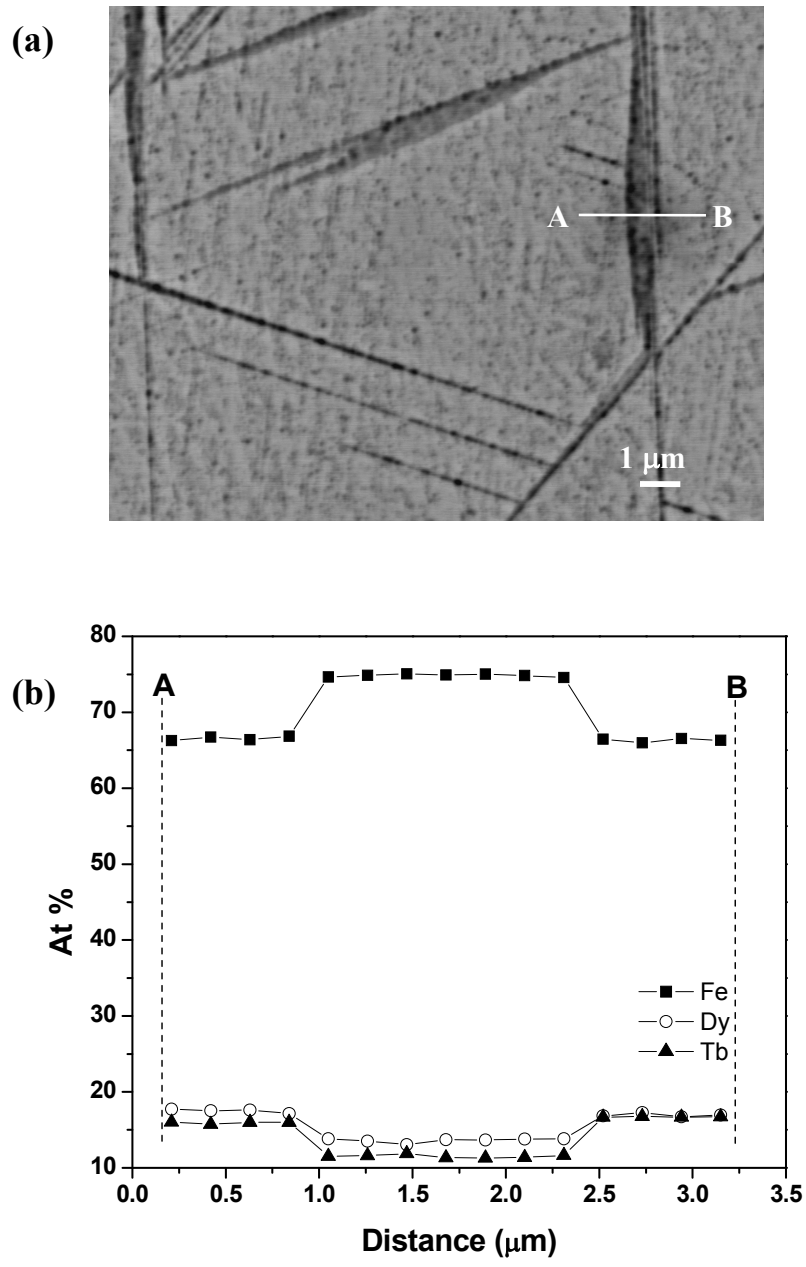

Figure 3.11: (a) BSE image depicting the precipitate observed in x=0.5 alloy and (b) the plot of elemental composition (determined by EPMA analysis) across the precipitate.

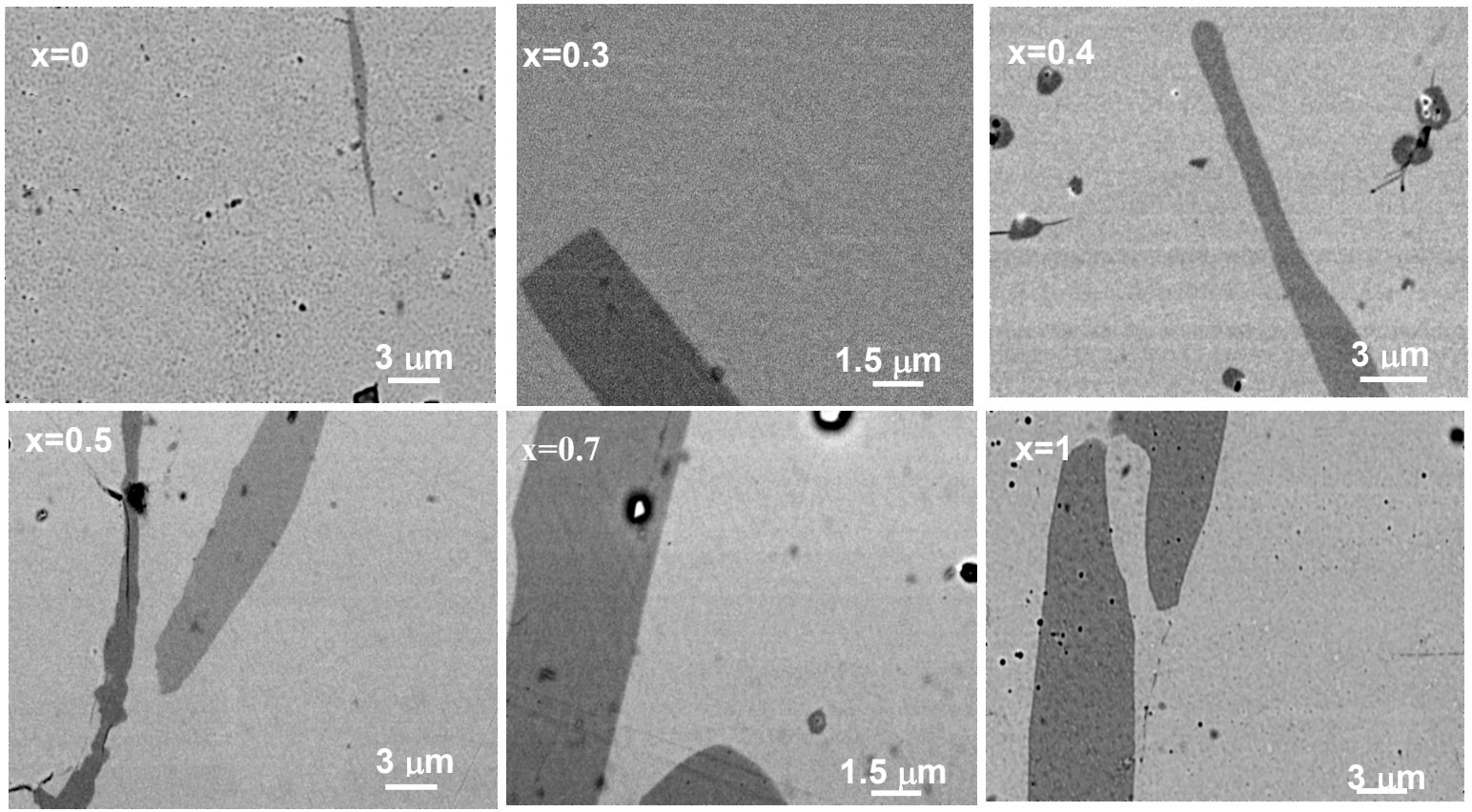

Figure 3.12: Microstructure exhibiting complete dissolution of Widmanstätten precipitate in $Tb_xDy_{1-x}Fe_{1.95}$ alloys heat treated at 1000^{o}C/ 48 h followed by oil quenching.

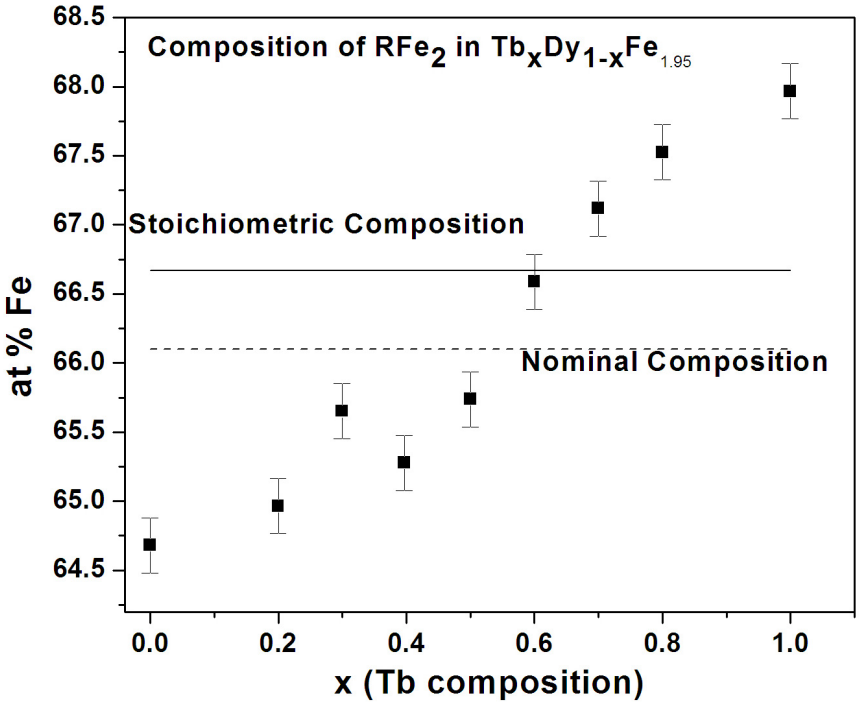

Figure 3.13: The composition of Laves phase in $Tb_xDy_{1-x}Fe_{1.95}$ taken in the vicinity of Widmanstatten precipitate phase as determined from EPMA analysis.

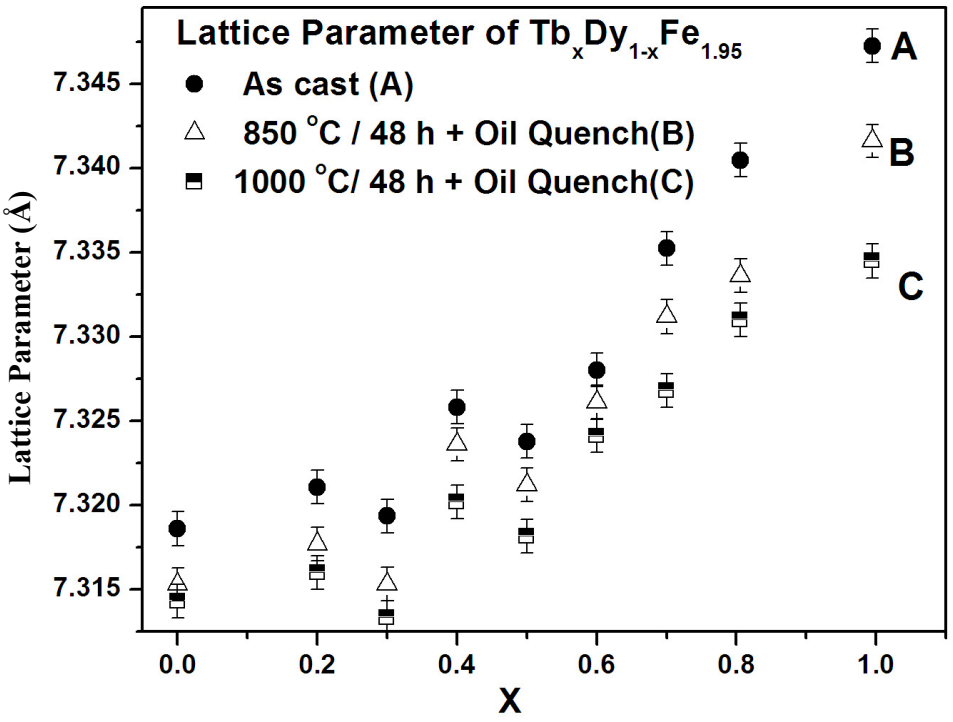

Figure 3.14: Lattice parameter of $(Tb,Dy)Fe_2$ phase plotted as a function of concentration of Tb in as-cast and heat treated $Tb_xDy_{1-x}Fe_{1.95}$ alloys.

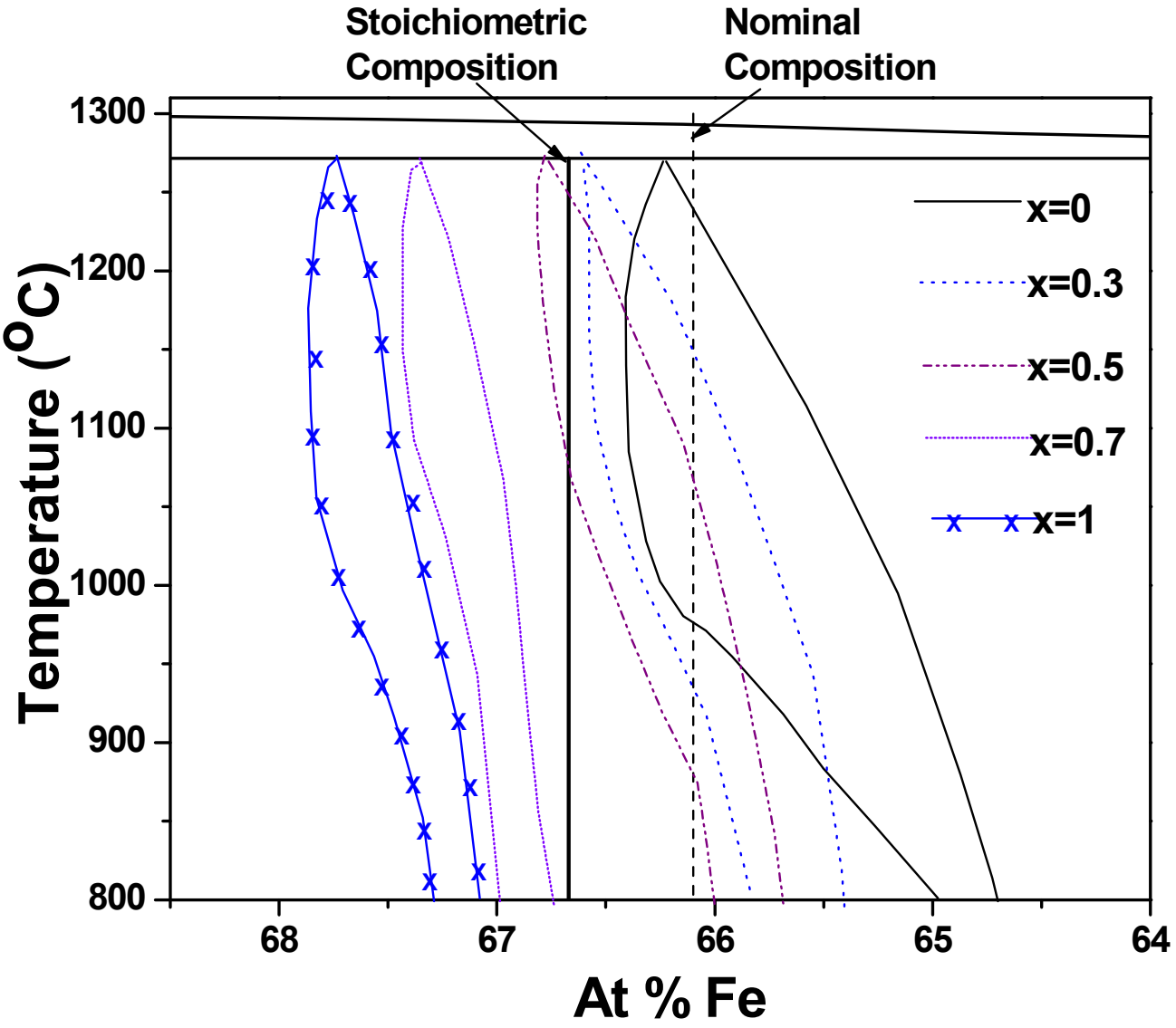

Figure 3.15: Proposed shape of phase field of Laves phase (Tb,Dy)Fe_2 in $Tb_xDy_{1-x}Fe_{1.95}$ alloys; the stoichiometric and nominal compositions are indicated as vertical lines in the figure.

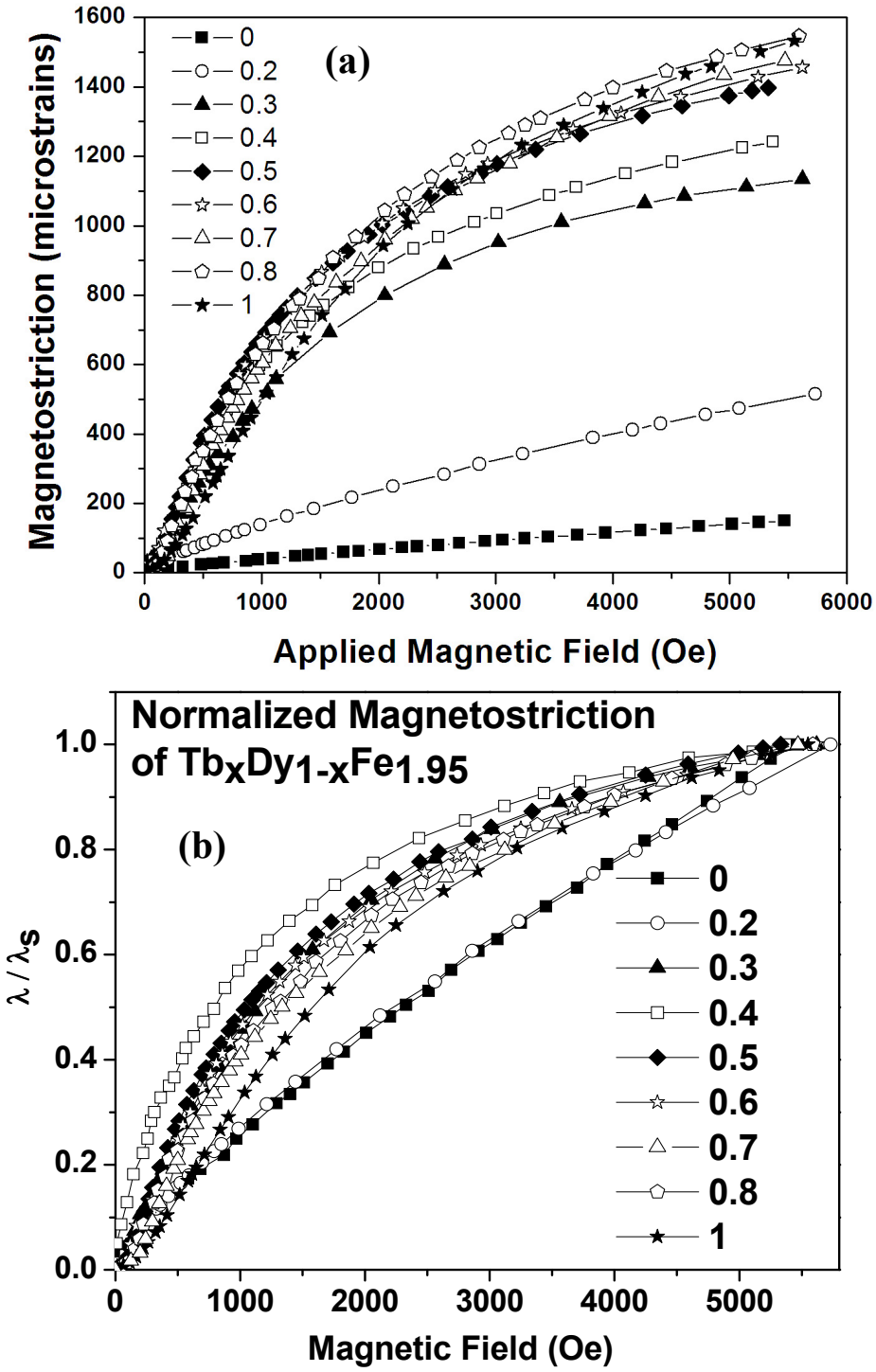

Figure 3.16: (a) Magnetostriction of as cast $Tb_xDy_{1-x}Fe_{1.95}$ alloys plotted as a function of applied magnetic field (b) Normalized magnetostriction (λ/λ_s) plotted as a function of applied magnetic field to indicate initial slope of the magnetostriction

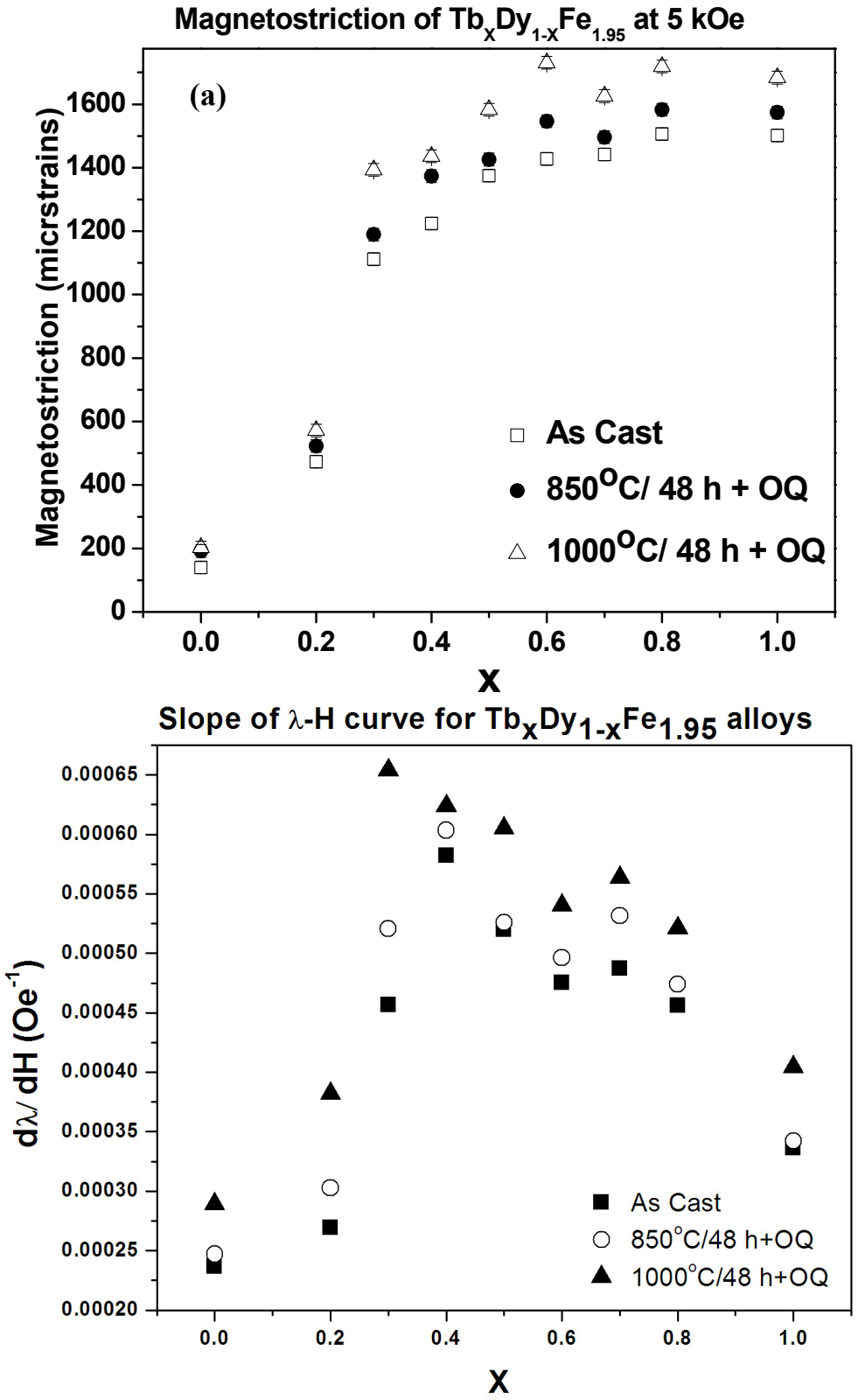

Figure 3.17: (a) Magnetostriction of cast and heat treated $Tb_xDy_{1-x}Fe_{1.95}$ alloys at an applied magnetic field of 5 kOe and (b) the change of the slope of λ-H curve upon heat treatment.

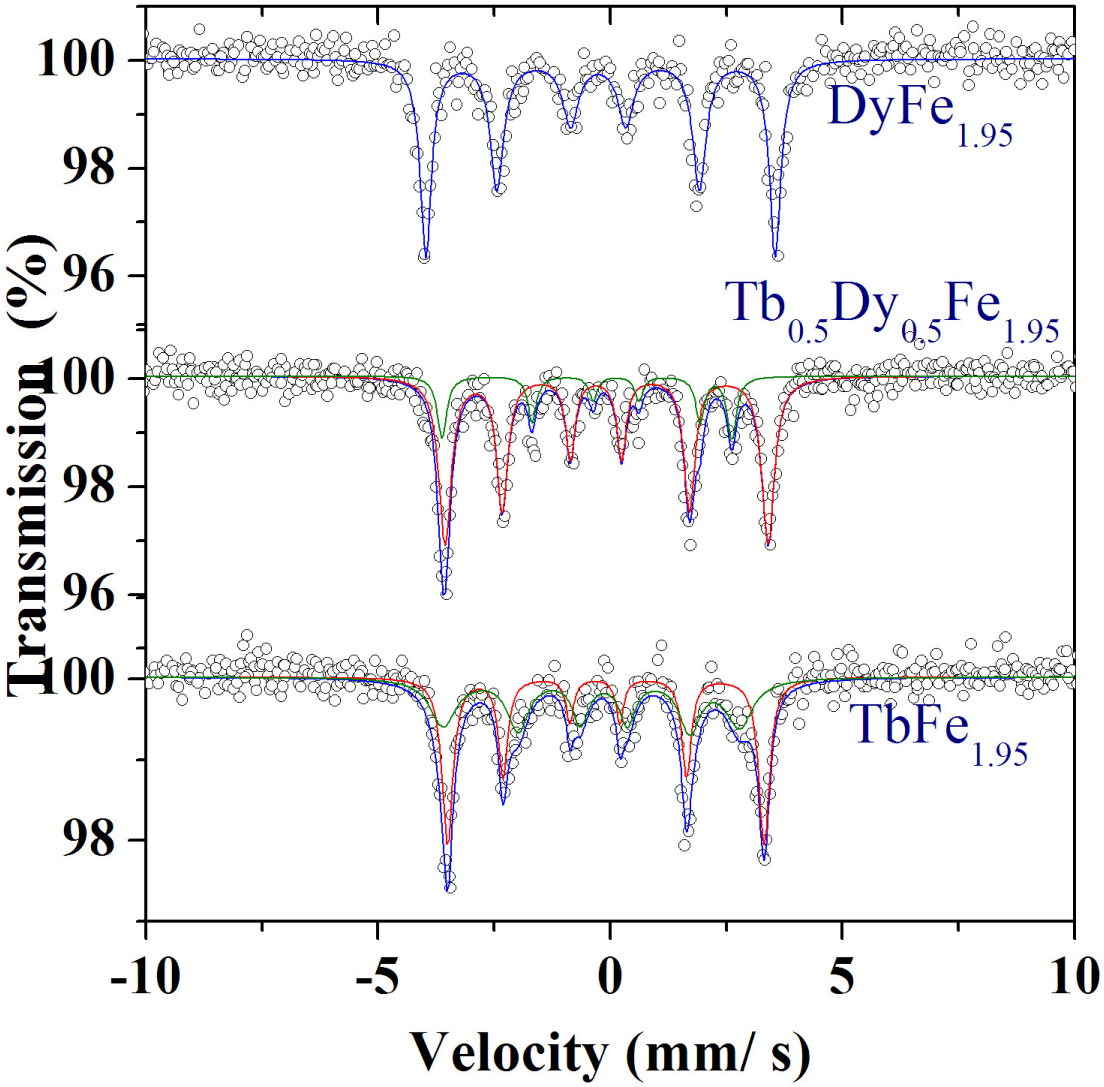

Figure 3.18: Mössbauer spectrum of $Tb_xDy_{1-x}Fe_{1.95}$ alloys, exhibiting spin reorientation with Tb addition.

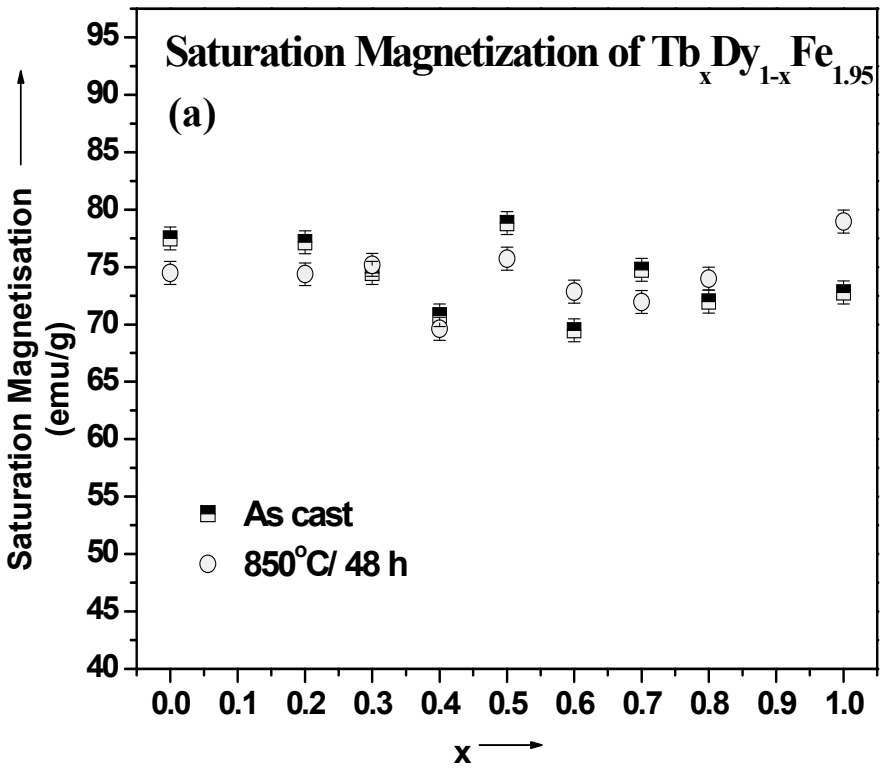

Figure 3.19: Saturation Magnetization of as-cast and heat treated $Tb_xDy_{1-x}Fe_{1.95}$ alloys

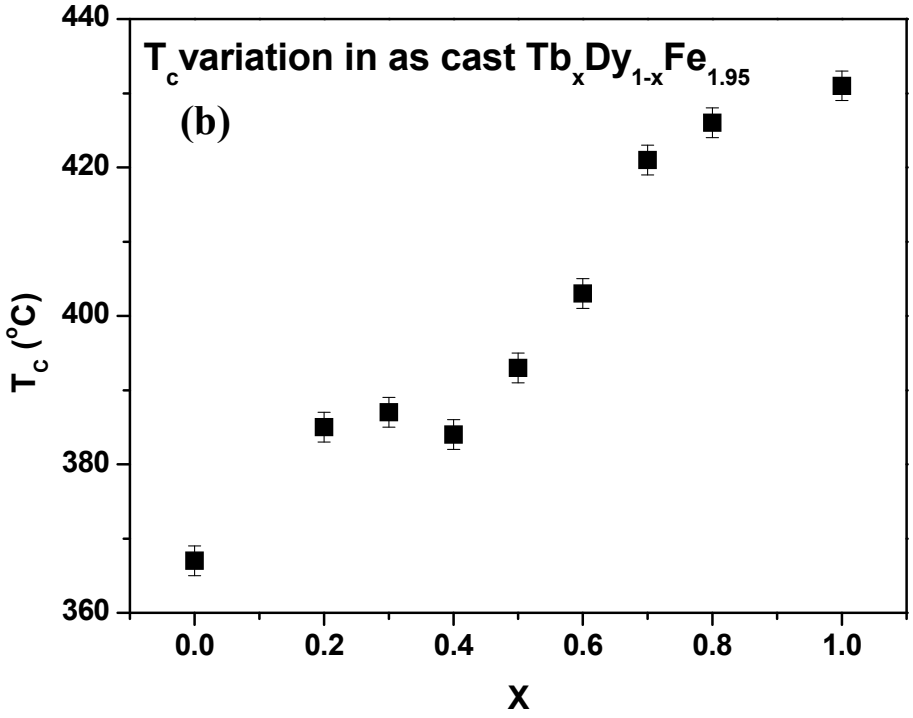

Figure 3.20: Curie temperature of $Tb_xDy_{1-x}Fe_{1.95}$ alloys, plotted as a function of concentration of Tb.

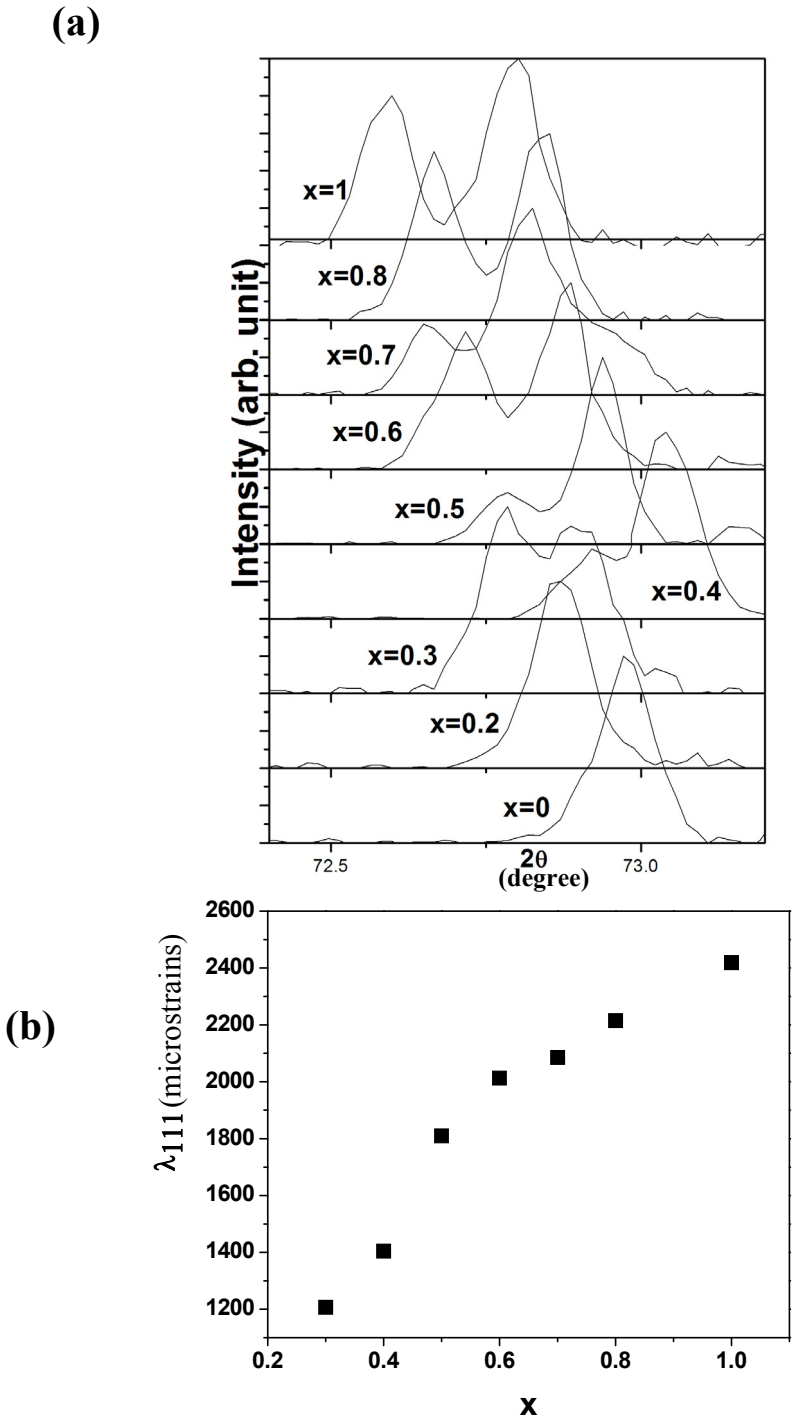

Figure 3.21: (a) Splitting of (440) peak due to spontaneous magnetostriction in $Tb_xDy_{1-x}Fe_{1.95}$ alloys (b) Calculated spontaneous magnetostriction λ_{111} plotted as a function of Tb concentration of $Tb_xDy_{1-x}Fe_{1.95}$ alloys

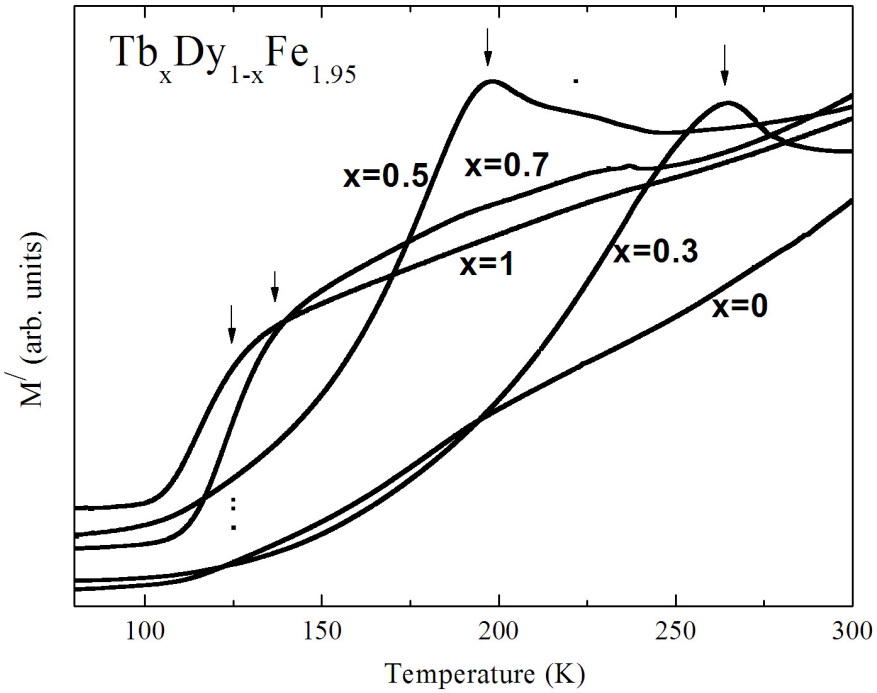

Figure 3.22: Temperature variation of ac susceptibility of $Tb_xDy_{1-x}Fe_{1.95}$ alloys, exhibiting spin reorientation with Tb addition.

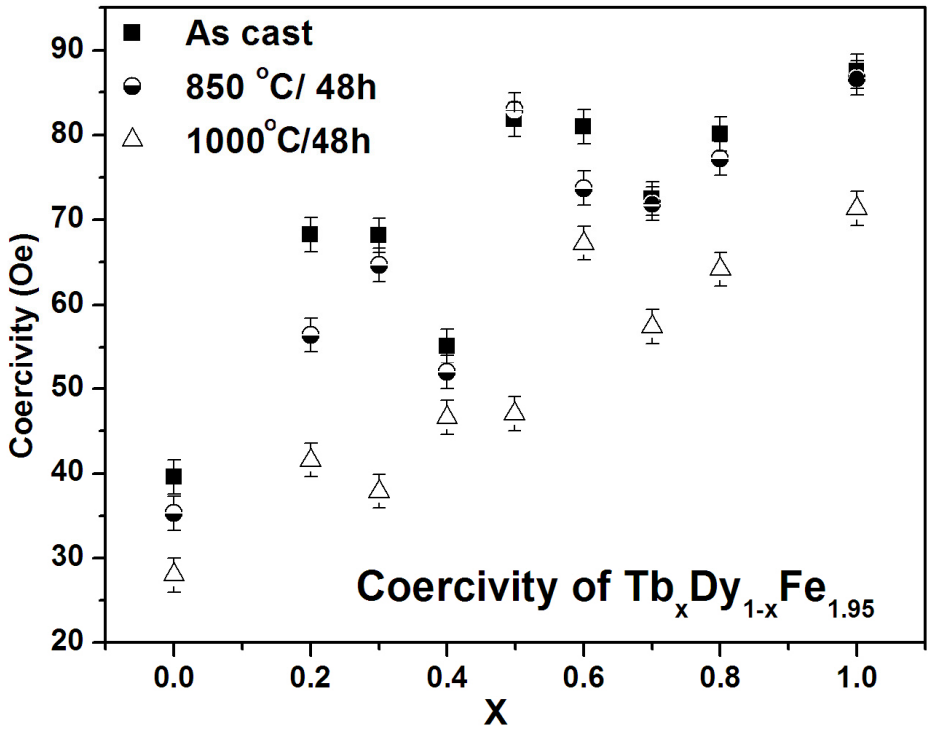

Figure 3.23: Variation of coercivity of as-cast and heat treated $Tb_xDy_{1-x}Fe_{1.95}$ alloys as a function of Tb concentration

References:

[1] A. E. Clark, H. S. Belson and N. Tamagawa, "*Magnetocrystalline Anisotropy in Cubic Rare Earth-Fe_2 Compounds"*, AIP Conf. Proc. 10 (1973) 749.

[2] D. C. Jiles, *"The development of highly magnetostrictive rare earth-iron alloys"*, J. Phys. D 27 (1994) 1.

[3] N.C. Koon, C.M. Williams, B.N. Das, *"Giant magnetostriction materials"*, J. Magn. Magn. Mater. 100 (1991) 173.

[4] K. N. R. Taylor, *"Intermetallic rare-earth compounds"*, Adv. Phys. 20 (1971) 551.

[5] K. H. J. Buschow, *"Ferromagnetism of SmCd"*, Rep. Prog. Phys. 40 (1977) 1179.

[6] A.E. Clark, in: E.P. Wohlfarth (Ed.), *"Ferromagnetic Materials"*, vol. 1, North Holland.

[7] W. J. Park, J. C. Kim, B. J. Ye, Z. H. Lee, *"Macrosegregation in Bridgman growth of Terfenol-D and effects of annealing"*, J. Cryst. Growth 212 (2000) 283.

[8] Mithun Palit, S. Banumathy, A.K. Singh, S. Pandian, K. Chattopadhyay, *"Crystallography of solid-liquid interface and evolution of texture during directional solidification of $Tb_{0.3}Dy_{0.7}Fe_{1.95}$ alloy"*, Intermetallics 19 (2011) 357.

[9] L. Wu, W. Zhan, X. Chen, *"Directional growth of single crystal Terfenol-D by the Electron beam zoning method"*, J. Magn. Magn. Mater. 164 (1996) 367.

[10] O.D. McMasters, J.D. Verhoeven, E.D. Gibson, *"Preparation of Terfenol-D by float zone solidification"*, J. Magn. Magn. Mater. 54 (1986) 849.

[11] J.D. Verhoeven, E.D. Gibson, O.D. McMasters, H.H. Baker, "*The growth of single crystal Terfenol-D crystals*", Metall. Trans. 18A (1987) 223.

[12] P. Westwood, J. S. Abell, and K. C. Pitman, "*Phase relationships in the Tb-Dy-Fe ternary system",* J. Appl. Phys. 67 (1990) 4998.

[13] Y. Zhao, C. Jiang, H. Zhang, and H. Xu, "*Magnetostriction of <110> oriented crystals in the TbDyFe alloy*" J. Alloys Compd. 354 (2003) 263.

[14] J. D. Snodgrass and O. D. McMaster, "*Optimized TERFENOL-D manufacturing processes*", J. Alloys Compd. 258 (1997) 24.

[15] Mithun Palit, S. Pandian, R. Balamuralikrishnan, A.K. Singh, Niranjan Das, V. Chandrasekharan, G. Markandeyulu, "*Microstructure and magnetostriction of $Tb_{0.3}Dy_{0.7}Fe_{1.95}$ prepared under different solidification conditions by zoning and*

modified Bridgman techniques", J. Appl. Phys. 100 (2006) 074913.

[16] Mithun Palit, J. Arout Chelvane, S. Pandian, Niranjan Das and V. Chandrasekaran, *"Effect of solidification rate on the microstructural features and magnetostriction of directionally solidified $Tb_{0.3}Dy_{0.7}Fe_{1.95}$"*, Scripta Mater. 58 (2008) 819.

[17] Mithun Palit, J. Arout Chelvane, S. Pandian, M. Manivel Raja and V. Chandrasekaran, "*Phase relationship, magnetic properties and Mössbauer studies in as cast and directionally solidified $Tb_{0.3}Dy_{0.7}Fe_{1.95}$",* Materials Char. 60 (2009) 40.

[18] Mithun Palit, J. Arout Chelvane, Himalay Basumatary, S. Banumathy, A.K. Singh, S. Pandian, V. Chandrasekaran, "*Comparative effect of texture and microstructure on the magnetostriction of directionally solidified $Tb_{0.3}Dy_{0.7}Fe_{1.95}$ alloy",* Intermetallics 18 (2010) 1027.

[19] M. Senthil Kumar, K.V. Reddy, K.V.S. Rama Rao, *"Observation of domain wall pinning in $Dy_{0.73}Tb_{0.27}Fe_{2-x}Ni_x$ and $Ho_{0.85}Tb_{0.15}Fe_{2-y}Ni_y$ systems",* IEEE Trans. Magn. 31 (1995) 4160.

[20] Mithun Palit, J. Arout Chelvane, Himalay Basumatary, S. Pandian and V. Chandrasekaran, Scripta Mater. "*The effect of Nb and Zr addition on the microstructural features and magnetic properties of $Tb_{0.3}Dy_{0.7}Fe_{1.95}$",* 60 (2009) 56.

[21] Susane Landin and John Ågen, *"Thermodynamic assessment of Fe-Tb and Fe-Dy phase diagrams and prediction of Fe-Tb-Dy phase diagram",* J. Alloys and Compd., 207/208 (1994) 449.

[22] W. Mei, T. Okane and T. Umeda, *"Phase diagram and inhomogeneity of (TbDy)-Fe(T) (T = Mn, Co, Al, Ti) systems",* J. Alloys and Compd., 248 (1997) 132.

[23] M.P. Dariel, J.T. Holthuis and M.R. Pickus, *"The terbium-iron phase diagram"***,** J. Less-Common Met., 45 (1976) 91.

[24] A.S. Van der Goot and K.H.J. Buschow, "*The dysprosium-iron system: Structural and magnetic properties of dysprosium-iron compounds*", J. Less-Common Met., 21 (1970) 151.

[25] E Scheil, Z. Metallkunde., 34 (1942) 70.

[26] D. J. Thoma, and J. H. Perepezko, , J. Alloys and Compd., *"A geometric analysis of solubility ranges in Laves phases",* 224 (1995) 330.

[27] J. H. Zhu and P. K. Liaw, L. M. Pike and C. T. Liu, Oak Ridge National Laboratory report No. ORNL/Sub/93-SP 173/03.

[28] J J Liu, W J Ren, D Li, N K Sun, X G Zhao, J Li, Z D Zhang, "*Magnetic transitions and magnetostrictive properties of $Tb_xDy_{1-x}(Fe_{0.8}Co_{0.2})_2$ (0.20<x<0.40"*, Phys. Rev. B, 75 (2007) 064429.

[29] V. Hari Babu, G. Markandeyulu, A. Subrahmanyam, "*Magnetostriction of $Tb_xHo_{0.75-x}Pr_{0.25}(Fe_{0.9}B_{0.1})_2$ (x=0–0.3) compounds",* J. Magn. Magn. Mater. 320 (2008) 990.

[30] M.S. Kumar, K.V. Reddy, K.V.S. RamaRao, *"A.c. magnetic susceptibility studies on the $Dy_{0.73}Tb_{0.27}Fe_{2-x}Ni_x$ and $Ho_{0.85}Tb_{0.15}Fe_{2-y}Ni_y$ intermetallics"***,** J. Alloys Compd. 242 (1996) 70.

[31] J.Arout Chelvane, G.Markandeyulu , N.HarishKumar, Ravi, R.Nirmala, S.K. Malik, "*Effect of Mn on the Magnetic and Electrical Properties of $Ho_{0.85}Tb_{0.15}Fe_2$",* IEEE Trans. Magn.42 (2006) 3117.

Chapter 4

Microstructure and texture of directionally solidified $Tb_{0.3}Dy_{0.7}Fe_{1.95}$ alloy prepared by modified Bridgman technique

4.1. Introduction:

Since the discovery of the anisotropy compensated giant magnetostrictive $Tb_{0.3}Dy_{0.7}Fe_{1.95}$, a substantial research has undergone for engineering the material to be suitable for transducer applications [1-3]. Achieving large magnetostriction in this compound at a small applied magnetic field essentially requires development of grains orientated closer to easy magnetization direction (EMD) <111>, by adopting directional solidification (DS) techniques. In order to develop grain orientation in the cylindrical rods of this material; methods such as zone melting (for dia ≤ 8 mm) and modified Bridgman (for dia. ≥10 mm) are adopted [4-8]. The processing parameters such as temperature gradient (G) and solidification rate (v) have profound influence on the post solidification microstructure and evolution of texture. Although several reports are available on directional solidification of Tb-Dy-Fe alloys [4-15], very few attempts [11-14] are noticed, that address the mechanisms of formation of different microstructural features and evolution of different texture components during directional solidification.

The evolution of texture as a function of solidification parameters is of interest to the research community for quite a sometime and as a result there are several proposed models for orientation selection. Tiller [16] proposed that in case of a planar growth the presence of grain boundary groove leads to a competitive lateral growth of the neighboring grains resulting in the evolution of a preferred orientation. However, it was also proposed that a solute enrichment at the interface will destroy such a grain boundary groove effect, and therefore lead to no preferred direction for an alloy under planar growth. Thus, orientation selection in the present study cannot be explained using this principle. Jackson considered the micro-topography of solid-liquid interface [17-19] and proposed that the growth of facets with different orientation is

controlled by a parameter $\alpha = (L_O/ kT)(\eta_1/ v)$ [19]. In a different approach Cahn [20] proposed that the growth of a particular orientation is controlled by lateral propagation of steps.

The previous literature [4-15] available on directional solidification of Tb-Dy-Fe alloys could not explicitly identify the orientation selection mechanisms. Further, the experimental technique used in most of the previous reports is zone melting, where the observed solidification morphology is generally cellular/ dendritic. However, fewer reports [9-15] are available in the literature that presents the study on directionally grown alloy by Bridgman technique. Most of the Bridgman grown samples except a few [14-15], exhibit plane front growth but the mechanism of evolution of growth texture for such plane front growth is not well studied. However, understanding the evolution of growth texture in a sample grown by Bridgman technique is of utmost practical importance as this technique is used to grow larger diameter rods required for transducer applications. Therefore, a study has been taken up to directionally solidify $Tb_{0.3}Dy_{0.7}Fe_{1.95}$ alloy in larger diameter (15 mm dia.) and develop an understanding on the evolution of texture as a function of solidification rate. The samples were directionally grown at wide range of growth rates 5-100 cm/h, under a temperature gradient of ~150^oC/ cm. Incidentally, the technique used in this study also offers high temperature gradient so that a high G/v value can be obtained for morphological stability of $(Tb,Dy)Fe_2$ so that orientation selection for plane front growth can be studied.

The alloy selected for the present study undergoes a peritectic reaction of $L+(Tb,Dy)Fe_3 \rightarrow (Tb,Dy)Fe_2$. The microstructural pattern formation during directional solidification of peritectic alloys is quite diverse and of research interest for last several years [21-33]. Prediction of phase and microstructure selection in these systems has been traditionally based on heterogeneous nucleation on a static interface or by comparing the relative growth rate of different phases/microstructures under steady-state growth conditions [27-33]. However, the actual selection process is more complex due to interaction between fresh nucleation and the growth competition between the pre-existing phases under non-steady-state conditions. As a result, a wide variety of microstructure can form involving pro-peritectic and

peritectic product phases. The existing literatures [28-33] indicate that depending on process conditions (G/v), initial alloy composition and sample diameter one can observe one of the following types of microstructural patterns: (i) discrete bands, (ii) partial bands, (iii) single band, (iv) oscillating structures, (v) coupled growth and (vi) dispersed phase through the nucleation ahead of the interface. Therefore, it is of utmost interest to investigate the formation of different microstructural pattern in peritectic $Tb_{0.3}Dy_{0.7}Fe_{1.95}$ alloy. Further, since the application of this material requires it to be produced in larger diameter, the microstructural evolution may be more complicated under the influence of convection, which may lead to formation of complicated features such as oscillatory pattern or tree-like structure [32-33]. Since, the pro-peritectic phase has been found to adversely affect the magnetostrictive property [6,9-10], the study on formation of microstructure in large diameter sample under different growth conditions is important in view of applications. Therefore, apart from orientation selection, the present study also aims to understand the microstructure formation in $Tb_{0.3}Dy_{0.7}Fe_{1.95}$ alloy grown by modified Bridgman technique with different growth rates ranging from 5-100 cm/h. The consequential effect of microstructural features and the growth texture on magnetostriction have also been discussed in this chapter.

4.2. Experimental details:

4.2.1. Directional solidification by Bridgman technique:

$Tb_{0.3}Dy_{0.7}Fe_{1.95}$ alloy was prepared by vacuum induction melting the constituent elements (of purity >99.5%) in a recrystallized alumina crucible under a vacuum of 5×10^{-5} mbar. The vacuum furnace of the make of M/s Consarc, UK (Fig. 3.1) was used for this purpose. The molten alloy was then subsequently cast into quartz tube moulds in the form of 15 mm ϕ and 80 mm long cylindrical rods. The rods were then directionally solidified by modified Bridgman technique.

The modified Bridgman setup (make M/s Hind Hi Vacuum, India) used for the present study is shown in Fig. 4.1a. A sectional view of the same equipment is shown in Fig. 4.1b. The modified Bridgman setup is having two zones (i) the melting chamber consisting of three independently controllable hot zones and (ii) the solidification chamber. The furnace is of resistance heating type with Molybdenum

wire mesh as heating in top two zones and Tungsten wire mesh as heating element in the third zone at the bottom. A stack of Mo sheets bent in cylindrical fashion fixed below the third hot zone, which acts as radiation baffle and thereby prevents heat dissipation from melting chamber to the solidification chamber.

The chill plate is initially placed at a position where its top surface stays just below the third hot zone but within the enclosure of radiation baffle. The chill plate has a groove (Fig. 4.2a) so that quartz tube mold can be firmly fixed inside the groove so that the quartz tube does not move during travel down of the chill plate. The vacuum induction melted cylindrical rods were placed inside the quartz tube during directional solidification. The chill plate is internally cooled by chilled water to impart desired directional cooling of the sample. In order to protect the chill plate being heated up by thermal radiation from the hot zones, stack of Mo rings were fixed on the bare top surface of the chill plate (Fig. 4.2b). During the experiments, the cylindrical rods of $Tb_{0.}Dy_{0.7}Fe_{1.95}$ kept inside quartz tube mold were melted and the chill plate along with molten alloy inside the quartz tube was moved down to solidification chamber at predefined rates. In the current study experiments were carried out using a set of pulling speed varying from 5 cm/h to 100 cm/h.

The chill plate can efficiently extract heat from the liquid in contact with it and any further heat extraction occurs through the already solidified portion of the rod. Therefore, an efficient auxiliary cooling is essential to cool the already solidified hot portion of the rod, so that heat extraction through it becomes efficient and thereby high thermal gradient across solid-liquid interface can be maintained throughout directional solidification process. The solidification chamber has the provision of auxiliary cooling. The experimental setup used for the present study is having a two stage auxiliary cooling (i) by water cooled Cu coil through which the chill plated with sample travels down and (ii) by impinging Argon gas jet on the surface of the hot solid. The highest temperature gradient obtained during the process is $150^{o}C$/ cm.

4.2.2. Characterization of microstructure and magnetic properties:

The microstructural features of the transverse and longitudinal sections of the zoned samples were investigated using a FEI Quanta 400 E-SEM scanning electron microscope (SEM). The phases were identified by EDS analysis of the back scattered

electron (BSE) image. Some detailed micro-chemical analysis was also carried out using WDS detector of EPMA of make M/s CAMECA.

Room temperature static magnetostriction was measured under dc magnetic field using field compensated resistance strain gauges as described in section 3.2.3.

4.2.3. Characterization of texture:

The evolution of texture during directional solidification at different rates was further characterized using texture goniometer. An Inel XRG 3000 diffractometer coupled with curved 'position sensitive detector' was employed for this purpose. In a texture goniometer the sample is rotated along two axes (i) around the normal direction of the sample (ϕ) and (ii) around transverse direction (χ). The schematic of the rotation is shown in Figure 4.3. A continuous translational motion is given to the sample for better sampling. The orientation was characterized by obtaining incomplete experimental pole figures. It is to be noted that all the specimens revealed triclinic sample symmetry due to large grain size effect and therefore, incomplete experimental pole figures have been utilized for the analysis. The pole figure of a (hkl) plane essentially indicates the plot of iso-intensity contours in (χ,ϕ) space. The pole figures were analysed using LABOTEX® software for identification of various texture components. Since, in a single pole figure all the components may not appear, a set of three pole figures *viz.* (220), (311) and (422) were generated for each sample.

4.3. Results and discussion

4.3.1. Microstructural features:

The BSE image of the longitudinal section of the sample directionally grown at 5 cm/h is shown in Fig. 4.4. The micrograph depicts plane front solidification of peritectic product phase (Tb,Dy)Fe_2 and discrete appearance of blocky pro-peritectic (Tb,Dy)Fe_3 phase present occasionally in some regions. The micrograph otherwise is free from (Tb,Dy)Fe_3. When the growth rate is increased to 10 cm/h, absence of pro-peritectic phase is observed (Fig. 4.5) in the bottom portion (closer to chilled end). However, after certain distance from chilled end, the pro-peritectic phase starts appearing as islands oriented perpendicular to growth direction (Fig. 4.5). Further,

away from the chilled end, the pro-peritectic phase is found to be formed parallel to the growth direction (Fig. 4.5), which is akin to the peritectic coupled growth morphology reported for Fe-Ni alloy [29-31]. The appearance of peritectic coupled growth (PCG) becomes much more prominent with increase of growth rate to 20 cm/h (Fig. 4.6). The coupled growth in this case also is found to be initiated from the $(Tb,Dy)Fe_3$ islands that formed perpendicular to growth direction. However, the PCG observed in this case is irregular in nature as compared to regular alternate lamellae of peritectic and pro-peritectic phases reported for other peritectic alloy systems [22, 28-31]. The similar solidification morphology is found persistent till the growth rate of 90 cm/h (Figs. 4.7 and 4.8). The growing lamellae of $(Tb,Dy)Fe_3$ phase are more dispersed in case of samples grown at 80 and 90 cm/h compared to the lamellae observed at 20-70 cm/h. The solidification morphology of $(Tb,Dy)Fe_2$ is found to be planar in the samples grown at 5-80 cm/h. However, in the sample grown at 90 cm/h, one can notice presence of occasional instabilities, which is indicated as small black arrows in Figure 4.8. The growth morphology of $(Tb,Dy)Fe_2$ changes to cellular when the growth rate is increased to 100 cm/h (Fig. 4.9). The pro-peritectic phase is also found absent in this sample. A solid solution of Tb and Dy is found to be distributed along the intercellular boundaries, which is depicted as bright phase in the micrograph (Fig. 4.9). The solid-solution is a product of a divorced eutectic reaction [$L \rightarrow$ (Tb,Dy)-solid solution + $(Tb,Dy)Fe_2$], that the last solidified liquid at the intercellular region undergoes. The micro-chemical analyses of the cell and intercellular boundary have been carried out by EPMA and the line profile of composition across a cell is shown in Figure 4.10. The line profiles as well as the elemental mapping (Fig. 4.11) indicate complete absence of Fe in the intercellular region. It is also evident from the line profiles, that the interface between cell and the cell boundary is very sharp (Fig. 4.10).

The island like features observed in the samples grown at 10-90 cm/h and the blocky appearance of pro-peritectic phase observed in the sample grown at 5 cm/h, resemble with the island banding or discrete banding reported earlier [28-31]. This banding is essentially observed due to nucleation of one phase (peritectic product or pro-peritectic) ahead of other phase. The formation of such bands and their spacing are controlled by nucleation rate of the phases and growth conditions (G/v). It has

been demonstrated earlier by phase field modeling that such banding are observed either hypo-peritectic or hyper-peritectic composition range when solidification is carried out at lower G/v ratio [30-31]. The condition of band formation persists till both the phases are morphologically stable under the imposed value of G/v. Further, it has also been predicted from phase field simulations [30], that the island banding can lead to PCG, if the spacing between islands falls within the range of stable lamellar spacing for coupled growth. The present study indicates the condition for band formation exists for a wide range of growth rates (5-90cm/h) and in each case the island banding leads to PCG except for the sample grown at 5 cm/h. Since, the blocky islands of $(Tb,Dy)Fe_3$ formed in larger spacing in case of the sample grown at 5 cm/h, probably it does not lead to PCG. The island banding observed earlier in Fe-Ni alloy [29-30], persists for many alternate layers of peritectic and pro-peritectic phases before it leads to PCG. However, in this study the island banding only persists for only one or two layers and immediately it leads to PCG.

The morphology of the PCG observed in this study is irregular, which resembles the irregular eutectic coupled growth (ECG) observed in the directionally solidified Al-Si and Fe-C alloys [34-36]. In case of irregular eutectics, generally one of the growing phases is either an intermetallic compound or other covalently bonded phase (having high entropy of fusion), having strong anisotropy of growth along a particular direction. As a result, the regular lamellar eutectic growth is disrupted and irregular eutectic forms. In the present study also both the pro-peritectic phase [$(Tb,Dy)Fe_3$] and peritectic product phase [$(Tb,Dy)Fe_2$] are intermetallic phases. The $(Tb,Dy)Fe_2$ is cubic Laves phase (Space Group $Fd\bar{3}m$) and the pro-peritectic $(Tb,Dy)Fe_3$ is rhombohedral (space group $R\bar{3}m$). Thus irregular coupled growth morphology is observed instead of regular coupled growth with alternate lamellae of phases.

4.3.2. Texture studies:

The x-ray pole figures obtained from the directionally solidified rods that correspond to different pulling rates are shown in Figs. 4.12, 4.13 and 4.14. The

description of the texture components, as observed in (220), (422) and (311) pole figures is presented briefly as a function of pulling rates.

4.3.2.1. *Samples grown at 5-30 cm/h*:

The (311) pole figure (Fig. 4.12) of the sample grown at 5 cm/h exhibits a very strong intensity contour at the centre (χ=0), indicates presence of a strong <311> orientation in this directionally solidified sample. The presence of same component is also evident from the high intensity at χ=43.2^o and 10.6^o in (422) pole figure and at χ=32.8^o and 65.1^o in (220) pole figure (Fig. 4.12). This is in agreement with earlier report on texture evolution during directional solidification of Ho-Tb-Fe [37]. The <311> texture component is also observed as major component in case of the sample grown at 10 cm/h, however the observed intensity of this component is less compared to that of the sample grown at 5 cm/h. In both the cases (5 and 10 cm/h), the intensity of other components is very weak as compared to the major texture component <311>. Minor components such as <110> and <331> can be identified from low intensity contours observed in (220) and (422) pole figures (Fig. 4.12). Considering the fact that the texture may evolve within ±15^o from the geometric axis of the directionally solidified samples [38], the texture component <331>, which is ~13^o away from <110>, will be termed hereafter as 'rotated <110>'.

The <311> continues to be the major texture component in the sample gown at 20 cm/h. The intensity of this component is found to be less as compared to the intensity of same component observed in the samples directionally grown at the rate of 5 and 10 cm/h. In addition to <311> component, <110> and 'rotated <110>' components also become stronger at this growth rate. The <110> component is identified from the strong intensity locations at χ= 2.4^o and 60^o in (220) pole figure, at χ=52.8^o in (422) pole figure and at χ=65^o in (311) pole figure (Fig. 4.12). The 'rotated <110>' component is evident from the intensity contours at χ= 19^o in (422) pole figure and at χ= 40^o, 70^o and 77.2^o in (311) pole figure. Similar texture components are also observed in the sample grown at 30 cm/h (Fig. 4.12). In this sample all three major components *i.e.* <311>, <110> and 'rotated <110>' are observed in nearly similar intensity and a very weak <531> is observed as minor

texture component. The <531> component being 14° away from <112>, will be denoted hereafter as 'rotated <112>' texture component.

4.3.2.2. *Samples grown at 40-70 cm/h*:

The sample directionally solidified at 40 cm/h, exhibits presence of 'rotated <112>' texture component in addition to the <110>, 'rotated <110>' and <311> components which were observed in the samples solidified at 30 cm/h. The intensity of <110> and 'rotated <110>' components are more compared to other two components. The presence of <110> component is evident from the high intensity locations at χ=30.8°and 65.2° in (311) pole figure and at (χ,ϕ)=(29.7°, 197.9°) and (30, 186.8°) in (422) pole figure. The presence of 'rotated <110>' component is observed from the high intensity locations at (χ,ϕ)= (25.4°, 287.4°) and (23.8°, 165.2°) in (220) pole figure, χ= 43.2° in (311) pole figure and χ= 20.9° and 79.7° in (422) pole figure (Fig. 4.13). Similar texture components were observed for the sample solidified at 50 cm/h. However, the intensity of 'rotated <112>' component becomes dominant and the intensity of <110> component becomes subdued. The intensity of <331> and <311> component almost remain same as it was observed for the sample grown at 40 cm/h. The major component <531> is evident from the presence of the high intensity locations at χ= 19.1° and 77.2° in (220) pole figure, χ= 14.8° and 55.4° in (311) pole figure and at χ= 13.8° and 45.1° in (422) pole figure (Fig. 4.13).

The absence of <110> texture component, which is observed in the samples grown at lower rates is not observed in the sample grown at 60 cm/h. Instead, <112> texture component starts appearing in this growth rate. The other texture components observed in this sample are 'rotated <112>', 'rotated <110>'and <311>, amongst which the intensity of 'rotated <112>' is highest. The intensity of <112> and 'rotated <112>' texture components become more prominent when the growth rate is increased to 70 cm/h. The decrease in intensities of <110> and 'rotated <110>' components in the samples grown at 60 and 70 cm/h indicates clearly the transition of preferred growth direction to <112> with increase of growth rate.

4.3.2.3. *Samples grown at 80-100 cm/h*:

The pole figures of the sample grown at 80 cm/h exhibits that <112>emerges as prominent texture component along with 'rotated <112>'. The intensity of <311> texture component is reduced in this sample. The presence of <112> component is evident from the high intensity locations at $\chi = 54.6^{o}$ in (220) pole figure and at $\chi = 43.6^{o}$ in (311) pole figure (Fig. 4.14). The <112> and 'rotated <112>' components continue to be major texture components in the sample grown at 90 cm/h. The <311> component which is observed in all the samples grown at 5-80 cm/h is not seen in this sample. The intensity of the major texture component <112> becomes very strong as the growth rate is increased to 100 cm/h.

A summary of the texture components observed in different samples is presented in Table 4.1. It is observed from the table, that at lower growth rates <311> is the dominant texture components, which decreases in intensity as the growth rate increases and finally this component becomes absent as the growth rate increases beyond 80 cm/h. In the intermediate growth rate regime (20-40 cm/h), the <110> and 'rotated <110>' evolve as dominant texture component. With increase of growth rate <112> and 'rotated <112>' components evolve as dominant and the evolution of <110> and 'rotated <110>' become subdued. At high growth rate regime (70-100 cm/h), <112> texture component becomes dominant with its intensity becoming strong with increase of growth rate.

4.3.3. Orientation selection with growth rate:

The present study indicates formation of <311> as prominent texture component at lower growth rates (5 and 10 cm/h). The <311> component also remains as one of the major component over a wide range of solidification rate of 5-70 cm/h. It is interesting to note that in the present study the microstructure indicates plane front solidification of major phase $(Tb,Dy)Fe_2$ for a wide range of solidification rate. Since, in case of plane front growth, the solid-liquid interface is formed by the plane, normal to the growth direction and hence the orientation selection should occur based on atomic packing density of the plane normal to the growth direction. Therefore to understand the orientation selection, it is important to understand the atomic packing density of the individual planes facing liquid at planar interface.

It is observed that, the atomic packing density of {311} plane is 85%, which is higher than the atomic packing density of {110} (81%) and {112} (71%) planes respectively (Table 4.2). Therefore, the kinetics of atomic attachment to {311} plane is sluggish as compared to {110} and {112}. Thus, <311> is observed as favored texture component at lower growth rate which subsequently changes to <110> with increase of growth rate. However, for the sample solidified at 90 and 100 cm/h exhibits cellular solidification morphology and <112> is observed as dominant texture component.

The tendency to grow higher packing density at lower growth rate is owing to lower interfacial energy of solid-liquid interface formed by more closed packed plane. However, at higher growth rates less close packed planes form the solid-liquid interface due to ease of atomic attachment kinetics. It can be seen from Table 4.2, the {111} planes have still higher packing density (95%), compared to (311). Therefore it is expected that <111> should appear as preferred growth direction as the growth rate decreases. In fact, it has been demonstrated earlier [39], that $(Tb,Dy)Fe_2$ can be grown along <111> direction by using extremely slow crystal pulling rate in Czochralski method.

In order to understand the growth of <311> in preference to <111>, the stacking sequence of {311} planes has been studied and compared with that of {111}(Fig. 4.15). It is observed that all the layers in the stacking sequence of {311} planes are identical and having population of both rare earth and iron atoms (Fig. 4.15). Whereas, one of the layers in the stacking sequence of {111} planes consists of only Fe atoms (Fig. 4.15). Therefore, atomic attachment to {311} interface is kinetically more favorable as compared to {111} interface. Further, looking closely at (311) interface, it is observed that the interface can be resolved into two {111} type planes. Figure 4.16 shows a closer view of a typical (311) interface, which can be resolved into (111) and $(1\bar{1}\bar{1})$ planes. The (111) is of the type layer I (Fig. 4.15) of {111} planes, whereas $(1\bar{1}\bar{1})$ plane is of the type layer II (Fig. 4.15) of {111} planes. The (111) [type I] plane consists of 0.079 R (Tb and Dy) atoms and 0.036 Fe atoms per unit area, whereas the $(1\bar{1}\bar{1})$ [type II] plane consists of only 0.131 Fe atoms per unit area. Therefore, considering (111) and $(1\bar{1}\bar{1})$ planes together, the total number R atoms

per unit area is 0.079 and the total number Fe atoms per unit area is 0.167 (= 0.036+0.131). Therefore, in this configuration the ratio of total Fe/R atoms is approximately 2, which is closer to the nominal composition. The kinetics of this growth is faster in this configuration, where the atoms can be arranged simultaneously into two (111) type planes, where together the stoichiometric composition RFe_2 is maintained. Therefore, by simultaneous atomic attachment to two different types of {111} planes can result into formation of {311} planar solid-liquid interface. In case of plane front growth {111}, the kinetics is sluggish as the layers of two different types (i) mixed population of R and Fe and (ii) Only Fe atoms have to be grown, which inhibits faster growth. Therefore, even at slowest growth rate adopted in this study, <311> is observed as preferred grain orientation in stead of <111>. However, if sufficient time be allowed for sluggish {111} planar growth, it may be possible to obtain <111> growth texture, as observed earlier [39] by slow crystal pulling in Czochralski technique.

4.3.4. Magnetostriction:

The magnetostriction of the DS samples was measured under static magnetic field. The magnetostriction at an applied field of 5kOe is plotted as a function of solidification rate in Figure 4.17. The figure indicates that the magnetostriction of most of the sample falls in the range of 1250-1300 microstrains. The sample grown at 100 cm/h however exhibits a large improvement in magnetostriction (1400 microstrains) owing to absence of pro-peritectic $(Tb,Dy)Fe_3$ phase. The initial slopes of the magnetostriction curve ($d\lambda/ dH$), known as static strain co-efficient, are shown in Figure 4.18a and the slope values are plotted in Figure 4.18b as a function of solidification rate. The static strain co-efficient is generally governed by three factors (i) presence/ absence of $(Tb,Dy)Fe_3$ (ii) Texture and (iii) magneto-crystalline anisotropy. Since, all the solidification experiments were carried out with alloy of same composition; the effect of magneto-crystalline anisotropy can be neglected. The sample grown at 100 cm/h only exhibits complete absence of $(Tb,Dy)Fe_3$, accordingly this sample exhibits highest slope. However, there is a considerable variation in the value of static strain co-efficient for the samples grown at other solidification rates. Since, all those samples exhibits presence of $(Tb,Dy)Fe_3$ phase,

the variation in slope is attributed to presence of different texture components in different samples.

In order to understand the variation in static strain co-efficient, the texture components observed in different samples have been plotted on a quadrant of (111) stereogram (Fig. 4.19). Since, <111> is the easy magnetization direction (EMD) of $(Tb,Dy)Fe_2$, the plot on (111) stereogram (Fig. 4.19) clearly depicts the deviation of different texture components from EMD. The minimum angles between EMD and different texture components are also presented in Table 4.3. The slope is found to be more for the samples having texture component more close to EMD. Therefore, the slope is highest for the sample solidified at 100 cm/h, owing to presence of strong <112> texture components which is only 19^o away from EMD. The slope should decrease due to presence of <331>, <531>, <311> and <110> components, which are more deviated from EMD than <112>. Accordingly, the static strain co-efficient values of the sample grown at 5 and 10 cm/h are more compared to 20 and 30 cm/h owing to presence of <311> (30^o away from EMD) as major texture component in first two samples as compare to presence of <110> texture component (35^o away from EMD) in later cases (Fig. 4.19, Table 4.3). With further increase of pulling rate <110> component becomes subdued and 'rotated <112>' and <112> component becomes dominant and as a result the static strain co-efficient increases.

4.4. Summary and conclusions:

The $Tb_{0.3}Dy_{0.7}Fe_{1.95}$ alloy was directionally solidified by modified Bridgman technique at different pulling rates ranging from 5 cm/h to 100 cm/h. The evolution of microstructure and texture with increase of growth rate has been studied and correlated with magnetostriction.

The microstructure of the directionally grown sample exhibits planar solidification morphology of $(Tb,Dy)Fe_2$ phase for a wide range of solidification rate (5-80 cm/h). Occasionally morphological instability is observed for the sample directionally solidified at 90 cm/h. However, complete cellular instability is observed in case of the sample directionally grown at 100 cm/h. Presence of (Tb,Dy)-solid solution is observed at the intercellular boundary of $(Tb,Dy)Fe_2$ phase in the sample

grown at 100 cm/h. Samples grown at 5-90 cm/h also exhibits presence of islands / discrete bands of pro-peritectic $(Tb,Dy)Fe_3$ phase, towards the chilled end of the sample. As the distance from the chilled end increases, the islands of $(Tb,Dy)Fe_3$ subsequently transforms into coupled growth of $(Tb,Dy)Fe_3$ and $(Tb,Dy)Fe_2$ phases. The coupled growth is not observed in the sample grown at 5 cm/h and is prominently observed for the samples grown at 20-90 cm/h. The growing lamellae of $(Tb,Dy)Fe_3$ phase are more dispersed in case of samples grown at 80 and 90 cm/h compared to the lamellae observed at 20-70 cm/h. The coupled growth observed in this study is irregular in nature and this is attributed to high growth anisotropy of both the growing intermetallic phases along particular direction.

The texture study using x-ray goniometer indicates at lower growth rates (5 and 10 cm/h) <311> is the dominant texture components, which decreases in intensity as the growth rate increases and finally this component becomes absent as the growth rate increases beyond 80 cm/h. In the intermediate growth rate regime (20-40 cm/h), the <110> and 'rotated <110>' evolve as dominant texture component. With increase of growth rate <112> and 'rotated <112>' components evolve as dominant and the evolution of <110> and 'rotated <110>' become subdued. At high growth rate regime (70-100 cm/h), <112> texture component becomes dominant with its intensity becoming strong with increase of growth rate.

The orientation selection with growth rate has been analyzed in the light of atomic attachment kinetics to the solid-liquid interface. The interface being planar for most of the growth rates (5-80 cm/h), the atomic attachment depends on atomic packing fraction of the plane in contact with liquid at solid-liquid interface. Therefore, {311} type planes being more close packed compared to {110} and {112} planes, the atomic attachment to {311} planes is expected to be sluggish compared to {110} and {112} planes. As a result, <311> evolves as dominant texture component as lower growth rates, which subsequently changes to <110> at intermediate growth rate regime and to <112> at higher growth rate regime. The close packed {311} planes also form solid-liquid interface of lower energy leading to favorable growth of <311> texture at lower solidification rates. Although, {111} planes are more close packed than {311}, the growth of <111> texture could not be observed even at slowest growth rate. In order to understand this, the atomic configuration of {311}

planes have been studied. It is observed that, {311} planes can be resolved into two different types of {111} planes, where atomic attachment can occur simultaneously. In case of plane front growth {111}, the kinetics is sluggish as the layers of two different types of stacks have to be grown, which inhibits faster growth. Therefore, even at slowest growth rate adopted in this study, <311> is observed as preferred grain orientation instead of <111>.

The sample solidified at 100 cm/h exhibits highest magnetostriction (1400 microstrains at 5 kOe), which is attributed to a microstructure devoid of detrimental $(Tb,Dy)Fe_3$. The magnetostriction of other samples are within a band of 1250-1300 microstrains (at 5 kOe), although a substantial variation in static strain co-efficient is observed amongst different samples. The static strain co-efficient values of the sample grown at 5 and 10 cm/h are more compared to 20 and 30 cm/h owing to presence of <311> (30^o away from EMD) as major texture component in first two samples as compare to presence of <110> texture component (35^o away from EMD) in later cases. With further increase of pulling rate <110> component becomes subdued and 'rotated <112>' and <112> (19^o away from EMD) component becomes dominant and as a result the static strain co-efficient increases.

Table 4.1: Major texture components observed in the samples directionally grown at different rates

Growth rate	Major texture components
5 cm/h	<311>
10 cm/h	<311>
20 cm/h	<311>, <110> , 'rotated <110>'
30 cm/h	<110>, 'rotated <110>', <311>
40 cm/h	<110>, 'rotated <110>', 'rotated <112>', <311>
50 cm/h	'rotated <112>', <110>, <311>, 'rotated <110>'
60 cm/h	'rotated <112>', <112>, <311>, <110>
70 cm/h	'rotated <112>', <112>, <311>
80 cm/h	'rotated <112>', <112>
90 cm/h	<112>, 'rotated <112>'
100 cm/h	<112>, 'rotated <112>'

Table 4.2: The planar packing density for different planes of C15 Laves phase $(Tb,Dy)Fe_2$.

Planes	Planar packing density
{111}	95 %
{311}	89%
{110}	81 %
{100}	78 %
{112}	71 %

Table 4.3: Minimum **a**ngles between major texture components and easy magnetization direction (EMD)

Texture Components	Minimum angle with EMD
<112>	19^o
'rotated <110>'	22^o
'rotated <112>'	28^o
<311>	30^o
<110>	35^o

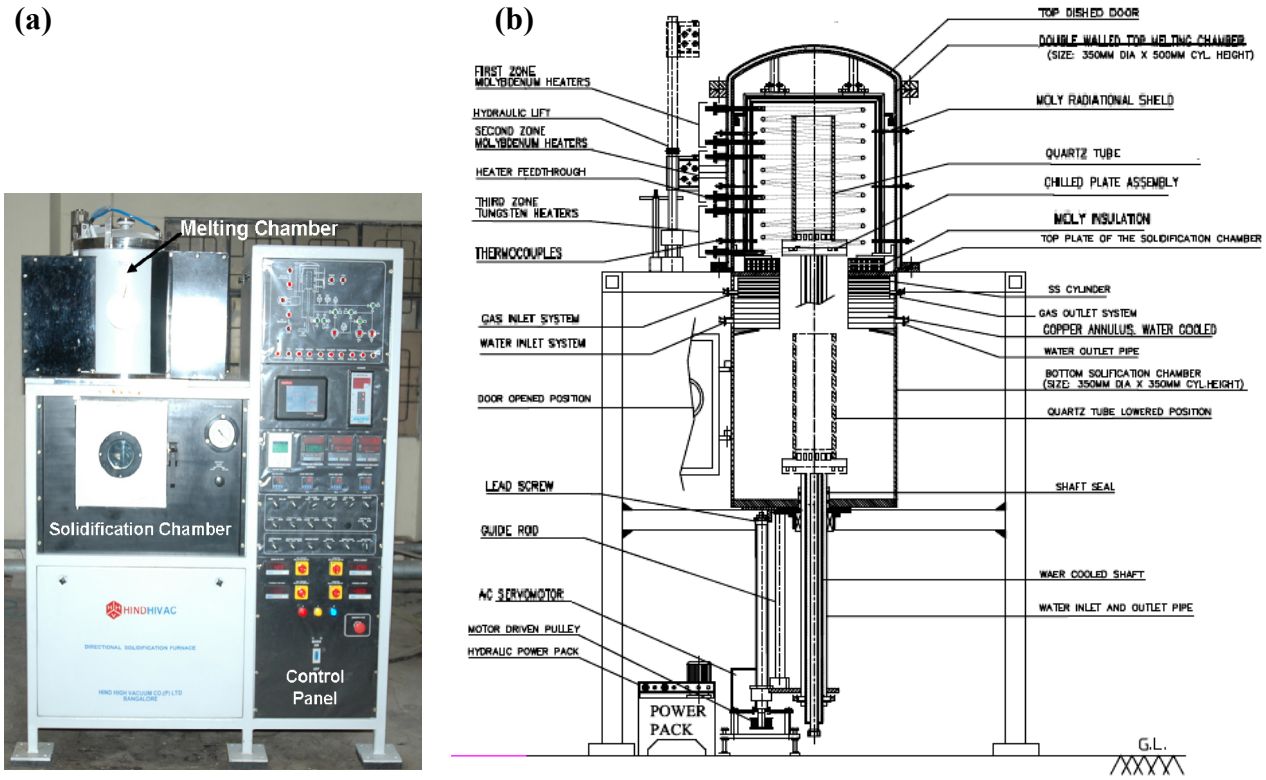

Figure 4.1: (a) The modified Bridgman furnace (make M/s Hind High Vacuum) used for directional solidification experiments and (b) the sectional view of the furnace

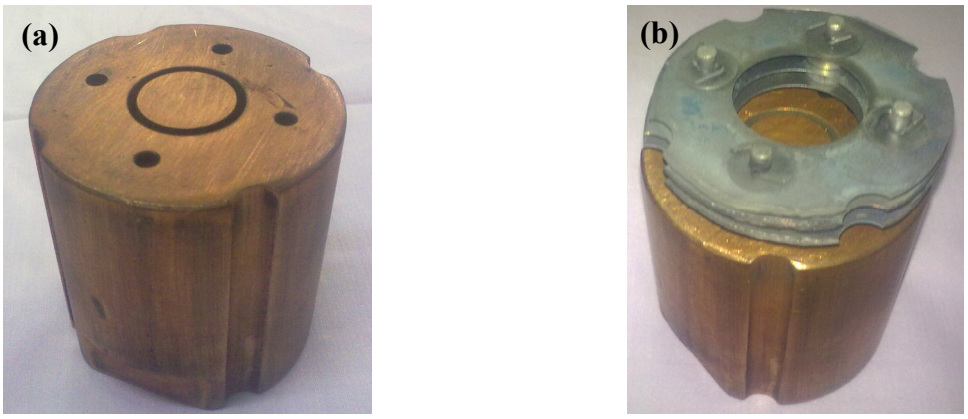

Figure 4.2: (a) The Cu-chill plate used for directional solidification experiments and (b) Mo shields used to protect the chill plate being heated up by radiation.

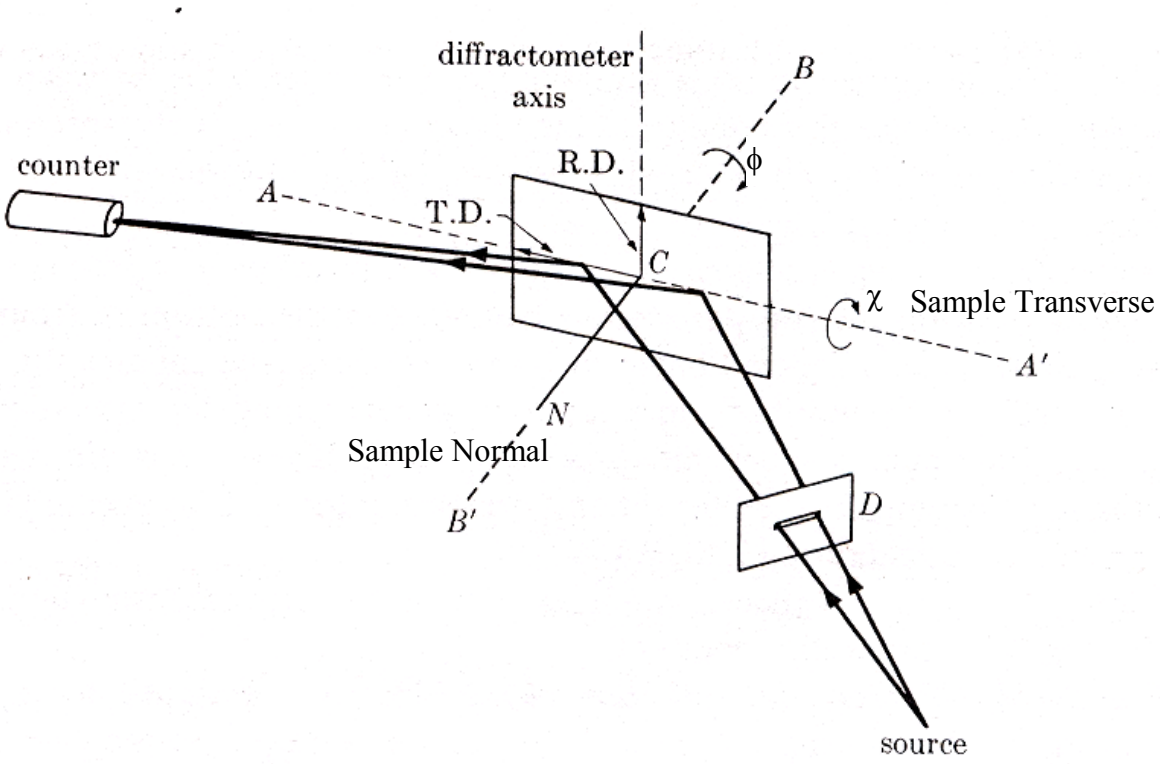

Figure 4.3: Schematic sketch of rotation given to the sample during texture study using texture goniometer.

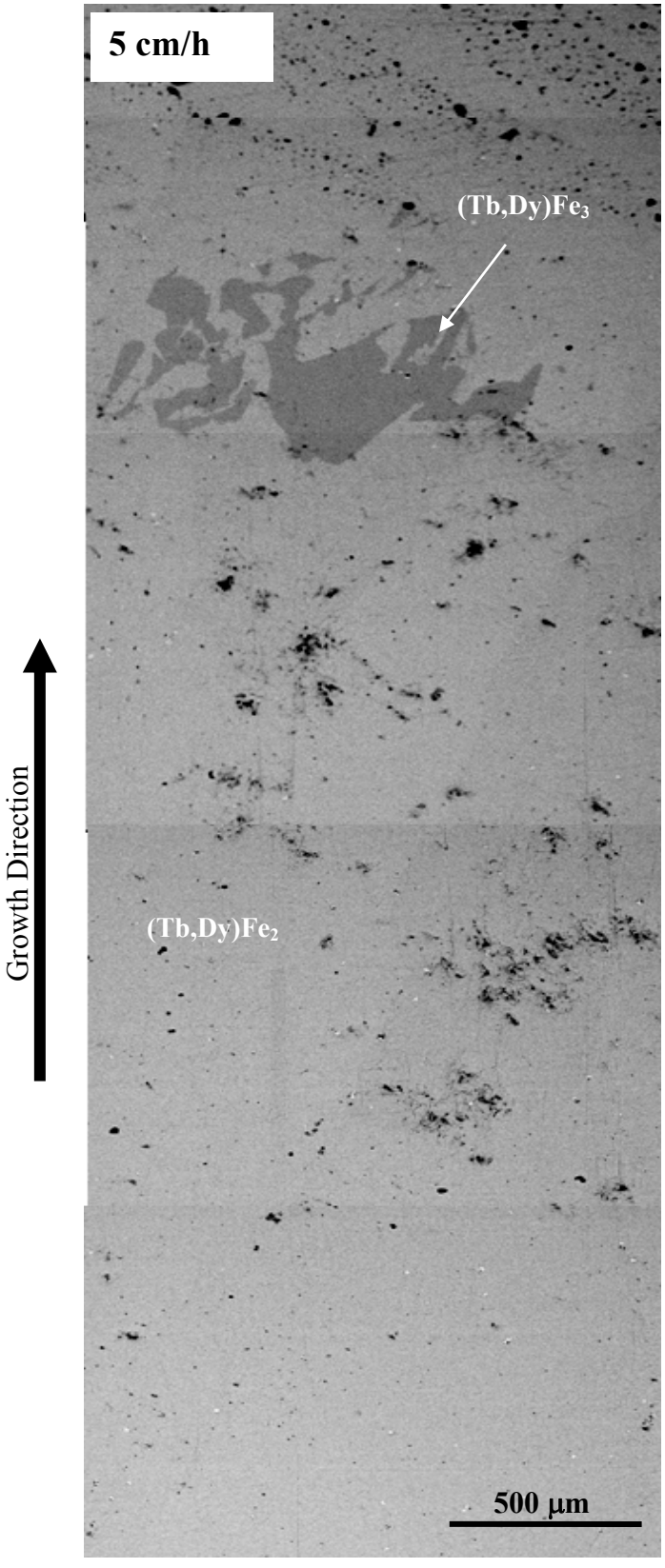

Figure 4.4: The microstructure of the longitudinal section of the sample directionally grown at 5 cm/h depicting blocky appearance of pro-peritectic $(Tb,Dy)Fe_3$ phase.

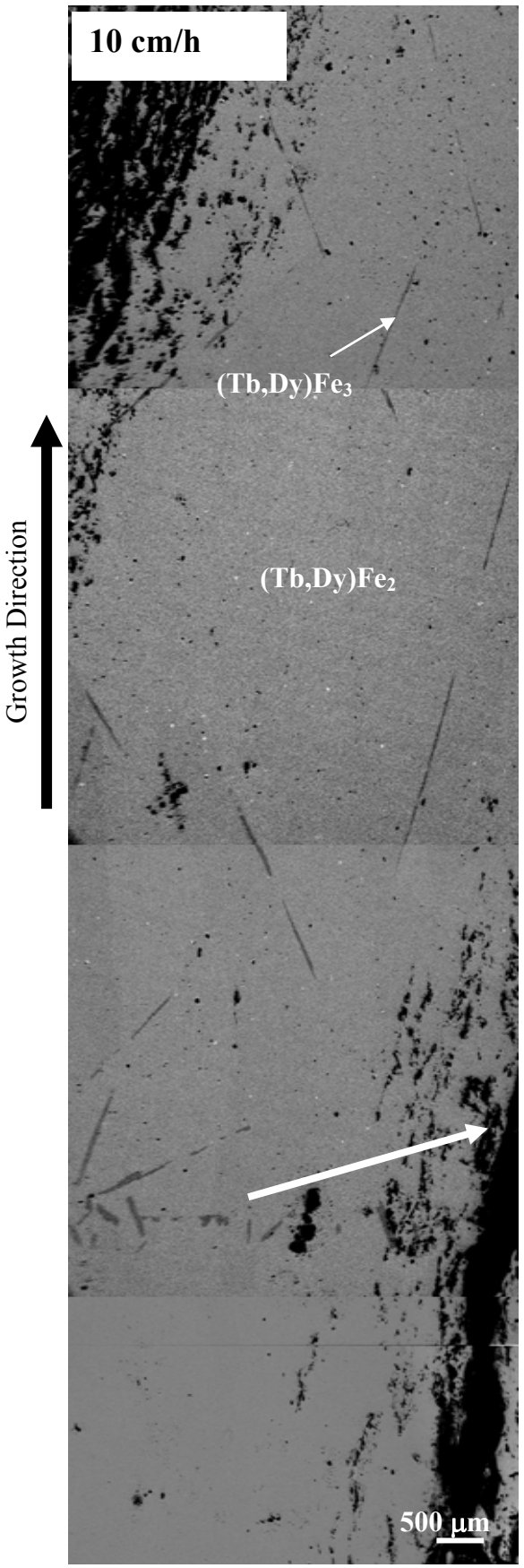

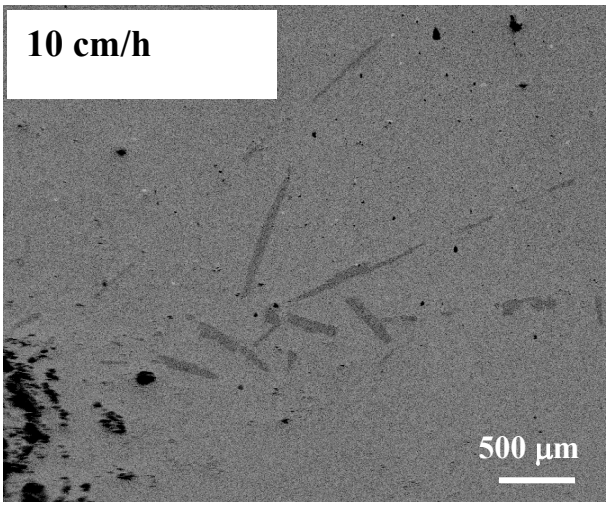

Figure 4.5: The microstructure of the longitudinal section of the sample directionally grown at 10 cm/h depicting islands of $(Tb,Dy)Fe_3$ and initiation of PCG.

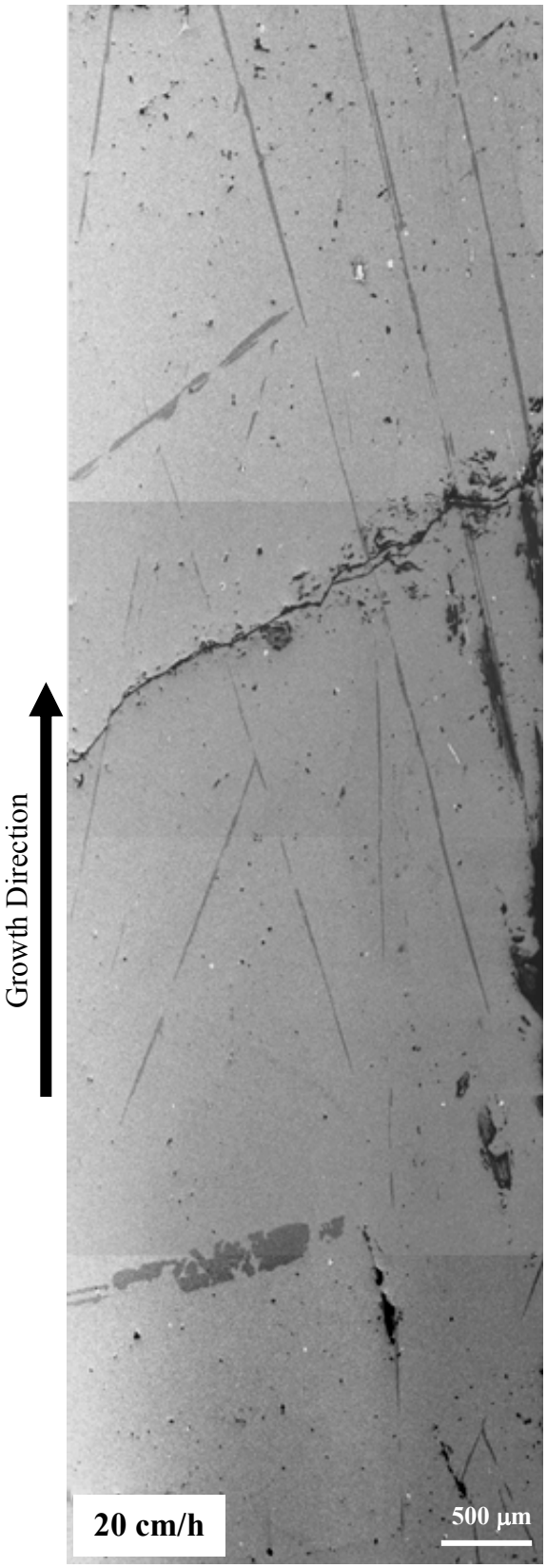

Figure 4.6: The microstructure of the longitudinal section of the sample directionally grown at 20 cm/h depicting band formation and dominant coupled growth morphology.

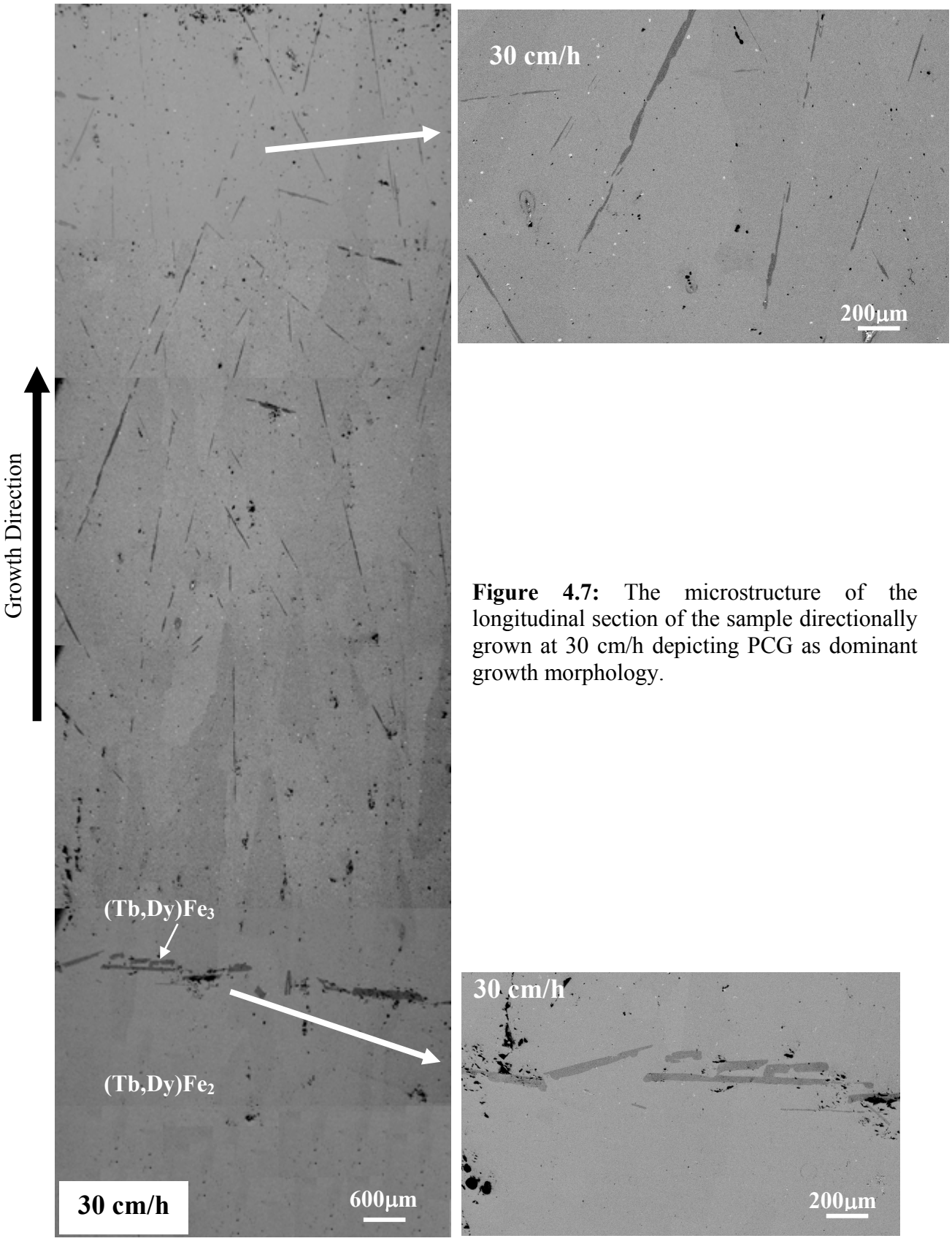

Figure 4.7: The microstructure of the longitudinal section of the sample directionally grown at 30 cm/h depicting PCG as dominant growth morphology.

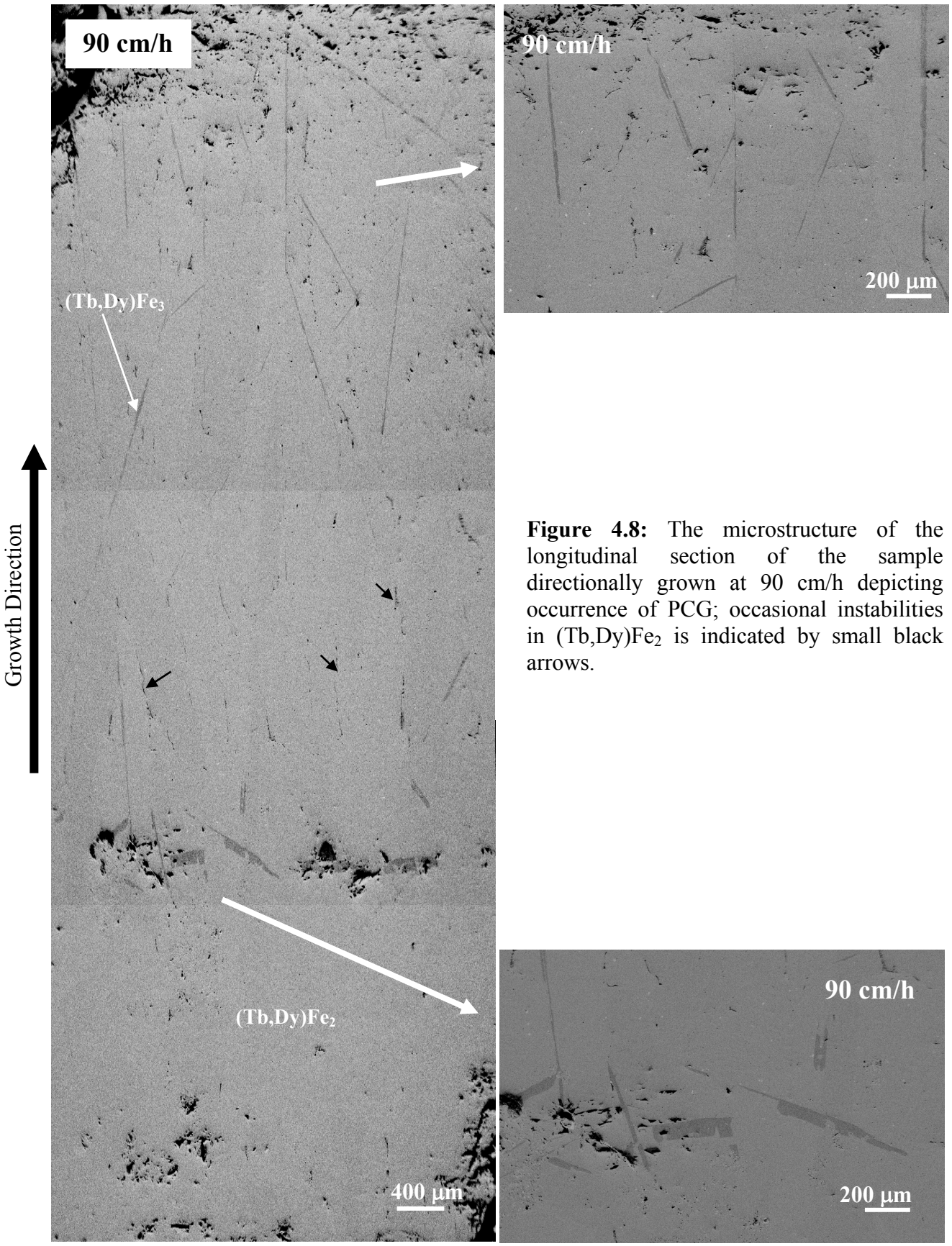

Figure 4.8: The microstructure of the longitudinal section of the sample directionally grown at 90 cm/h depicting occurrence of PCG; occasional instabilities in $(Tb,Dy)Fe_2$ is indicated by small black arrows.

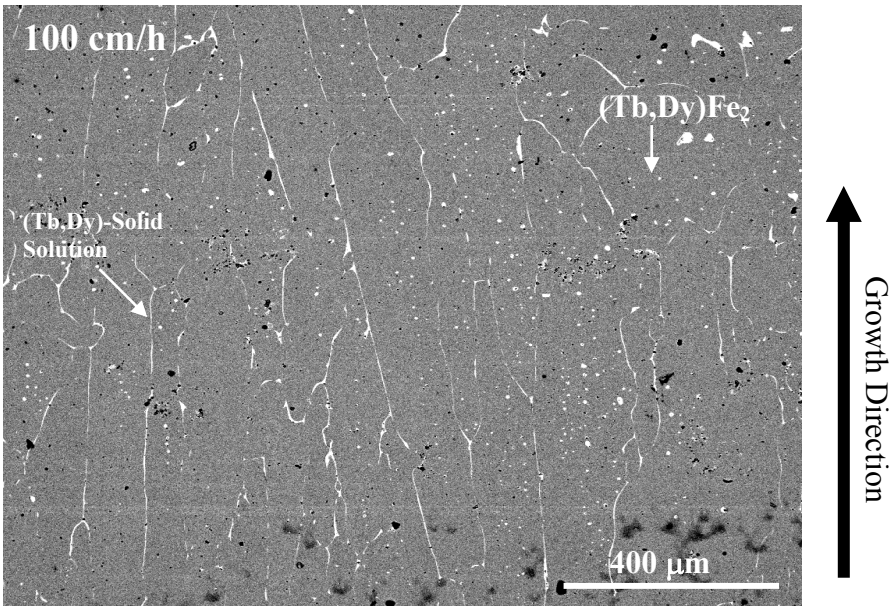

Figure 4.9: The microstructure of the longitudinal section of the sample directionally grown at 100 cm/h indicating cellular solidification morphology of $(Tb,Dy)Fe_2$.

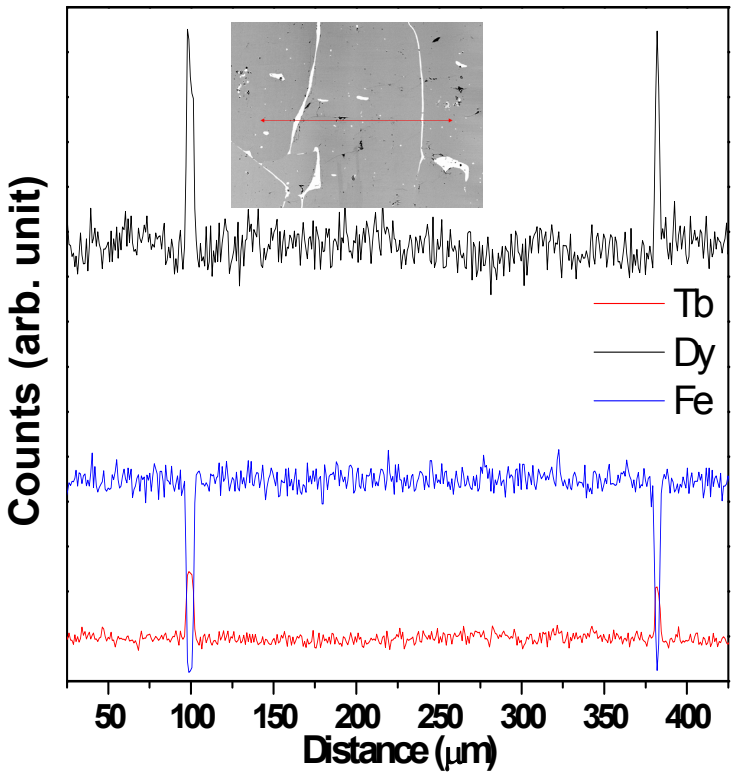

Figure 4.10: The plot of elemental composition (determined by EPMA analysis) across the cell and cell boundaries in the sample directionally grown at 100 cm/h.

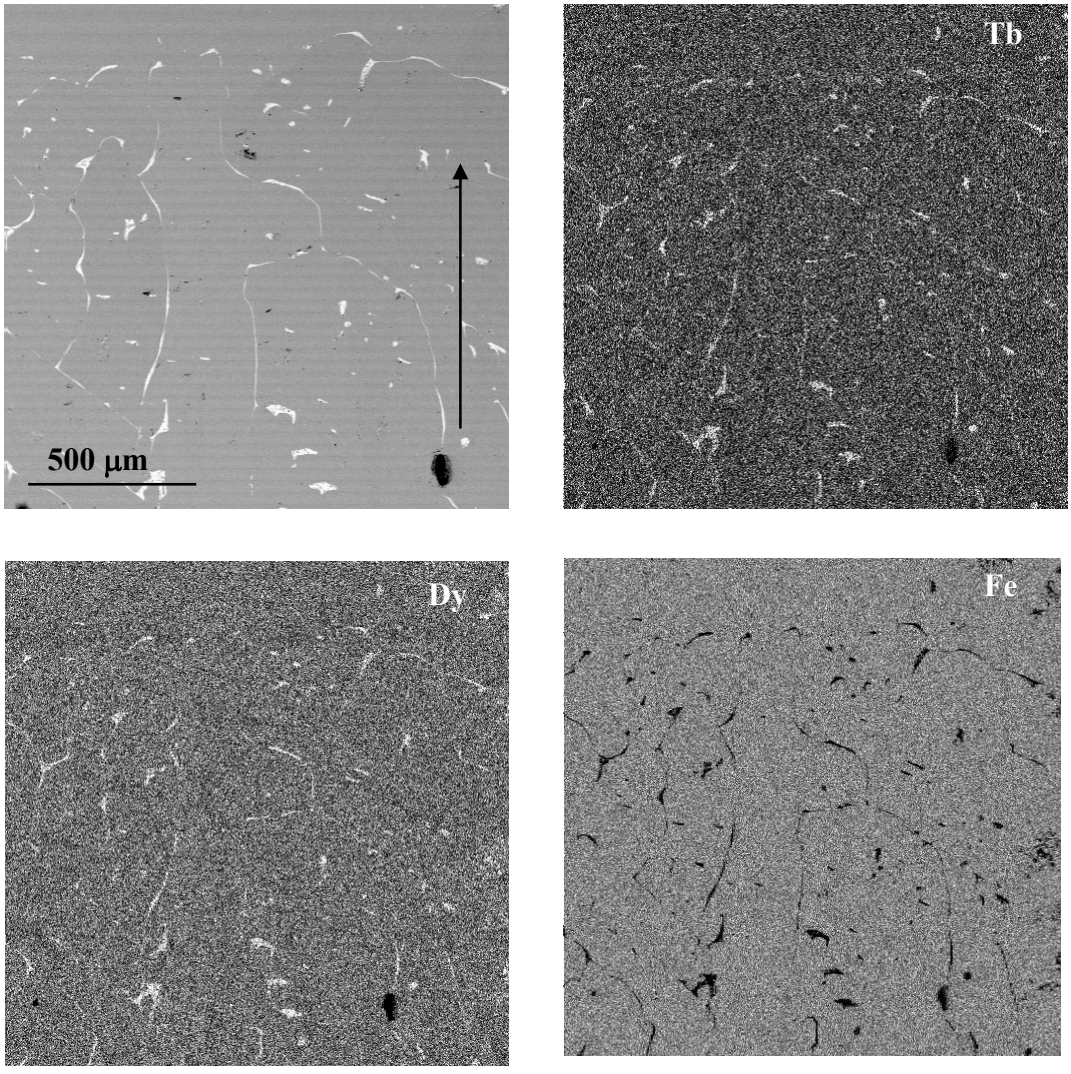

Figure 4.11: Elemental mappings of Tb, Dy and Fe on micrograph of BSE image of longitudinal section of the sample directionally grown at 100 cm/h (arrow indicates growth direction).

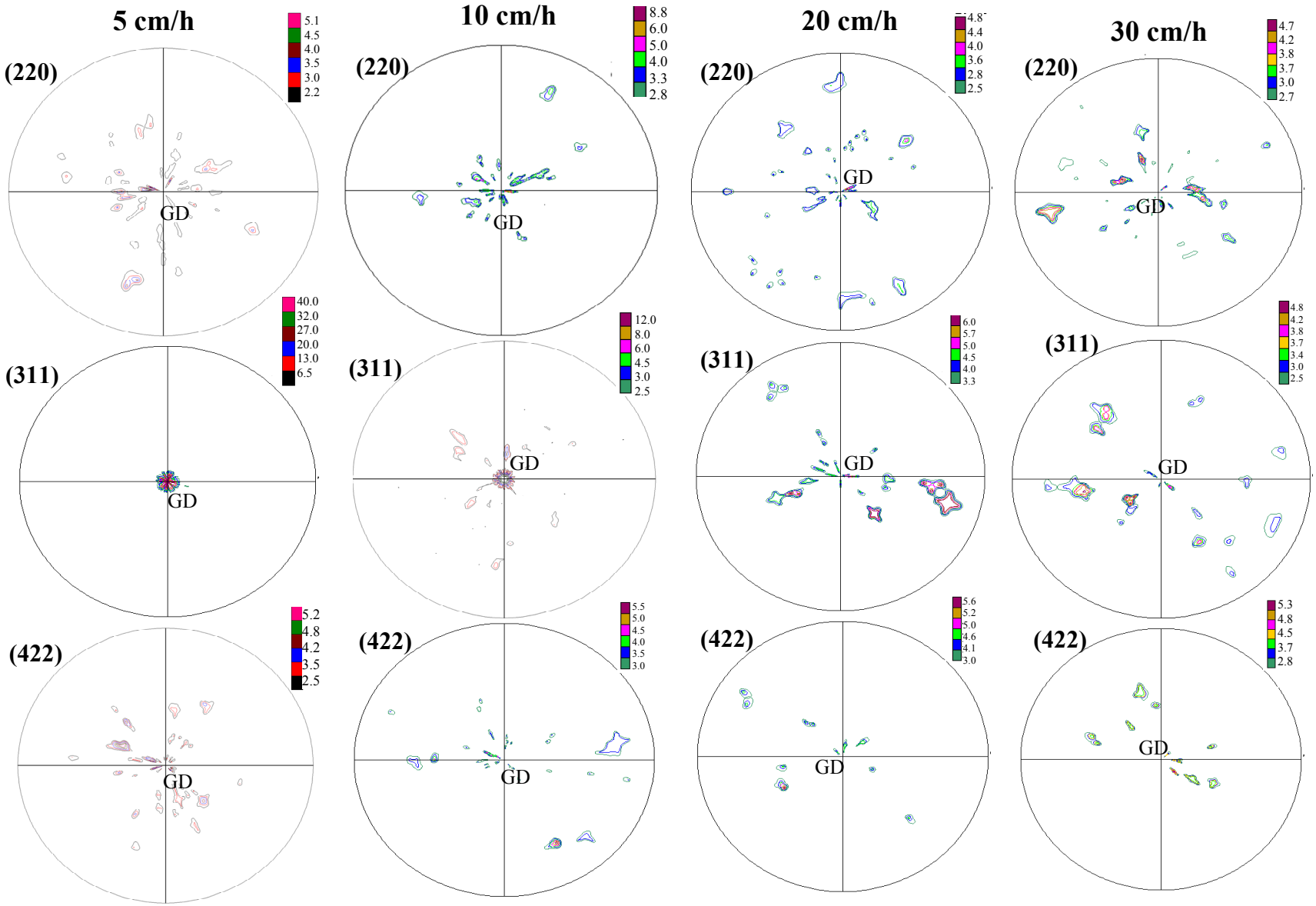

Figure 4.12: (220), (311) and (422) pole figures taken on the transverse sections of the sample grown at 5, 10, 20 and 30 cm/h. [GD indicates direction of growth]

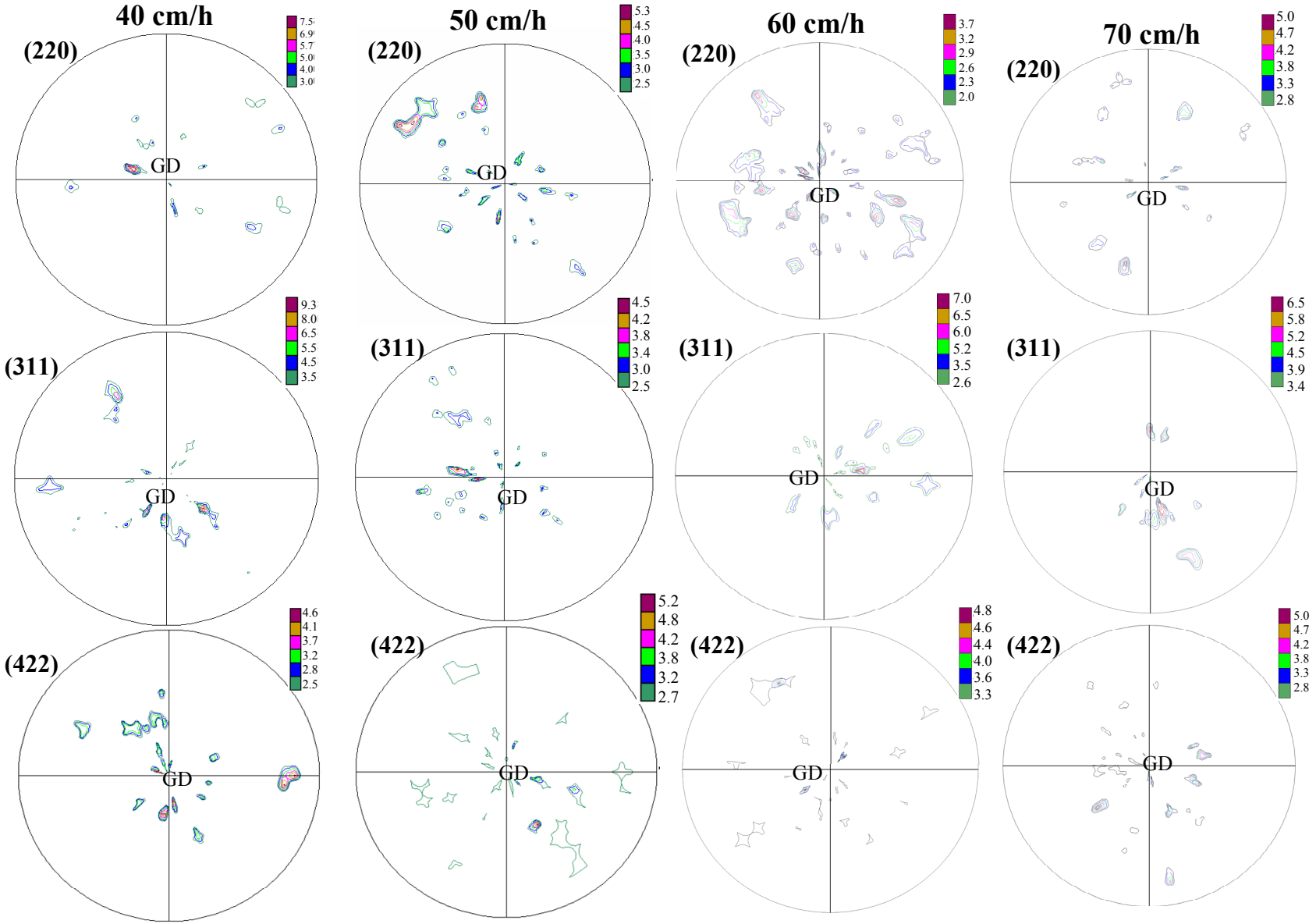

Figure 4.13: (220), (311) and (422) pole figures taken on the transverse sections of the sample grown at 40, 50, 60 and 70 cm/h. [GD indicates direction of growth]

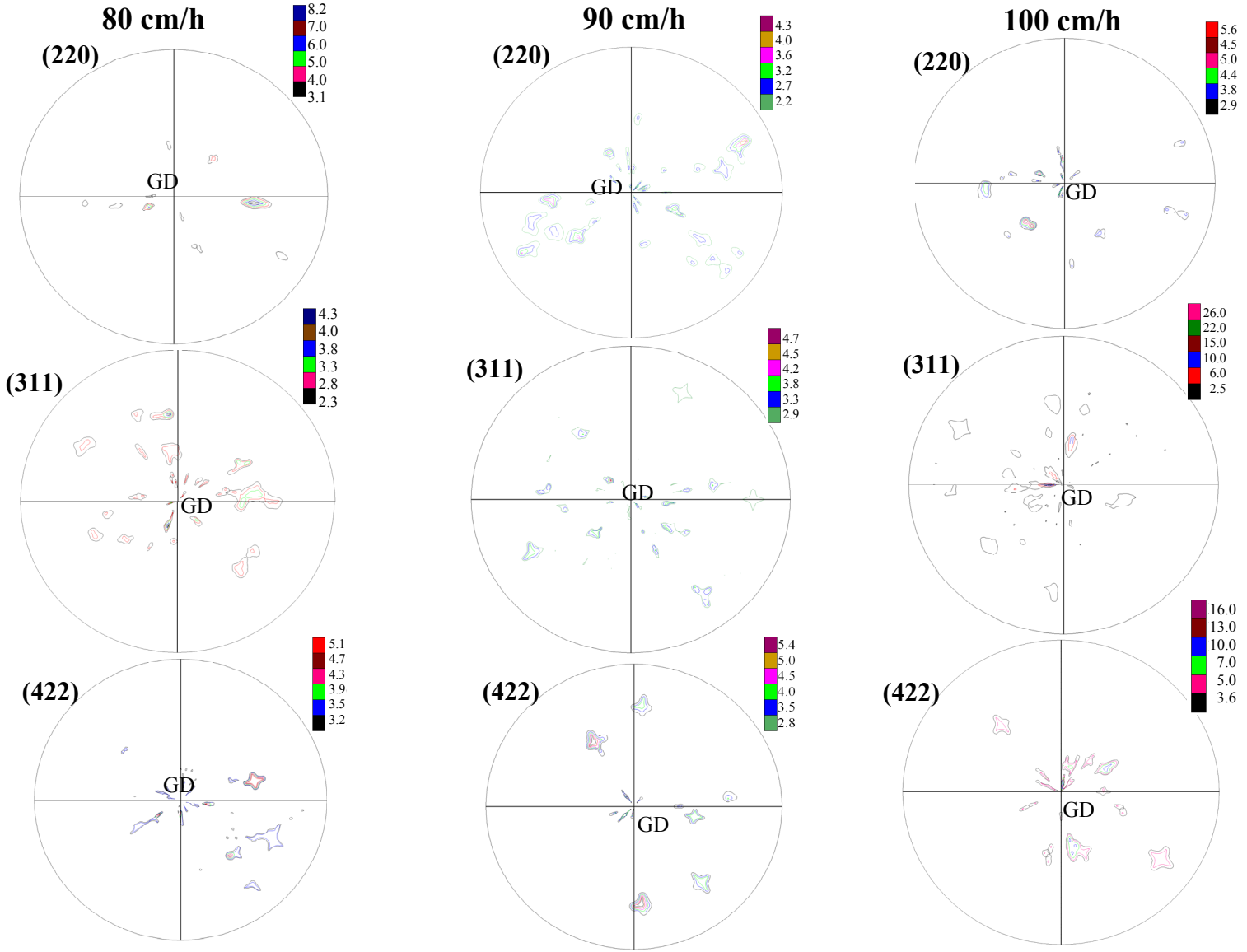

Figure 4.14: (220), (311) and (422) pole figures taken on the transverse sections of the sample grown at 80, 90 and 100 cm/h. [GD indicates direction of growth]

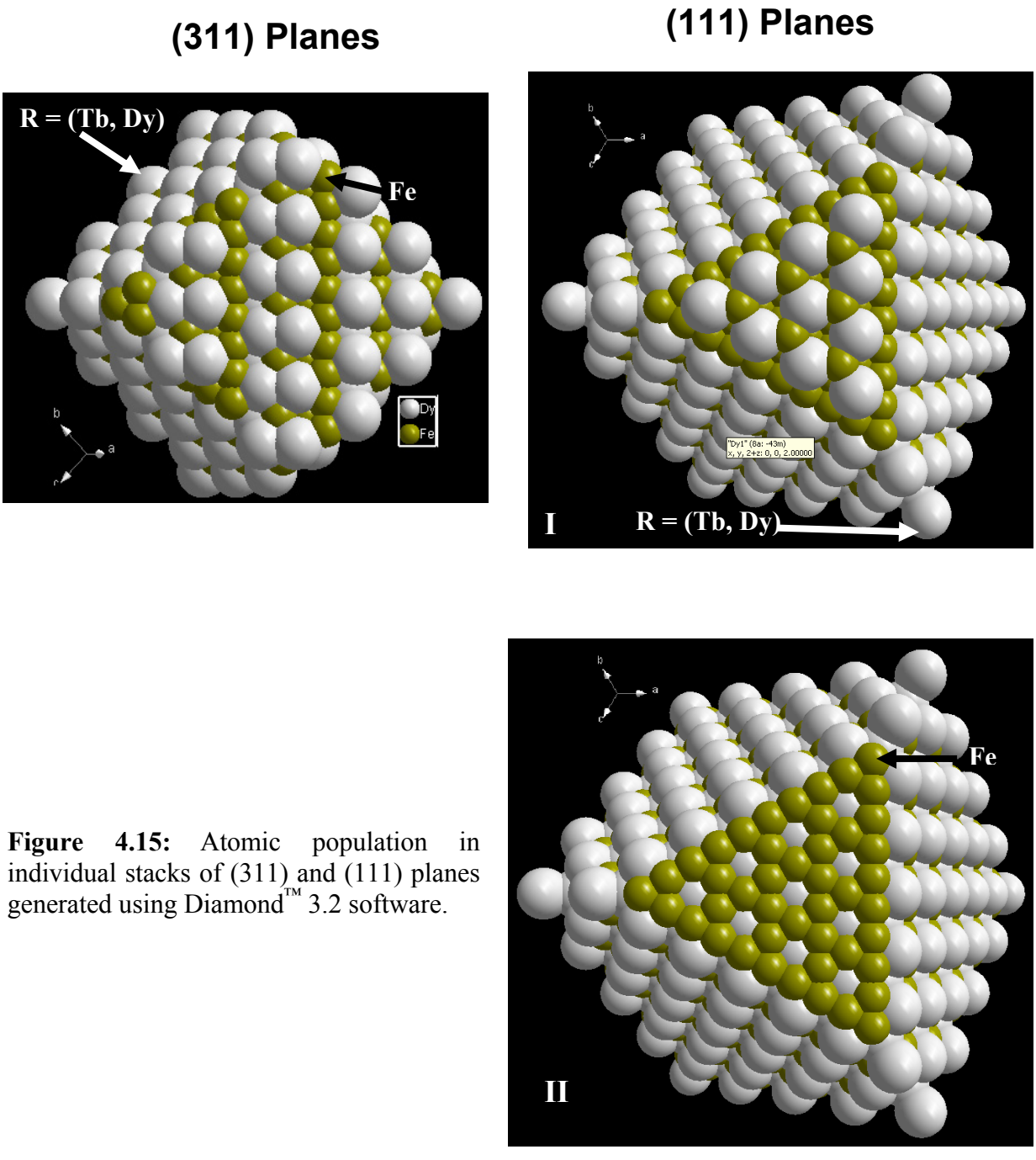

Figure 4.15: Atomic population in individual stacks of (311) and (111) planes generated using Diamond™ 3.2 software.

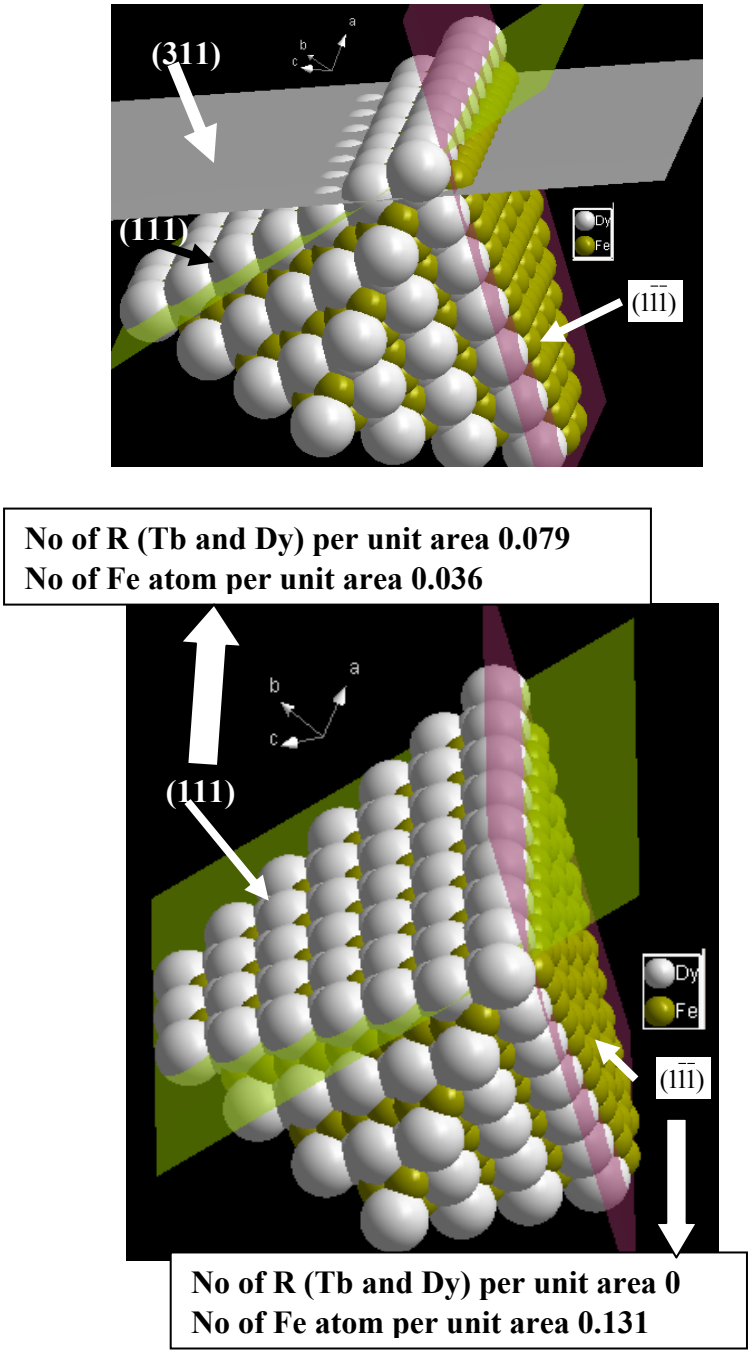

Figure 4.16: Configuration of (311) interface; resolved into two {111} type planes

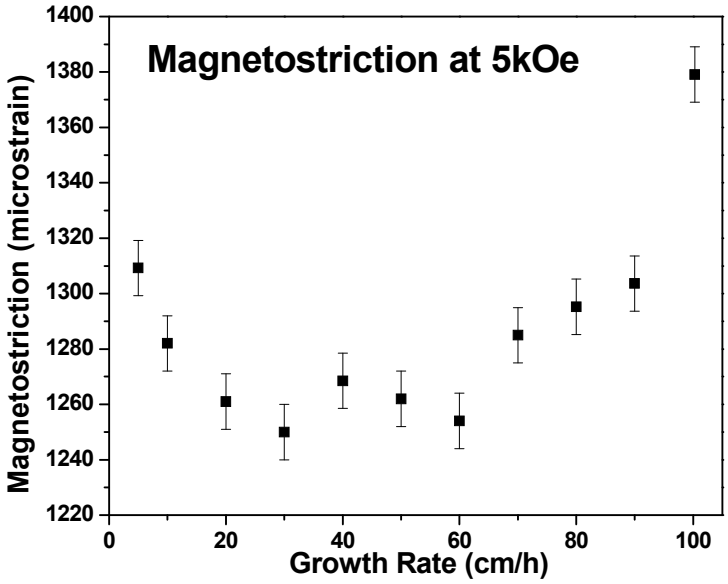

Figure 4.17: Magnetostriction of directionally solidified samples measured at an applied field of 5 kOe, plotted as a function of growth rate.

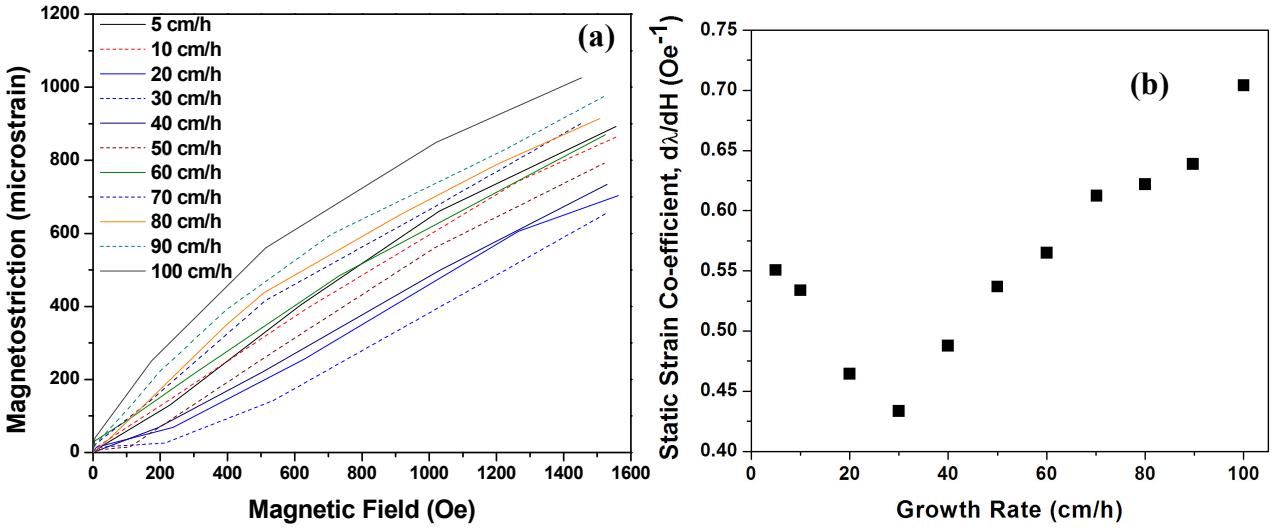

Figure 4.18: (a) Initial portion of magnetostriction (λ) vs. applied magnetic field (H) plots of the samples grown at different solidification rates and (b) the plot of slope (dλ/dH) of the initial λ-H plot as a function of growth rate.

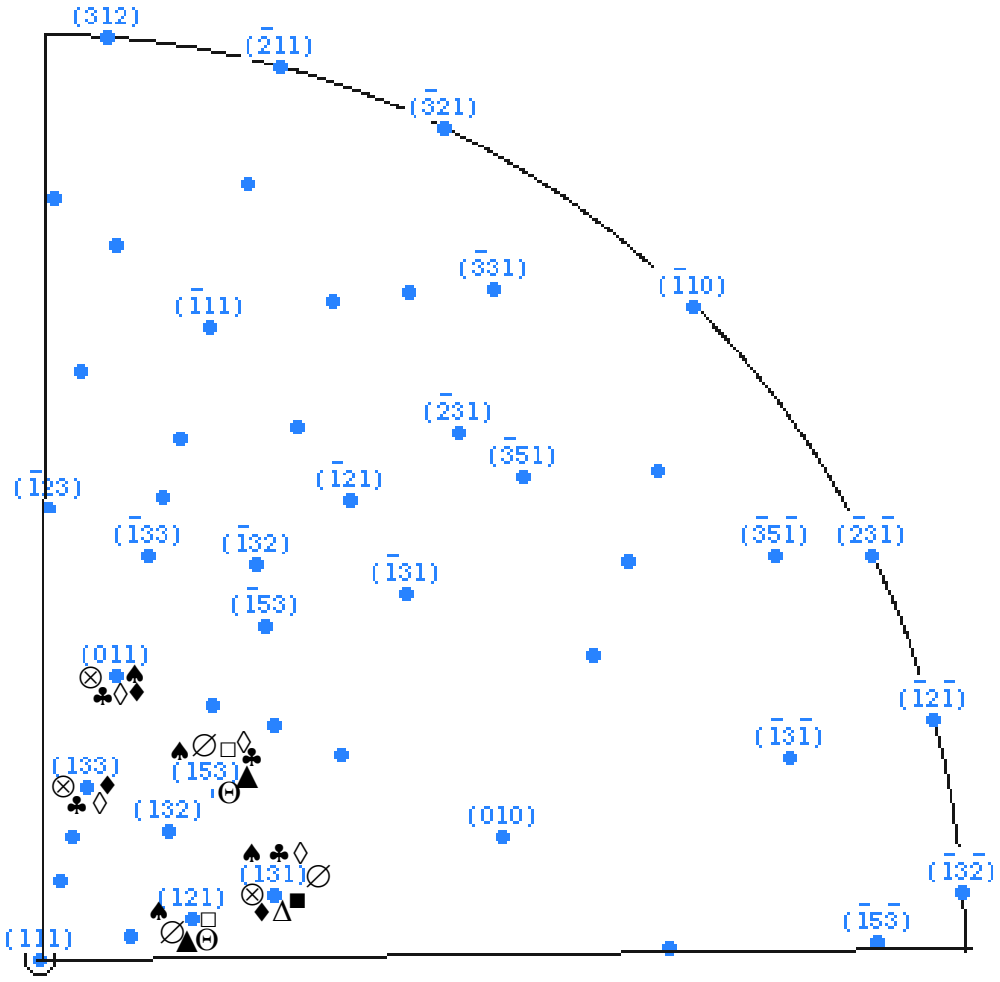

■ 5 cm/h; Δ 10 cm/h; ♦ 20 cm/h; ⊗ 30 cm/h; ♣ 40 cm/h; ◊ 50 cm/h;

♠ 60 cm/h; ∅ 70 cm/h; □ 80 cm/h; Θ 90 cm/h; ▲ 100 cm/h;

Figure 4.19: Observed texture components of different samples plotted in a quadrant (111) stereogram to depict the relative deviation of different texture components from EMD.

References:

[1] A. E. Clark, H. S. Belson and N. Tamagawa, "*Magnetocrystalline Anisotropy in Cubic Rare Earth-Fe_2 Compounds"*, AIP Conf. Proc. 10 (1973) 749.

[2] K. H. J. Buschow, *"Ferromagnetism of SmCd"*, Rep. Prog. Phys. 40 (1977) 1179.

[3] N.C. Koon, C.M. Williams, B.N. Das, *"Giant magnetostriction materials"*, J. Magn. Magn. Mater. 100 (1991) 173.

[4] J.D.Verhoeven, E.D.Gibson, O.D.McMasters, H.H.Baker, "*The growth of single crystal Terfenol-D crystals*", Metall.Trans.18A (1987) 223.

[5] J.D. Snodgrass and O. D. McMaster, "*Optimized TERFENOL-D manufacturing processes",* J. Alloys Compd. 258 (1997) 24.

[6] Mithun Palit, S. Pandian, R. Balamuralikrishnan, A.K. Singh, Niranjan Das, V. Chandrasekharan, G. Markandeyulu, "*Microstructure and magnetostriction of $Tb_{0.3}Dy_{0.7}Fe_{1.95}$ prepared under different solidification conditions by zoning and modified Bridgman techniques*", J. Appl. Phys. 100 (2006) 074913.

[7] Chengchang Ji, Jianguo Li, Weizeng Ma, Yaohe Zhou, *"Preparation of Terfenol-D with precise <110> orientation and observation of the oriented growth crystal morphology",* J. Alloys Compd. 333 (2002) 291.

[8] Y. Zhao, C. Jiang, H. Zhang, and H. Xu, *"Magnetostriction of <110> oriented crystals in the TbDyFe alloy",* J. Alloys Compd. 354 (2003) 263.

[9] Mithun Palit, J. Arout Chelvane, S. Pandian, Niranjan Das and V. Chandrasekaran, *"Effect of solidification rate on the microstructural features and magnetostriction of directionally solidified $Tb_{0.3}Dy_{0.7}Fe_{1.95}$*", Scripta Mater. 58 (2008) 819.

[10] Mithun Palit, J. Arout Chelvane, Himalay Basumatary, S. Banumathy, A.K. Singh, S. Pandian, V. Chandrasekaran, "*Comparative effect of texture and microstructure on the magnetostriction of directionally solidified $Tb_{0.3}Dy_{0.7}Fe_{1.95}$ alloy",* Intermetallics 18 (2010) 1027.

[11] W. Mei, T. Okane, T. Umeda, and S. Zhou, *"Directional solidification of Tb-Dy-Fe alloy"*, J. Alloys Compd. 248 (1997) 151.

[12] J D Verhoeven, E D Gibson, O D McMasters and J E Ostenson, *"Directional solidification and heat treatment of TerfenoI-D magnetostrictive materials"*, Metall. Trans. A, 21 (1990) 2249.

[13] Mithun Palit, S. Banumathy, A.K. Singh, S. Pandian, K. Chattopadhyay, *"Crystallography of solid-liquid interface and evolution of texture during directional solidification of $Tb_{0.3}Dy_{0.7}Fe_{1.95}$ alloy"*, Intermetallics 19 (2011) 357.

[14] J.D. Verhoeven, E.D. Gibson, O.D. McMasters, H.H. Baker, "*The growth of single crystal Terfenol-D crystals*", Metall. Trans. 18A (1987) 223.

[15] W. J. Park, J. C. Kim, B. J. Ye, Z. H. Lee, *"Macrosegregation in Bridgman growth of Terfenol-D and effects of annealing"*, J. Cryst. Growth 212 (2000) 283.

[16] W.A. Tiller, *"Preferred Growth Direction of Metals"*. Trans. AIME, 209 (1957) 847.

[17] K A Jackson, *"Growth and perfection of Crystals"*, ed. Doremus, Roberts and Turnbull, John Willey and Sons, New York (1958) 319.

[18] K A Jackson, *"On surface roughness"*, Acta Mater., 7, (1959) 747.

[19] K A Jackson, *"Liquid Metals and Solidification"*, American Soc. for Metals, Cleeveland (1958) 17.

[20] J W Cahn, *"Theory of crystal growth and interface motion in crystalline materials"* Acta Mater., 8, 554 (1960)

[21] W. Löser, M. Leonhardt, H. G. Lindenkreuz, B. Arnold, "*Phase selection in undercooled binary peritectic alloy melts",* Mater Sci. Engg. A, 375 (2004) 534.

[22] M. Takeyama, Y. Yamamoto, H. Morishima, K. Koike, S.Y. Chang, T. Matsuo, "*Lamellar orientation control of Ti-48Al PST crystal by unidirectional solidification",* Mater Sci. Engg. A, 329 (2002) 7.

[23] M. Leonhardt, W. Löser, H. G. Lindenkreuz, "*Phase selection in undercooled peritectic Fe–Mo alloys*", Acta Mater. 50 (2002) 725.

[24] K. Nagashio, K. Kuribayashi, "*Phase selection in the undercooled peritectic $Y_3Fe_5O_{12}$ melt"*, Acta Mater. 50 (2002) 1973.

[25] J. Strohmenger, T. Volkmann, J. Gao, D.M. Herlach, "*Phase selection in undercooled Fe–Nd alloy melts*", Mater Sci. Engg. A, 375 (2004) 561.

[26] Gandham Phanikumar, Krishanu Biswas, Oliver Funke, Dirk Holland-Moritz, Dieter M. Herlach, Kamanio Chattopadhyay, *"Solidification of undercooled peritectic Fe–Ge alloy"*, Acta Mater. 53 (2005) 3591.

[27] R. Trivedi, *"The role of heterogeneous nucleation on microstructure evolution in peritectic systems"*, Scripta Mater. 53 (2005) 47.

[28] O. Hunziker, M. Vandyoussefi and W. Kurz, *"Phase and microstructure selection in peritectic alloys close to the limit of constitutional undercooling"*, Acta Mater. 46 (1998) 6325.

[29] S. Dobler, T.S. Lo, M. Plapp, A. Karma and W. Kurz, *"Peritectic coupled growth",* Acta Mater. 52 (2004) 2795.

[30] T.S. Lo, S. Dobler, M. Plapp, A. Karma and W. Kurz, *"Two-phase microstructure selection in peritectic solidification: from island banding to coupled growth",* Acta Mater. 51 (2003) 599.

[31] Tak Shing Lo, Alain Karma, and Mathis Plapp, *"Phase-field modeling of microstructural pattern formation during directional solidification of peritectic alloys without morphological instability",* Phys. Rev. E 63 (2001) 031504.

[32] R. Trivedi, J.H. Shin, *"Modelling of microstructure evolution in peritectic systems"*, Mater. Sci. Engg. A, 413 (2005) 288.

[33] J. S. Park and R. Trivedi, *"Convection induced novel oscillating microstructure formation in peritectic system",* J. Cryst. Growth 187 (1998) 511.

[34] P. Magnin, W. Kurz, *"An analytical model of irregular eutectic growth and its application to Fe - C." Acta Metallurgica*, 35 (1987) 1119.

[35] M. Gündüz, H. Kaya, E. Çadırlı, A. Özmen, *"Interflake spacings and undercoolings in Al–Si irregular eutectic alloy"*, Mater. Sci. Engg. A, 369 (2004) 215.

[36] H. Kaya, E. Çadırlı, M. Gündüz, and A. Ülgen, *"Effect of the Temperature Gradient, Growth Rate and the Interflake Spacing on the Microhardness in the Directionally Solidified Al-Si Eutectic Alloy"*, J. Mater. Engg. Perform., 12 (2003) 544.

[37] J. Arout Chelvane, S Banumathy, Mithun Palit, Himalay Basumatary, A K Singh, S. Pandian, *"Texture and magnetostriction studies in Bridgman solidified $Ho_{0.85}Tb_{0.15}Fe_{1.95}$ alloys"*, J. Alloys and Compd., 507 (2010) 162.

[38] M.G. Ardakani, N. D'Souza, A. Wagner, B.A. Shollock and M. McLean, Superalloys 2000, Edited by T.M. Pollock, R.D. Kissinger, R.R. Bowman, K.A. Green, M. McLean, S. Olson, and J.J. Schirra TMS (The Minerals, Metals & Materials Society), 2000.

[39] Guang-heng Wu, Xue-gen Zhao, Jing-hua Wang, Jing-yuan Li, Ke-chang Jia and Wen-shan Zhan, *"<111> oriented and twin-free single crystals of Terfenol-D grown by Czochralski method with cold crucible"*, Appl. Phys. Lett. 67 (1995) 2005.

\

Chapter 5

Evolution of texture during directional solidification of magnetostrictive $Tb_{0.3}Dy_{0.7}Fe_{1.95}$ alloy by zone melting

5.1. Introduction:

The directional solidification studies on anisotropy compensated giant magnetostrictive $Tb_{0.3}Dy_{0.7}Fe_{1.95}$ alloy has been carried out extensively [1-15] in order to achieve high magnetostriction at lower applied field. Although it has been established that post solidification microstructure and texture have profound influence on the resultant magnetostrictive properties of directionally grown rods [4-9,11,13-16], less attention have been paid to understand the evolution of texture and microstructure as a function of growth conditions.

In the previous chapter (Chapter 4), attempts have been made to understand the evolution of microstructure and texture of $Tb_{0.3}Dy_{0.7}Fe_{1.95}$ alloy, directionally gown by Bridgman technique. However, the growth conditions adopted correspond to plane front growth morphology. A discussion has been made in the chapter 4 for the orientation selection mechanisms of plane front solid-liquid interface morphology and a mechanism based on atomic attachment kinetics has been presented. However, it is also of interest to understand the evolution of growth texture in case of cellular/ dendritic morphology of solid-liquid interface. Unfortunately, due to higher temperature gradient in the previous experiments (~150^{o}C/ cm), the instability could only be observed at highest growth rate adopted (100 cm/h) and therefore the evolution of texture for cellular/ dendritic growth condition could not be studied. In this context, a study has been taken up to study the evolution of texture and microstructure of $Tb_{0.3}Dy_{0.7}Fe_{1.95}$ alloy, directionally gown by zone melting technique. The temperature gradient obtained during zone melting process is much less of ~100^{o}C/cm and therefore offers opportunity to study the evolution of texture with increasing growth rate. Further, since zone melting is adopted as an established method for fabricating magnetostrictive actuators of smaller diameters (<10 mm), it is also of technological importance to establish the mechanisms for orientation selection.

The available literature of directional solidification provides very less information about the evolution of growth texture during cellular/ dendritic growth. It has been proposed

that growth of dendrite in cubic system is generally along <100> and the tip is enclosed with close-packed {111} planes [17-18]. However, although the (Tb,Dy)Fe_2 phase is cubic it is never reported to grow along <111> or <100> directions [4-9,11]. Thus, for any other growth directions such as <110> or <112>, the cell/ dendrite tip is not likely to be enclosed only with close-packed {111} planes. Also the principles of orientation selection for plane front growth discussed in the previous section are not applicable to cellular/ dendritic growth. Therefore, there is a need for new approach to understand the principle of orientation selection in Tb-Dy-Fe system.

Recently, Mei *et.al.* [19] proposed a model of orientation selection in Tb-Dy-Fe alloys based on interface temperature of cell/ dendrite with different orientations. His work is based on earlier reports [20-21], which proposes favorable growth of cell/ dendrite of a particular orientation having higher local interface temperature. However, the approach of Mei *et.al.* [19] was limited by only considering different undercooling at interface and the model did not take into account the effect of the atomic attachment kinetics. Further, in his model it was assumed that cell/ dendrite tips are surrounded by only {111} planes, which may not be feasible as discussed earlier. (Tb,Dy)Fe_2 being a topologically close-packed crystal system Further, the magnetostrictive phase (Tb,Dy)Fe_2 being a topologically close packed phase (C15 type Laves phase, space group [227]: $Fd\bar{3}m$), it may be required to understand the growth kinetics in relation to the atomic arrangement, which is strikingly different from normal cubic structure. Therefore, the present work was undertaken to carry out a detailed study of the texture evolution in $Tb_{0.3}Dy_{0.7}Fe_{1.95}$ alloy as a function of solidification parameter in order to understand both the process of texture evolution at the solid-liquid interface and to evaluate the possibility of improvement in magnetostrictive properties. The evolution of texture are further analyzed by invoking the kinetics of atomic attachment during solidification, packing density of growing planes at solid-liquid interface and their stacking sequence.

5.2. Experimental details:

5.2.1. Directional solidification by zone melting:

$Tb_{0.3}Dy_{0.7}Fe_{1.95}$ alloy was prepared by vacuum induction melting the constituent elements (of purity >99.5%) in a recrystallized alumina crucible under a vacuum of 5 x 10^{-5} mbar. The vacuum furnace of the make of M/s Consarc, UK (Fig. 3.1) was used for this

purpose. The molten alloy was then subsequently cast into quartz tube moulds in the form of 8 mm ϕ and 60 mm long cylindrical rods. The rods were then sealed in quartz tubes under high vacuum (~10^{-4} mbar) and directionally solidified (DS) by zone melting technique.

The zone melting setup (make M/s Pillar India) used for directional solidification is shown in Figure 5.1a. The alloy rod sealed inside a quartz tube was affixed at the top end and vertically positioned inside an induction coil. A conical induction coil (length 25 mm) was powered at 15kW with 450 kHz frequency and a melt pool was created at the bottom of the sealed tube. The induction coil is connected to a motorized drive unit, in order to be able to scan the entire length of the sample at a predefined rate. During this process the melt pool moved from bottom to top and as a result directional solidification is achieved. The picture of a molten sample during the zone melting process is shown in Figure 5.1b. The process offers high temperature gradient of 100^{o}C/cm. Three different scanning rates *viz.* 18, 36 and 72 cm/h were adopted to directionally solidify the samples.

5.2.2. Characterization of microstructure and magnetic properties:

The microstructural features of the transverse and longitudinal sections of the zoned samples were investigated using optical microscope and a FEI Quanta 400 E-SEM scanning electron microscope (SEM). The phases were identified by micro-chemical analysis of the back scattered electron (BSE) image and by X-ray diffraction (XRD) technique.

Room temperature static magnetostriction was measured under dc magnetic field using field compensated resistance strain gauges as described in section 3.2.3. The coercivity of all the samples was measured using a coercivitymeter of the make M/s Laboratorio Elektrophysique.

5.2.3. Characterization of texture:

In order to investigate the nature of grain orientation throughout the length of the rod, samples were cut perpendicular to the axis of the rod at three locations, equidistance from the bottom end of the rod (Fig. 5.2). The texture of the DS samples was investigated using a Philips PW 3020 diffractometer that is attached with a graphite monochromator and operated at 40kV and 30mA. The sample surface perpendicular to the growth direction is exposed to

obtain XRD pattern and the texture co-efficient (TC) was calculated using the following equation [22]:

$$TC_{(hkl)} = \frac{I_{(hkl)}/I_{R(hkl)}}{\frac{1}{N}\sum_{i=1}^{N}\left(I_{(hkl)}/I_{R(hkl)}\right)_i} \quad \text{.....(1)}$$

where, $I_{(hkl)}$ and $I_{R(hkl)}$ are the intensity of (hkl) plane corresponding to the textured and powder samples, respectively. All the samples were irradiated under identical conditions such as equal irradiated area and identical sample orientation. The XRD profiles of the specimens were recorded using Cu k_α radiation. A step size of 0.02^o (2θ) and counting time of 4 sec per step were used for all the samples.

The evolution of texture during directional solidification at different rates was characterized using texture goniometer. An Inel XRG 3000 diffractometer coupled with curved 'position sensitive detector' was employed for this purpose. The principal of texture goniometer has been discussed in section 4.2.3. The pole figures were analysed using LABOTEX® software for identification of various texture components. A set of three pole figures *viz.* (220), (311) and (422) were generated for each sample.

5.3. Results:

5.3.1. Solidification morphology and microstructure:

The study on the phase equilibria reported in chapter 3 indicates that the microstructure of $Tb_{0.3}Dy_{0.7}Fe_{1.95}$ generally consist of $(Tb,Dy)Fe_2$ as major phase along with pro-peritectic $(Tb,Dy)Fe_3$ and eutectic [$(Tb,Dy)Fe_2$ + solid solution of (Tb,Dy)] phases. In concurrence to this observation, the microstructure of as prepared starting alloy used in this study is found to consist of all three phases. The $(Tb,Dy)Fe_2$ has cubic Laves phase (C15) structure with lattice parameter of 7.32 Å and is formed by a peritectic reaction between liquid and $(Tb,Dy)Fe_3$ phase, which forms first from the melt. The pro-peritectic phase has a rhombohedral structure and is found in the microstructure as a result of incomplete peritectic reaction. The remaining liquid after peritectic reaction undergoes eutectic decomposition into $(Tb,Dy)Fe_2$ and the solid solution of Tb and Dy. The solid solution is having rhombohedral structure.

The microstructures of the directionally solidified samples (Fig. 5.3) indicate the absence of pro-peritectic phase, which is present in as prepared starting alloy. The $(Tb,Dy)Fe_2$ phase grew along the crystal pulling direction and the solidification morphology

was found to be cellular for the growth rate of 18-72 cm/h, employed in this investigation (Fig. 5.4). Occasionally one can observe secondary instability in the sample grown at 72 cm/h. This is in contrast to the plane front growth observed in case of the Bridgman grown samples discussed in chapter 4, even for the samples grown with rates similar to those adopted in the present study. This is attributed to the lower temperature gradients (~100^{o}C/cm) of the zone melting process compared to that of Bridgman process (~150^{o}C/cm). Further, peritectic coupled growth as observed in case of the Bridgman grown samples (Chapter 4) has not been observed in case of zone melted alloys.

The microstructure of the transverse section of the sample grown at 18 cm/h indicates presence of colonies of elongated cells (Figs. 5.4). The angles between the colonies are ~ 75^o, which closely matches with the angles between {111} planes. At higher growth rates, the cells increasingly acquire irregular shape. The micrographs of longitudinal and transverse sections of the samples grown at 18, 36 and 72 cm/h, taken in atomic number contrast mode of SEM are shown in Figure 5.5. The micrographs indicate presence of (Tb,Dy)-rich solid solution along the intercellular boundary. The high magnification micrographs of the intercellular region of the samples (Fig. 5.6) indicate that the thickness of this region does not change much with growth rate. The average cell spacings at different growth rates were calculated from the micrographs of transverse sections of the directionally grown samples and are plotted in Figure 5.7. The cell spacing decreases with increase in growth rate. The micro-chemical analysis of the major phase has been analyzed by energy dispersive spectrometry (EDS) and found to be, Fe: 66 ± 1 at %, Tb: 9 ± 1 at % and Dy: 25 ± 1 at %. The cell boundary region consists of solid solution of Tb and Dy.

5.3.2. X-ray diffraction and texture Co-efficient:

The XRD patterns of the unidirectionally solidified are presented in Fig. 5.8 and are compared in the same figure, with the powder diffraction pattern of the as-cast alloy. A strong <110> texture (Fig. 5.8b) is indicated by the XRD pattern taken on the sample region (A) that depicts the onset of solidification. This feature is observed in the region A of all the zoned samples. In the middle portion (B) of the zoned samples, however, preference for <112> texture (Fig. 5.8c) seems to emerge with higher pulling rate. The XRD of the as cast and zoned samples also confirms the phases observed in the microstructure of the samples.

The plots of texture co-efficient for different (hkl) reflections as a function of Bragg angle (2θ) for each of the three sections (A, B and C) of zoned samples are shown in Fig. 5.9. In additions to the major reflections *viz.* (220) and (422), other reflections such as (331), (531) *etc.* are also seen in significant intensity. Following the convention used in the previous chapter, <331> and <531> texture components will be termed as 'rotated <110>' and 'rotated <112>', respectively. The plots of texture co-efficient (Fig.5.9) depict that the zoned samples consist of a major texture component and in addition, one or two minor ones. During the onset of solidification (section A), a strong preference for either <110> or 'rotated <110>' texture is observed, irrespective of solidification rate. Yet, a preference for <112> seems to emerge at higher solidification rate, as evidenced from the texture co-efficient plots (Fig. 5.9) of section B of all the zoned samples. As the solidification front moves from the bottom to the top, the growing texture components rotate and as a result, rotated components such as '<331>' and '<531>' are evolved. A comparison of texture co-efficient plots of region B of all the zoned samples indicate a strong <110> and <112> texture for samples zoned at 18 and 72 cm/h respectively, whereas a mixed 'rotated <110>' and 'rotated <112>' for the sample solidified at 36 cm/h.

5.3.3. Pole figures obtained from texture goniometer:

The X-ray pole figures obtained from the zoned rods that correspond to different pulling rates are shown in Fig. 5.10, 5.11 and 5.12. The description of the texture components, as observed in (220), (422) and (311) pole figures is presented briefly as a function of pulling rates.

5.3.3.1. *Sample zoned at 18 cm/h:*

The (311) pole figure of the bottom portion (A) of the zoned sample exhibits high intensity at $\chi = 32.8^{o}$, indicating a strong <110> texture component. The (220) pole figure, on the other hand, shows strong intensity at $\chi = 10.6^{o}$, 54.4^{o} and 45.4^{o}, and it is inferred from this that the orientation at the centre of the pole figure (Fig. 5.10) is nearly (331), which is approximately 13^{o} away from (220). This implies the presence of 'rotated <110>' component together with the strong <110> texture component, and validates the inference derived from the TC plots (Fig. 5.9). The locations of other intensity contours observed in (311) and (422) pole figures (Fig. 5.10) of the same sample reconfirms the presence of <110> and 'rotated <110>' texture components. These two major texture components in section A

of the zoned sample are also accompanied by 'rotated <112>' component of feeble intensity, evidenced from the intensity contours at $\chi = 55.2^o$ of (311) pole figure, which too is in accordance with the observation made from TC plots (Fig. 5.9). The 13^o tilt of <110> component, observed in section A of the zoned rod is reduced in section B of the same rod as the (220) pole figure of section B indicates the presence of strong intensity contours at $\chi = 5.3^o$. Further, in the same pole figure, the location of maximum intensity at $\chi = 35^o$ and 65^o gives further credence to the presence of (220) pole being closer to the centre of pole figure. This too indicates the presence of a strong <110> texture component in the section B of the zoned rod. Alternatively, the presence of <110> texture component is also evident from the location of high intensity observed in the (422) pole figure (Fig. 5.10).

It is observed from (311) pole figure that, in addition to <110> orientation, 'rotated <110>' component (intensity contour at $\chi=25.8^o$) is also present in section B of the rod. Interestingly, a third component <531> i.e. 'rotated <112>' is observed in this section of the sample from the intensity contour at $\chi = 14.4^o$ of the (311) pole figure. The 'rotated <110>' component continues to be present even in section C of the zoned rod, as is evident from the intensity contours at $\chi=13.5^o$ and 33.2^o of (220) pole figure. The 'rotated <112>' component is also seen from the intensity contour at $\chi= 17^o$ of (220) pole figure and at $\chi=49^o$ of (311) pole figure. However, in contrast to the inference drawn from TC plots, pole figure analysis indicates the presence of <112> as minor component in section C of the zoned rod, as observed from the intensity at $\chi= 60^o$ of (422) pole figure.

5.3.3.2. ***Sample zoned at 36 cm/h:***

The (422) pole figure of the section A of the zoned rod exhibits high intensity contours at $\chi = 54.6^o$, from which the presence of <110> texture component is inferred. Along with <110> texture component, the 'rotated <110>' texture component is also present as indicated by the strong intensity contours at $\chi = 49.3^o$ and 69.8^o of (220) pole. The presence of 'rotated <110>'component is further evidenced from the high intensity contours at $\chi = 22.5^o$ of (311) pole figure and at $\chi = 20.2^o$ of (422) pole figure. In contrast to the observation made on section A of the sample zoned at 18 cm/h, presence of <112> texture component with substantial intensity has been observed in the section A of sample zoned at 36 cm/h. The presence of <112> component is indicated by high intensity at $\chi = 30.1^o$ and

55.1° locations of (220) pole figure (Fig. 5.11). The presence of strong intensity at $\chi = 60^o$ of (311) pole figure (Fig. 5.11) also confirms the presence of <112> texture. Apart from these texture components, a feeble presence of <531> *i.e.* 'rotated <112>'component is also seen at $\chi = 15.6^o$ and 58.1^o of (220) pole figure and at $\chi = 65.2^o$ of (422) pole figure (Fig. 5.11). Although 'rotated <112>' and 'rotated <110>' appear at the onset of solidification, the tilt reduces and the resultant texture components try to attain a mixture of <110> and <112> components, as solidification proceeds to region B. The presence of strong <110> is seen from the intensity at $\chi = 5.5^o$ of (220) pole figure, at $\chi = 64.9^o$ of (311) pole figure and from two locations at $(\chi,\phi) = (30^o,174.9^o)$ and $(30.2^o,65.5^o)$ of (422) pole figure. The strong <112> texture component is located at $\chi = 30.3^o$ of the (220) pole figure, at $\chi = 60^o$ of (311) pole figure and at $\chi = 5^o$ of (422) pole figure. Along with the main <110> and <112> components, 'rotated <110>' and 'rotated <112>' as minor components (Fig. 5.11) are also observed in (220), (311) and (422) pole figures. While the 'rotated <110>' component is seen at $\chi = 11.8^o$ of (220) pole figure and at $\chi = 69.5^o$ of (311) pole figure, the 'rotated <112>' component, lies only at locations $\chi = 14.8^o$ of (220) pole figure, at $\chi = 55.1^o$ of (311) pole figure and at $\chi = 34.6^o$ of (422) pole figure. The section C of the sample exhibits the significant presence of 'rotated <112>' component at $\chi = 14.9^o$ of (422) pole figure, at $\chi = 40.8$ of (220) pole figure and at $\chi = 49.8^o$, 55.5^o of (311) pole figure (Fig. 5.11). Apart from this, a feeble appearance of 'rotated <110>' component is noticed at locations $\chi = 49.8^o$ of (311) pole figure and $\chi = 25^o$ of (220) pole figure.

5.3.3.3. *Sample zoned at 72 cm/h:*

The (220) pole figure obtained from section A of the rod zoned at 72 cm/h exhibits the presence of three major components at $\chi = 16.3^o$, 30.3^o and 59.8^o. These correspond to 'rotated <112>', <112> and <110> texture components, respectively. The intensities of both <112> and 'rotated <112>' texture components are higher as compared to that of <110> component (Fig. 5.12). The <112> component is also located at $\chi = 8.8^o$ of (422) pole figure and at $\chi = 10^o$ of the (311) pole figure (Fig. 5.12). Apart from these components, the 'rotated <110>' component is also observed at $\chi = 25^o$ of (311) pole figure and $\chi = 40.9^o$ of (422) pole figure. In contrast to the section A of the samples zoned at 18 and 36 cm/h, the sample zoned at 72 cm/h exhibits presence of <311> component, which is evident from the intensity

at χ =5.6°, 35° in (311) pole figure and at χ = 10.2° in (422) pole figure (Fig. 5.12). The <311> component however, does not seem to stabilize during solidification as this component is not observed in the pole figures obtained from section B and C of the zoned rod. In region B, <112> evolves as major texture component which is evident from the intensity contours at χ =10°, 60° of (311) pole figure and at χ = 30.8° of (220) pole figure. In the same section of the zoned rod, the presence of 'rotated <112>' is also seen from the intensity contours at χ = 55° of (311) pole figure. The intensity of <112> and 'rotated <112>' components are relatively higher in section B of the zoned rod as compared to section A. In addition to these two components, 'rotated <110>' is also observed at χ = 40° of (311) pole figure, χ = 27° of (220) pole figure and at χ = 40° of (422) pole figure. When the solidification proceeds to the top portion (section C), the <112> component transforms into 'rotated <112>'component and this observation is in accordance with the plots of TC as a function of 2θ (Fig. 5.9). The presence of 'rotated <112>'component is quite clear from the presence of intensity at χ = 44.9°, 15.5° and 64.5° of (220) pole figure, at χ = 49.9°, 50.5° of (311) pole figure and at χ = 54.8° of (422) pole figure. In addition, the 'rotated <110>' component is also present at χ = 14.5° of (220) pole figure and at χ = 39.9°, 70° of (311) pole figure. Besides these components, the <110> component with low intensity is also observed at a location χ = 31.7° of (311) pole figure (Fig. 5.12). A summary of texture components observed in different regions of the samples zoned at different rates are presented in Table 5.1. It is interesting to note that, <311> texture component which was observed prominently for the samples grown by Bridgman technique (chapter 4) is not observed in this case.

5.3.4. Coercivity:

The coercivity of the as prepared starting alloy is found to be 68 Oe (Table 5.2), which decreases to 19 Oe for the sample, solidified at 18 cm/h. The coercivity is however not significantly influenced by the rate of pulling as all the directionally solidified samples exhibit similar coercivity. The decrease in coercivity after directional solidification is attributed to the absence of pro-peritectic $(Tb,Dy)Fe_3$ phase which imparts resistance to domain wall movement. However, the effect of reduction in cell size with increase of pulling rate is not significant, as the coercivity remains unaffected with pulling rate.

5.3.5. Magnetostriction:

The magnetostriction of the zoned samples as a function of applied d.c. magnetic field is compared with that of the pre-cast sample in Figure 5.13a. The zoned samples exhibit a large magnetostriction (1000 -1300 microstrains) as compared to the pre-cast sample (500 microstrains). The improvement in magnetostriction due to directional solidfication is attributed to (i) the development of <110> and <112> texture components and (ii) the absence of $(Tb,Dy)Fe_3$ phase. In addition, a comparison of the samples zoned at different growth rates indicates that magnetostriction increases with increasing growth rate. This correlates with the evolution of <112> as major texture component with increase of solidification rate. Thus, it appears that the presence of <112> as major texture component enhances magnetostriction.

The static strain co-efficient ($d\lambda/dH$) is also found to improve with increase of growth rate (Fig. 5.13b). The value of static strain co-efficient is generally influenced by (i) magneto-crystalline anisotropy, (ii) Grain orientation and (iii) Coercivity. Since all the experiments were conducted with alloy of same composition, the anisotropy is similar in all the cases. Further, the coercivities of all the directionally solidified alloys are also nearly similar. Therefore, the increase in static strain co-efficient with pulling rate can be attributed to the evolution of <112> as major texture component with increase of growth rate. Amongst the major texture components observed in the samples directionally solidified at 18, 36 and 72 cm/h (Table 5.1), <112> component is most close to easy magnetization direction (EMD) *i.e.* <111> of $(Tb,Dy)Fe_2$ phase. Therefore the emergence of <112> as major texture component with increase in growth rate is responsible to the increase in the static strain co-efficient.

5.4. Discussions:

The observation from the TC plots (Fig. 5.9) and pole figures (Fig. 5.10, 5.11 and 5.12) indicates that the evolution of texture during solidification follows an orientation selection which is strongly dependent on growth rate. The experimental results indicate <112> orientation grows stronger as the growth rate is increased. This observation is in concurrence with reports by Mei. *et. al.* [19], where the orientation selection was explained based on tip temperature of <110> and <112> oriented growing facets. However, in this paper the orientation selection is explained in the light of mass transport kinetics during

directional solidification and thus, we have attempted to model the growing interface oriented along <110> or <112>.

5.4.1. The concept of the theoretical model:

The micrographs of the directionally solidified alloys indicate cellular or cellular/ dendritic morphology of the major phase (Tb,Dy)Fe_2. Thus, the solid-liquid interface is not flat but having instabilities. Therefore, it was assumed that the cell tip that is in contact with the liquid should consist of low index planes such as {100}, {110}, {111} and {112). For example, if the cell is growing along <110> direction, the cell tip is pyramidal in shape with side faces made of low index planes mentioned above and the perpendicular to the base plane constructed through the vertex of the pyramid is parallel to <110>. There are several such possibilities to construct pyramids with low index planes enclosing the growth directions <110> or <112>. The objective was to identify the configuration for each of <110> and <112> growth, having highest atomic packing density of side surfaces. The configuration having highest packing density of side surfaces will have minimum solid-liquid interfacial energy and therefore would be most preferred for growth. Further, once such configurations are identified, the atomic attachment kinetics at solid-liquid interface also can be understood.

5.4.2. Identification of most preferred interface configurations for <110> and <112> growth:

As discussed earlier, there are several possibilities to construct pyramid shaped solid-liquid interface configurations using different combinations of low index planes. The possible configurations for <110> and <112> growth were identified with the aid of stereographic projections of (011) and (112), where the possible configurations were identified by looking at envelops formed by great circles of low index planes encircling the pole (011) or (112) in the respective stereographic projections. Typical examples of construction of envelope with great circles of low index planes have been illustrated in Figures 5.14 and 5.15, which exhibit sketch of one envelope on each of the (011) and (112) stereograms. The poles indicated at the point of intersection of two great circles denote the direction of edge formed by intersection of two planes corresponding to the great circles. The number of possible configurations found for <110> and <112> growth directions are 123 and 76 respectively. The 3D skeleton models for all possible configurations were constructed and

the dimensions of the edges of the triangular faces of the model have been calculated by vector addition method. These obtained dimensions are then used to compute the surface area of the triangular faces, which enclose around the growth directions and forms solid-liquid interface. It is expected that during directional solidification, the configuration that is having highest surface packing density at the interface of liquid, would grow in preference to others. Therefore, it is required to compute average packing density at solid-liquid interface for all the configurations that have been identified for both the cases of <110> and <112> growth. The identification of highest interfacial packing density for configurations discussed above, requires planar packing density of {100}, {110}, {111} and {112} planes.

In order to estimate the planar packing density of these low index planes, the stacking sequence of these planes were studied with the aid of $(1\bar{1}0)$ projection (Fig. 5.16). It is observed that, the planes are vicinal for the case of {111} and {100}, whereas they are not vicinal for {112} and {110}. The individual layers of stacking for all the low index planes *viz.* {100}, {110 and {112} are shown in Figure 5.17 and the stacking layers for {111} are shown in Figure 4.15. The Figures 5.17 and 4.15 exhibit presence of two different stacking layers for {111}, {110}, {100} planes have two different stacking layers. The {112} planes however consist of only a single stacking layer having mixed population of rare earth and iron atoms. The interesting feature that is evident from the Figures 5.17 and 4.15 is that the Fe atoms form a separate stacking layer for {111} and {110} planes, however, every layer of stacking consists of both Rare-earth (Tb,Dy) and Fe atoms in the case of {110} and {112} planes. For each of the low index planes mentioned above, the total area fraction occupied by atoms and the number of atom per unit area (number density) for each type of constituent element (rare earth and iron) are given in Table 5.3. The planes which are having more than one stacking, the calculations were performed averaging the values obtained for individual stacking layers. Further, for calculation of number density of planes that are vicinal in nature, it has been assumed that all the atoms that constitutes vicinal layer, lie on the area of the plane that passes through the mean position of the layer. The average interfacial packing density (P_{avg}) of a configuration is calculated by obtaining the weighted average of the packing densities of triangular surfaces that constitutes the solid-liquid interface. For example, if the interface is composed of N triangular surfaces with surface area A_i and

packing density (area fraction or total number density *i.e.* total number of rare-earth and iron atom per unit area) P_i, the P_{avg} is given by, $P_{avg} = \frac{\sum_{i=1}^{N} A_i P_i}{\sum_{i=1}^{N} A_i}$ ……..(2)

The most close-packed configurations were identified by comparing P_{avg} for all possible configurations of growth interface of <110> and <112> (Tables 5.4 and 5.5). It has been observed the same configuration gives highest value of average packing density (P_{avg}), when calculated either considering area fraction or total number density of individual triangular faces. For both the cases of <110> and <112> growth the same trend is observed. For <110> and <112> growth, the configurations which exhibit highest values of P_{avg} are shown with highlight in the Tables 5.4 and 5.5.

The total surface area of the interface for most close-packed <110> and <112> growth interface are 244.74 $Å^2$ and 114.38 $Å^2$ respectively. The details of the area of individual triangular interfacial faces for most close-packed interfacial configuration of <110> and <112> growth are given in Table 5.6. The calculations of P_{avg} for these two configurations indicate that the average area fractions for <110> and <112> interface are 86.4 % and 86.6% respectively and the average number densities for <110> and <112> interfaces are 0.109 $Å^{-2}$ and 0.111 $Å^{-2}$ respectively (Table 5.6). The construction of growth configurations from stereogram that are shown in Figures 4.15 and 4.16 as example, actually corresponds to these most closed packed interface configurations for <110> and <112> growth respectively.

The physical model for these obtained preferred configurations for <110> and <112> growth directions were generated using Diamond™ 3.2 software and are illustrated in Figures 5.18 and 5.19. The shape of the base plane of the pyramidal configurations shown in Figures 5.18 and 5.19 also corroborate to the shape of the cells observed in transverse section of the directionally solidified sample (Fig. 5.4). The base plane for the configuration for <110> orientation is of parallelogram shape (Fig. 5.18) and accordingly, elongated colonies of cells are observed in the sample solidified at 18 cm/h (Fig. 5.45). The irregular shape of the cells as observed in case of the sample grown at 72 cm/h (Fig. 5.4) also corroborates to the irregular shape of base plane of the closest packed pyramidal configuration for <112> orientation (Fig. 5.19).

5.4.3. Orientation selection with growth rate and atomic attachment kinetics:

It is observed from the Table 5.6, that the most preferred growth configurations those are identified for <110> and <112> growths have similar atomic packing density of pyramidal solid-liquid interface. Therefore, the reason for the selection of <110> growth at lower growth rate and predominance of <112> growth at higher solidification rate is not obvious.

It is observed from Figure 5.18 and Table 5.6 that the preferred growth interface of <110> consists of two {110} type and two {111} type planes, for both of which the atom attachment kinetics during solidification is very sluggish owing to presence of separate Fe-layer in their stacking (Figs. 5.17 and 4.15). The growth interface of <112> (Fig. 4.21) however, consists of two {111} type and one each of {100} and {110} type. The atomic attachment to {100} type plane during solidification is relatively faster, owing to the fact that, all the stacking layers consist of both rare-earth and iron atoms (Fig. 5.17). The Table 5.6 also indicates that almost 16 % of the total interfacial area for <112> growth, is occupied by (010) plane. Although, the P_{avg} for both the configurations of <110> and <112> growth are nearly same, due to presence of (010) plane in the interfacial configuration of <112> growth, the overall atomic attachment becomes faster as compared to that of <110>. Thus, at faster solidification rate, the atomic attachment kinetics would aid formation of <112> as preferred orientation as the atomic attachment to this interface is easier. This interpretation also corroborates to the result of texture study where <112> was observed as major component for the sample directionally solidified at 72 cm/h and <110> as the major component for the sample solidified at 18 cm/h. However, at the onset of solidification process, the nucleation of more close packed orientation is favored owing to less solid-liquid interfacial energy. Thus, {110} planes being more close-packed than {112}, <110> texture is observed as nucleation texture in all samples irrespective of growth rate.

5.4.4. Transition from <110> to <112> through intermediate orientations:

The texture observed in the present study indicates that the transition in growth direction occurs through a series of intermediate orientations lying between <110> and <112> on {111} plane. The major texture components observed in case of different samples and the rotation of growth direction are indicated on a quadrant of (011) stereogram (Fig. 5.20). It is evident from this plot (Fig. 5.20) that texture components obtained from many

samples lie around the pole $(\bar{1}33)$ and $(\bar{1}53)$, although none of the directions are lying on any {111} plane. The quadrant of (011) stereogram (Fig. 5.20) indicates, all these texture components clustered around $(\bar{1}33)$ and $(\bar{1}53)$ are probably obtained from $(\bar{1}32)$, which however lie on the $(11\bar{1})$ plane. Thus, it is probable that the directional growth for those samples would have taken place along <123> type directions. Since (123) is not an allowed reflection for C15 Laves phase structure, the orientation is manifested in terms of nearest allowed reflections such as (331) or (531); the closest angle that (123) makes with (331) and (531) are 11^o and 6^o, respectively. Further, from Figure 5.20 it is evident that the pole $(\bar{1}32)$ lies between (011) and $(\bar{2}1\bar{1})$ along the trace of $(11\bar{1})$. Therefore, it is proposed that the preferred growth direction changes from <110> (18cm/h sample) to <112> (72cm/h sample) through the intermediate <123> orientation. Most of the texture components which are assigned to $(\bar{1}32)$ pole are from the sample solidified at 36 cm/h which indicates that when the growth rate is increased from 18 to 72 cm/h, the <123> direction observed as preferred growth direction for an intermediate solidification rate. Thus, the <110> growth orientation, which is preferred at lower growth rate regime, changes over to <112> at higher growth rate regime and the changeover takes place through <123> as growth direction observed in intermediate growth rate regime. This proposition is also in agreement with the work of Haximali *et.al.* [23] on Al-Zn system, which describes that the transition in preferred growth direction with change of growth rate always occurs through some intermediate orientations.

The evolution of texture in $Tb_{0.3}Dy_{0.7}Fe_{1.95}$ during directional solidification initially starts with the nucleation of <110> and 'rotated <110>' as major components, irrespective of growth rate. These two components become minor with increase in growth rate and new orientations *viz.* <112> and 'rotated <112>' evolve. With further increase of growth rate, the <112> texture component becomes predominant. Thus, it appears from the experimental evidences obtained in the present study that the transition in the preferred growth direction from <110> to <112> occurs through intermediate <123> texture components.

5.5. Summary and conclusions:

Pre-cast rods of $Tb_{0.3}Dy_{0.7}Fe_{1.95}$ were prepared and directionally solidified by zone melting technique at three different rates *viz.* 18, 36 and 72 cm/h. The evolution of texture at

different locations along the length of the zoned sample has been studied and correlated with magnetostriction.

The directionally solidified samples exhibit absence of pro-peritectic $(Tb,Dy)Fe_3$ phase and as a result the magnetostriction values of directionally solidified alloys are more than that of as prepared starting alloy. The absence of $(Tb,Dy)Fe_3$ phase also leads to low coercivity of 19 Oe in directionally solidified alloys as compared to 68 Oe in as prepared starting alloy. An increase of the magnetostriction and the static strain co-efficient ($d\lambda/dH$) of directionally solidified alloys are observed with increase of growth rate. This increase is attributed to presence of <112> texture in the sample grown at 72 cm/h as compared to <110> texture in the sample grown at 18 cm/h. The <112> component being closer to EMD attributes to increase in magnetostriction and the static strain co-efficient.

The evolution of texture was studied by determining TC and obtaining x-ray pole figures of the transverse sections cut at different locations of all the directionally grown samples. A set of (220), (311) and (422) pole figures were used for this purpose. The texture studies indicate, irrespective of rate of solidification <110> or 'rotated <110>' formed as nucleation texture at the onset of solidification. However as the growth proceeds, same <110> or 'rotated <110>' are found as major texture components at lower growth rates. The <112> or 'rotated <112>' texture components evolve stronger when the rate of solidification is increased from 18 cm/h to 72 cm/h.

In order to understand the principle of orientation selection, a detailed analysis has been carried out on the solid-liquid interface configurations. The atomic packing density of non-planar solid-liquid interface configurations have been computed to identify the most favored interfacial configurations for <110> and <112> growth. It has been observed that the atomic packing density of the most favored configurations of <110> and <112> growth are nearly same and the orientation selection is rather related to ease of atomic attachment kinetics at solid-liquid interface. The analysis indicates that 16% of its solid-liquid interfacial area of most favored configuration of <112> growth is consisting of (010) plane, which is not having separate Fe-layer in its stacking sequence. Whereas, the most favored interfacial configuration of <110> growth is consisting of planes having separate Fe-layer in its stacking sequence. Therefore, atomic attachment kinetics to <112> interface is faster compared to <110> and hence at higher growth rate <112> emerges as major texture component. The change of preferred orientation from <110> to <112> occurs through an intermediate

orientation <123> lying on the {111} plane of dendrite. The <123> orientation is manifested in terms of <331> or <531> orientation in the pole figures or TC plots.

Table 5.1: Summary of major texture components observed in region A, B and C of samples grown at different rates

Samples	Major texture components		
	18 cm/h	**36 cm/h**	**72 cm/h**
Sample A	<110> & 'rotated <110>'	<110>, <112> & 'rotated <110>'	<112>, 'rotated <110>' & 'rotated <112>'
Sample B	<110>	<110>, <112> & 'rotated <110>'	<112>
Sample C	'rotated <110>'	'rotated <110>' & 'rotated <112>' with comparable intensity	'rotated <112>'

Table 5.2: Coercivity of as prepared initial alloy compared with directionally solidified alloys.

Sample	Coercivity (Oe)
As prepared	**68**
18 cm/h	**19.2**
36 cm/h	**18.6**
72 cm/h	**18.0**

Table 5.3: The area fraction and number of rare earth and iron atoms per unit area of {100}, {110}, {111} and {112} planes of C15 Laves phase $(Tb,Dy)Fe_2$.

Planes	Area Fraction of atoms	Number of Rare Earth atoms (Tb & Dy) Per unit area ($Å^{-2}$)	Number of Fe atoms Per unit area ($Å^{-2}$)
{111}	95 %	0.064	0.050
{110}	81 %	0.053	0.053
{100}	78 %	0.279	0.074
{112}	71 %	0.038	0.045

Table 5.4: The P_{avg} values of 123 possible configurations of solid-liquid interface for <110> growth.

Sl No.	Area of Individual Low Index Planes of different types (Å^2)				Average Area Fraction as per equation (2)	Average Number Densities of R (Tb+Dy), Fe and total R=Fe atoms as per equation [2] (Å^{-2})		
	{111}	**{110}**	**{112}**	**{100}**		**R**	**Fe**	**R+Fe**
1	0	0	0.8164	0	72	0.037989	0.044879	0.082868
2	0	0.3534	0.6122	0	75.29391	0.043373	0.047742	0.091115
3	0	1.414	0	0	81	0.052701	0.052701	0.105401
4	0	0.8837	0.3061	0	78.68457	0.048916	0.050688	0.099604
5	0	0.707	0.6122	0	76.82338	0.045873	0.049071	0.094944
6	0	0.1767	0.9183	0	73.45233	0.040363	0.046141	0.086505
7	0	0.707	0.4082	0	77.7057	0.047316	0.049838	0.097153
8	0	0.1767	0.9017	0	73.47468	0.0404	0.046161	0.086561
9	0	0.3534	0.6122	0	75.29391	0.043373	0.047742	0.091115
10	0	0.7072	1.2246	0	75.29475	0.043375	0.047743	0.091117
11	0	0	1.2244	0	72	0.037989	0.044879	0.082868
12	0.5768	0	1.6322	0	78.00561	0.044894	0.046241	0.091135
13	0	0	2.4494	0	72	0.037989	0.044879	0.082868
14	0	0	7.7113	0	72	0.037989	0.044879	0.082868
15	0	0	2.4474	0.9996	73.73995	0.035073	0.053466	0.088539
16	1.7316	0	0	1.9994	85.8899	0.044873	0.063166	0.108039
17	0	0	1.2246	1	74.69711	0.033469	0.058189	0.091658
18	0	0.1767	0.7143	0	73.78485	0.040907	0.04643	0.087337
19	0	0	1.0204	0	72	0.037989	0.044879	0.082868
20	0	0.4285	1.0205	0	74.66149	0.04234	0.047192	0.089532
21	0.2622	0	1.2246	0	76.05609	0.042652	0.045799	0.088451
22	0	0	1.6326	0	72	0.037989	0.044879	0.082868
23	0	0	2.5941	0	72	0.037989	0.044879	0.082868
24	0	0.5303	0.9184	0	75.29447	0.043374	0.047742	0.091117
25	0.2884	0.1767	1.1225	0	77.17983	0.04443	0.046697	0.091127
26	0	0.1767	1.5306	0	72.93147	0.039512	0.045689	0.0852
27	0	0.1767	2.7551	0	72.54243	0.038876	0.045351	0.084226
28	0	0.3536	1.2245	0	74.0166	0.041285	0.046632	0.087917
29	0.2884	0	1.4285	0	75.86347	0.042431	0.045755	0.088186
30	0	0	1.8368	0	72	0.037989	0.044879	0.082868
31	0	0	3.0611	0	72	0.037989	0.044879	0.082868
32	0.2884	0.3536	1.4284	0	76.74092	0.044185	0.046941	0.091127
33	0	0.3536	1.837	0	73.45275	0.040364	0.046142	0.086506
34	0	0.3536	3.0612	0	72.93194	0.039512	0.045689	0.085202
35	0.2884	0	2.0408	0	74.84784	0.041263	0.045525	0.086788
36	0.2884	0	3.2656	0	73.8664	0.040135	0.045302	0.085437
37	0	0	3.6736	0	72	0.037989	0.044879	0.082868

38	0	0	1.6325	0.4998	73.40637	0.035632	0.05182	0.087452
39	0	0.1767	1.5307	0.4998	74.07915	0.03689	0.05221	0.0891
40	0	0	1.8367	0.4998	73.28346	0.035838	0.051213	0.087051
41	0	0.3536	1.836	0.4998	74.29836	0.038055	0.05141	0.089465
42	0.2884	0	2.0398	0.4998	75.40594	0.038909	0.050644	0.089553
43	0	0	2.4484	0.4998	73.01716	0.036284	0.049899	0.086183
44	0	0	3.6723	0.4998	72.71877	0.036784	0.048426	0.085211
45	0	0	1.4781	1.4998	75.02186	0.032925	0.059792	0.092716
46	0	0.707	0.6123	0.9999	77.33046	0.038138	0.060029	0.098168
47	0	0.3535	0.9187	0.25	75.07548	0.039754	0.051559	0.091313
48	0	0.707	0.9184	0.25	76.19271	0.042195	0.051775	0.09397
49	0.2884	0.707	0.8161	0.25	79.03187	0.045514	0.051882	0.097396
50	0.8658	0.707	0	1.4997	83.48075	0.043917	0.062601	0.106518
51	0	1.414	0	1	79.75725	0.042441	0.061726	0.104167
52	0	0.707	0.9659	0.5	76.30899	0.040462	0.054237	0.094699
53	0.8658	0.707	0	1.4997	83.48075	0.043917	0.062601	0.106518
54	0	0.707	1.2245	1.9996	76.6706	0.03552	0.061347	0.096867
55	0	0.707	1.2245	1.9997	76.67063	0.03552	0.061347	0.096867
56	0	0	1.8368	1.9998	75.12746	0.032748	0.060313	0.09306
57	0	0	1.8368	1.9998	75.12746	0.032748	0.060313	0.09306
58	0	0.8837	0.3061	0.5	78.48201	0.042707	0.057731	0.100438
59	0	0.9587	0.3061	0.9997	78.45904	0.039778	0.061262	0.10104
60	0	0.5302	0.6758	0.7499	76.74012	0.038122	0.058352	0.096473
61	0.8658	0	1.2245	2.4993	79.60615	0.037501	0.061987	0.099488
62	0	0	2.449	2.9994	75.30306	0.032453	0.061179	0.093633
63	0	0	2.449	2.9992	75.30296	0.032453	0.061179	0.093632
64	0	1.414	2.4484	0	75.29484	0.043375	0.047743	0.091118
65	0	0	7.3468	0	72	0.037989	0.044879	0.082868
66	0	0	1.6398	0	72	0.037989	0.044879	0.082868
67	0	0.8837	0.3061	0	78.68457	0.048916	0.050688	0.099604
68	0	0.8837	0.3061	0.5	78.48201	0.042707	0.057731	0.100438
69	0	0.8837	0.9184	0	76.41335	0.045203	0.048715	0.093918
70	0	1.2372	0.9184	0	77.16552	0.046433	0.049368	0.095801
71	0.8658	1.5906	0.3061	0	84.39052	0.054747	0.051017	0.105764
72	0	1.7675	0.6123	0	78.68439	0.048915	0.050688	0.099604
73	0	1.414	0	0.5	80.2163	0.046231	0.058392	0.104623
74	0	1.414	0.6123	0	78.28041	0.048255	0.050337	0.098592
75	0.8658	2.1209	0	0	85.05839	0.056102	0.051945	0.108046
76	0	1.4186	0.6123	0.5	78.22996	0.044248	0.055113	0.099361
77	0	1.7671	0.6123	0.5	78.56522	0.045271	0.054821	0.100092
78	0.8658	2.1201	0	0.5	84.0469	0.052062	0.055178	0.10724
79	0	1.414	0	1	79.75725	0.042441	0.061726	0.104167
80	0	1.414	1.2246	0	76.82301	0.045873	0.049071	0.094944
81	0	1.7671	1.2246	0	77.31601	0.046679	0.049499	0.096178

82	0.8658	2.1205	0.6123	0	82.83696	0.05302	0.050743	0.103763
83	0	2.1202	1.2246	0	77.70492	0.047314	0.049837	0.097151
84	**1.7316**	**2.8262**	**0**	**0**	**86.41888**	**0.057158**	**0.05171**	**0.108868**
85	0.8658	2.4732	0.6123	0	82.67299	0.052992	0.050917	0.103909
86	0	0	1.7073	0	72	0.037989	0.044879	0.082868
87	0	0	2.1903	1	73.8807	0.034837	0.05416	0.088997
88	0	0.707	2.449	0	74.01616	0.041285	0.046631	0.087916
89	0	1.0605	1.8367	1	75.98863	0.039412	0.054605	0.094017
90	0	1.414	2.4488	0	75.2945	0.043374	0.047742	0.091117
91	0	1.0601	4.2856	0	73.78478	0.040907	0.04643	0.087337
92	0	2.1202	1.2246	0	77.70492	0.047314	0.049837	0.097151
93	0	0	2.4494	0	72	0.037989	0.044879	0.082868
94	3.6748	0	2.4484	0	85.80331	0.053859	0.048009	0.101868
95	0	0.707	1.2245	0	75.29433	0.043374	0.047742	0.091116
96	0	0	1.2248	0.5	73.73933	0.035074	0.053463	0.088537
97	0	0	3.6733	0	72	0.037989	0.044879	0.082868
98	0	0	3.6731	0.5	72.71889	0.036784	0.048427	0.085211
99	0	0	3.6731	0.5	72.71889	0.036784	0.048427	0.085211
100	0	1.414	1.2246	0	76.82301	0.045873	0.049071	0.094944
101	0	0.707	3.6739	0	73.45244	0.040363	0.046142	0.086505
102	0	0.707	3.6729	0	73.45277	0.040364	0.046142	0.086506
103	0	0	6.1232	0	72	0.037989	0.044879	0.082868
104	0	0	6.1211	0	72	0.037989	0.044879	0.082868
105	0.2884	0	1.1227	0.7499	77.1516	0.038029	0.05585	0.093879
106	0.2884	0	3.8779	0	73.59211	0.03982	0.04524	0.08506
107	1.1541	1.0604	0.8162	0	83.90745	0.053206	0.049601	0.102808
108	0.8658	0	3.3673	0.7499	76.89922	0.04107	0.050241	0.091312
109	1.7314	0.8991	0.3061	0.7499	86.21769	0.051951	0.055259	0.10721
110	2.5983	0	2.7544	0.7499	82.52999	0.048012	0.050738	0.09875
111	1.7314	1.0604	3.0613	0	80.43413	0.048477	0.047839	0.096315
112	0.8658	0	6.1221	0	74.8497	0.041265	0.045525	0.086791
113	4.3341	0	4.8962	0	82.79968	0.050406	0.047328	0.097733
114	1.1542	0	0.8161	0.9997	82.95785	0.044881	0.056872	0.101753
115	2.8867	0	3.2651	0	82.79263	0.050398	0.047326	0.097724
116	3.4641	0	2.449	0.9997	84.39331	0.049786	0.051774	0.10156
117	5.1999	0	4.898	0	83.84382	0.051606	0.047564	0.09917
118	5.1966	0	4.898	0	83.84017	0.051602	0.047564	0.099165
119	1.7316	2.8262	0	0	86.31888	0.057158	0.05171	0.108868
120	3.4619	1.4131	2.449	0	84.60808	0.053327	0.048853	0.10218
121	0	1.4137	1.2246	0	76.82254	0.045872	0.04907	0.094942
122	0.8658	1.7667	0.6123	0	83.03726	0.053055	0.050529	0.103584
123	0	1.0605	0.6123	0.5	77.77343	0.042855	0.05551	0.098366

Table 5.5: The P_{avg} values of 76 possible configurations of solid-liquid interface for <112> growth.

Sl No.	Area of Individual Low Index Planes of different types (Å^2)				Average Area Fraction as per equation (2)	Average Number Densities of R (Tb+Dy), Fe and total R=Fe atoms as per equation [2] (Å^{-2})		
	{111}	**{110}**	**{112}**	**{100}**		**R**	**Fe**	**R+Fe**
1	0	0	0.5248	0	72	0.037989	0.044879	0.082868
2	0	0.4706	0.4082	0	76.81953	0.045867	0.049068	0.094935
3	0	0.4706	0	0.666	79.24213	0.038188	0.065467	0.103655
4	0.232	0	0.091	0	84.92879	0.056983	0.048624	0.105607
5	0	0.2357	0.385	0.1332	75.87386	0.040812	0.052556	0.093368
6	0	0.2357	0.4665		75.02093	0.042927	0.047505	0.090432
7	0	0.4714	0.3264	0.1332	77.41547	0.043999	0.053076	0.097075
8	0	0.2357	0.4665	0	75.02093	0.042927	0.047505	0.090432
9	0.2308	0.3766	0.4082	0	79.42792	0.049454	0.048965	0.098418
10	0.2308	0.3766	0.3264	0.1332	79.81912	0.047646	0.052464	0.10011
11	0	0.4708	0.68		75.68196	0.044008	0.048079	0.092087
12	0	0.4708	0.5982	0.1292	76.18327	0.042685	0.051145	0.09383
13	0.2309	0.3768	0.3264	0.1292	79.82714	0.047723	0.052381	0.100104
14	1.1536	0	0	0.666	85.60783	0.051073	0.059022	0.110096
15	0.2309	0.3768	0	0.666	81.06289	0.041877	0.063621	0.105497
16	0	0.4708	0.2042	0.833	78.12414	0.037027	0.063677	0.100704
17	0.5768	0	0.5786	0.833	79.73506	0.041447	0.058796	0.100243
18	0.2308	0.3766	0	0.666	81.0622	0.041873	0.063623	0.105497
19	0.3298	0	0.4197	0.5328	79.12251	0.040612	0.058523	0.099135
20	0	0.2353	0.245	0.5328	77.24578	0.036117	0.062268	0.098385
21	0	0.4706	0.3264	0.1332	77.41238	0.043992	0.053076	0.097068
22	0	0.4708	0.5306	0.2999	76.6389	0.040994	0.054533	0.095527
23	0	0.2353	0.5414	0.2999	75.6384	0.038403	0.054837	0.09324
24	0.1444	0	0.7858	0.2999	75.57581	0.038642	0.05271	0.091352
25	0	0.2355	1.0209	0.5	74.91477	0.037099	0.054357	0.091456
26	0.3301	0.2355	0.5834	0.3332	78.78755	0.043955	0.053939	0.097895
27	0	0.4709	0.4083	0.3332	77.14459	0.040939	0.056055	0.096994
28	0	0.2355	1.3617	0.3332	74.1336	0.038048	0.050944	0.088992
29	0.5773	0	0	1.9945	80.69368	0.036126	0.069012	0.105139
30	1.1546	0	0.5446	0.6669	82.47471	0.048059	0.055769	0.103828
31	0.2309	0.3769	0.5446	0.6669	78.34843	0.040707	0.058015	0.098722
32	1.1547	0	1.6333	0.6669	79.17416	0.044886	0.052337	0.097223
33	0.5501	0.7306	0	0.3332	83.44829	0.051586	0.05631	0.107896
34	**1.4434**	**0.3535**	**0**	**0.3332**	**86.62931**	**0.056776**	**0.054342**	**0.111118**
35	0.5773	0.707	1.2245	0.3332	78.59873	0.045841	0.051356	0.097197
36	0	1.1787	0.8169	0.3332	77.41373	0.043996	0.053074	0.097071
37	2.3099	4.9495	0	0.3332	83.60642	0.055183	0.052864	0.108046

38	0.4988	1.0608	2.653	0	76.39766	0.044825	0.047466	0.092291
39	0.8661	1.0608	2.4503	2.9998	77.84734	0.03912	0.058657	0.097777
40	0	0	2.6537	0.8335	73.4341	0.035586	0.051956	0.087542
41	1.0891	1.4147	0.2721	0	83.64887	0.055861	0.050911	0.106773
42	0	0	1.6401	2.3338	75.52369	0.032083	0.062268	0.094352
43	0.8658	1.414	0	0.5	83.26354	0.0519	0.055808	0.107707
44	0.5773	1.4143	1.2245	1.3334	78.84042	0.042971	0.05665	0.099621
45	0	0.707	1.2245	1.9997	76.67063	0.03552	0.061347	0.096867
46	0	2.8285	4.8991	0	75.29423	0.043374	0.047742	0.091116
47	0	0	4.8978	0	72	0.037989	0.044879	0.082868
48	0	1.4143	4.898	0	74.01649	0.041285	0.046632	0.087917
49	0	1.4143	1.2245	2.9988	77.44939	0.036331	0.062591	0.098922
50	0.4931	0.7248	0	0.3332	83.21668	0.05111	0.056552	0.107662
51	0	0.7072	0.5447	0.3332	77.27664	0.042439	0.054593	0.097032
52	0	0.2355	2.1095	0.5	73.79947	0.03744	0.05073	0.08817
53	0	0.2358	0.8162	0.6669	75.56251	0.036106	0.05744	0.093546
54	0	3.5355	1.8372	0.5	77.92904	0.04599	0.052109	0.098098
55	0	0	1.2248	2.6682	76.1123	0.031097	0.065173	0.09627
56	0	1.4137	2.042	1.3341	76.32751	0.03953	0.055435	0.094965
57	2.3099	4.9495	0	0.3332	83.60642	0.055183	0.052864	0.108046
58	0	1.6492	1.6346	1	76.86549	0.041305	0.054802	0.096108
59	0	1.6499	0.7344	0.1332	78.21581	0.047099	0.051572	0.09867
60	0	1.414	0.9184	0.5	77.55218	0.043558	0.054011	0.097569
61	0	0.707	1.2246	0.5	75.85055	0.040199	0.053242	0.093441
62	0	0.9428	0.8169	0.6669	77.14572	0.040941	0.056056	0.096997
63	0	0.4717	1.6338	0.6669	74.97457	0.038073	0.053333	0.091406
64	0	2.3572	0.8169	0.6669	78.56501	0.045271	0.05482	0.100092
65	0	0.9432	1.0212	0.8335	76.8214	0.039953	0.056337	0.096289
66	0	0	2.6537	0.8335	73.4341	0.035586	0.051956	0.087542
67	0	2.8285	2.6541	0.8335	76.8222	0.04325	0.052289	0.095539
68	0	0	2.0414	2.3338	75.20049	0.032625	0.060673	0.093298
69	0	1.4142	0.8169	3.3341	77.88162	0.035703	0.064606	0.100309
70	0	0.707	2.4497	0.3332	74.39611	0.040009	0.049291	0.0893
71	0	0.2355	0.9185	0.5	75.09522	0.037044	0.054944	0.091988
72	0	0.9432	3.0613	0	74.11982	0.041454	0.046721	0.088176
73	0	0.2355	1.47	0.1998	73.74162	0.038753	0.048951	0.087704
74	0	0.2355	0.8169	2.3337	76.76114	0.032082	0.06583	0.097912
75	0	0.2355	1.933	3.3339	76.02059	0.032526	0.063154	0.09568
76	1.1547	0.2355	1.3611	0.3332	80.07369	0.047925	0.050627	0.098552

Table 5.6: The P_{avg} values and the area of triangular faces that constitutes the most close packed interfaces of <110> and <112> growth.

<110> Growth Interface		**<112> Growth Interface**	
Planes	**Area (Å^2)**	**Planes**	**Area (Å^2)**
$(\bar{1}10)$	75.88	$(\bar{1}11)$	31.00
(111)	46.49	(010)	17.89
(101)	75.88	(110)	18.98
$(\bar{1}11)$	46.49	$(1\bar{1}1)$	46.51
Total	244.74	Total	114.38
P_{avg}		**P_{avg}**	
Area Fraction	86.4 %	**Area Fraction**	86.6 %
Total Number Density	0.109 Å^{-2}	**Total Number Density**	0.111 Å^{-2}

Figure 5.1: (a) The zone melting setup (make M/s Pillar India) used for directional solidification and (b) molten sample during the zone melting process.

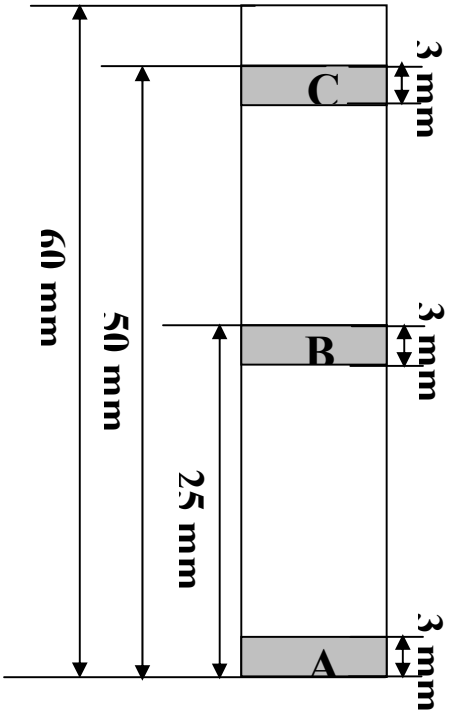

Figure 5.2: Schematic of directionally solidified sample depicting the locations of sample region selected for texture study.

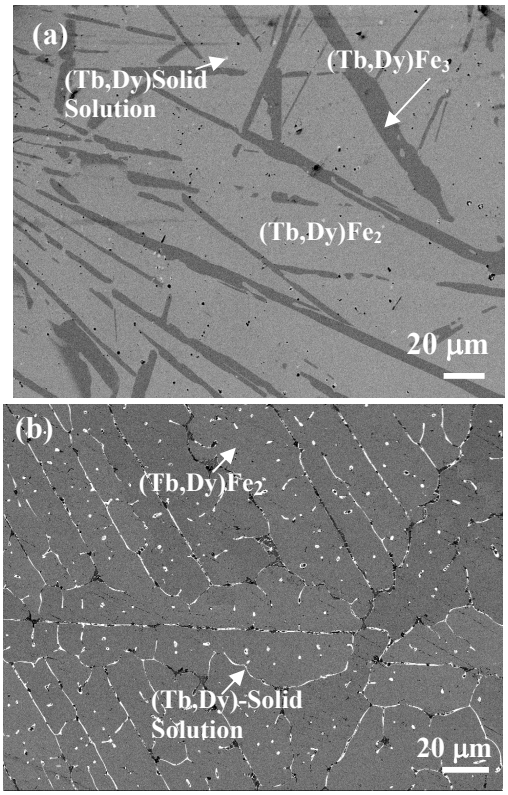

Figure 5.3: Back scattered electron image of (a) as received starting alloy (b) directionally solidified (18 cm/h) samples, exhibiting absence of pro-peritectic phase in directionally solidified sample.

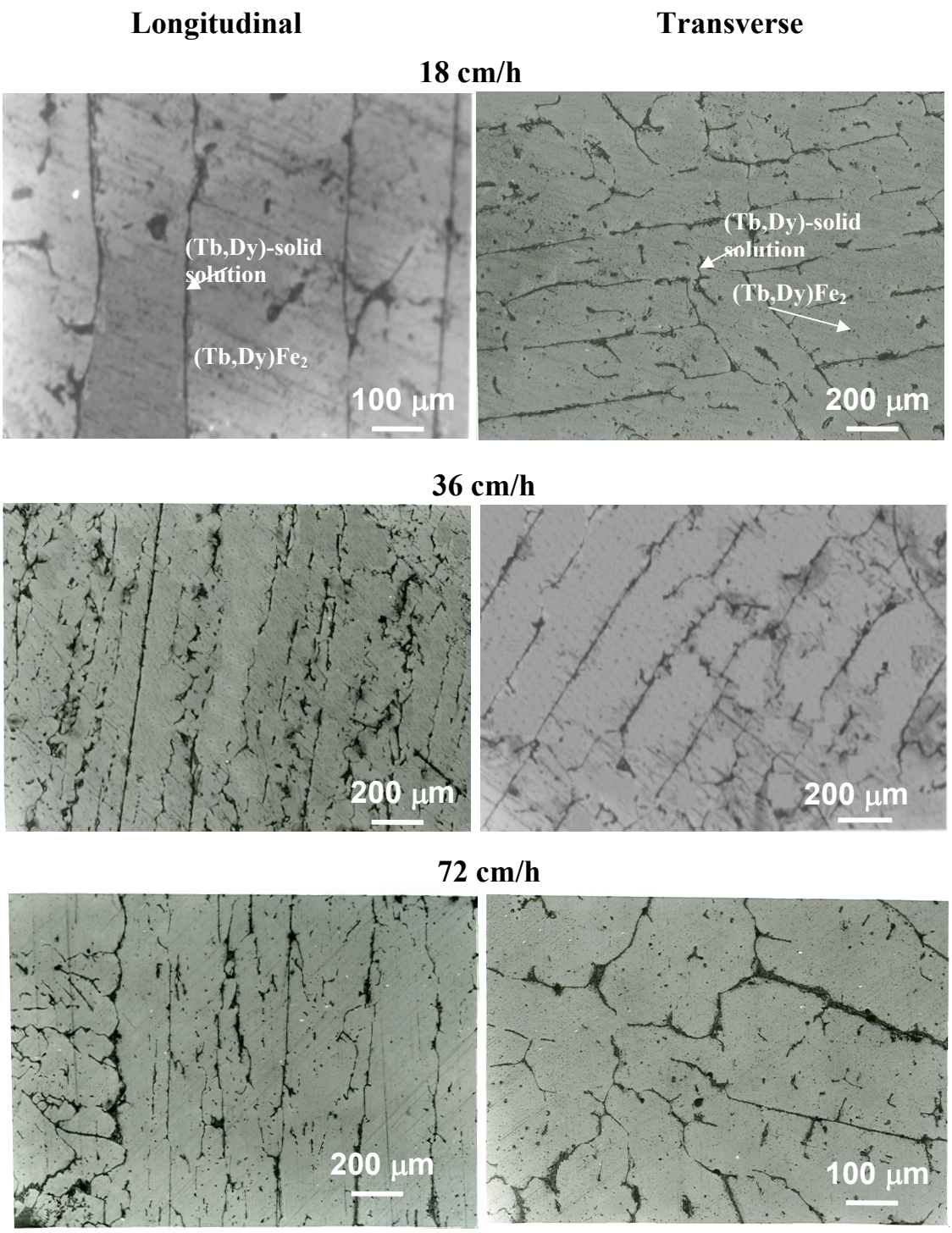

Figure 5.4: Optical micrographs of longitudinal and transverse sections of samples solidified at 18, 36 & 72 cm/h depicting the change in solidification morphology as a function of rate of solidification.

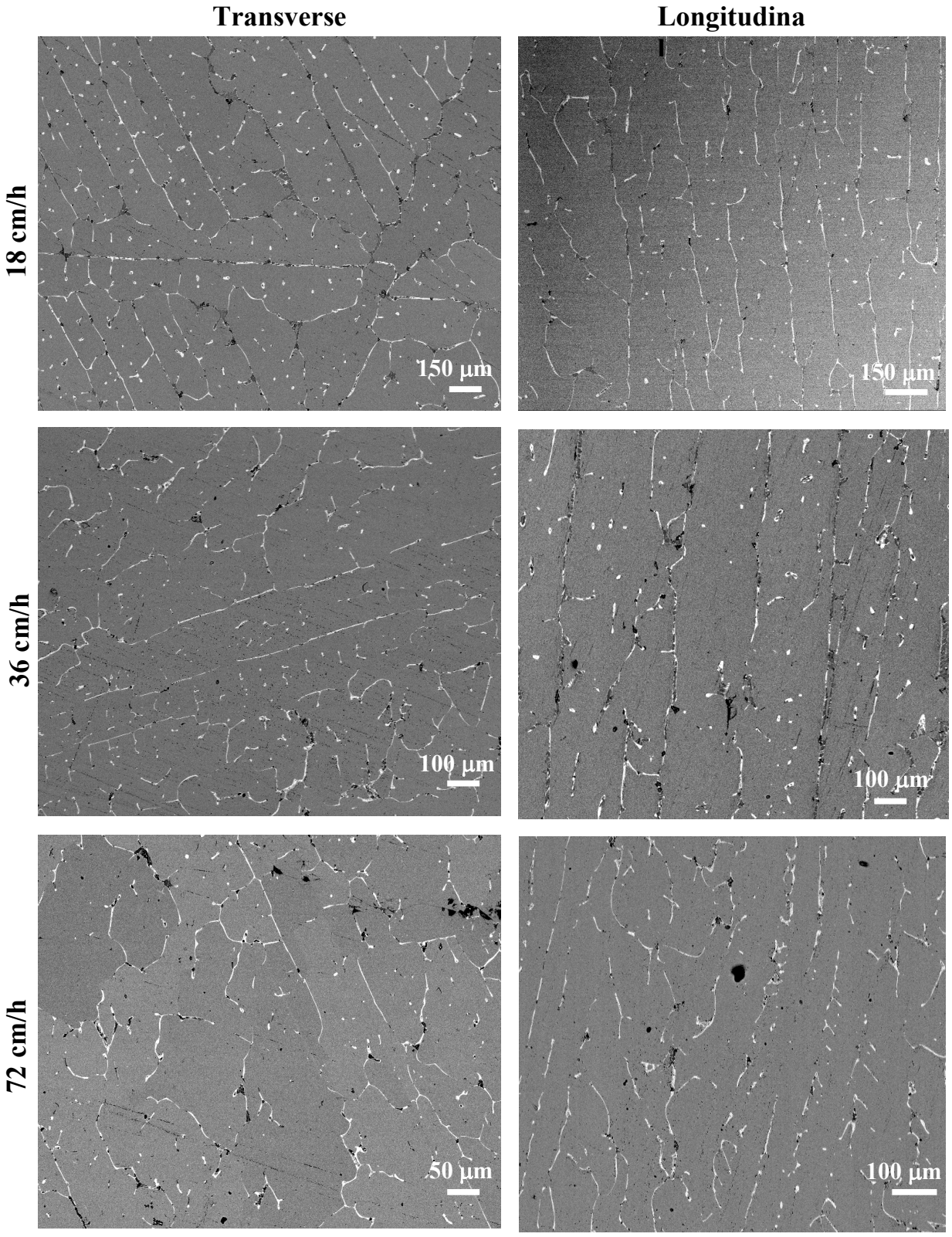

Figure 5.5: Back scattered electron (BSE) image of longitudinal and transverse sections of samples solidified at 18, 36 & 72 cm/h.

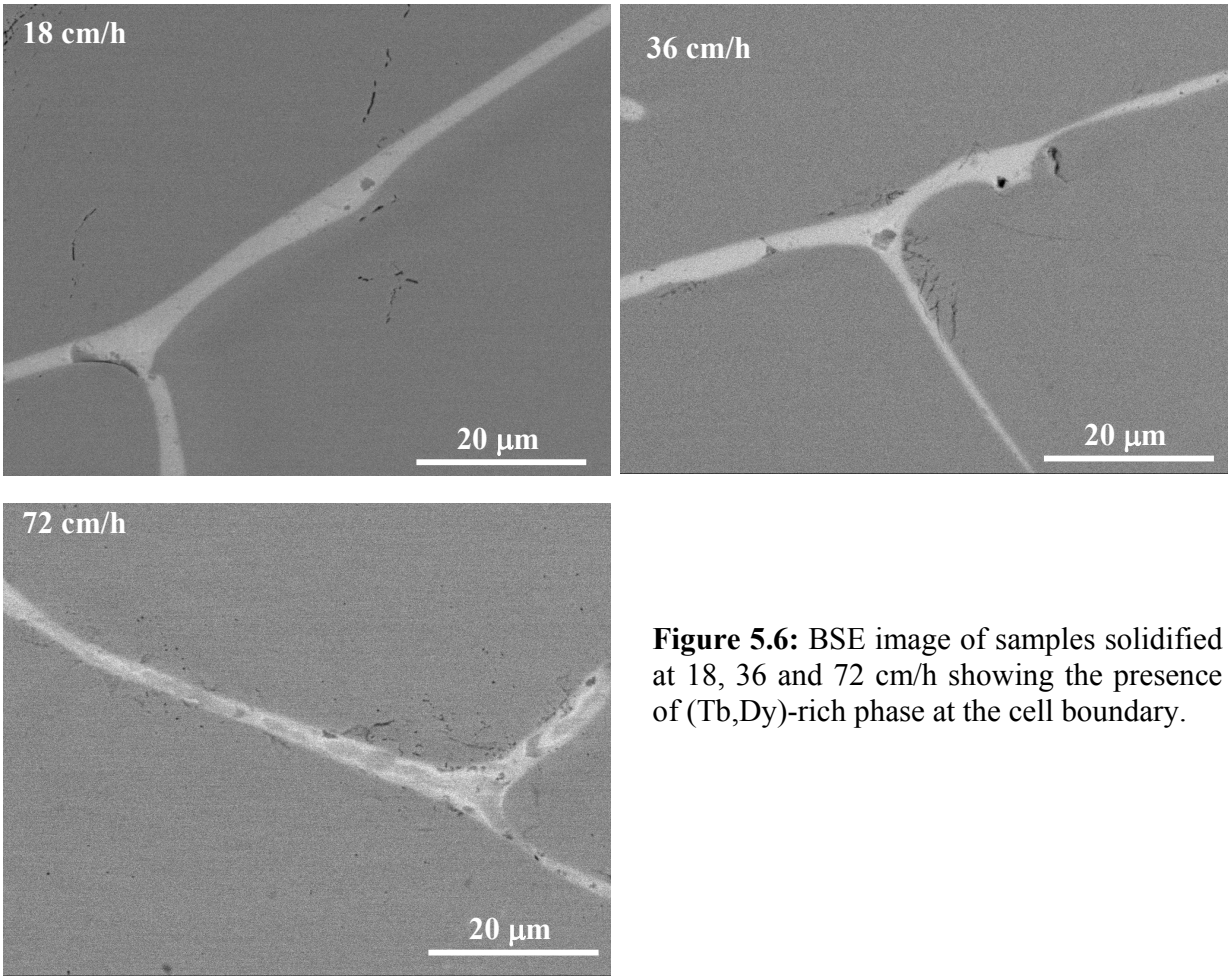

Figure 5.6: BSE image of samples solidified at 18, 36 and 72 cm/h showing the presence of (Tb,Dy)-rich phase at the cell boundary.

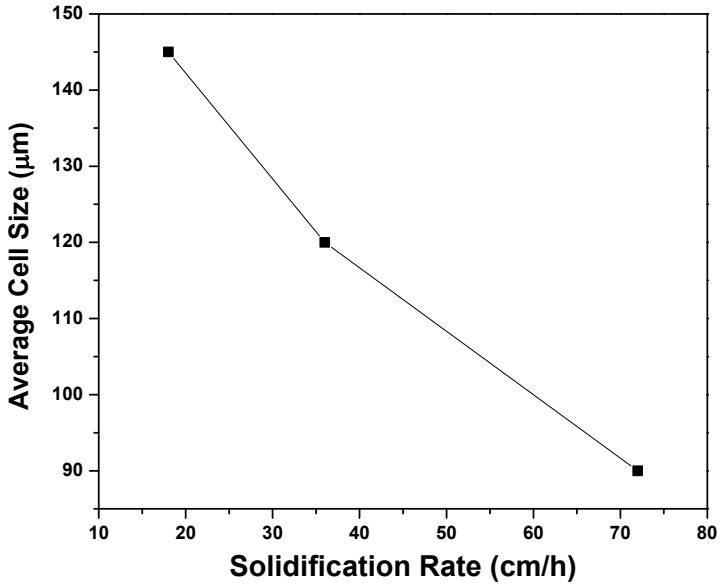

Figure 5.7: The plot of cell spacing as a function of growth rate, indicating the decrease in cell spacing with increase of growth rate.

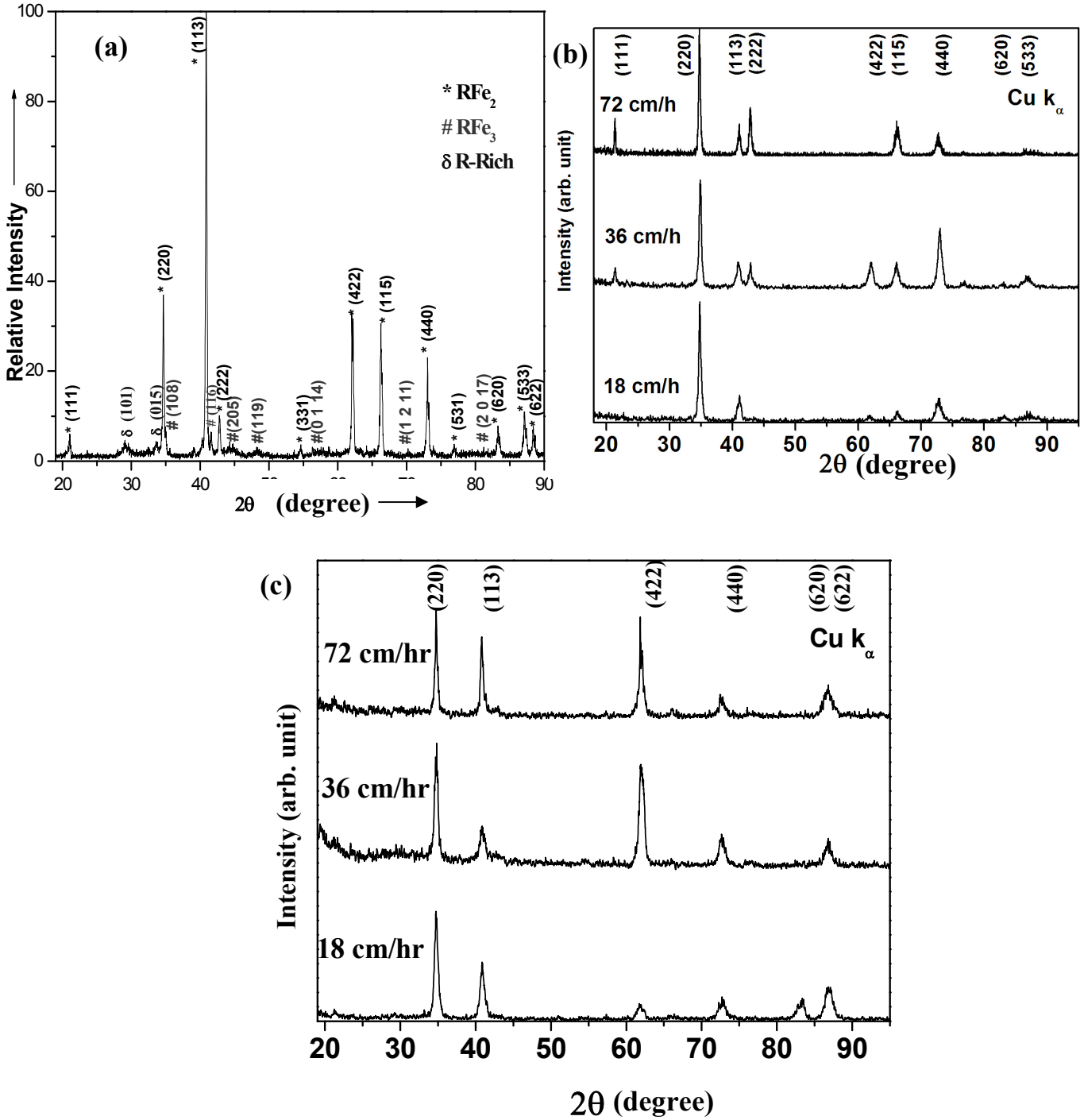

Figure 5.8: X-ray diffractogram of (a) pre-cast powder sample (b) transverse section of region A and (c) transverse section of region B of the directionally solidified rods. The patterns exhibit the change in texture from <110> to <112> with increase in rate of solidification.

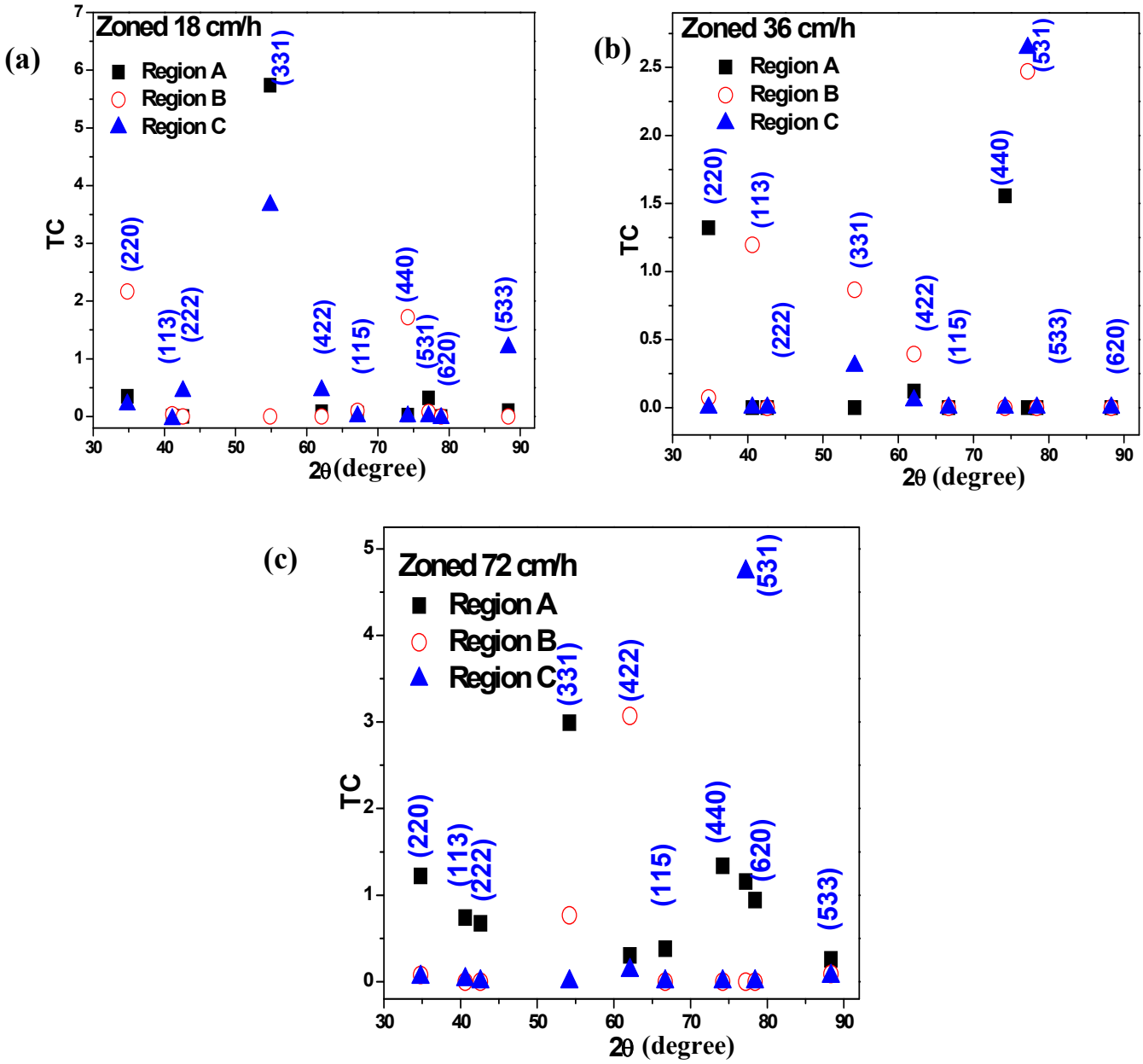

Figure 5.9: Texture co-efficient (TC) as a function of Bragg angle (2θ) for regions A, B and C of the samples solidified at (a) 18 cm/h, (b) 36 cm/h and (c) 72 cm/h.

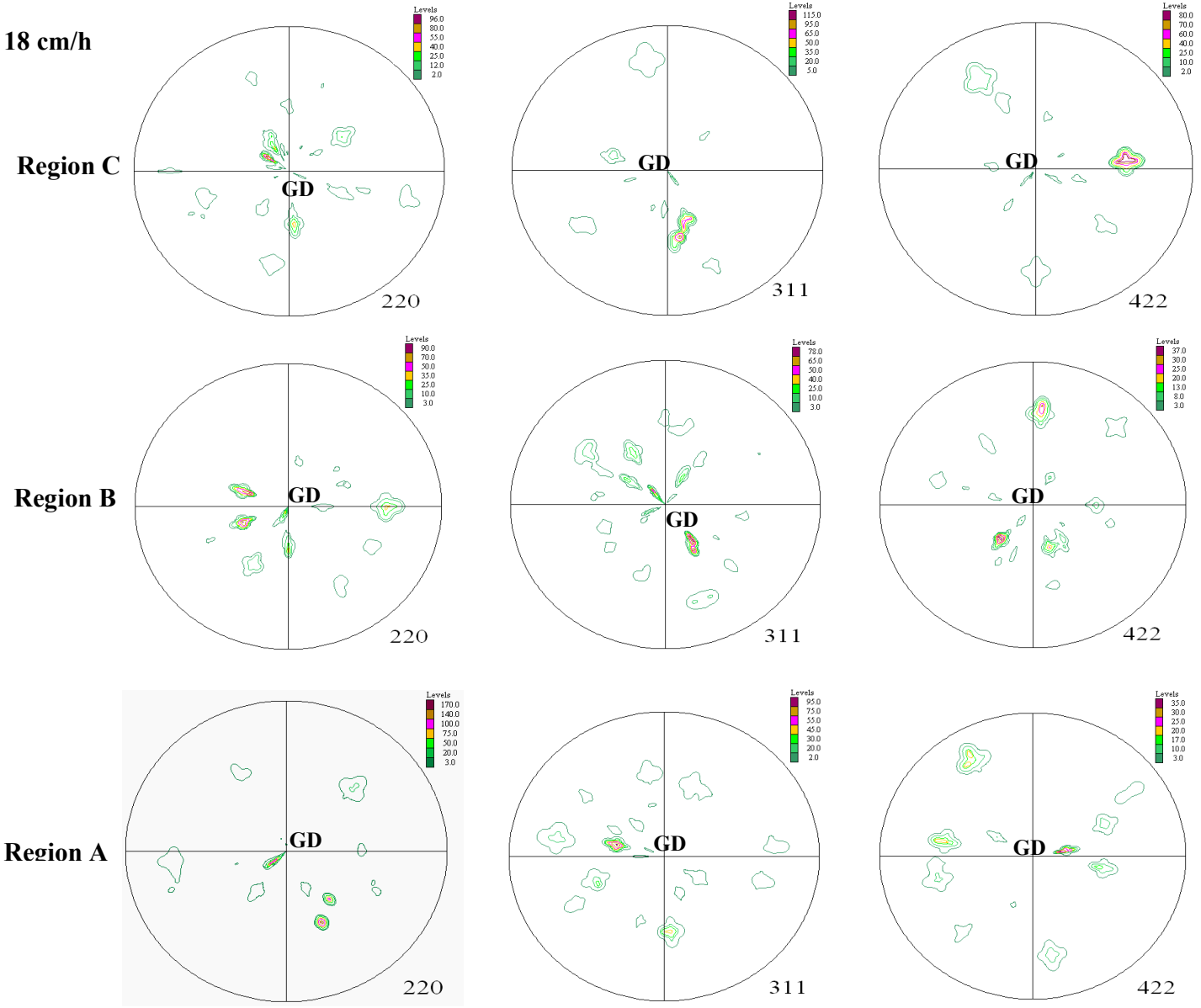

Figure 5.10: (220), (311) and (422) pole figures taken on the transverse section of regions A, B and C of the sample grown at 18 cm/h [GD indicates direction of growth].

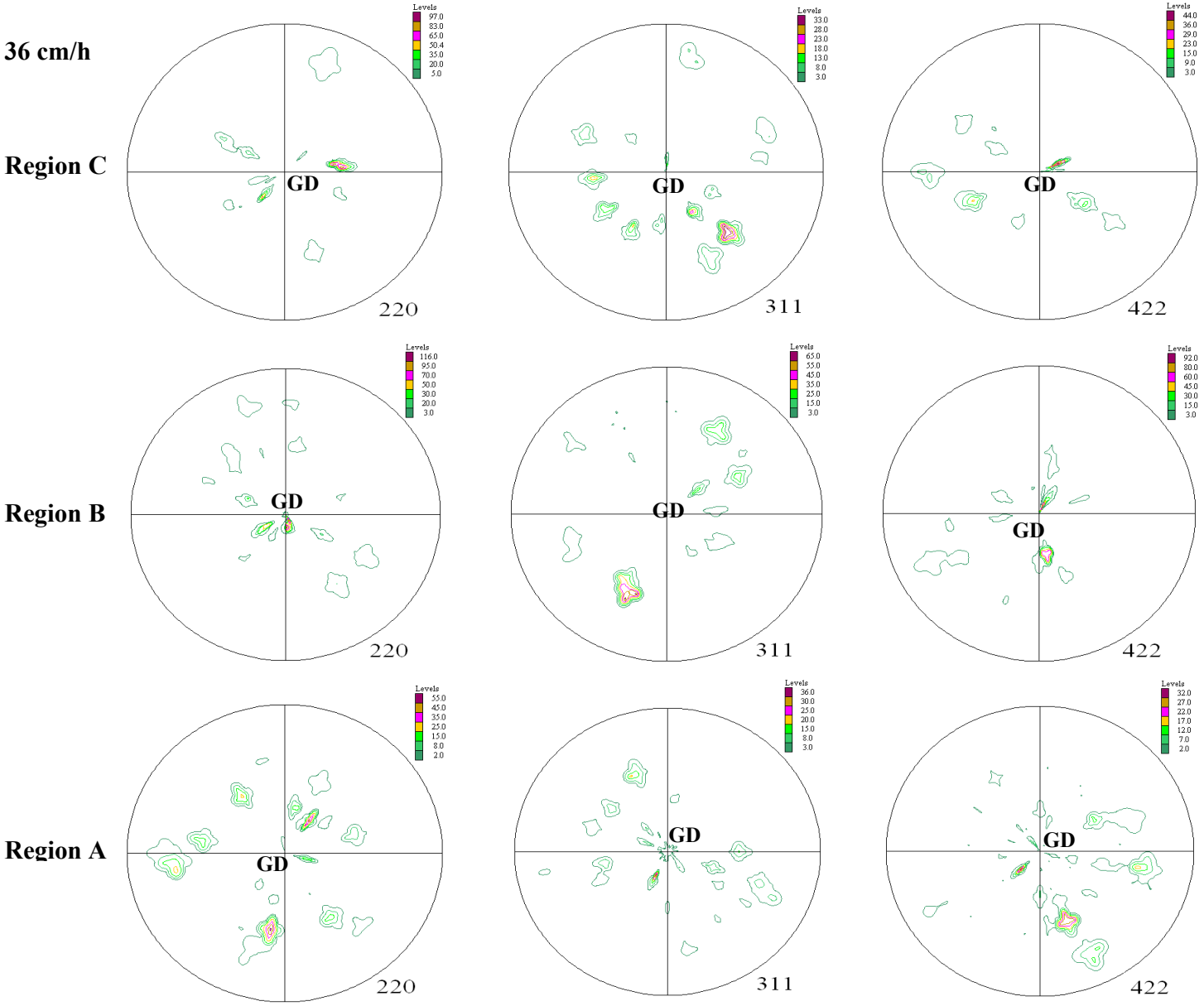

Figure 5.11: (220), (311) and (422) pole figures taken on the transverse section of regions A, B and C of the sample grown at 36 cm/h [GD indicates direction of growth].

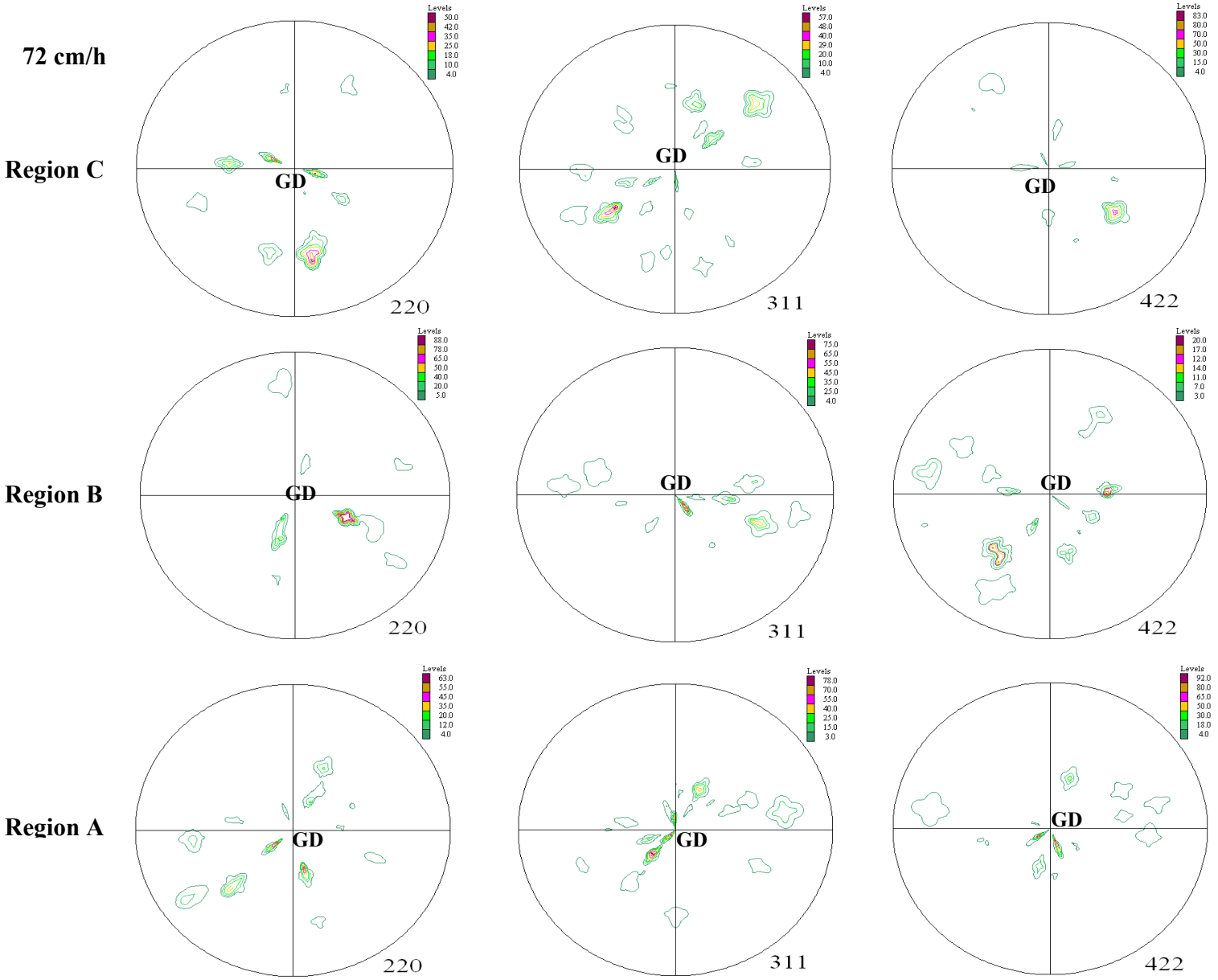

Figure 5.12: (220), (311) and (422) pole figures taken on the transverse section of regions A, B and C of the sample grown at 72 cm/h [GD indicates direction of growth].

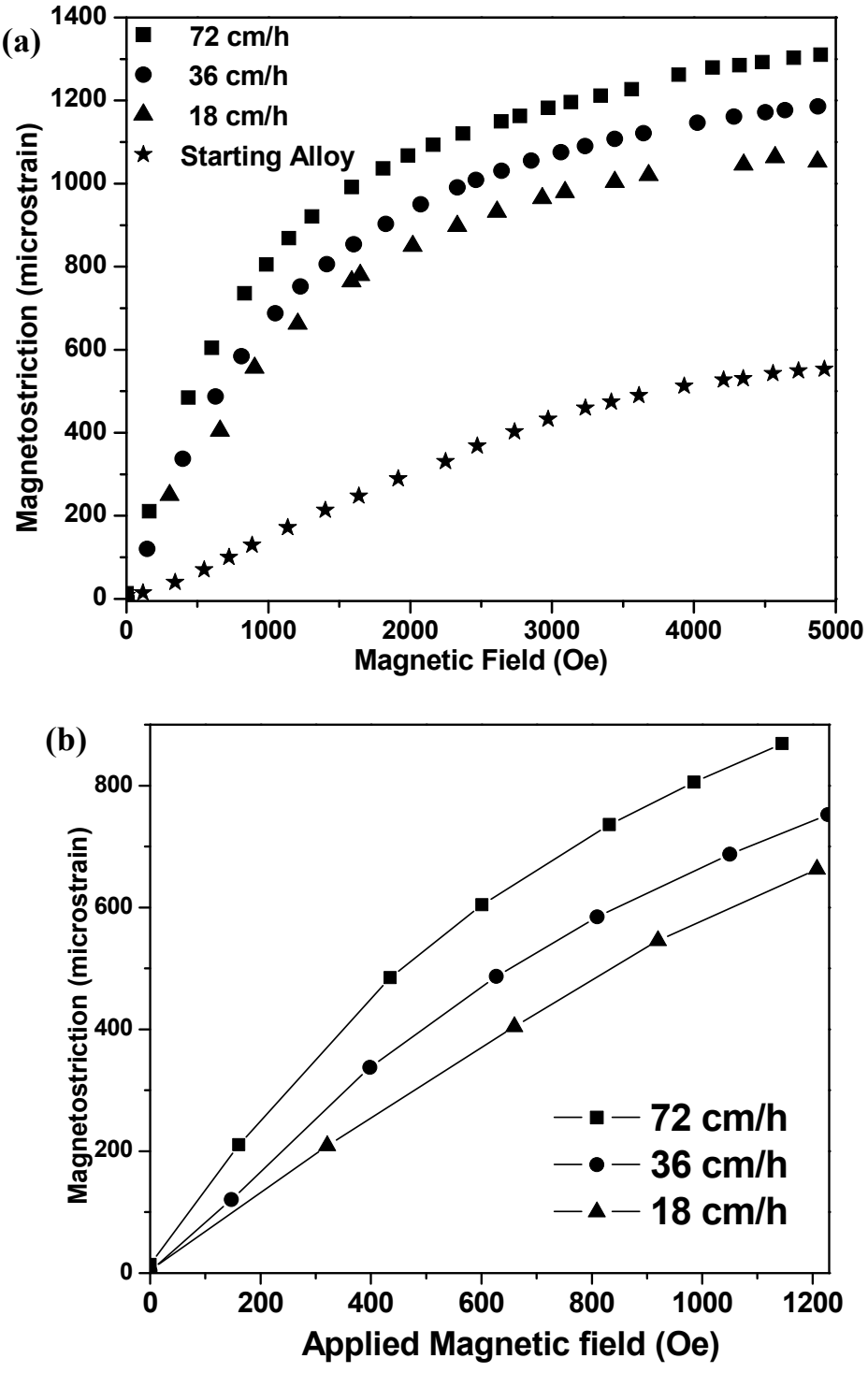

Figure 5.13: (a) Static magnetostriction plots for the starting alloy and directionally solidified samples and (b) exploded view of initial magnetostriction plots.

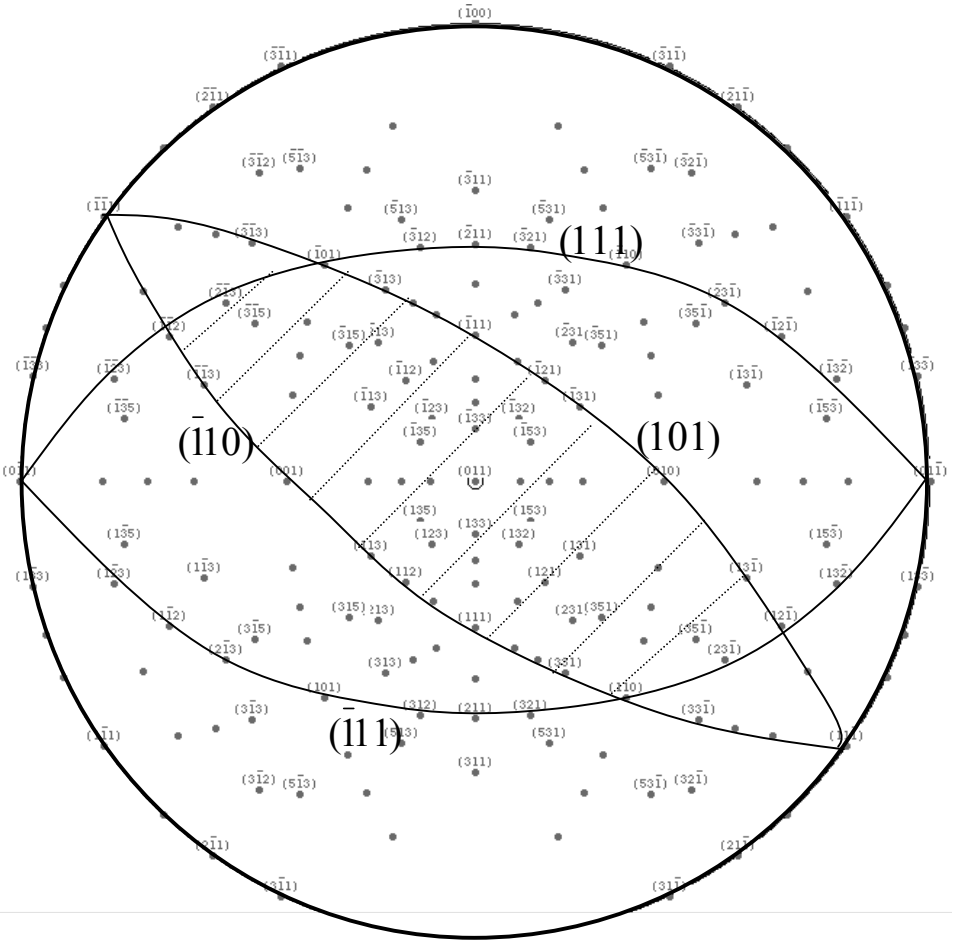

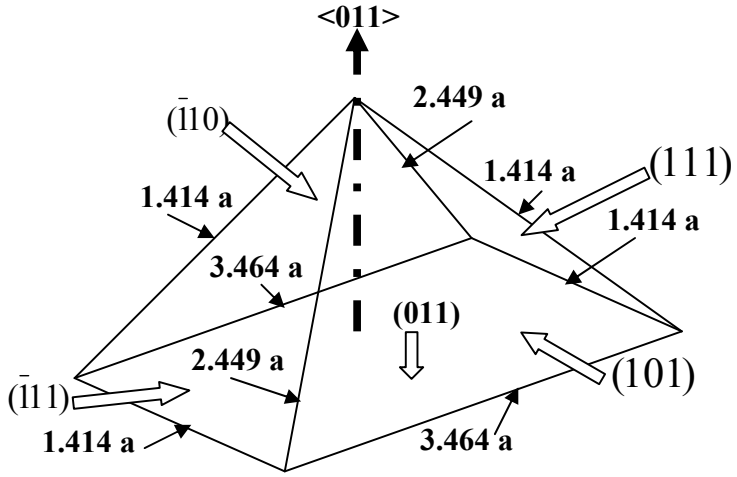

'a' is the lattice parameter of $(Tb,Dy)Fe_2$ having value 7.328 Å

Figure 5.14: A typical example for construction of one of the possible configurations of <110> growth interface from (011) stereographic projection

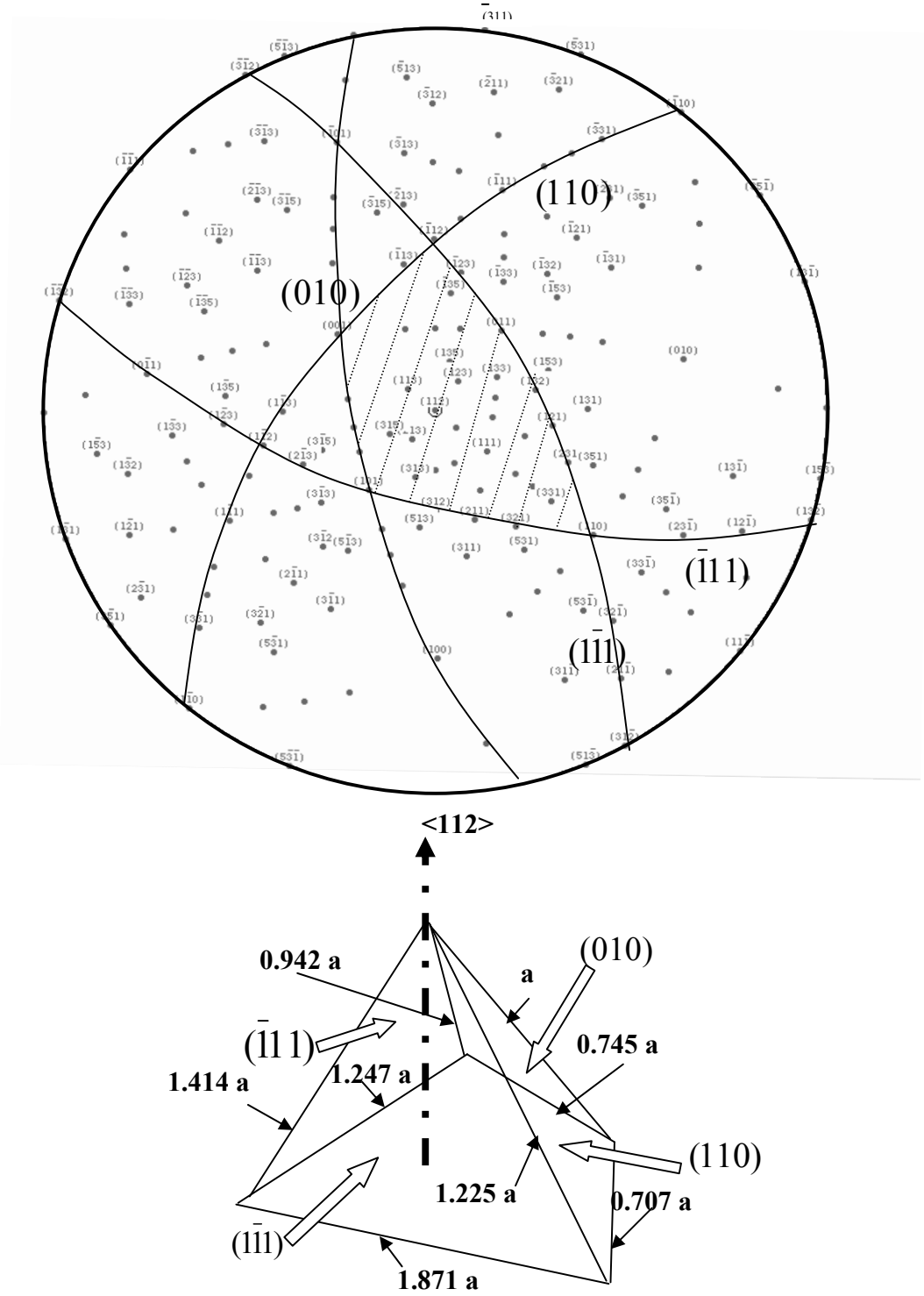

'a' is the lattice parameter of $(Tb,Dy)Fe_2$ having value 7.328 Å

Figure 5.15: A typical example for construction of one of the possible configurations of <112> growth interface from (112) stereographic projection.

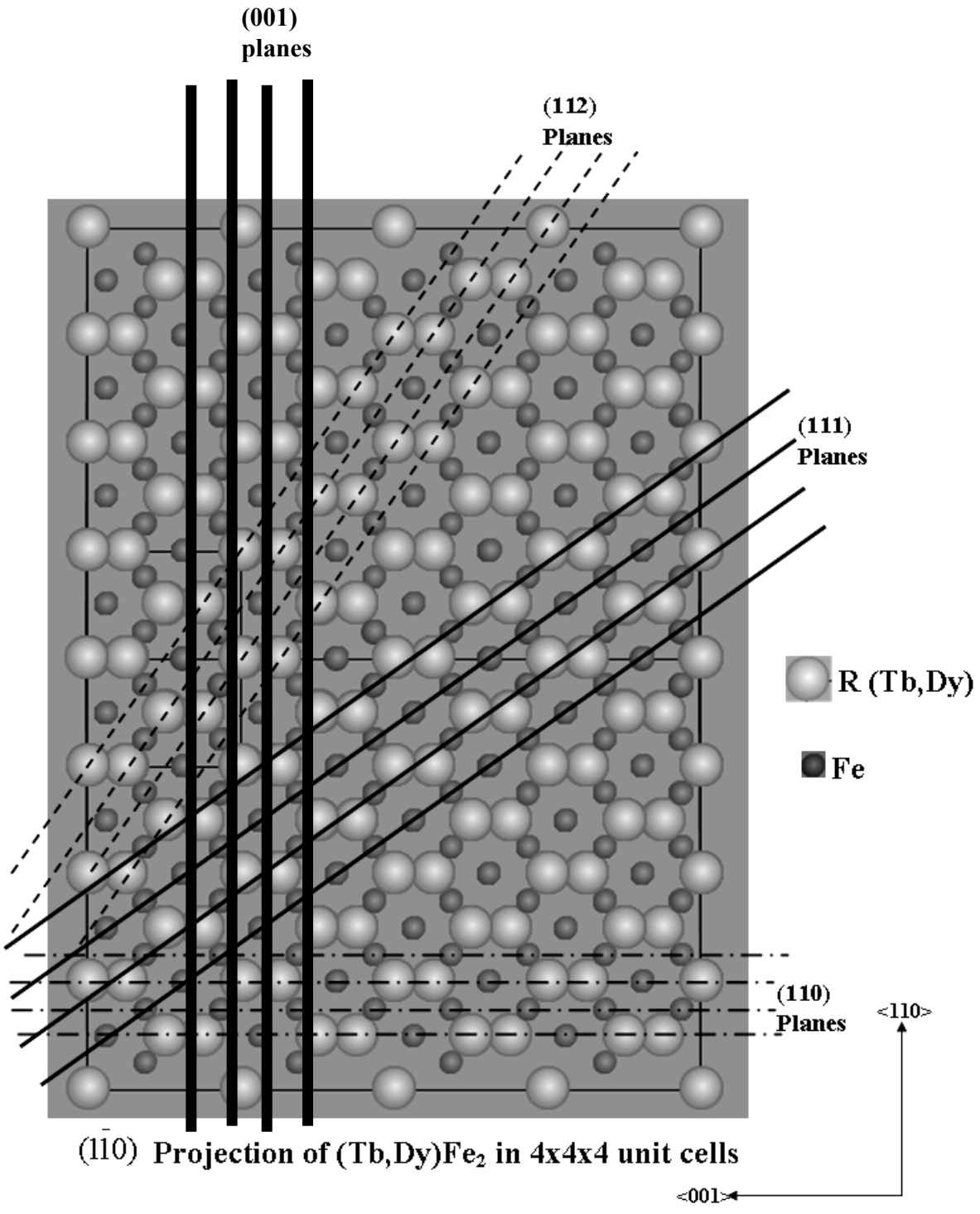

Figure 5.16: Stacking of (110), (111), (112) and (001) planes shown in the $(\bar{1}10)$ projection of a 4x4x4 unit cells of C15 Laves phase $(Tb,Dy)Fe_2$

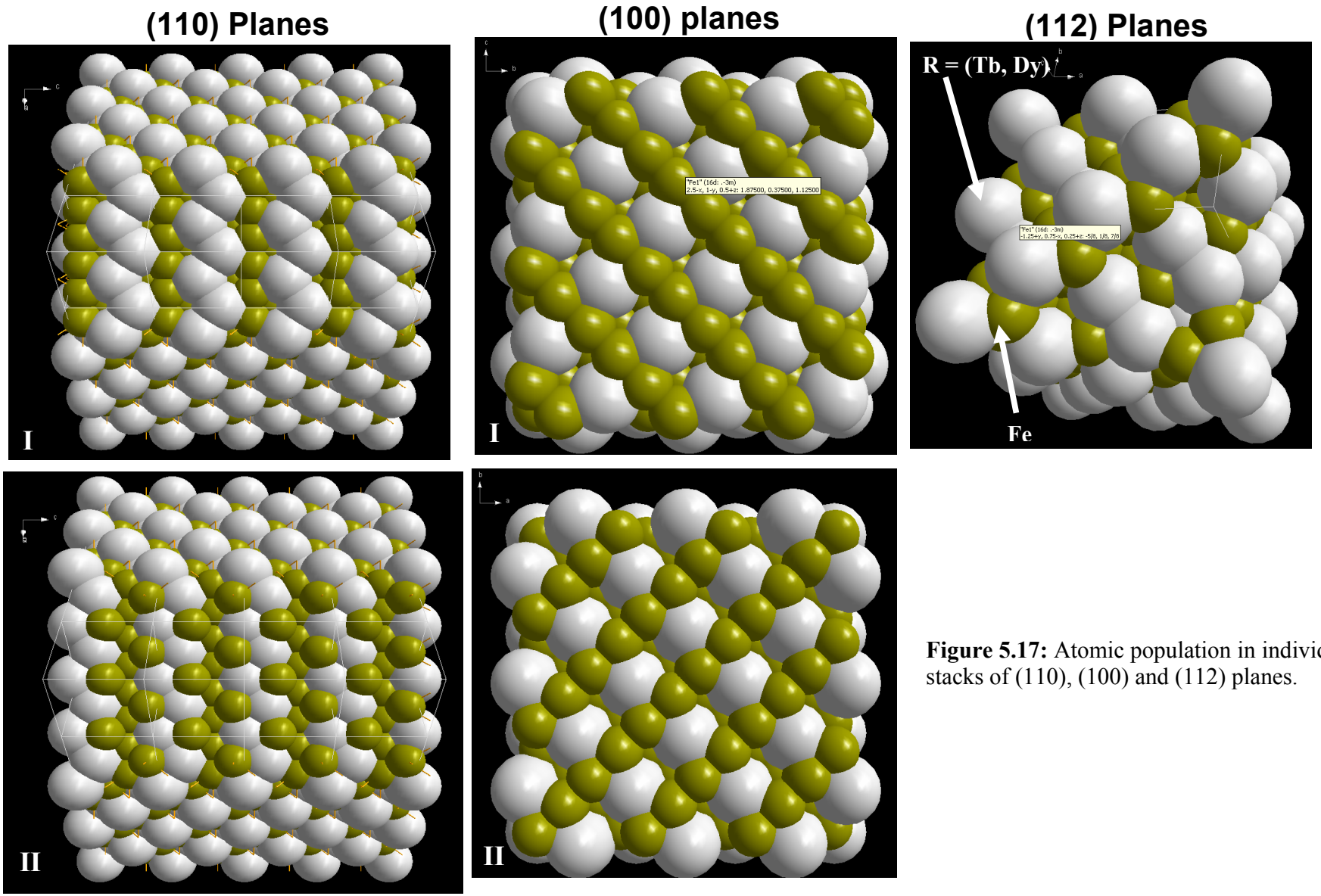

Figure 5.17: Atomic population in individual stacks of (110), (100) and (112) planes.

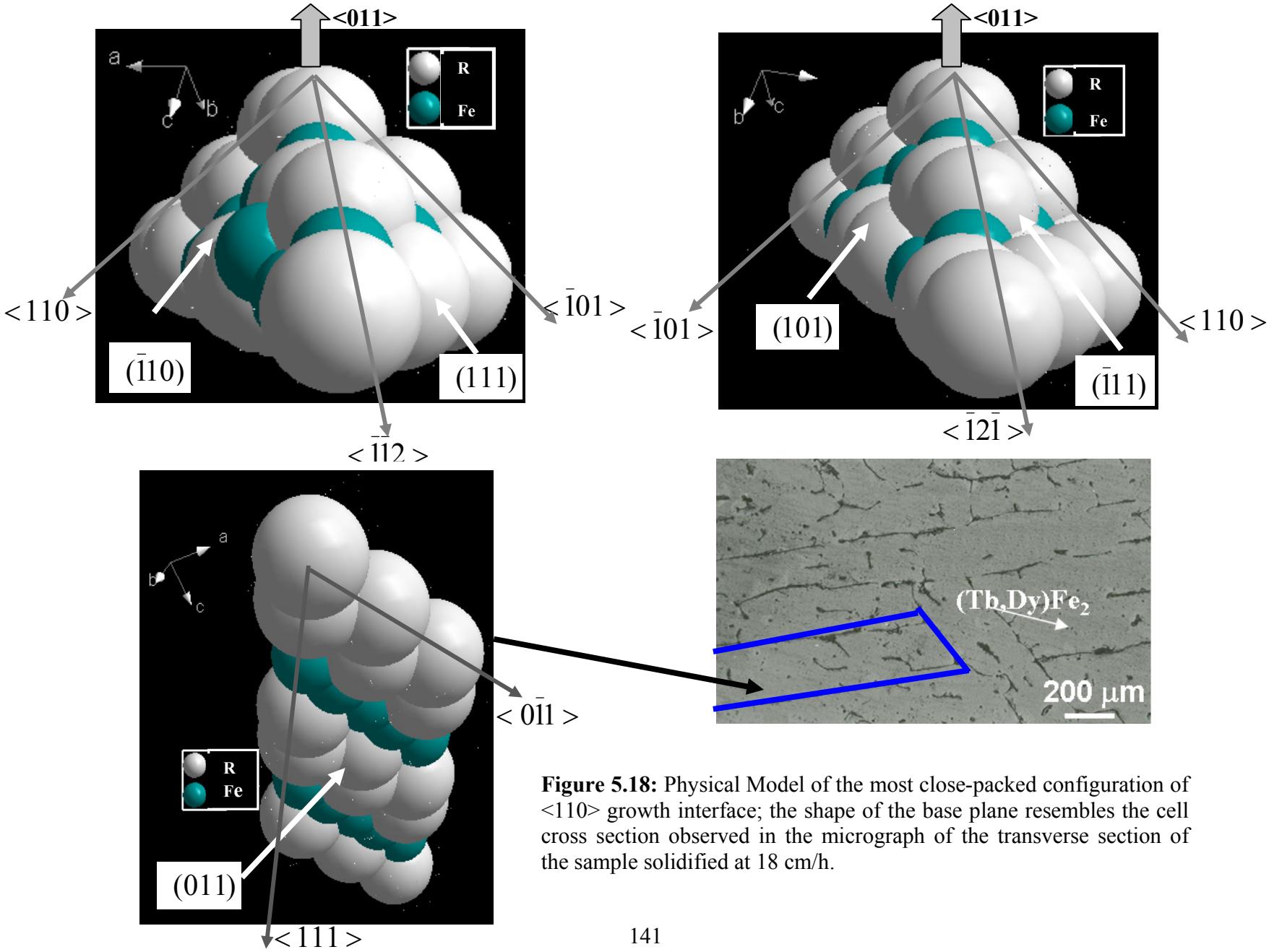

Figure 5.18: Physical Model of the most close-packed configuration of <110> growth interface; the shape of the base plane resembles the cell cross section observed in the micrograph of the transverse section of the sample solidified at 18 cm/h.

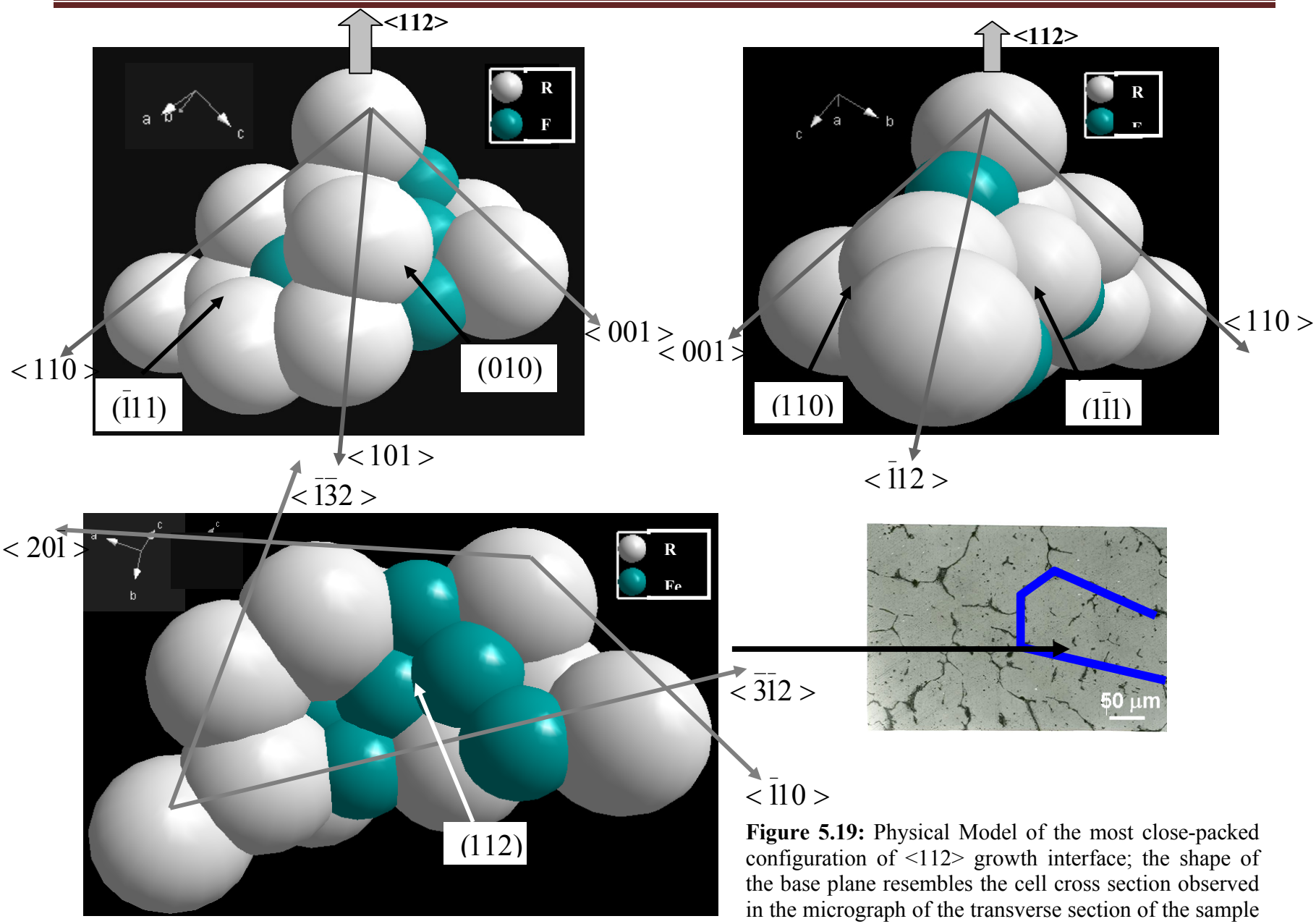

Figure 5.19: Physical Model of the most close-packed configuration of <112> growth interface; the shape of the base plane resembles the cell cross section observed in the micrograph of the transverse section of the sample solidified at 72 cm/h.

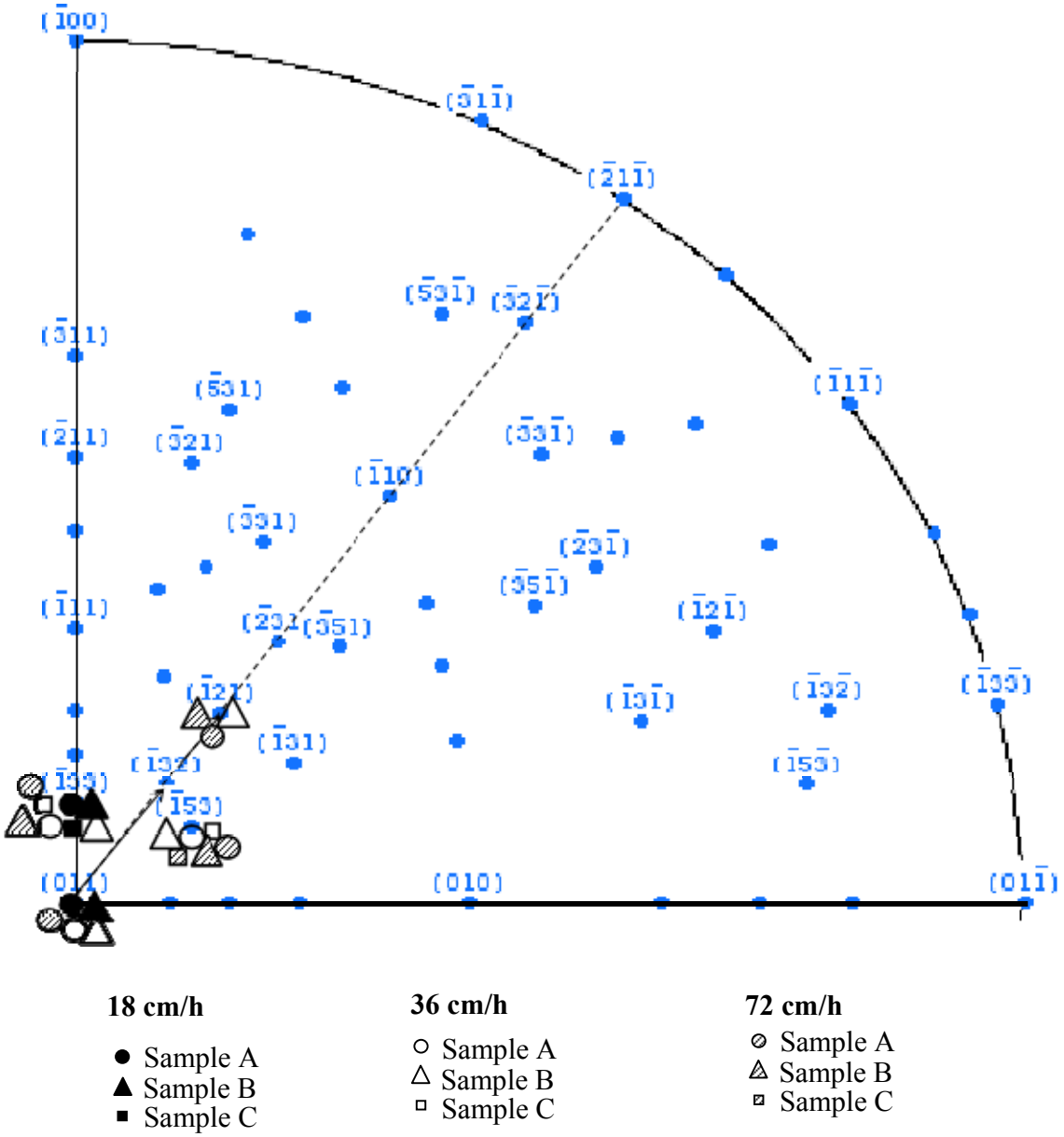

Figure 5.20: Observed texture components of different samples plotted in a quadrant (011) stereogram, depicting the change in preferred orientation from <110> to <112> through intermediate directions.

References:

[1] O D McMasters, *"Method of forming magnetostrictive rods from rare earth-iron alloys"*, US Patents No: 4,609,402 (1986).

[2] M Xhang, X Gao, S Zeng Zhou and Z Shi, *"High performance giant magnetostrictive alloy with <110> crystal orientation"*, J. Alloys and Compd., 381 (2004) 226.

[3] O.D. McMasters, J.D. Verhoeven, E.D. Gibson, *"Preparation of Terfenol-D by float zone solidification"*, J. Mag. Mag. Mat., 54 (1986) 849.

[4] Chengchang Ji, Jianguo Li, Weizeng Ma, Yaohe Zhou, *"Preparation of Terfenol-D with precise <110> orientation and observation of the oriented growth crystal morphology",* J. Alloys Compd., 333 (2002) 291.

[5] Hideki Minagawa, Keiji Kamada, Hideaki Nagai, Yoshinori Nakata, Takeshi Okutani, *"Synthesis of $Tb_{0.3}Dy_{0.7}Fe_{1.9}$ magnetostrictive alloy by unidirectional solidification in magnetic field and microgravity"*, J. Magn. Magn. Mater., 248 (2002) 230.

[6] C Ji, S Zhu, J Li and Y Zhou, *"Solidification characteristics of $Tb_{0.27}Dy_{0.73}Fe_x$ (x=1.8,1.95) alloys during the directional solidification"*, Mat. Sci. Engg. B, 122 (2005) 174.

[7] O.D. McMasters, J.D. Verhoeven, E.D. Gibson, *"Preparation of Terfenol-D by float zone solidification"*, J. Magn. Magn. Mater., 54 (1986) 849.

[8] J.D. Verhoeven, E.D. Gibson, O.D. McMasters, H.H. Baker, "*The growth of single crystal Terfenol-D crystals*", Metall. Trans A., 18 (1987) 223.

[9] W. J. Park, J. C. Kim, B. J. Ye, Z. H. Lee, *"Macrosegregation in Bridgman growth of Terfenol-D and effects of annealing"*, J. Cryst. Growth, 212 (2000) 283.

[10] L. Wu, W. Zhan, X. Chen, *"Directional growth of single crystal Terfenol-D by the electron beam zoning method"*, J. Magn. Magn. Mater., 164 (1996) 367.

[11] Y. Zhao, C. Jiang, H. Zhang, and H. Xu, *"Magnetostriction of <110> oriented crystals in the TbDyFe alloy",* J. Alloys Compd., 354 (2003) 263.

[12] J. D. Snodgrass and O. D. McMaster, "*Optimized TERFENOL-D manufacturing processes"*, J. Alloys Compd., 258 (1997) 24.

[13] Mithun Palit, S. Pandian, R. Balamuralikrishnan, A.K. Singh, Niranjan Das, V. Chandrasekharan, G. Markandeyulu, "*Microstructure and magnetostriction of*

$Tb_{0.3}Dy_{0.7}Fe_{1.95}$ prepared under different solidification conditions by zoning and modified Bridgman techniques", J. Appl. Phys., 100 (2006) 074913.

[14] Mithun Palit, J. Arout Chelvane, S. Pandian, Niranjan Das and V. Chandrasekaran, *"Effect of solidification rate on the microstructural features and magnetostriction of directionally solidified $Tb_{0.3}Dy_{0.7}Fe_{1.95}$*", Scripta Mater., 58 (2008) 819.

[15] Mithun Palit, J. Arout Chelvane, S. Pandian, M. Manivel Raja and V. Chandrasekaran, "*Phase relationship, magnetic properties and Mössbauer studies in as cast and directionally solidified $Tb_{0.3}Dy_{0.7}Fe_{1.95}$",* Materials Char., 60 (2009) 40.

[16] P. Westwood, J. S. Abell, and K. C. Pitman, "*Phase relationships in the Tb-Dy-Fe ternary system",* J. Appl. Phys. 67 (1990) 4998.

[17] B Chalmers, "*Principles of Solidification",* John Willey and Sons, New York (1964) 119.

[18] M.C. Flemings, "*Solidification Processing"*, McGraw-Hill, New York (1974) 159.

[19] W. Mei, T. Okane, T. Umeda, and S. Zhou, *"Directional solidification of Tb-Dy-Fe alloy"*, J. Alloys Compd., 248 (1997) 151.

[20] D. Watson and B. Chalrners, *"Crystal size and orientation in the columnar zone"*, Trans. Metall. Soc. AIME, 215 (1959) 447.

[21] W.A. Tiller, *"Preferred Growth Direction of Metals"*,Trans AIME, 209 (1957) 847.

[22] B. D. Cullity, *"Elements of X-Ray Diffraction"*, Addison-Wesley Publishing Company, Reading, MA (1978).

[23] Tomorr Haxhimali, Alain Karma, Fre´De´ Ric Gonzales and Michel Rappaz, *"Orientation selection in dendritic evolution",* Nature materials, 5 (2006) 660.

Chapter 6

Microstructure and magnetostrictive property of Fe-Ga alloys

6.1. Introduction:

The discovery of Fe-Ga [1] alloys as a potential magnetostrictive material opened up a possibility to use this material as an alternative to conventionally used sensor/ actuator materials such as Terfenol-D [2-7]. The rare earth based Terfenol D though possesses high magneto-mechanical energy, posed to the research community several challenges such as poor mechanical property, reactivity and high cost. These challenges can be overcome in Fe-Ga alloys and thereby it can be best exploited for sensor and actuator applications with superior device design. Further the material exhibits unique properties such as weak dependence of magnetostriction on temperature [8,9] and a low magnetic field for saturation [10] which makes it promising for future actuator applications.

Several attempts [11-20] have been made to understand the structure-property relationship in this system and it has been observed that the variation in the field dependent magnetostriction of Fe- x at% Ga (x =17-30) is strongly dependent on composition. Number of reports on single crystal alloys of 17-30 at% compositions reveal [3,8,18,20] that the magnetostriction peaks at 20 at% and 27 at% compositions. The two peak behavior is also found to vary based on thermal history of the material [3,8,13,18]. In order to understand the two peak behavior, researchers resorted to experimental [3,8,18-20] as well as theoretical approach [21-23] to understand the relationship of magnetostriction with microstructure. However, a clear picture is yet to emerge on phase transformations and the effect of different phases on magnetostriction. Several reports indicate detrimental role of ordered phases on magnetostriction [13,15,18]. On the contrary, some indicates beneficial role of ordered DO_3 phase [19]. Wuttig *et.al.* [2] reported elastic softening of Fe with Ga addition and attributed the second peak of magnetostriction to this phenomenon.

Most of the studies reported in literature were carried out on single crystalline alloys [11-20]. However, from the perspective of future application potential of this class of material, it is important to understand the nature of phase transformation and resultant microstructure in a polycrystalline alloy. In this context, this study has been taken up to

investigate the microstructural features and magnetostriction of polycrystalline Fe-x at% Ga (x=17, 20, 23 and 25) alloys having different thermal history. The objective of the study is to understand the nature of phase transformation and to elucidate the structure-property relationship.

6.2. Experimental Details:

Alloys with nominal compositions Fe-x at% Ga (x=17, 20, 23 and 25) were prepared by vacuum arc melting of constituent elements of purity > 99.5%. The compositions selected for this study are marked on the equilibrium and metastable phase diagrams (Fig. 6.1) of Fe-Ga [5,7]. A vacuum arc melting furnace of the make M/s Vacuum Techniques, India was used for this purpose (Fig. 6.2). After evacuating the chamber to a vacuum level of 5 x 10^{-5} mbar, the chamber was partially filled with Ar gas and the melting was carried out by striking an arc from a tungsten electrode. Melting was carried out for five times after flipping the alloy button in each melt to get homogenous composition. Subsequently, cylindrical rods of 6 mm ϕ x 40 mm length were machined out of arc melted button by wire cut EDM.

The cylindrical rod samples were subjected to a thermal treatment at 1000^{o}C for 5 hrs after vacuum sealing inside quartz tube ampoules. One set of samples was furnace cooled to room temperature, whereas the other set was water quenched. The quartz ampoules were broken inside water bath to ensure high cooling rate experienced by the samples. The quenched samples were also annealed at 480^{o}C upto 8 h. The microstructure of the heat treated samples was characterized using optical microscope, FEI Quanta 400 E-SEM scanning electron microscope (SEM) and Technai G2 Transmission Electron Microscope (TEM). The samples for observation in optical microscope and SEM were prepared using standard metallographic technique and the polished samples were etched with a solution of Methanol + 10% (V/V) HNO_3. The samples for TEM were prepared by electro-polishing technique at -30^{o}C with a mixed acid solution (78% Methanol + 10 % Lactic acid + 7% H_2SO_4 + 3% HNO_3 + 2% HF) as electrolyte. The surfaces of the electro-polished foils were cleaned in a GATAN make precision ion polishing stage (PIPS) just before TEM investigations. The magnetization was measured at room temperature using vibrating sample magnetometer and the magnetostriction was measured using magnetic field and temperature compensated resistance strain gauge.

6.3. As cast alloys:

The optical micrographs of the as cast Fe-Ga alloys are shown in Figure 6.3. The micrographs exhibit formation of grains of average size ~150 μm and the grain size is not found to vary significantly with composition. The XRD patterns of the as cast samples are shown in Figure 6.4, where peaks corresponding to α-Fe are observed. The lattice parameter of α-Fe phase increases with addition of Ga (Fig. 6.5). The α-Fe phase is having disordered BCC (A2) structure and will be termed hereafter as A2 phase. Although, the equilibrium as well as metastable phase diagrams (Fig. 6.1) predicts formation of ordered phases such as $L1_2$ or DO_3 along with A2 phase, such ordered phases could not be detected from XRD plots. We note that similar atomic scattering factor of Fe and Ga results in low intensity of superlattice reflections, thus making the detection difficult. The magnetization plots of Fe-Ga alloys as a function of applied magnetic field are shown in Figure 6.6. The saturation magnetization is found to decrease with increase of Ga concentration (inset of Figure 6.6).

6.4. Samples furnace cooled from 1000^{o}C:

The micrographs of the furnace cooled Fe-17 at% alloy are shown in Figure 6.7. The secondary electron image using SEM (Fig. 6.7a) reveals presence of single phase with equiaxed grains. The selected area diffractions (SAD) along [001] and [011] zone axes (Fig. 6.7 b & C) reveal presence of weak superlattice reflections corresponding to B2 and DO_3 ordering. The dark field micrograph obtained using DO_3 superlattice reflection (111) (Fig. 6.7 d) shows distribution of fine scale domains. Similar contrast has also been observed while imaging with (200) superlattice reflection of the B2 phase. Since, the B2 and DO_3 domains do not exhibit any difference in appearance; it indicates that A2 phase has transformed directly to DO_3 during slow cooling from 1000^{o}C to yield A2+DO_3 phase mixture. The SADs are indexed in this case with respect to larger lattice of DO_3.

The micrographs of furnace cooled Fe-20 at% Ga alloy are shown in Figure 6.8a. Similar to the Fe-17 at% alloy, the SEM micrograph reveals presence of single phase with equiaxed grains. In this case also, the superlattice reflections corresponding to B2 and DO_3 ordering is evident from the SAD obtained along [001] and [011] zone axes (Fig. 6.8 b &c). Similar to the Fe-17 at% Ga alloy, this alloy also does not exhibit difference in appearance of B2 and DO_3 domains which indicates transformation to yield A2 + DO_3 phases during cooling

The micrographs of the furnace cooled Fe-23 at% Ga alloy are shown in Figure 6.9. As observed in earlier cases the SEM micrograph (Fig. 6.9a) does not reveal presence of any second phases. The diffraction patterns again indicate the presence of DO_3 phase (Fig. 6.9 b & c). Similar microstructural observations can also be made from the micrographs of furnace cooled Fe-25 at% Ga alloy (Fig. 6.10).

6.5. Quenched and aged samples:

The micrographs of Fe-17at% Ga alloy water quenched from 1000^{o}C are shown in Figure 6.11. The micrographs of the quenched sample after 8 hrs of ageing are also shown in the same figure (Fig. 6.11). The SAD patterns of the quenched sample obtained along [001] and [011] zone axes exhibit only fundamental reflections of a BCC lattice without any superlattice reflection. Thus, the quenched Fe-17at% alloy contains only A2 phase which remains untransformed due to quenching from high temperature. The bright field image of the quenched alloy is also free from any anomalous contrast indicating absence of ordered phases. Therefore, the SADs in this case have been indexed with respect to smaller lattice of A2 instead of indexing it with respect to DO_3 phase. The SAD patterns of the aged Fe-17at% Ga alloy also exhibit absence of superlattice reflections (Fig. 6.12) indicating presence of only disordered A2 phase. Since, DO_3 phase is absent; the SADs in this case also have been indexed with respect to smaller lattice of A2.

The micrographs of quenched and aged samples of Fe-20at% Ga alloy are shown in Figure 6.12. Similar to the previous sample, the [001] and [011] SADs obtained from quenched sample also exhibits only fundamental reflections from A2 phase, indicating absence of ordered phases such as B2 or DO_3. Contrasting to the observation in aged sample of Fe-17 at% alloy, aged Fe-20at% alloy exhibits presence of (111) superlattice reflections of DO_3 phase in addition to (200) reflections (Fig. 6.12). Therefore, ageing results in formation of DO_3 type ordering in Fe-20at% alloy. Since, DO_3 phase is absent in the quenched sample, the SADs have been indexed with respect to smaller lattice of A2, whereas the indexing has been carried out with respect to bigger lattice of DO_3 in case of aged sample.

The micrographs of the quenched Fe-23 at% alloy and Fe-25 at% alloy are shown in Figure 6.13 and Figure 6.14 respectively. The [001] and [011] SADs of these alloys indicate presence of strong superlattice reflections of DO_3 ordered phase (Figs. 6.13 and 6.12). The dark field imaging with (111) superlattice reflection of DO_3 displays fine domain structure

(Figs. 6.13 and 6.14). The microstructure of these two alloys does not change appreciably with ageing.

6.6. Phase transformations in Fe-x at% Ga alloys (x=17, 20, 23 and 25):

The microstructural features observed in this study indicate that the phase formation during heat treatments follows metastable phase diagram (Fig. 6.1b) instead of equilibrium diagram (Fig. 6.1a). The equilibrium diagram predicts formation of $L1_2$ ordering for the studied compositions, which is not observed even by slow cooling. It has been predicted earlier [21-23] by theoretical studies that the transformation from DO_3 to $L1_2$ is very sluggish and occurs through a series of intermediate phases. As a result, the formation of $L1_2$ phase could not be observed in this study, which is in agreement with earlier observations [18]. Therefore, the metastable phase diagram shown in Figure 6.1b is appropriate to explain the phase formation observed by microstructural investigations.

According to the metastable phase diagram, the Fe-17at% alloy should exhibit A2 + DO_3 phase at room temperature and the same has been observed in the microstructure of furnace cooled Fe-17 at% Ga alloy. The superlattice reflections corresponding to DO_3 phase are weak owing to less volume fraction of the ordered phase at room temperature. This is in contrary to the observation of single phase A2 in slow cooled single crystal of Fe-17 at% composition reported by Datta et. al and Xing et.al. [13,18]. The quenched alloy of this composition exhibits no ordering as the microstructure shows presence of single phase A2. The microstructure of the slow cooled Fe-20at% Ga alloy also corroborates to the metastable phase diagram and a presence of DO_3 phase is noticed in the microstructure. The ordering in this case also could be prevented by quenching. The quenched alloy on ageing at 480^{o}C however shows formation of DO_3 phase, as the point 480^{o}C for Fe-20at% Ga composition lies completely within A2+DO_3 phase field.

The earlier studies on phase transformations around tri-critical point reported in similar alloy systems *viz.* Fe-Al [24], Fe-Si [25] indicates that the A2$\rightarrow$ DO_3 transformation generally occurs through formation of B2 as intermediate phase. However, in case of 17 and 20 at % Ga alloys of the present study, the DO_3 phase forms directly from the A2 phase and the transformation is understandably is of first order type and therefore expected to proceed by nucleation and growth. Since, nucleation and growth transformations are diffusion

limited; the A2→A2+DO_3 transformation could be suppressed by quenching of 17 and 20 at% Ga alloys. In case of 23 and 25 at % Ga alloys, the phase transformation kinetics is different. In these cases, the A2 phase undergoes two successive continuous ordering transformations *i.e.* A2→B2 and B2→DO_3. The kinetics of continuous ordering is very fast and as a result, formation of DO_3 phase could not be suppressed during quenching of 23 and 25 at % Ga alloys.

Since, most of the previous studies [11-20] have been carried out on single crystal specimens, a significant difference in phase transformation has been observed in the present study, which has been carried out on a polycrystalline starting alloy. The difference is especially pronounced in 17 and 20 at% alloys. In single crystal, slow cooled samples of these compositions did not exhibit formation of DO_3 whereas in the present study DO_3 formation is observed. As discussed earlier the A2→ A2+DO_3 transformations in these alloys occurs by nucleation and growth kinetics and therefore in a polycrystalline samples the nucleation becomes easier owing to presence of pre-existing grain boundaries and as a result DO_3 formation becomes easier in polycrystalline samples.

6.7. Magnetostriction:

The saturation magnetostrictions (λ_{sat}) of the samples having different thermal history are plotted in Figure 6.15. It can be observed that the magnetostriction of the quenched Fe-17at% Ga and Fe-20at% Ga alloys are more compared to furnace cooled and aged samples. Whereas, the λ_{sat} of quenched Fe-23at% Ga alloy is less compared to furnace cooled or aged alloys. The λ_{sat} of furnace cooled Fe-25at% Ga alloy is in the same range with aged alloy, whereas the quenched alloy of same composition displays less magnetostriction.

The quenched 17 and 20 at% alloys have single phase A2 in the microstructure which exhibits higher magnetostriction. This is also in agreement with earlier reports which also exhibit higher magnetostriction for single phase A2 alloys [13, 15-18]. The slow cooled alloy of these compositions exhibit presence of ordered DO_3 phase and as a result magnetostriction decreases. The aged alloys of Fe-20at% Ga also exhibit less magnetostriction as compared to quenched alloy of same composition owing to the formation of DO_3 ordered phase.

The presence of DO_3 phase is found to be detrimental for slow cooled alloys of 17 and 20 at% compositions. However, the furnace cooled Fe-25 at% Ga alloy exhibits good

magnetostriction although nearly single phase DO_3 is observed. Therefore, DO_3 phase when present as single phase displays good magnetostriction but the magnetostriction is impaired when it co-exists with a second phase e.g. A2 phase in case of slow cooled 17 and 20 at % alloys. Since the metastable phase diagram (Fig. 6.1b) indicates that the volume fraction of DO_3 phase increases with Ga concentration, the slow cooled alloy 23 and 25 at% exhibit more magnetostriction than 20 at% alloy. The aged alloys of 23 and 25 at% however exhibit better magnetostriction than corresponding quenched or furnace cooled alloy owing to more extent of DO_3 ordering formed during isothermal ageing. Thus, it can be concluded that A2 phase or DO_3 phase exhibit better magnetostriction when they exist as single phase. The magnetostriction comes down when they co-exist in the microstructure.

The decrease in magnetostriction in the mixed phase field regime is owing to different easy magnetization directions (EMD) of A2 and DO_3 phases. Kumagai et.al. [26] reported that A2 phase exhibits EMD along <100>, whereas DO_3 is having EMD along <111>. Therefore, when magnetic field is applied on a sample having mixed phase microstructure, the domains belong to different phases do not rotate in a coordinated fashion, as a result magnetostriction decreases. However, when single phase A2 or DO_3 is present, the domain rotation is more coordinated and the sample demonstrates more magnetostriction.

6.8. Summary and Conclusions:

Fe- x at% Ga alloys (x= 17, 20 23 25) were prepared by vacuum arc melting and the alloys were annealed at 1000^{o}C for 5 hrs. One set of the alloys was water quenched and the other set was furnace cooled from 1000^{o}C. The quenched alloys were subsequently aged at 480^{o}C upto a duration of 8 hrs. TEM studies on the samples with different thermal history were carried out to understand the phase transformation. The observed microstructural features were correlated with magnetostriction measured for the samples.

The furnace cooled alloys of 17 and 20 at% alloys exhibit presence of DO_3 ordering along with disordered A2 phase. The volume fraction of the DO_3 phase increases with increase in Ga concentration and nearly single phase DO_3 phase has been observed for the 25 at% Ga alloy. The quenched sample of 17 and 20 at% alloys exhibit presence of single phase A2. Upon ageing, 17 at% alloy does not exhibit presence of any ordering whereas, the 20 at% alloy exhibits presence of DO_3 type ordering along with A2 phase. The quenched samples of 23 and 25 at% alloys also exhibit presence of DO_3 phase and the extent of DO_3

ordering increases with ageing. The presence of DO_3 along with A2 phase can be correlated to less magnetostriction in the quenched 23 and 25 at% alloys, which increases after ageing owing to increase in DO_3 ordering.

In case of 17 and 20 at% Ga alloys, the DO_3 formation is a first order transformation and therefore occurs by nucleation and growth through a diffusion controlled mechanism. As a result the formation of DO_3 phase could be suppressed during quenching in the case of 17 and 20 at% Ga alloys. Whereas, for 23 and 25 at% Ga alloys, the A2 phase undergoes two successive continuous ordering A2$\rightarrow$B2 and B2$\rightarrow DO_3$. The continuous ordering being a faster process, formation of DO_3 could not be suppressed in case of 23 and 25 at% Ga alloys.

The magnetostriction is higher when single phase A2 or DO_3 are present and the magnetostriction decreases when DO_3 phase co-exists with A2. The decrease in magnetostriction in the mixed phase field regime is owing to non-coordinated response of the magnetic domains to the applied field, which is attributed to different EMDs of different phases present in the microstructure.

Figure 6.1: The vacuum arc melting furnace (male M/s Vacuum Technique), used for preparation of the alloy.

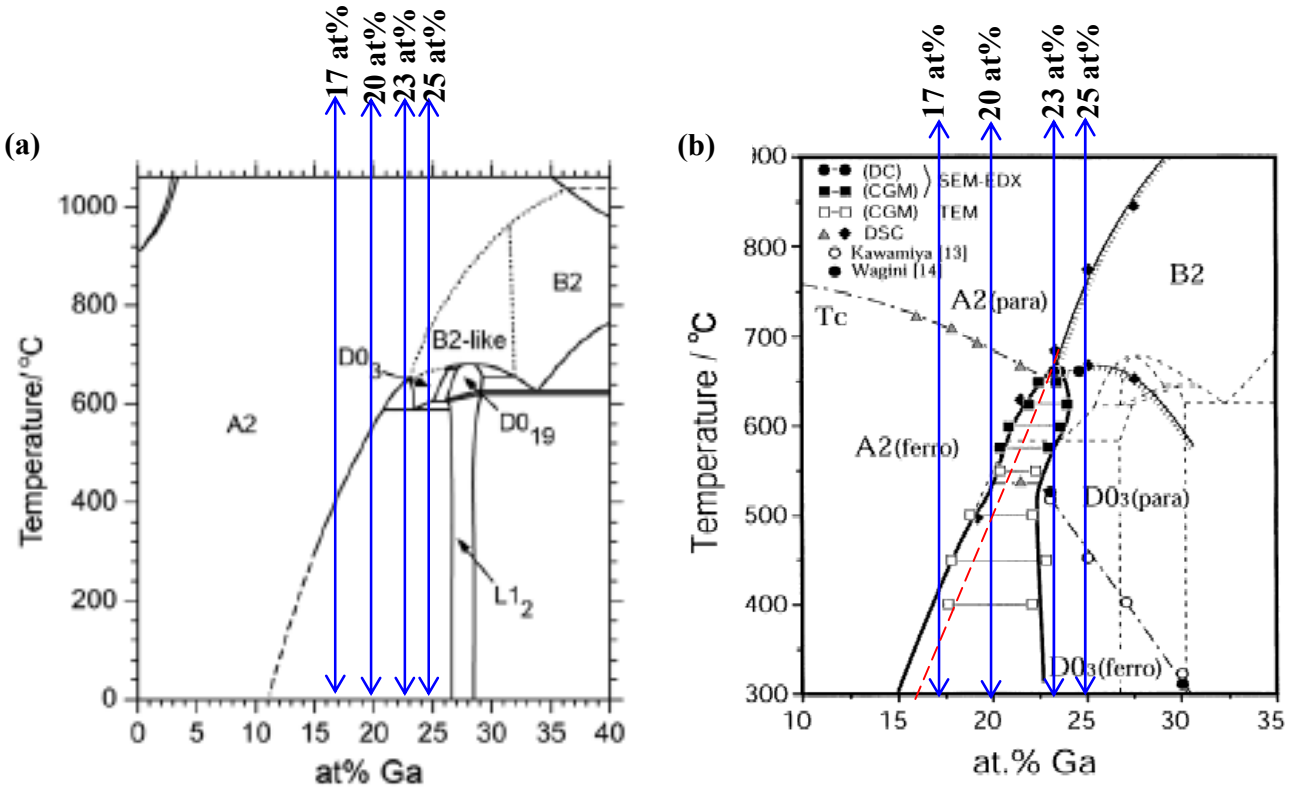

Figure 6.2: Compositions investigated in this study are shown in Fe-Ga phase diagrams (a) Equilibrium [5] (b) Metastable [7].

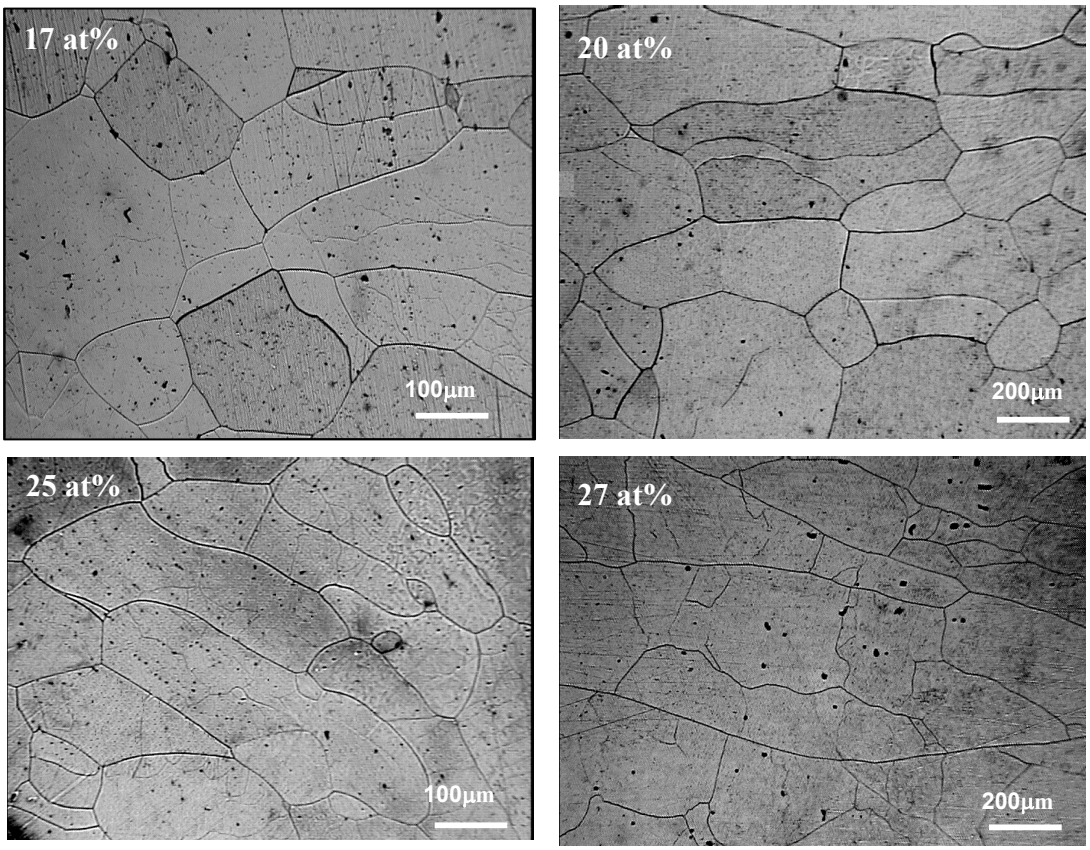

Figure 6.3: Optical micrographs of as cast Fe- x at% Ga alloys (x= 17, 20, 23 and 27).

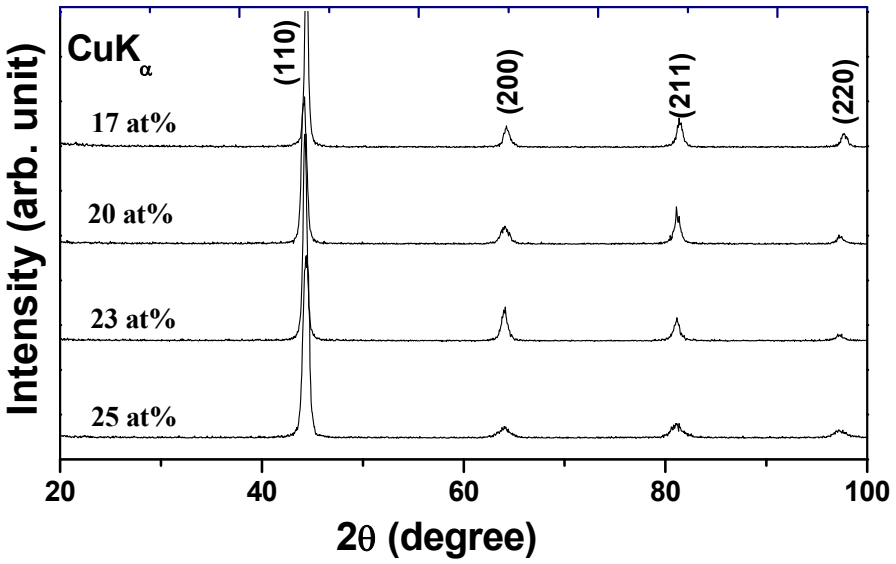

Figure 6.4: X-ray diffractograms of as cast Fe- x at% Ga alloys (x= 17, 20, 23 and 27).

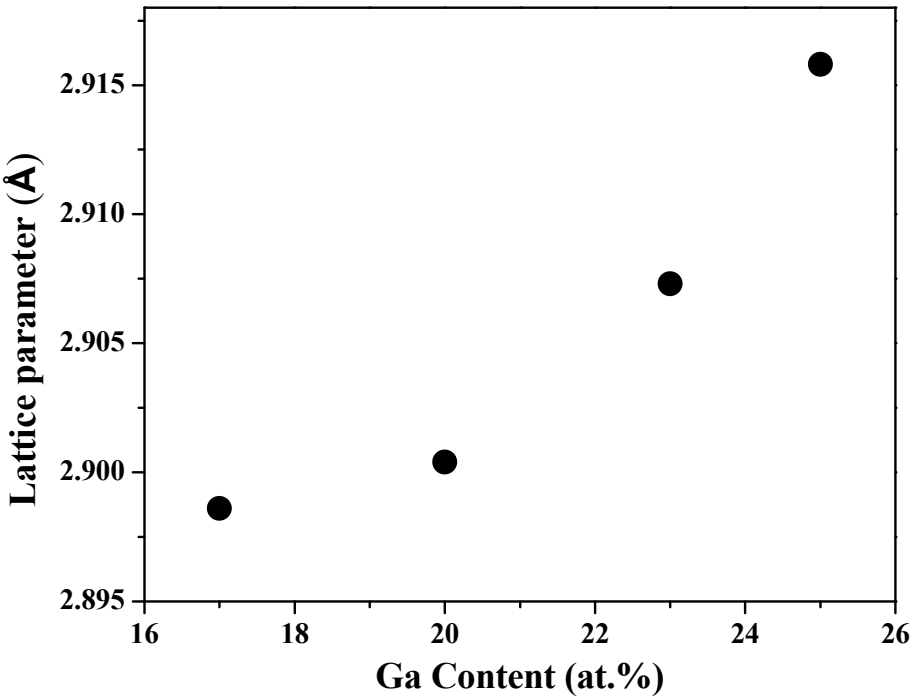

Figure 6.5: Lattice parameter as a function of Ga concentration

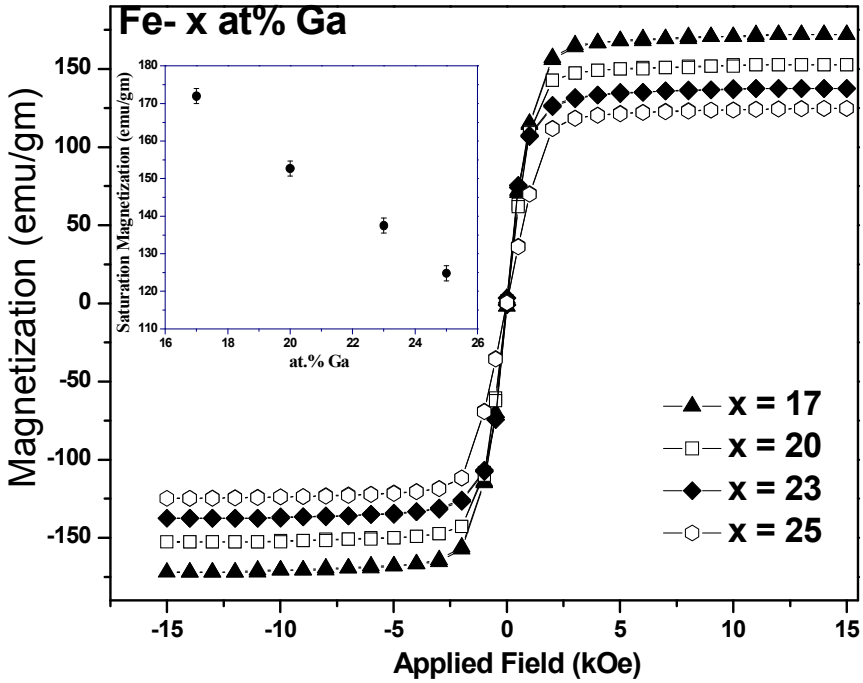

Figure 6.6: Magnetization of as cast Fe-Ga alloys as a function of applied magnetic field. Inset: Saturation magnetization as a function of Ga concentration.

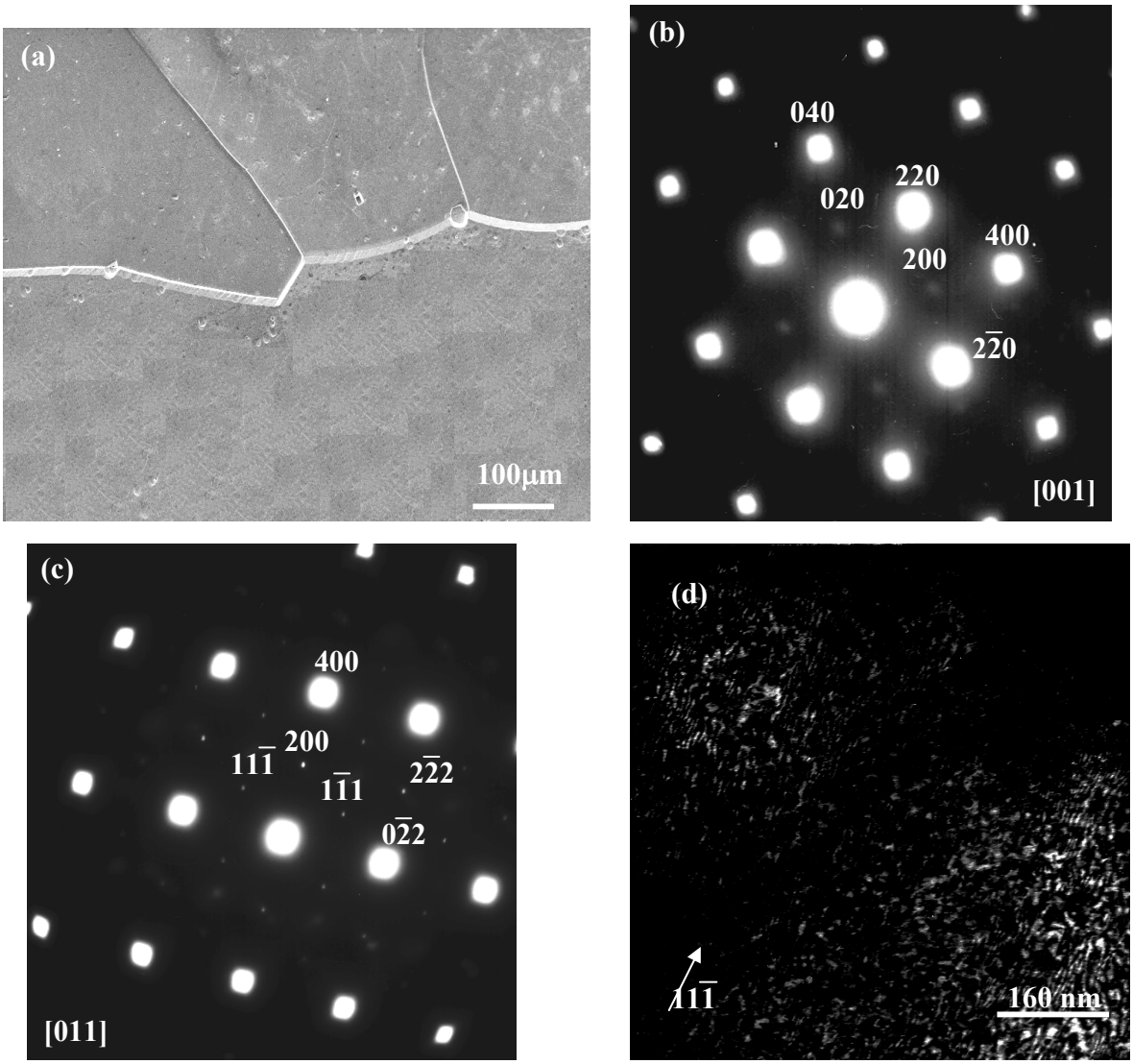

Figure 6.7: Furnace cooled Fe-17 at% Ga alloy - (a) Secondary electron image, (b) SAD along [001], (c) SAD along [011] and (d) dark field image using (111) superlattice reflection of DO_3.

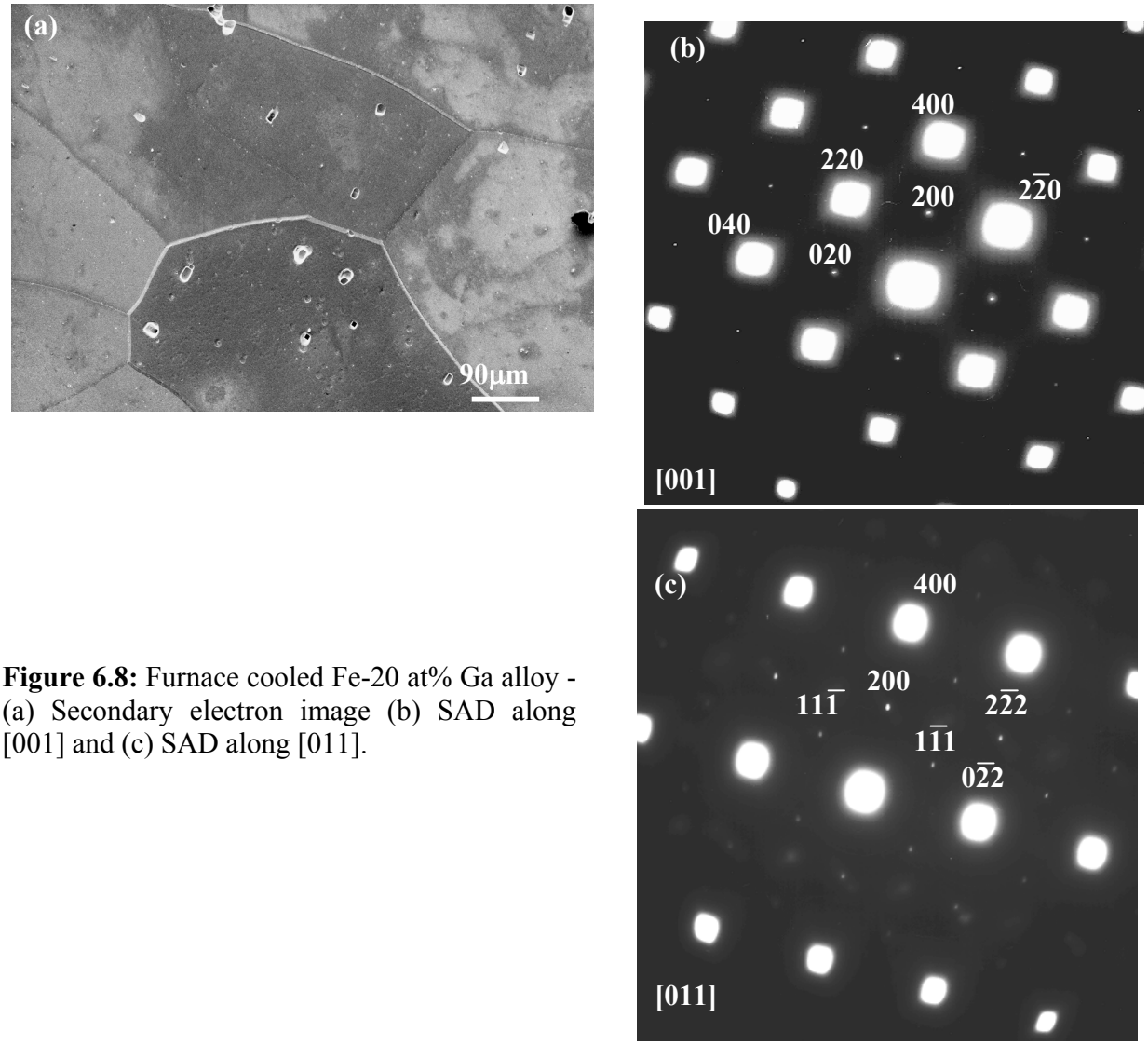

Figure 6.8: Furnace cooled Fe-20 at% Ga alloy - (a) Secondary electron image (b) SAD along [001] and (c) SAD along [011].

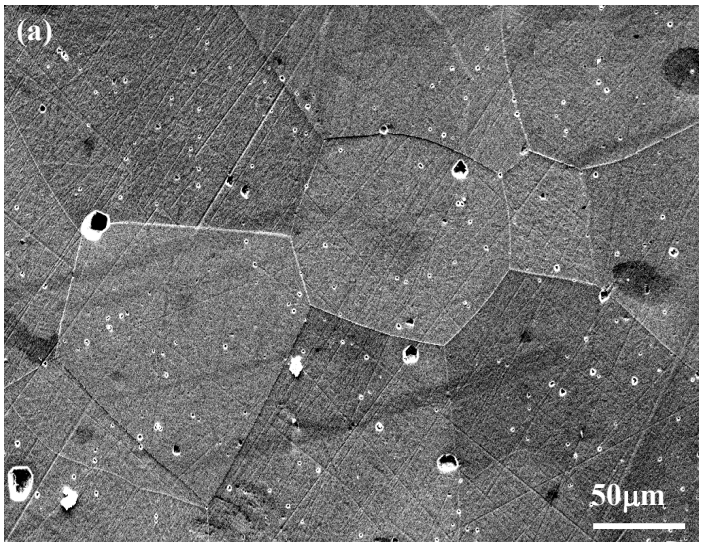

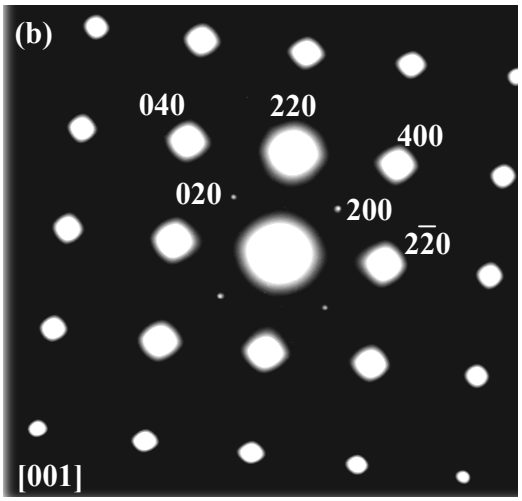

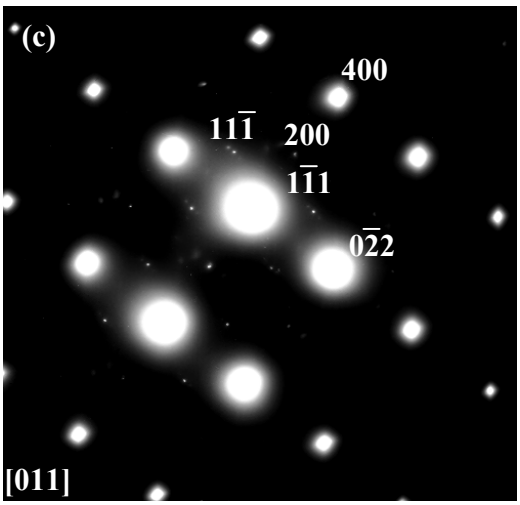

Figure 6.9: Furnace cooled Fe-23 at% Ga alloy - (a) Secondary electron image, (b) SAD along [001] and (c) SAD along [011]

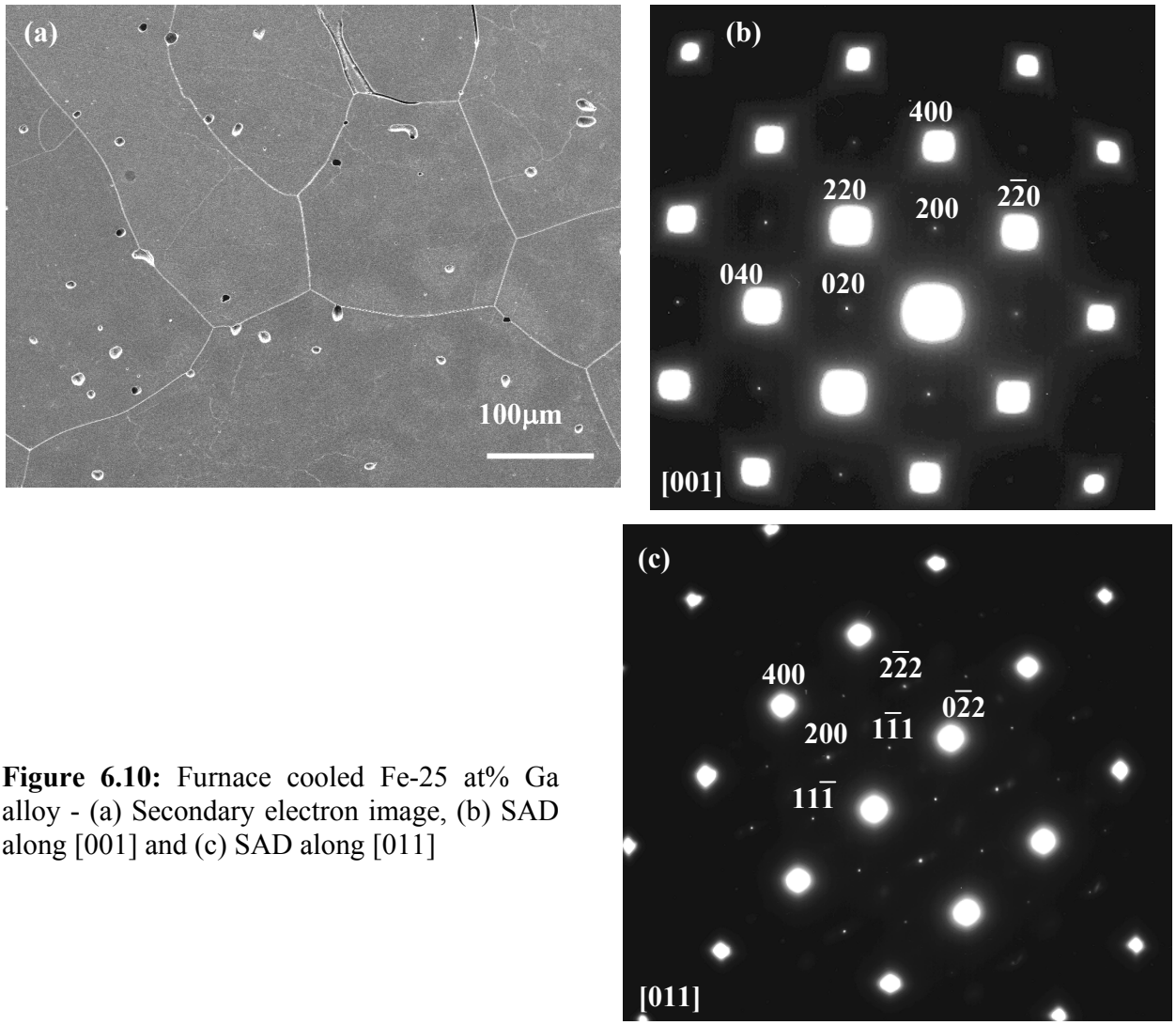

Figure 6.10: Furnace cooled Fe-25 at% Ga alloy - (a) Secondary electron image, (b) SAD along [001] and (c) SAD along [011]

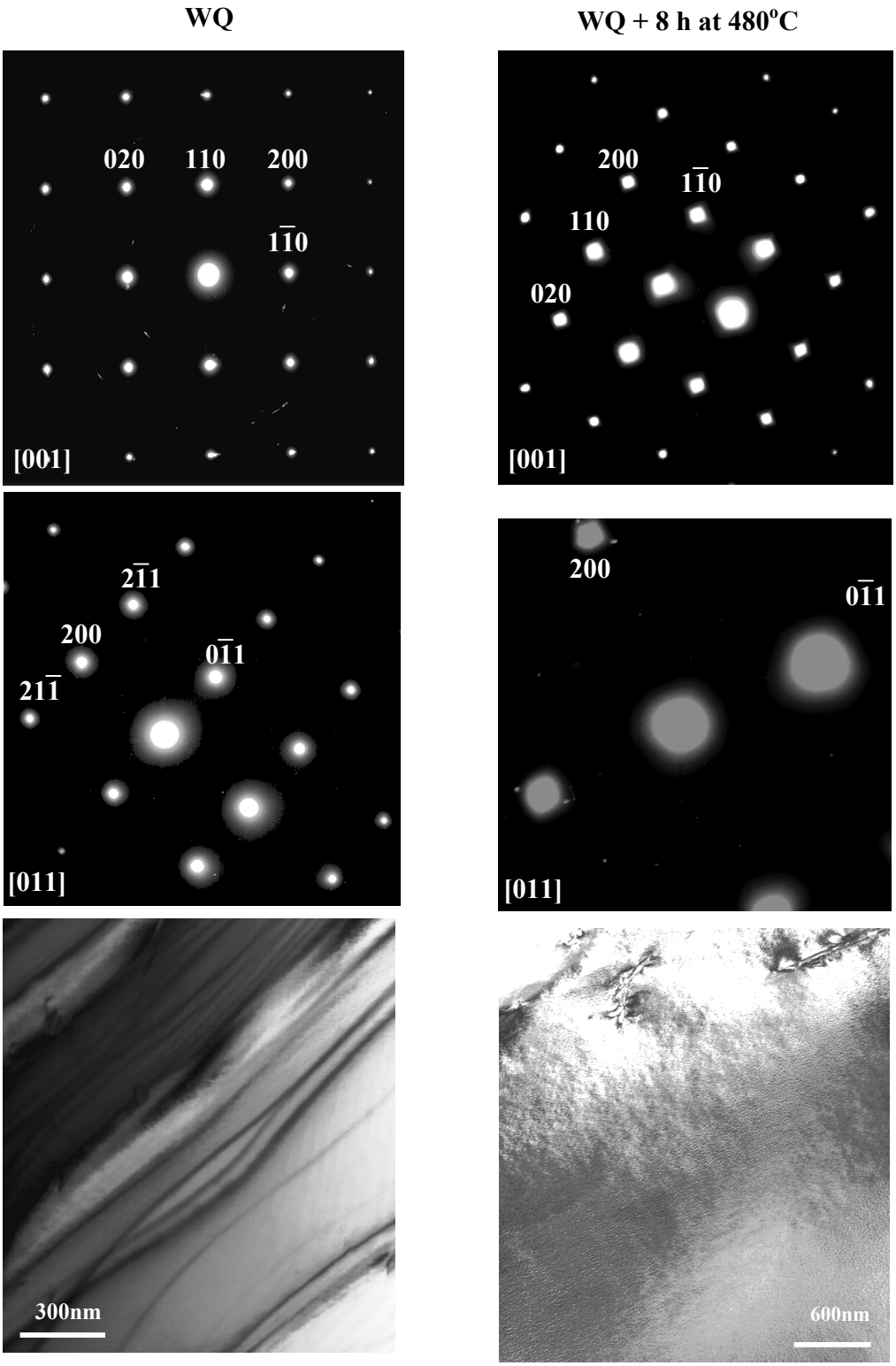

Figure 6.11: SADs along [001] and [011] zone axes and bright field images of quenched and quenched + 8 hr aged Fe-17 at% Ga alloys.

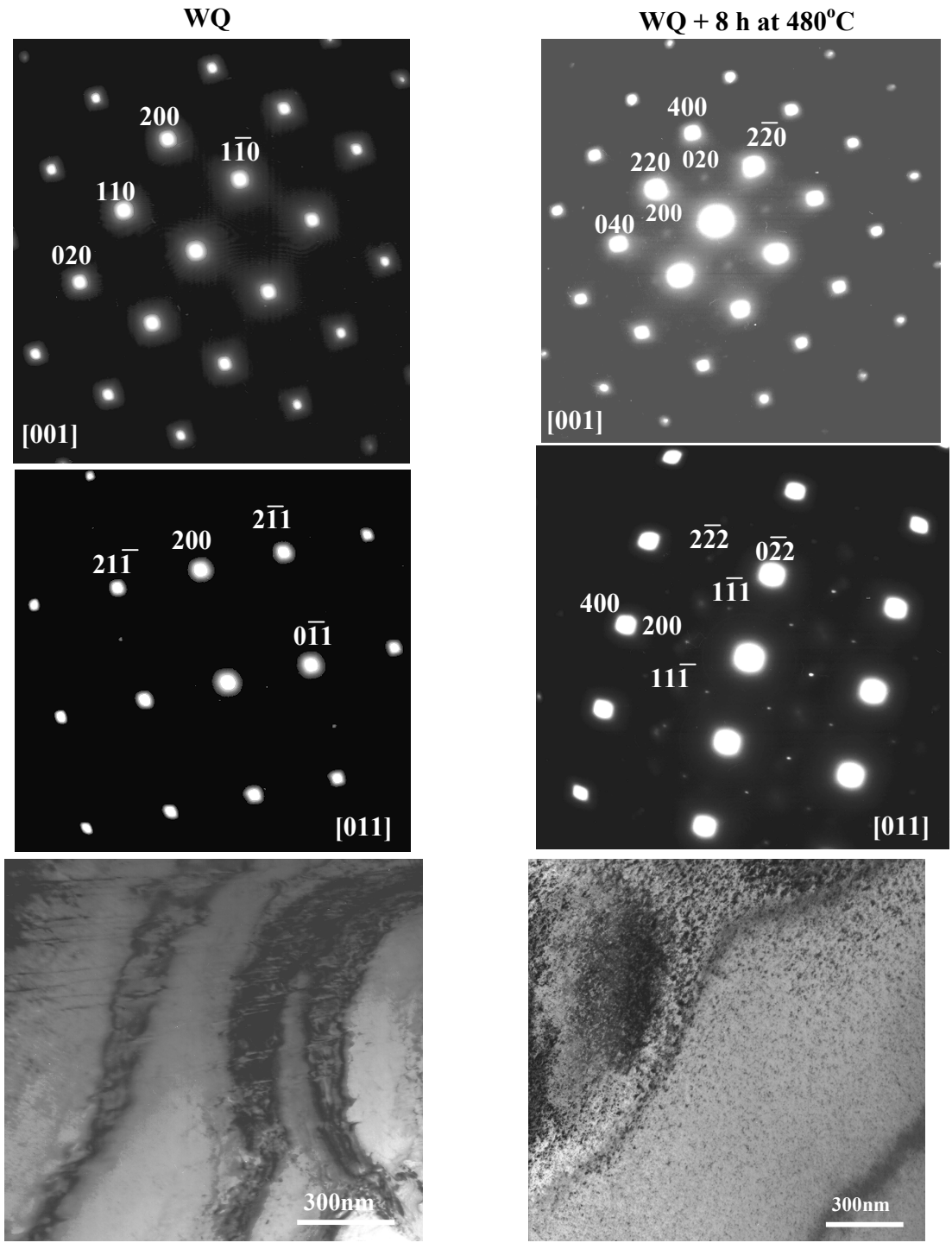

Figure 6.12: SADs along [001] and [011] zone axes and bright field images of quenched and quenched + 8 hr aged Fe-20 at% Ga alloys.

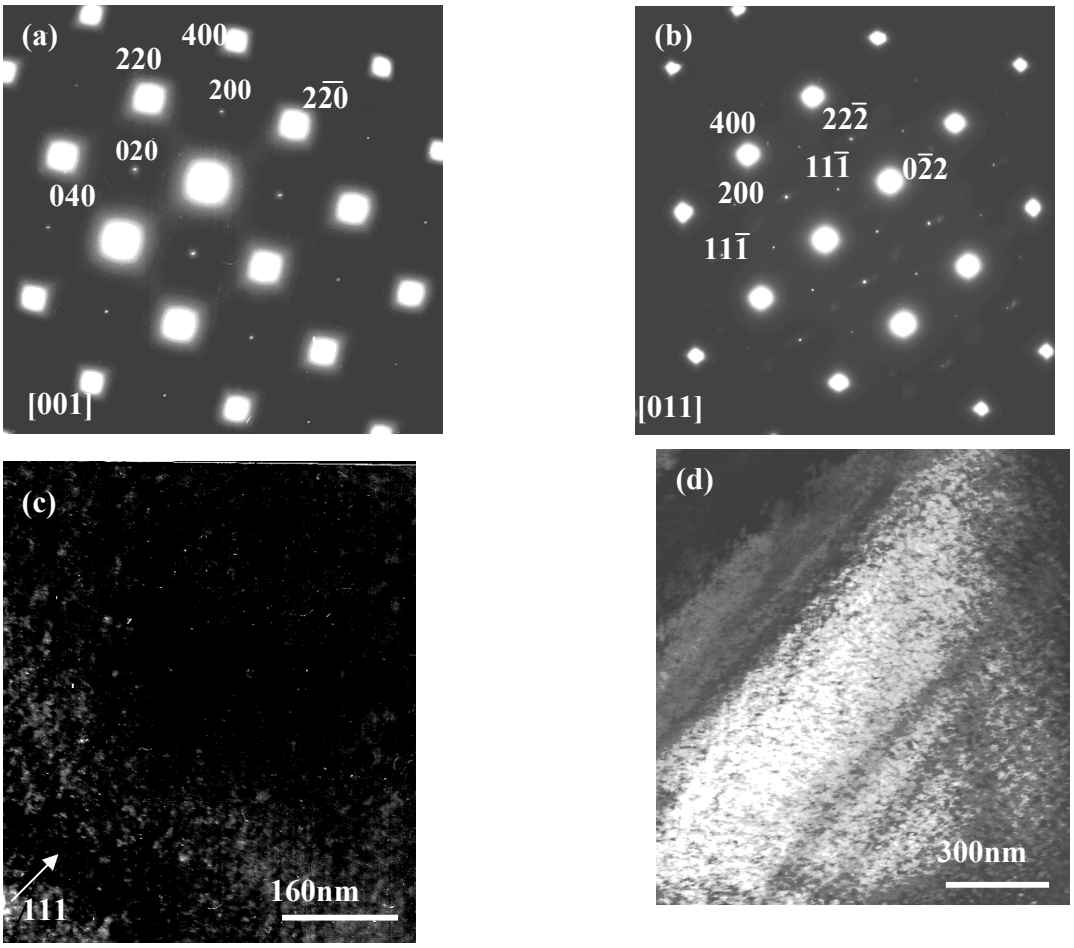

Figure 6.13: Quenched Fe-23 at% alloy - (a) SAD along [001], (b) SAD along [011], dark field image using (111) superlattice reflection of DO_3 and (d) bright field image.

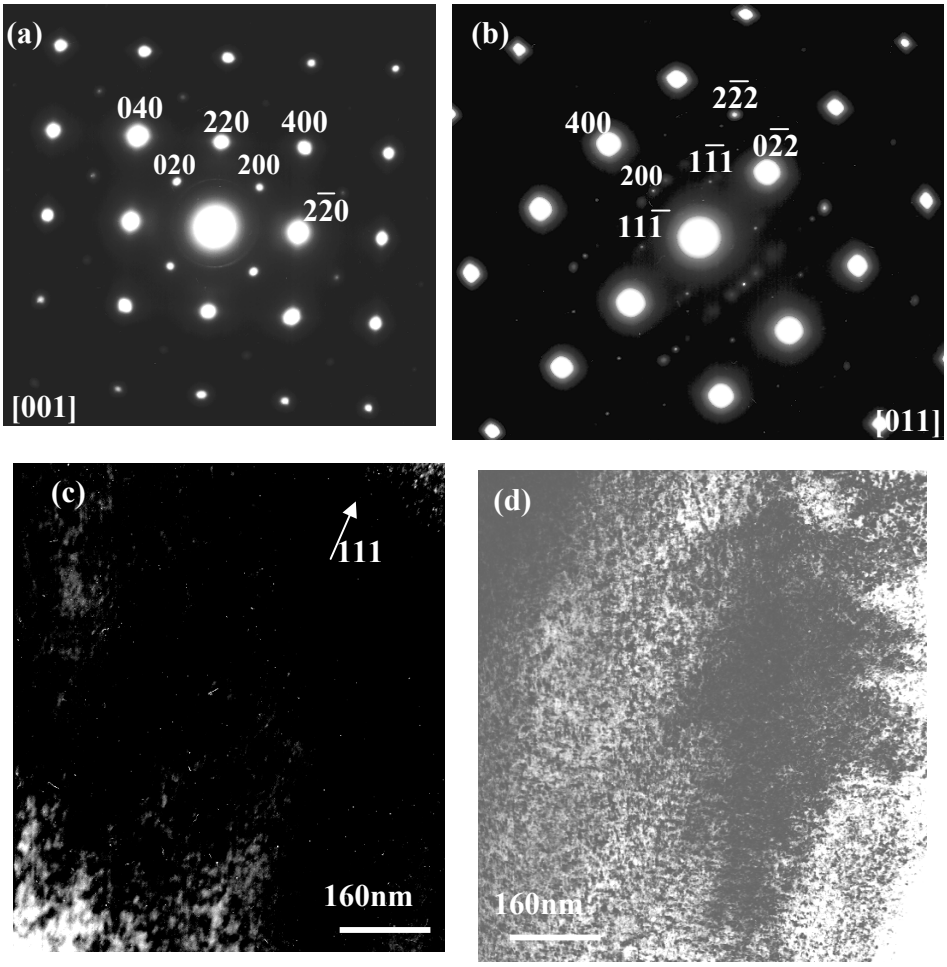

Figure 6.14: Quenched Fe-25 at% alloy- (a) SAD along [001], (b) SAD along [011], (c) dark field image using (111) superlattice reflection of DO_3 and (d) bright field image.

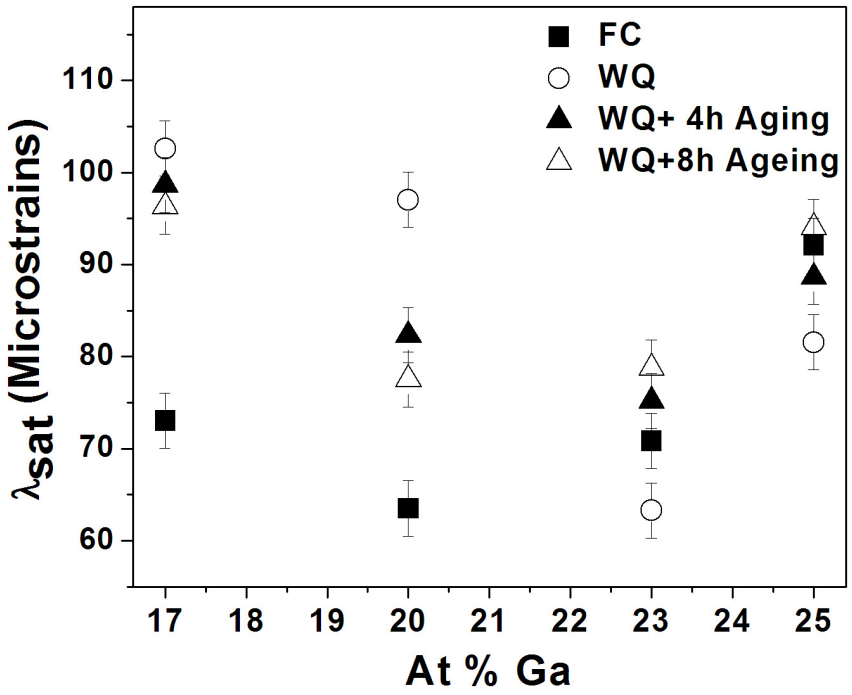

Figure 6.15: Saturation magnetostriction (λ_{sat}) of furnace cooled, quenched and aged Fe-Ga alloys plotted as a function of composition.

References:

[1] A.E. Clark, J.B. Restorff, M. Wun-Fogle, K.B. Hathaway, T.A. Lograsso, M. Huang and E. Summers, *"Magnetostriction of ternary Fe–Ga–*X *(*X = *C,V,Cr,Mn,Co,Rh) alloys*", J. Appl. Phys., 101 (2007) 09C507.

[2] Manfred Wuttig, Liyang Dai and James Cullen, *"Elasticity and magnetoelasticity of Fe–Ga solid solutions"*, Appl. Phys. Lett., 80 (2002) 1135.

[3] J.R. Cullen, A.E. Clark, M. Wun-Fogle, J.B. Restorff and T.A. Lagrasso, *"Magnetoelasticity of Fe–Ga and Fe–Al alloys",* J. Magn. Magn. Mater., 2260 (2001) 948.

[4] S. Guruswamy, N. Srisukhumbowornchai, A.E. Clark, J.B. Restorff and M. Wun-Fogle, *"Strong, ductile, and low-field-magnetostrictive alloys based on Fe-Ga",* Scripta Mater., 43 (2002) 239.

[5] H. Okamoto, Binary Alloy Phase Diagram, ASM International, Materials Park, OH, 1996.

[6] J.M. Borrego, J.S. Blazquez, C.F. Conde, A. Conde and S. Roth, *"Structural ordering and magnetic properties of arc-melted FeGa alloys",* Intermetallics, 15 (2007) 193.

[7] O. Ikeda, R. Kainuma, I. Ohnuma, K. Fukamichi and K. Ishida, *"Phase equilibria and stability of ordered b.c.c. phases in the Fe-rich portion of the Fe–Ga system",* J. Alloy Compd., 347 (2002) 198.

[8] A E Clark, K B Hathaway, M Wun-Fogle, J B Restorff, T A Lograsso, V M Keppens, *"Extraordinary magnetoelasticity and lattice softening in bcc Fe-Ga alloys"*, J Appl. Phys., 93 (2003) 8621.

[9] A E Clark, J B Restorff, M Wun-Fogle, K W Dennis, T A Lograsso, and R W McCallum, *"Temperature dependence of the magnetic anisotropy and magnetostriction of* $Fe_{100-x}Ga_x$ *(*x = *8.6, 16.6, 28.5)"*, J Appl Phys., 97 (2005) 10M316.

[10] A.E. Clark, M. Wun-Fogle, J.B. Restorff and T.A. Lagrasso, J R Cullen, *"Effect of quenching on the magnetostriction on* $Fe_{1-x}Ga_x$ *(0.13<x<0.21)"*, IEEE Trans Magn., 37 (2001) 2678.

[11] Himalay Basumatary, Mithun Palit, J. Arout Chelvane, S. Pandian, M. Manivel Raja and V. Chandrasekaran, *"Structural ordering and magnetic properties of* $Fe_{100-x}Ga_x$ *alloys",* Scripta Mater., 59 (2008) 878.

[12] Y Du, M Huang, S. Chang, D L Schlagel, T A Lograsso, and R J McQueeney, *"Relation between Ga ordering and magnetostriction of Fe-Ga alloys studied by x-ray diffuse scattering",* Phys. Rev. B, 81(2010) 054432.

[13] S. Datta, M Huang, J Raim, TA Lograsso, AB Flatau, *"Effect of thermal history and gallium content on magneto-mechanical properties of iron gallium alloys"*, Mat. Sci. Engg. A, 435 (2006) 221.

[14] N. Srisukhumbowornchai and S. Guruswamy, *"Influence of ordering on the magnetostriction of Fe–27.5 at.% Ga alloys"*, J. Appl. Phys., 92 (2002) 5371.

[15] Q. Xing and T.A. Lograsso, *"Phase identification of quenched Fe–25at.% Ga",* Scrpta Mater., 60 (2009) 373.

[16] T A Lograsso, A.R. Ross , D L Schlagel, A E Clark, M Wun-Fogle, *"Structural transformations in quenched Fe–Ga alloys"*, J. Alloys Compd., 350 (2003) 95.

[17] Somnath Bhattacharyyaa, J.R. Jinschek, J.F. Li, D. Viehland, *"Nanoscale precipitates in magnetostrictive $Fe_{1-x}Ga_x$ alloys for 0.1 < x < 0.23"*, J. Alloys Compd., 501 (2010) 148.

[18] Q. Xing, Y. Du, R.J. McQueeney, T.A. Lograsso, *"Structural investigations of Fe–Ga alloys: Phase relations and magnetostrictive behavior"*, Acta Mater. 56 (2008) 4356.

[19] Liu Libao, Fu Shiyou, Liu Guodong, Wu Guangheng, Sun Xiudong, Li Jianqi, *"Transmission electron microscopy study on the microstructure of $Fe_{85}Ga_{15}$ alloy"*, Physica B, 365 (2005) 102.

[20] H Cao, P M Gehring, C P Devreugd, J A Rodriguez-Rivera, J Li, and D Viehland, *"Role of Nanoscale Precipitates on the Enhanced Magnetostriction of Heat-Treated Galfenol ($Fe_{1-x}Ga_x$) Alloys",* Phys. Rev. Lett., 102 (2009) 127201.

[21] A G Khachaturyan, D Viehland, *"Structurally Heterogeneous Model of Extrinsic Magnetostriction for Fe-Ga and Similar Magnetic Alloys: Part I. Decomposition and Confined Displacive Transformation"*, Metall Mater Trans A, 38 (2007) 2308.

[22] A G Khachaturyan, D. Viehland, *"Structurally Heterogeneous Model of Extrinsic Magnetostriction for Fe-Ga and Similar Magnetic Alloys: Part II. Giant Magnetostriction and Elastic Softening"*, Metall Mater Trans A, 38 (2007) 2317.

[23] J. Boisse, H. Zapolsky, A.G. Khachaturyan, "*Atomic-scale modeling of nanostructure formation in Fe–Ga alloys with giant magnetostriction: Cascade ordering and decomposition"*, Acta Mater., 59 (2011), 2656.

[24] Samuel M Allen and John W. Cahn, *"Mechanisms of phase transformations within the miscibility gap of Fe-rich Fe-Al alloys"*, Acta Metallurgica 24 (1976) 425.

[25] K Raviprasad and K Chattopadhyay, *"The influence of critical points and structure and microstructural evolution in Fe-rich Fe-Si alloys"*, Acta Metall., Mater., 41 (1993) 609.

[26] A Kumagai, A Fujita, K Fukamichi, K Oikawa, R Kainuma, K Ishida, *"Magnetocrystalline anisotropy and magnetostriction in ordered and disordered Fe–Ga single crystals"*, J. Magn. Magn. Mater., 272 (2004) 2060.

Chapter 7

Summary

In this thesis, effect of Tb/Dy ratio on phase equilibria and magnetic properties of $Tb_xDy_{1-x}Fe_{1.95}$ (x=0-1) have been studied. The study revealed that the ternary phase equilibria is substantially different from the pseudo-binary behavior assumed so far in the available literature. The microstructural investigations indicate that the gradual substitution of Dy by Tb does not change the phase equilibria in monotonic linear manner. This is evident from the observation of minimum and maximum in volume fraction of pro-peritectic $(Tb,Dy)Fe_3$ phase in as-cast alloys of $Tb_{0.4}Dy_{0.6}Fe_{1.95}$ and $Tb_{0.6}Dy_{0.4}Fe_{1.95}$compositions respectively. The variation in volume fraction of pro-peritectic phase is found to be related to its volume fraction formed at peritectic temperature, which changes in a non-linear fashion with Tb/Dy ratio. The deviation from the pseudo-binary behavior becomes more clearly evident with the observation of a Widmanstatten type precipitate of $(Tb,Dy)Fe_3$ for Dy rich compositions ($0 \leq x \leq 0.5$) and not for the compositions richer in Tb. The precipitate however dissolves when samples were quenched after the heat treatment of 1000^oC/ 48h. This indicates there is an extension of the phase field of $(Tb,Dy)Fe_2$ phase towards rare earth-rich side for Dy-rich compositions. The study of lattice parameter and micro-chemical composition using EPMA indicates that the phase field of Laves phase shifts towards Fe-rich side with Tb addition; as a result the condition for Widmanstatten precipitate formation does not remain prevalent. The proposed nature of the phase field also corroborates to volume fraction of remnant pro-peritectic phase and the eutectic phase in the microstructure. The proposed nature of the phase field is also supported by variation in the Curie temperature (T_C) of the Laves phase [$(Tb,Dy)Fe_2$] with Tb/Dy ratio. Higher T_C, observed for Tb-rich alloys, is attributed to stronger Fe-Fe interactions derived from higher Fe-concentration in Laves phase present in these compositions. The increase in Curie temperature with Tb addition, results from stronger (Tb,Dy)-Fe interaction, which is derived from an increase in Fe-hyperfine field in Tb-rich alloys.

The study of magnetic properties of $Tb_xDy_{1-x}Fe_{1.95}$ (x=0-1) alloys also indicates deviation from a pseudo-binary behavior. This is evident from the observation of a spin

reorientation transition on Tb addition from [100] easy direction of magnetization to [111] easy direction of magnetization. This transition has been observed from the data obtained by Mössbauer, ac susceptibility and x-ray studies. The magnetostriction (λ) at high field (> 3kOe), however, exhibits a monotonic increase with Tb addition but the slope of the λ-H curve shows maximum for x=0.4 alloy. The increase in magnetostriction with Tb addition is related to increase in magneto-crystalline anisotropy with Tb addition. The slope of the curve is however found to be related to coercivity and the anisotropy of the alloys. The minimum coercivity occurring at x=0.4 is mainly attributed to the near zero anisotropy compensation and further to the presence of minimum volume fraction of the pro-peritectic phase. At x>0.4 however, the effect of large anisotropy offered by Tb contributes for increasing the coercivity. As a result the slope of λ-H curve decreases.

The evolution of microstructure and texture during directionally solidification of $Tb_{0.3}Dy_{0.7}Fe_{1.95}$ alloy has also been studied. Two different techniques have been used for directional solidification *viz.* modified Bridgman and zone melting. The microstructure of the directionally grown samples by modified Bridgman technique exhibit planar solidification morphology of (Tb,Dy)Fe_2 phase for a wide range of solidification rate (5-80 cm/h), whereas cellular/ dendritic morphological instability is observed for the samples directionally solidified at 18, 36 and 72 cm/h by zone melting. In case of Bridgman grown sample the complete cellular instability is observed only at 100 cm/h which is higher than the growth rates used for zone melting. The appearance of morphological instability at lower growth rate in zone melted samples is attributed to the lower temperature gradient of ~100^{o}C/cm as compared to the temperature gradient of ~150^{o}C/cm obtained in Bridgman solidification. Presence of (Tb,Dy)-solid solution is observed at the intercellular/ inter dendritic boundary of (Tb,Dy)Fe_2 phase in all zone melted samples and Bridgman grown samples directionally solidified at 90 and 100 cm/h. Samples grown at 5-90 cm/h by modified Bridgman technique also exhibit presence of islands / discrete bands of pro-peritectic (Tb,Dy)Fe_3 phase, towards the chilled end of the sample. As the distance from the chilled end increases, the islands of (Tb,Dy)Fe_3 subsequently transforms into coupled growth of (Tb,Dy)Fe_3 and (Tb,Dy)Fe_2 phases. The coupled growth is not observed in the sample grown at 5 cm/h and is prominently observed for the samples grown at 20-90 cm/h. The growing lamellae of (Tb,Dy)Fe_3 phase are more dispersed as the growth rate increases. The peritectic coupled

growth observed in this study is irregular in nature and this is attributed to high growth anisotropy of both the growing intermetallic phases [$(Tb,Dy)Fe_2$ and $(Tb,Dy)Fe_3$] along particular direction. However, such peritectic coupled growth or island banding have not been observed in zone melted samples.

The texture study of the directionally solidified alloys indicates that in case of Bridgman grown samples, <311> forms as single dominant texture at lower growth rates (upto 10 cm/h) which remains present till growth rate of 80 cm/h. The intensity of <311> texture decreases with increase of growth rate. In the intermediate growth rate regime (20-40 cm/h), the <110> and 'rotated <110>' evolve as dominant texture component, whereas <112> is observed as dominant texture component at high growth rate regime (70-100 cm/h). In case of zone melted samples, <110> or 'rotated <110>' are found as major texture components at lower growth rates and <112> or 'rotated <112>' texture components evolve stronger with increase in the rate of solidification. However, irrespective of growth rates, <110> or 'rotated <110>' are observed as nucleation texture, formed at the onset of solidification. The orientation selection with growth rate has been analyzed in the light of kinetics of atomic attachment to the solid-liquid interface. It has been observed that for plane front growth interface (as mostly observed in Bridgman grown samples), the atomic attachment depends on atomic packing fraction of the plane in contact with liquid at solid-liquid interface. {311} type planes being more close packed compared to {110} and {112} planes, the atomic attachment to {311} planes is expected to be sluggish compared to {110} and {112} planes. As a result, <311> evolves as dominant texture component as lower growth rates, which subsequently changes to <110> at intermediate growth rate regime and to <112> at higher growth rate regime. It can be seen that the {311} planes can be resolved into two {111} planes of different types of atomic population. The same two layer appear in stacking sequence of {111} planes also. Therefore, growth of <311> texture offers distinct advantage in atomic attachment kinetics over growth of <111>, as atoms can be attached simultaneously instead of sequentially building two such layers required for growth of <111> texture. In case of zone melted alloy the interface however is not planar and as a result several possible growth configurations have been worked out where in each case the growth direction is encapsulated by low index planes. The atomic packing density of each possible non-planar solid-liquid interface configurations have been computed to identify the most favored interfacial configurations for <110> and <112> growth. It has been observed that the

atomic packing density of the most favored configurations of <110> and <112> growth are nearly same and the orientation selection is rather related to ease of atomic attachment kinetics at solid-liquid interface of the growth envelope. The analysis indicates that 16% of the solid-liquid interfacial area of most favored configuration for <112> growth is consisting of (010) plane, which is not having separate Fe-layer in its stacking sequence. Whereas, the most favored interfacial configuration of <110> growth is consisting of planes having separate Fe-layer in its stacking sequence. Therefore, atomic attachment kinetics to <112> interface is faster compared to <110> and hence at higher growth rate <112> emerges as major texture component. The change of preferred orientation from <110> to <112> occurs through an intermediate orientation <123>. The texture of directionally solidified samples is found to play major role in variation of static strain co-efficient ($d\lambda/dH$). The texture component which is nearer to easy magnetization direction <111> results in larger values of static strain co-efficient. As a result, samples with <110> texture component (35^o away from EMD) exhibit lowest static strain co-efficient and the samples with <112> (19^o away from EMD) as major component exhibits highest static strain co-efficient.

Apart from the investigation on magnetostrictive Tb-Dy-Fe alloy, the current study also aimed at understanding of the structure-property relationship in emerging magnetostrictive materials Fe-Ga. Thus, Fe- x at% Ga alloys (x= 17, 20 23 25) were prepared by vacuum arc melting and subjected to different thermal treatments. The furnace cooled alloys of 17 and 20 at% alloys exhibit presence of DO_3 ordering along with disordered A2 phase. The formation of ordered DO_3 phase however could be suppressed by quenching and as result quenched alloys of same composition are found to exhibit better magnetostriction. The volume fraction of the DO_3 phase in furnace cooled alloy increases with increase in Ga concentration and nearly single phase DO_3 phase has been observed for the 25 at% Ga alloy. Interestingly, the same alloy is also found to exhibit better magnetostriction. The formation of DO_3 phase could not be suppressed in case of 23 and 25 at% alloys although it could be suppressed in 17 and 20 at% alloys. The $A2 \rightarrow A2+DO_3$ transformation is found to be a first order transformation that occurs by nucleation and growth and therefore is diffusion controlled. As a result the formation of DO_3 phase could be suppressed during quenching, in case of 17 and 20 at% Ga alloys. However, the driving force for the formation of DO_3 phase increases with Ga concentration and as a result the formation of DO_3 could not be suppressed

for 23 and 25 at% Ga alloys. The magnetostriction is found to be more when single phase A2 or DO_3 are present and the magnetostriction decreases when DO_3 phase co-exists with A2. The decrease in magnetostriction in the mixed phase field regime is owing to non-coordinated response of the magnetic domains to the applied field, which is attributed to different EMDs of different phases present in the microstructure.

Chapter 8

Scope for future work

The present work on phase equilibria of Tb-Dy-Fe has clearly demonstrated that the ternary phase equilibria can not be interpreted with pseudo-binary assumption. Therefore it is important to understand the phase equilibria in similar pseudo-binary magnetostrictive system *e.g.* Ho-Tb-Fe and Sm-Dy-Fe. On the theoretical side, thermodynamic calculations can be carried out to validate the experimental observations and to understand the underlying physics. So far, the efforts towards theoretical computation of phase diagram of Tb-Dy-Fe neglected ternary interactions and as a result, the prediction and experimental observations differ. One issue is of course the non-availability of thermodynamic data, which can be generated by several experiments so that the ternary behavior can be closely predicted.

The mechanism of evolution of texture during directional solidification of $(Tb,Dy)Fe_2$ presented in this study indicates atomic attachment kinetics plays a major role in orientation selection. The mechanism proposed in this study can be validated with computer simulation of microscopic events that occurs at solid-liquid interface during growth of a particular texture component. Further, using liquid metal cooling technique, the growth interface can be quenched and the orientation of the planes surrounding tip of cell/ dendrite can be studied by micro-texture studies of carefully prepared samples. Such precision experiment can validate the orientation selection model proposed in his study and will offer more insight on the kinetics of orientation selection. The present study on Bridgman solidification indicates formation of microstructural features such as island banding and PCG. The process or underlying mechanism of such microstructural evolution can be better understood with the aid of phase field modeling. Further, the microstructure can be diverse in nature if effect of convection can be studied by directional solidification experiments inside very small to large dia containers. In this particular alloy system, such studies may yield interesting results as both the peritectic product and pro-peritectic phases are intermetallic compounds having strong growth anisotropy.

The Fe-Ga alloy, being the material for future actuators has numerous practical challenges and therefore offers plenty of research opportunities. The results presented in this

study indicates profound role of microstructure in magnetostrictive properties. However, the microstructural studies reported here is on polycrystalline bulk alloy, which shows relatively lower magnetostriction than the textured alloys. In recent past few reports are appearing that describe the studies on directionally oriented and rolled alloys. However, the texture evolution and role of ordering on texture formation of rolled and extruded alloys are not well understood. Such studies will be useful for research community to shape up Fe-Ga alloys for practical applications.